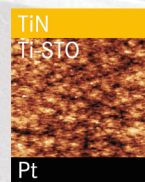
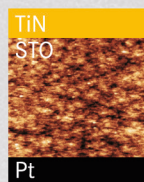
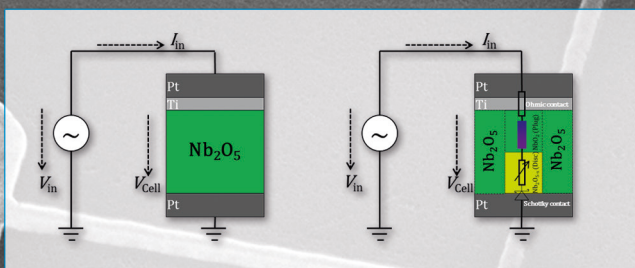


# Resistive switching memory devices from atomic layer deposited binary and ternary oxide thin films

Nabeel Aslam

$\text{Nb}_2\text{O}_5$  after electro-forming

$$R_{\text{Filament}} \approx R_{(1\text{MS}+1\text{TS})} = [R_{\text{Disc}(\text{Nb}_2\text{O}_{5-x})} + R_{\text{Plug}(\text{NbO}_2)}]$$







Forschungszentrum Jülich GmbH  
Peter Grünberg Institute (PGI)  
Electronic Materials (PGI-7)

# **Resistive switching memory devices from atomic layer deposited binary and ternary oxide thin films**

Nabeel Aslam

Schriften des Forschungszentrums Jülich  
Reihe Information / Information

Band / Volume 52

ISSN 1866-1777

ISBN 978-3-95806-274-0



Bibliographic information published by the Deutsche Nationalbibliothek.  
The Deutsche Nationalbibliothek lists this publication in the Deutsche  
Nationalbibliografie; detailed bibliographic data are available in the  
Internet at <http://dnb.d-nb.de>.

Publisher and  
Distributor: Forschungszentrum Jülich GmbH  
Zentralbibliothek  
52425 Jülich  
Tel: +49 2461 61-5368  
Fax: +49 2461 61-6103  
Email: [zb-publikation@fz-juelich.de](mailto:zb-publikation@fz-juelich.de)  
[www.fz-juelich.de/zb](http://www.fz-juelich.de/zb)

Cover Design: Grafische Medien, Forschungszentrum Jülich GmbH

Printer: Grafische Medien, Forschungszentrum Jülich GmbH

Copyright: Forschungszentrum Jülich 2017

Schriften des Forschungszentrums Jülich  
Reihe Information / Information, Band / Volume 52

D 82 (Diss. RWTH Aachen University, 2017)

ISSN 1866-1777

ISBN 978-3-95806-274-0

Vollständig frei verfügbar über das Publikationsportal des Forschungszentrums Jülich (JuSER)  
unter [www.fz-juelich.de/zb/openaccess](http://www.fz-juelich.de/zb/openaccess).



This is an Open Access publication distributed under the terms of the [Creative Commons Attribution License 4.0](https://creativecommons.org/licenses/by/4.0/),  
which permits unrestricted use, distribution, and reproduction in any medium, provided the original work is properly cited.

# Abstract

Redox-based resistive switching memory (ReRAM) is rigorously investigated for next generation non-volatile storage devices, which comprise the new storage class memory (SCM) and realizations of logic in memory functions that aim towards the internet of things (IoT) and to neuromorphic computing. These applications require an aggressive downscaling of the energy consumption of the new memory devices as compared to actually used volatile dynamic random access memory (DRAM) or non-volatile Flash memory. ReRAM perfectly fits here due to its high energy efficiency, that means, low voltage operation, good endurance and stable retention at high integration density. The ReRAM function is based on the capability of certain metal/metal oxide/metal cells to change the resistance when electric stimuli are applied.

For cell dimensions of a few 10 nm in each direction, the local uniformity of the resistive switching (RS) layer and its compositional homogeneity become an issue. So far, a lot of ReRAM research has been performed on rather thick (>25 nm) oxides grown by physical vapor deposition. For industrial application, atomic layer deposition (ALD) will be given priority because of its potential to grow ultrathin metal oxide films of high density and homogeneity with a conformal coverage. Most ALD oxide films are as grown in the amorphous state and crystallization heat treatment is performed prior to integration. However, for ultrathin (~10 nm) films there is rather limited information on compositional homogeneity after annealing. This effect is of particular importance for ternary thin films where the local cation (off-) stoichiometry might affect the microstructure and also the switching performance of the entire device. Highest integration density of ReRAM is achieved if the individual memristors are integrated into a passive crossbar array. However, sneak path currents through unselected cells neighbouring the switching cell put a severe restriction on the maximal achievable amount of cells in this array. Therefore, bipolar-type selectors have to be added to each memristor. Selectors can be obtained from volatile threshold switches, like, for example, NbO<sub>2</sub>, while the adjustment of the required phase is an issue.

Inspired by the dynamics of the constantly growing ReRAM research this work deals with two oxidic materials where stoichiometries and phase formations play a crucial role. Both systems, namely strontium titanate (Sr<sub>x</sub>Ti<sub>y</sub>O<sub>z</sub> (short: STO)) and niobium oxide (Nb<sub>2</sub>O<sub>5</sub>/NbO<sub>2</sub>), have been so far seldomly utilized in ReRAM devices when grown by

ALD. The study covers compositional and morphological effects of the ALD oxide films, device integration issues and investigations on the resistive switching (RS) and threshold switching (TS) performance.

The first part focuses on the RS characteristics of plasma-assisted ALD grown 15 and 12 nm thin STO films integrated into Pt/STO/TiN crossbar structures of 100  $\mu\text{m}^2$  to 0.01  $\mu\text{m}^2$  size. Effects of composition and microstructure were evaluated for three Sr/ (Sr+Ti) stoichiometries of 0.57 (Sr-rich STO), 0.50 (stoichiometric STO), and 0.46 (Ti-rich STO). The STO composition clearly influences the crystallization behavior as probed by nano-structural characterizations. Local current maps match with local changes of the films' microstructures and with the integral electrical response of the nanostructured devices. From this study it is possible to differentiate between compositional and microstructural origins of various resistive switching effects.

The second part deals with ALD grown 10 nm thin amorphous  $\text{Nb}_2\text{O}_5$  films integrated into Pt/ $\text{Nb}_2\text{O}_5$ /Ti/Pt nano-crossbar structures. After the electroforming step the cells revealed interesting current-voltage characteristics which showed up as a combination of non-volatile memory switching and volatile threshold switching.  $\text{Nb}_2\text{O}_5$  is a high band gap insulator allowing for VCM-type resistive switching upon local reduction to  $\text{Nb}_2\text{O}_{5-x}$ . In contrast,  $\text{NbO}_2$ , is a low band gap material that enables electric-field stimulated threshold switching and shows an insulator-to-metal-transition at 1080 K. The combination of memory and selector function in a single metal/memristor/selector/metal stack plays a key role for the realization of  $4\text{F}^2$  highest density passive crossbar ReRAM arrays. Accurate tuning of the electrical stimuli during electroforming and resistive switching enables an adjustment of the fraction of the volatile threshold switching  $\text{NbO}_2$  phase and the non-volatile memory switching  $\text{Nb}_2\text{O}_{5-x}$  phase. This finding, which was confirmed by electron-beam nanodiffraction analysis, is crucial for the design of highly integrated selector-memristor-structures. Furthermore, it provides additional physical insight into ion migration processes occurring during the electroforming and switching events.

# Kurzfassung

Im Bereich zukünftiger nicht-flüchtiger Datenspeicher wird intensiv an redox-basierten widerstandsschaltenden (memristiven) wahlzugriffsfreien Speichern, sogenannten ReRAM, geforscht. ReRAM sind interessant für eine neue Klasse in der Speicherhierarchie, dem sogenannten ‚storage class memory‘ (SCM), sowie für neue Konzepte wie Logik-in-Speicher Funktionen und neuromorphe Architekturen. Zukünftige Anwendungen wie das ‚Internet der Dinge‘ (IoT: internet of things) fordern einen extrem geringen Energieverbrauch verglichen mit aktuellen Speichern wie DRAM und Flash. ReRAM besitzt diese hohe Energieeffizienz durch niedrige Schaltspannungen, eine hohe Zyklenstabilität, und stabile Speicherzustände in Kombination mit einer hohen Integrationsdichte. Diese Eigenschaften begründen sich aus der Funktionsweise von ReRAM, die auf einem Widerstandswechsel in Metall/Metalloxid/Metall Strukturen basiert in Folge eines elektrischen Feldes mit einhergehender stromgetriebener Erwärmung.

Die technologisch relevanten Abmessungen von ReRAM Zellen von wenigen zehn Nanometern in jeder Richtung stellen hohe Anforderungen an die Gleichmäßigkeit und Homogenität von Morphologie und Zusammensetzung der resistiv schaltenden Oxidschichten. Während in der Vergangenheit vielfach gesputterte Schichten mit Dicken oberhalb von 25 nm untersucht wurden, werden für zukünftige Bauteile die Schichten auf dreidimensional strukturierten Oberflächen abgeschieden und die Schichtdicken werden im Bereich einiger Nanometer liegen. Ideal dafür ist das chemische Verfahren der Atomlagenabscheidung (ALD: atomic layer deposition), welches über einen zyklischen Beschichtungsprozess ultradünne Schichten mit hoher Dichte und Homogenität bei Temperaturen unterhalb von 400 °C oberflächenkonform abscheiden kann. ALD gewachsene Oxidschichten sind meist amorph und müssen meist über eine Temperaturbehandlung kristallisiert werden. Hierbei ist jedoch wenig bekannt über die Homogenität in der chemischen Zusammensetzung ultradünner (~ 10 nm) Oxidschichten nach einer Temperaturbehandlung. Besonders für komplexe Oxide können lokale Inhomogenitäten in der Kationenstöchiometrie sowohl die Mikrostruktur als auch das Schaltverhalten signifikant beeinflussen.

Die höchste Speicherblockdichte wird für passive Kreuzstrukturen erreicht, wobei die Speicherelemente in den Kreuzungen der Leiterbahnen platziert sind. Die maximal

erzielbare Blockgröße wird dabei jedoch von Kriechströmen begrenzt, die durch nicht-ausgewählte Nachbarzellen im ‚An‘-Zustand fließen. Zur Unterdrückung dieser Kriechströme sind bipolare Auswahllemente, sogenannte Selektoren, erforderlich. Selektorelemente, die zusammen mit der memristiven Zelle im Kreuzungspunkt der Leiterbahnen integriert werden könnten, sind beispielsweise flüchtige Schwellwertschalter aus Niobdioxid ( $\text{NbO}_2$ ).

In der vorgelegten Arbeit werden zwei Oxidmaterialien behandelt, die für zukünftige ReRAM Anwendungen relevant sind, jedoch bislang nicht als ALD Schichten in ReRAM Zellen integriert wurden. Dies sind Strontiumtitanat ( $\text{Sr}_x\text{Ti}_y\text{O}_z$ , STO)) und Nioboxid ( $\text{Nb}_2\text{O}_5/\text{NbO}_2$ ). Durch systematischen Vergleich von Pt/STO/TiN ReRAM Zellen aus 12 und 15 nm dünnen STO Schichten mit unterschiedlicher Zusammensetzung, Sr/ (Sr+Ti) von 0.57 (Sr-reich), 0.50 (stöchiometrisch), and 0.46 (Ti-reich) kann ein deutlicher Einfluss der Kationenstöchiometrie auf das Kristallisationsverhalten gezeigt werden. Durch Vergleich der Schaltcharakteristiken der unterschiedlichen ReRAM Zellen ist es möglich, Einflüsse der chemischen Zusammensetzung klar von morphologischen Effekten auf die Schaltcharakteristik komplexer STO Zellen zu trennen. Dies ist für das Design zukünftiger Speicherelemente von entscheidender Bedeutung.

Amorph abgeschiedene 10 nm dünner ALD  $\text{Nb}_2\text{O}_5$  Schichten integriert in nano-Kreuzungspunktstrukturen, Pt/ $\text{Nb}_2\text{O}_5$ /Ti/Pt, zeigen nach dem Elektroformierungsschritt interessante Strom-Spannungszyklen. Diese für die Integration in passive Speicherelemente interessante Schaltcharakteristik lässt sich nur durch eine Kombination aus nicht-flüchtigem memristiven Schalten und flüchtigem Schwellwertschalten beschreiben. Diese Interpretation setzt im Bereich des schaltenden Filaments eine Phasenseparation in einen memristiven  $\text{Nb}_2\text{O}_{5-x}$  Bereich und einen Schwellwert-schaltenden  $\text{NbO}_2$  dominierten Bereich voraus. Die Existenz einer kristallinen  $\text{NbO}_2$  Phase mit ungefähr 20 nm im Durchmesser konnte durch Elektronenbeugung an einer geschalteten Zelle eindeutig nachgewiesen werden.

Am Beispiel zweier aktueller ReRAM Materialien zeigt die Arbeit wie ein Verständnis des Materialverhaltens und möglicher Drift- und Diffusionsprozesse beim Elektroformieren und Schalten zur physikalischen Erklärung der Schaltprozesse in Nanostrukturen wesentlich beitragen kann.

# Acknowledgements

During my PhD work, I met many delightful people who I would like to thank for helping me to end my PhD. I would like to express my deepest gratitude to these people as professionals or simply friends. I would like first to thank Prof. Rainer Waser for giving me the great opportunity to participate in the interesting field of new class of non-volatile memories and let me work in his institute (PGI-7) for three and a half years. Furthermore, I thank Prof. Georg Roth and Prof. Regina Dittmann for being the reviewers for my thesis. One of the greatest honours of pursuing my PhD research has been the chance to work closely with my supervisor Dr. Susanne Hoffmann-Eifert. I am everlastingly grateful to her, whose serenity, forbearance, reassurance, and firm commitment have saved me from risk more times than I can reminiscence. I thank her for the productive discussions throughout the work, for her priceless comments and suggestions that gave me the chance to come up with significant scientific results. I thank Dr. Marcel Reiners, my best friend like a brother, for the great time together in office and hours of fun and happiness while working together. I would like to thank Hehe Zhang for helping to during the last days of my PhD. I thank Dr. Irina Kärkkänen for social, scientific and cultural discussions. I thank Dr. Christian Rodenbücher for his great participation to the most of my research activities. I would like to give very special thank to Dr. Felix Gunkel for giving me courage, help and moral support during week times. He is truly a great man and inspiration for me. I will allways miss great times which I have spent with Dr. Paul Meuffels while smoking and discussing science, religion, politics and culture.

My next special thanks goes to the engineers in PGI-7, in particular, René Borowski for assisting and helping me to solve and use different tools and systems in the cleanroom (and for giving me the permission to use the cleanroom at weekends). You have truly witnessed my love and passion for varied fabrication processes. I want to owe a great debt to my all PGI-7 colleagues for their nice, cheering and friendly company, especially Bernd Rösgen, Dr. Florian Lentz, Dr. Michael Paßsens, Dr. Katharina Skaja, Dr. Christoph Bäumer, Dr. Christian Rodenbücher, Dr. Nicolas Raab, Carsten Funck, Alexander Hardtdegen and all others for fantastic time and atmosphere at the institute. I thank Dr. Vikas Rana for supporting me throughout my PhD. My special thanks go to Maria Garcia for all the leagel issue and moral support during my PhD.

Thanks to the Enhance consortium (EU Marie Curie Initial Training Network project 230409) through which I have received in addition a very strong training in science and technology, a lot of very good friends, scientific collaborations and contacts that are precious for my future career. Thanks to this project I have had a chance to travel all over Europe for invaluable workshops and summer-schools. These have been the events to share the great moments with very smart and great people: Valentino, Tim, Yoann, Bruno, Marco, Daniela, Mostafa, and Matthieu. Within the *ENHANCE* network I had opportunities to establish collaborations. For this I would like to thank Dr. Valentino Longo, Prof. Dr. W.M.M. Kessels, Prof. Fred Roozeboom (Technical University Eindhoven) and Dr. Timothee Blanquart, Prof. Markku Leskelä, Prof. Mikko Ritala and Dr. Jaakko Niinistö (University of Helsinki).

I would like to thank my mother Shameem Akhter and father late Muhammed Aslam whose prayers and undefined, unlimited love makes me strong and blessed always. I cannot forget my uncle Muhammad Akram for his faith in me and allowing me to be as ambitious as I wanted to be in my life. I also thank my friends, in particular Dr Khan Zaib Jadoon and Shahid Ali Khan, for their encouragement and continues support. Last but not least, I thank to my wife Tayyaba Nabeel for her love and support. Her support, encouragement, quite patience and unwavering love were undeniably the bedrock upon which the PhD time of my life has been built.

# Contents

<b>1. Introduction</b>	<b>1</b>
1.1 State of the art	1
1.2 Scope of this work	3
<b>2. Fundamentals</b>	<b>7</b>
2.1 Redox-based resistive switching mechanisms	7
2.2 High density integration and constraints of ReRAM	9
2.3 Nanoscale integration utilizing atomic layer deposition	11
2.4 Material properties	13
2.4.1. $\text{SrTiO}_3$	13
2.4.2. $\text{Nb}_2\text{O}_5$	15
<b>3. Integration of the Micro- and Nano-Crossbar Devices</b>	<b>19</b>
3.1 Thin film deposition techniques	19
3.1.1. Atomic layer deposition (ALD)	19
3.1.2. Plasma assisted ALD of $\text{Sr}_x\text{Ti}_y\text{O}_z$ thin films	22
3.1.3. Thermal ALD of $\text{Nb}_2\text{O}_5$ thin films	23
3.1.4. Sputter deposition of metal layers	25
3.1.5. Thermal evaporation of metal films	26
3.2 Patterning techniques	28
3.2.1. Micro-crossbar patterning	28
3.2.2. Nano-crossbar patterning	34
3.2.3. Mask layout	35
3.2.4. Nanoimprint lithography (NIL)	35
3.2.5. Electron beam lithography (EBL)	40
3.3 Structuring	51
3.4 Characterization of thin films and devices	53
3.4.1. Thin film characterization methods	53
3.4.2. Electrical characterization methods	55
<b>4. Material Properties of ALD grown <math>\text{Sr}_x\text{Ti}_y\text{O}_z</math> Films</b>	<b>57</b>
4.1 Chemical and physical properties of ALD $\text{Sr}_x\text{Ti}_y\text{O}_z$	57
4.1.1. Chemical properties of ALD grown $\text{Sr}_x\text{Ti}_y\text{O}_z$	59



4.1.2. Optical properties of ALD grown $\text{Sr}_x\text{Ti}_y\text{O}_z$ .....	61
4.2 Crystallization behavior of ALD grown $\text{Sr}_x\text{Ti}_y\text{O}_z$ films.....	64
4.3 Morphologies of ALD grown $\text{Sr}_x\text{Ti}_y\text{O}_z$ films.....	64
4.4 Summary .....	68
<b>5. Resistive Switching Behavior of the <math>\text{Sr}_x\text{Ti}_y\text{O}_z</math> Films .....</b>	<b>69</b>
5.1 Electrical properties of crossbar cells in the initial state .....	69
5.1.1. Micro-crossbar devices.....	70
5.1.2. Nano-crossbar devices.....	72
5.2 Electro-forming of the crossbar devices.....	73
5.3 Resistive switching of the crossbar devices .....	75
5.3.1. Set and reset-voltages .....	77
5.3.2. ON- and OFF- resistance states .....	80
5.3.3. Area dependence.....	80
5.4 Local-conductivity probed by LC-AFM .....	83
5.5 Summary .....	86
<b>6. Material and Electrical Properties of ALD <math>\text{Nb}_2\text{O}_5</math> .....</b>	<b>87</b>
6.1 Thin film properties of ALD grown $\text{Nb}_2\text{O}_5$ .....	87
6.1.1. Chemical properties.....	87
6.1.2. Morphological and structural properties.....	89
6.2 Local conductivity of $\text{Nb}_2\text{O}_5$ probed by LC-AFM .....	92
6.3 Resistive switching in $\text{Nb}_2\text{O}_5$ micro-crossbar devices .....	95
6.3.1. ALD $\text{Nb}_2\text{O}_5$ films in symmetric Pt micro-crossbar structures.....	96
6.3.2. ALD $\text{Nb}_2\text{O}_5$ in micro-crossbars with asymmetric electrodes .....	98
6.4 Summary .....	102
<b>7. Resistive Switching of <math>\text{Nb}_2\text{O}_5</math> Nano-Crossbar Cells .....</b>	<b>103</b>
7.1 Threshold switching triggered by an electric field.....	104
7.2 Threshold and memory type (1TS+1MS) switching.....	106
7.2.1. Initial Leakage, Electro-forming and RESET process.....	106
7.2.2. Basic switching operation of (1TS+1MS) devices .....	110
7.3 Analysis of combined (1TS+1MS) switching.....	113
7.3.1. Voltage controlled switching.....	113
7.3.2. Extraction of the threshold (1TS) switching.....	116
7.3.3. SPICE simulation based on (1TS+1MS) devices .....	118
7.3.4. Current-controlled negative differential resistance (CC-NDR).....	121

7.3.5. Current Controlled Switching .....	124
7.4 Area dependency .....	126
7.5 Nanodiffraction of a Nb <sub>2</sub> O <sub>5</sub> nano-crossbar device .....	127
7.5.1. Nanodiffraction analysis .....	130
7.6 Summary.....	133
<b>8. Applications of (1TS+1MS)-type Nb<sub>2</sub>O<sub>5</sub> Devices .....</b>	<b>135</b>
8.1 Write and read operations of (1TS+1MS) devices .....	135
1.1 Write operation.....	135
2.1 Read operation .....	136
8.2 LRS-non-linearity in (1TS+1MS) nano-crossbar devices .....	139
8.3 Constraints for (1TS+1MS)-based crossbar-arrays .....	141
8.4 Achievable size for a (1TS+1MS) based crossbar array .....	143
8.5 Summary.....	146
<b>9. Summary and Outlook.....</b>	<b>147</b>
9.1 Resistive switching in ALD grown Sr <sub>x</sub> Ti <sub>y</sub> O <sub>z</sub> thin films .....	147
9.2 Resistive switching in ALD grown Nb <sub>2</sub> O <sub>5</sub> thin films .....	148
9.3 Outlook .....	150
<b>Bibliography .....</b>	<b>151</b>



# 1. Introduction

---

The continuous down scaling in size of semiconductor devices is driven by the requirements for power saving, cost reduction, and speed as well as by the performance enhancement of electronic circuits. This is made possible due to steadily increasing integration densities in semiconductor manufacturing coming along with an increased performance and enhanced functionalities. The relation between cost saving and the development of new products, from the past decades until today, has verbalized a roadmap directing to keep alive the Moore's law [1]. The demand for more and faster digital mobile applications including cloud-services of higher complexity generates a need for higher storage capacity, as well as cheaper, highly reliable, and faster non-volatile memory. At the moment Flash Memory is the leading player in the market of non-volatile memories. However Flash memory devices are approaching their physical limits regarding long-time data retention as well as short-time data access write/ read times. More important, Flash memory uses a transistor as select device for each memory cell which is becoming a challenge for the integration prospective towards tera-byte memory. Additionally, the transistor scaling approach is also becoming very challenging since passing the 16 nm node and will not continue to be available with the current economical effort [2]. Among future alternatives for an energy-efficient, non-volatile memory device the redox-based memristive device (ReRAM) is one of the most promising concepts enabling high integration density, fast access time, high endurance, and sufficient data retention [6].

## 1.1 State of the art

New alternative memory should be non-volatile and scalable, which means that it should not rely on purely electronic charge storage [200]. Two main concepts are currently intensively investigated. The magnetic RAM (MRAM) utilizing the spin-information and the resistive RAM (RRAM) where the information is stored in the ionic configuration of the system. Different types of resistive RAM are classified with respect to their working

principles, like for example the phase change mechanism (PC-RAM) and the redox-based resistive switching mechanism (ReRAM), comprising electrochemical metallization cells (ECM) and devices based on the valence change mechanism (VCM). In the latter one, the valence state of a host cation is changed by oxidation or reduction, respectively, induced by oxygen ion (or vice versa oxygen vacancy) drift under the application of an electric field [201]. In general, ReRAM devices are realized by simple two terminal metal-insulator-metal thin film structures. The electroforming process which equals a soft dielectric breakdown of the insulator often leads to the formation of an electronically conducting filament connecting the metal electrodes. The length of the filament changes during the resistive switching SET and RESET events. Due to the rather small diameter of the filamentary switching regime of about a few 10 nm, ReRAM devices offer high density integration in addition to endurance, multilevel capability and low fabrication cost depending upon the material engineering and the device design [3-5]. This makes ReRAMs also interesting for a new type of memory, the so called storage class memory (SCM) which is proposed to fill the ‘performance gap’ between the extremely fast, but volatile, dynamic RAM (DRAM), and the non-volatile, but rather slow Flash memory. Energy efficient, non-volatile, and ultra-high density integrated memory is a prerequisite for the ‘internet of things (IoT)’ [199]. In addition, ReRAM might be utilized for logic-in-memory applications as well as for ‘beyond von Neumann’ architectures up to neuromorphic computing [41].

Although recent research has provided a lot of insight into the switching mechanisms of ReRAM devices, like, for example, pointing out the importance of oxygen vacancy generation and drift/diffusion in VCM-type ReRAM devices, further control of the switching properties with respect to switching power, endurance and retention for example remain challenging [31]. These properties are strongly related to the materials’ design, with respect to composition and microstructure, of a multi-component oxide utilized for switching applications, as well as the design of advanced device stacks with integrated selective and memristive functions, especially on the length scale of only a few 10 nm of technological relevant device structures.

## 1.2 Scope of this work

The main objectives of this work comprise (1) the effect of materials design regarding composition and microstructure of a multi-component oxides on the resistive switching performance of derived nano-crossbar ReRAM cells, and (2) the importance of the design of device stacks with integrated selective and memristive functions. In this work, ReRAM cells with dimensions close to industrial relevance, i.e. a size of about 100 nm x 100 nm and thickness of the switching oxide film of about 10 nm, should be fabricated and characterized. The oxide layers with a thickness of about 10 nm should be grown by means of an industrially compatible process which for later application should also enable conformal coverage over three dimensional structures. Therefore, atomic layer deposition (ALD) was chosen for the deposition of the ternary  $\text{Sr}_{1+x}\text{Ti}_{1+y}\text{O}_{3+z}$  and the binary  $\text{Nb}_2\text{O}_5$  thin films. The films should be integrated into micro- and nanocrossbar structures built from Pt bottom electrodes and TiN or Ti/Pt top electrodes, respectively, patterned by nanoimprint and electron beam lithography, and structured by reactive ion beam etching.

For topic (1)  $\text{SrTiO}_3$  is chosen as the multicomponent VCM-type material for several reasons. First,  $\text{SrTiO}_3$  is a well known model material representing perovskite type oxides and therefore the defect structure and redox-type behavior is very well understood [206-207]. The cubic structure is stable from about -200°C up to high temperatures, and superstoichiometric phases, like for example the Sr-rich Ruddlesden-Popper phases [208] or the Ti-rich Magnéli-type phases [209] are well described.  $\text{SrTiO}_3$  is available and characterized in the form of single crystals [210], heteroepitaxial thin films grown by pulsed laser deposition [211] and molecular beam epitaxy, and as polycrystalline bulk ceramic [211, 212]. Polycrystalline thin films grown by chemical solution deposition (CSD) [213], sputtering [214], metal organic chemical vapor deposition (MOCVD), and atomic layer deposition (ALD) [215-217] have been intensively investigated in recent years for application as high permittivity material in storage capacitors or in tunable filters. Effects of the Sr/Ti cation stoichiometry on the resistive switching properties of  $\text{SrTiO}_3$  thin films has been extensively investigated by Dittmann and co-workers, however, for heteroepitaxial layer stacks utilizing Nb:SrTiO<sub>3</sub> or SrRuO<sub>3</sub> as the bottom electrode, for thicker films, i.e. 20 – 50 nm, and for larger devices, i.e. 100 µm [230]. The aim of this work was to study the effect of  $\text{SrTiO}_3$  composition and microstructure for small devices which utilize a deposition process which is of industrial relevance and a cell structure which includes metal electrodes. Therefore, ALD has been chosen as the growth

method because it enables the growth of homogeneous, dense, amorphous films with well controlled composition and conformal coverage of three dimensional electrodes.

For topic (2) amorphous films of niobium oxide has been selected for reason of the interesting properties of the different polymorphs. Di-niobium pentaoxide ( $\text{Nb}_2\text{O}_5$ ) is known as a high band-gap insulating material frequently used as tunnel oxide [218].  $\text{NbO}_2$  is a low band gap material which shows an insulator to metal transition at about 1080 K [219].  $\text{NbO}_2$  thin films show a volatile threshold switching which makes these layers interesting for selector applications utilized in passive ReRAM crossbar architectures [220]. Again, the cells were realized by industrial relevant processes utilizing ALD for the growth of the amorphous  $\text{Nb}_2\text{O}_5$  layer integrated into nanocrossbar structures of Pt and Ti/Pt.

The present thesis is structured into nine chapters. Chapter 2 is brief introduction to the basics of redox based resistive switching memories and their integration at the nanoscale for future non-volatile memory applications. In addition, material properties of the investigated binary and ternary oxides are resumed. Details on the experimental techniques used for the integration of the atomic layer deposited binary and ternary oxides into single nano and microcross bar devices are described in Chapter 3.

Chapters 4 and 5 are dedicated to topic (1), i.e., the  $\text{Sr}_x\text{Ti}_y\text{O}_z$  system. Chapter 4 summarizes the results from chemical, morphological and structural analysis of the  $\text{Sr}_x\text{Ti}_y\text{O}_z$  films grown by plasma assisted ALD on planar  $\text{Si}/\text{SiO}_2/\text{Ti}$  (5nm)/ Pt (30nm) substrates after post annealing. The composition calculated from X-ray photoemission spectroscopy provides the average cation stoichiometry of the very thin  $\text{Sr}_x\text{Ti}_y\text{O}_z$  layers. The effect of the cation stoichiometry on the band gap, overall film morphology, and crystallization behavior is revealed by means of ellipsometry, atomic force microscopy and grazing incidence X-ray diffraction (GIXRD), respectively. In Chapter 5, the influence of the cation stoichiometry and crystallization behavior of the  $\text{Sr}_x\text{Ti}_y\text{O}_z$  films on the resistive switching properties of micro- and nanoscale devices are discussed. Local defects in the film's microstructures varying for the different compositions of  $\text{Sr}_x\text{Ti}_y\text{O}_z$  significantly affects the electrical properties of the  $\text{Pt}/\text{Sr}_x\text{Ti}_y\text{O}_z/\text{TiN}$  system regarding initial leakage, electroforming and resistive switching voltages. The polarity and the area independency of the resistive switching characteristics are discussed in details.

Chapters 6 to 8 are dedicated to topic (2), i.e., the  $\text{NbO}_2/\text{Nb}_2\text{O}_5$  system. In Chapter 6, the thin film properties of amorphous ALD  $\text{Nb}_2\text{O}_5$  layers grown on planar  $\text{Si}/\text{SiO}_2/\text{Ti}$  (5nm)/Pt (25nm) substrate are discussed with respect to morphology, composition, crystal structures and their electrical properties in the view of resistive switching application and the influence of the electrode materials. In the subsequent chapter 7, the threshold-type resistive switching characteristics are analyzed for nanoscale devices, which were fabricated by sandwiching the as-deposited stoichiometric  $\text{Nb}_2\text{O}_5$  film in between asymmetric nano-scale electrodes. Electrical and nanostructural analysis results are discussed. Utilizing the system introduced in chapter 6 and 7; chapter 8 demonstrates memory application of threshold-type resistive switching (1TS-ReRAM) devices with respect to reading and writing. This concept consists of bipolar and threshold-type resistive switching functions in-situ generated during electroforming out of an amorphous  $\text{Nb}_2\text{O}_5$  thin layer. With this intrinsic forming of a select function in combination with a memory function, large crossbar arrays might be feasible. The system is electrically characterized and the current-voltage characteristics are analysed by means of a SPICE model.

Finally, in Chapter 9 the new results and the achieved understanding of memory and threshold-type resistive switching behavior gained by this thesis' research will be summarized and an outlook towards further questions will be given.





## 2. Fundamentals

---

### 2.1 Redox-based resistive switching mechanisms

ReRAM cells basically consist of an insulating layer (e.g. a metal oxide) sandwiched between two metal electrodes (MOM stacks), and the information is stored in form of at least two or even multiple resistance states [7]. Reversible switching between the different resistance states is induced by certain voltage signals:  $V_{\text{set}}$  sets the device to the low resistance state (LRS, or ON-state) and  $V_{\text{reset}}$  resets the device to the high resistance state (HRS, or OFF-state). Basically, two modes of operation can be distinguished (see Fig.2.1). In unipolar resistive switching (URS) the cell changes its resistance with the same polarity for SET and RESET operation whereas for bipolar resistive switching (BRS) voltages of opposite polarity have to be applied for the SET and RESET operation. For ReRAM applications a resistance ratio  $R_{\text{OFF}}/R_{\text{ON}} > 10$  is required, while absolute values in the M $\Omega$ -range guarantee low power operation. Among the class of resistive switching (RS) materials transition metal oxides increasingly attract interest [8, 9].

Differentiating the physical mechanisms redox-based resistive switching is further divided into chalcogenide dominated and electrode dominated effects. The ‘chalcogenide dominated’ switching effects are classified into PCM (phase change mechanism), TCM (thermo-chemical mechanism) and VCM (valence change mechanism). In PCM-type devices, for example, the switching is controlled by temperature-induced phase transition between a well conducting crystalline phase (low resistive state) and an insulating amorphous phase (high resistive state) [11,221]. In contrast, electrochemical metallization cells (ECM) are controlled by dissolution of the electrochemical active electrode and subsequent growth of a metallic conducting filament. The filament is ruptured by applying a voltage of opposite polarity [12]. Among the redox-based resistive switching memories VCM-type devices are considered as one of the most promising candidates for future non-volatile memory application [6].

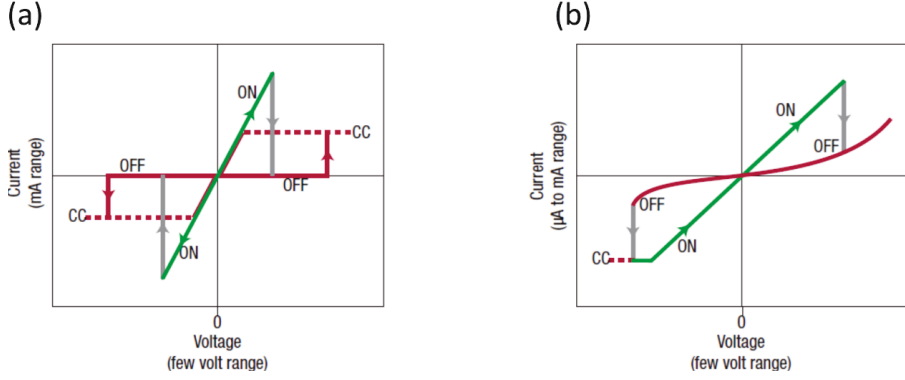


**Figure 2.1:** *I-V hysteresis of two basic resistive switching operations: (a) The unipolar resistive switching (URS) mode realized with same applied voltage polarity and (b) the bipolar resistive switching (BRS) mode requires different polarities for SET and RESET event. Reprinted with the permission of [10]*

For a wide range of metal oxides the valence change memory effect (VCM) applies, often explained by a migration of oxygen vacancies [10], while recently, also effects of mobile cations are discussed [228]. The local change of the metal to oxygen stoichiometry results from a nanoionic redox reaction and causes a valence change in the cation sublattice leading to a change in the electronic conductivity. VCM is characterized by a bipolar-type RS effect where the polarity of the applied voltage determines the direction of the redox reaction, i.e., reduction (set) or oxidation (reset) [13]. Basically, VCM cells consist of a high work function, chemically inert electrode, at which the RS takes place, a mixed ionic-electronic conducting (MIEC) layer, and an ohmic reference electrode from a material of higher oxygen affinity, which also serves as an oxygen exchange layer (OEL). In most M/O/M' stacks utilizing a single oxide layer an electroforming (EF) process at higher voltages  $V_{\text{form}}$  is required before stable bipolar RS can be obtained. In today's understanding of the VCM-type RS phenomena, the electroforming process locally removes oxygen ions from the insulating oxide lattice forming a well conducting filamentary type paths which enables a high current flow [13]. However, high forming voltages are undesirable because they are not applicable to integrated devices [14] and because a high forming power induces a major material reconstruction [15]. Therefore, the RS behavior of a device under study depends strongly on the performed EF procedure which needs therefore to be discussed along with the RS characteristics themselves. The diversity of the resistive switching materials that has been studied comprises binary and

ternary metal oxides, like  $\text{TiO}_2$  [16],  $\text{HfO}_2$  [17],  $\text{Ta}_2\text{O}_5$  [18],  $\text{ZrO}_2$  [19],  $\text{Nb}_2\text{O}_5$  [20],  $\text{SrTiO}_3$  [21],  $\text{Al}_2\text{O}_3$  [22],  $\text{SiO}_2$  [23]. However, good resistive switching (RS) characteristics do not just depend on the oxide material properties, but also the complete layer stack of the metal-oxide-metal (M/O/M') device is of great importance. For example, the electrodes' material and thickness show an important influence on the perseverance of the device operation and properties. Using different electrode materials and their thickness as top or bottom electrode might change the switching characteristics of the device [24, 26]. By changing the thickness of the electrodes it is possible to regulate the resistive switching modes, like for example unipolar, bipolar, and even complementary switching effects [24, 27-30].

## **2.2 High density integration and constraints of ReRAM**

Redox-based resistive memories (ReRAM) based on the valence change mechanism (VCM) are very attractive candidates for realizing future ultra-dense passive crossbar memories [31] proposing excellent retention [32, 33], endurance [34, 35], and scaling potential [36, 37]. Additionally, these cells might be directly integrated into the junctions of word and bit lines in passive crossbar arrays allowing for the highly dense  $4F^2$  integration.[6] Furthermore, the non-volatility of these devices permits logic operations directly to be performed within the memory array allowing for fast data processing by means of 'logic-in-memory operations' [38, 39]. In general, VCM-type cross-point junction devices can be considered as basic processing units for performing logic operations [40, 41].

Two dimensional stacking of resistive switching passive crossbar junctions is one approach for integration [42, 43]. Fig. 2.2 (a) shows a two dimensional (2D) passive crossbar array which might be placed on top of CMOS chip. However, three dimensional (3D) stacking requires alternative approaches to reduce the number of masks and etching steps which are necessary for the realization of the 3D structure. Promising concepts (see Fig. 2.2 b) make use of vertically stacked ReRAM cells, so called 3D-VRAM, in contrast to the horizontally integrated cells utilized in 2D arrays [44, 45, 46]. Improved scaling costs and the bit area miniaturization trend in 3D RRAM make these very suitable candidates for future crossbar architectures [47].

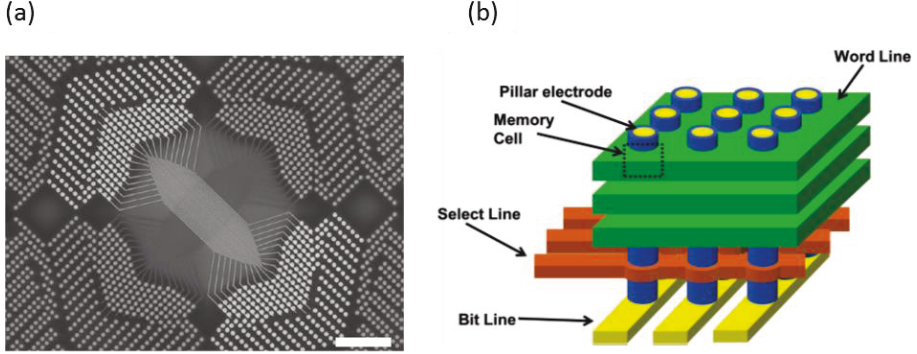


**Figure 2.2:** *a) Top view SEM micrograph of a two dimensional (2D) passive crossbar array fabricated on top of a CMOS chip. Reprinted from [43] with permission. b) Schematic diagram of a 3D-vertical RRAM. The switching oxide layer is sandwiched between the horizontal and vertical electrodes. Reprinted with permission of [48]*

Unlike 2D RRAM construction entailing the crossed metallic electrodes, here vertical electrodes realized for example by vias or trenches are used to enhance the storage density. Fig 2.2 (b) shows the schematic diagram of a vertical RRAM cell [48]. The vertical electrodes are crossing the horizontal electrodes layer by layer, separated by highly insulating material. The switching layer is sandwiched between crossed electrodes and forms a core-shell-like structure around the pillar-type electrode. In this geometry the switching area is defined by the horizontal electrode thickness and the circumference of the oxide layer. This gives an advantage for integrating a large number of cells. The deposition of the switching layer and the vertical metal electrode to fill the vias is challenging and can only be fulfilled by utilizing atomic layer deposition (ALD) technique.

Although, passive crossbar arrays from ReRAM devices offer huge potential for high density integration, sneak path currents, remain an issue that might cause program disturb on half-selected cells as shown in Fig 2.3 [49, 50]. To overcome this problem a certain select pattern must be applied. The conventional approach would be to add a selector element [222] in series to each cross-point junction device [51]. However, the current density requirements for the bipolar rectifying selector are challenging. Therefore, also options for selector-less approach are under discussion: The first one relies on inherent non-linearity offered by RRAM devices intrinsically during the ON-state [52] or rather a threshold type resistive switching behavior, i.e. 1TS-ReRAM [53, 54].

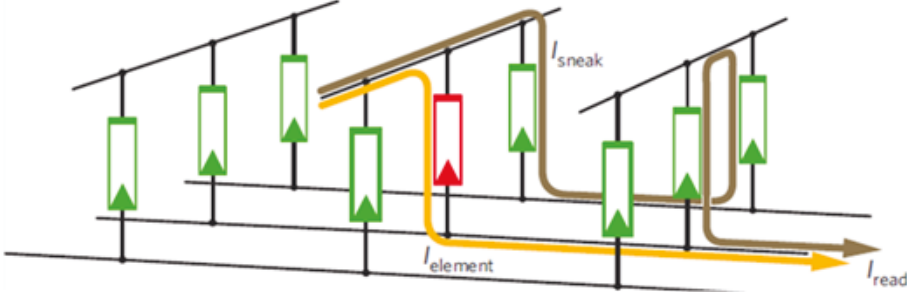


**Figure 2.3:** Sneak path issue while reading the state of the memory in a worst case scenario causes the significant amount of current flow through the unselected cells and limits the size of the passive cross bar arrays. Reprinted with permission of [49]

## 2.3 Nanoscale integration utilizing atomic layer deposition

The continuous down-scaling of microelectronic components, especially in memory technology, has enhanced the demand for advanced deposition techniques that permit mask less, defect free, and 3D coverage of any kind of surface and structure compatible with CMOS technology [2]. The most protuberant method for coating complicated structures is atomic layer deposition (ALD). ALD is the technique which offers precise, homogenous, dense, and pinhole free film growth, especially for oxides [56]. It also offers deposition of the thin films over high aspect ratio three dimensional (3D) structures with scaling potential below  $F < 22$  nm and with large area batch capability[224]. These are the major reasons why ALD is attractive for the deposition of the oxide layers of redox-based resistive switching devices, most importantly for 3D VRAM devices. For example, the deposition of  $\text{HfO}_2$  thin film by ALD in a three-dimensional (3D) RRAM device sitting on top of a via-hole is illustrated in Fig 2.4. A via hole anisotropically etched down to the Pt bottom electrode was filled by atomic layer deposition of first  $\text{HfO}_2$  and second TiN which serves as the top electrode [55]. Beside the thickness and conformity control, ALD process also gives access to control the material properties by means of tailoring the process parameters. Especially the composition of multi-component materials is typically adjusted by the ALD super-cycle sequence. In general ALD processes can be divided into three main cycle schemes as illustrated in Fig 2.5 [57].

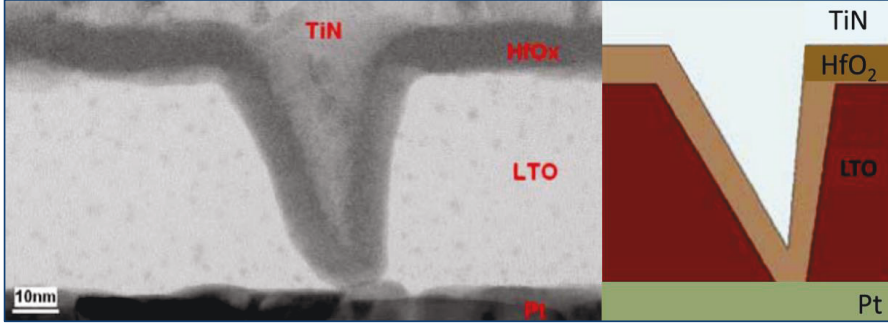


**Figure 2.4:** 3D-RRAM: on left side, a HRTEM image and, on the right side the schematic overview of the nano via-hole ReRAM device is shown. Reprinted with permission of [55]

The ‘Regular  $(AB)_m$  mode’ cycle scheme (c.f. Fig 2.5 (a)), as used for example in the case of  $\text{Al}_2\text{O}_3$ , employs pulsing of two co-reactants, i.e.  $A$ : metal precursor and  $B$ : oxygen source, separated by purging steps. In this work the ALD process of the  $\text{Nb}_2\text{O}_5$  films was performed by a regular injection scheme. The ‘Multistep  $(ABC)_m$  mode’ approach (c.f. Fig 2.5 (b)) encompasses the addition of one extra co-reactant  $C$ . This multi-step approach gives the possibility for further tuning of the material’s properties. This process is applied for ALD of Pt films from  $\text{Me}_3(\text{MeCp})\text{Pt}$  ( $A$ ), oxygen ( $\text{O}_2$ ) plasma ( $B$ ), and  $\text{H}_2$  plasma ( $C$ ) [58]. In general, doped binary oxide layers or multicomponent oxide thin films are deposited by means of the ‘Supercycle  $((A_1B_1)_m(A_2B_2)_n)_x$  mode’ as depicted in Fig 2.5 (c).

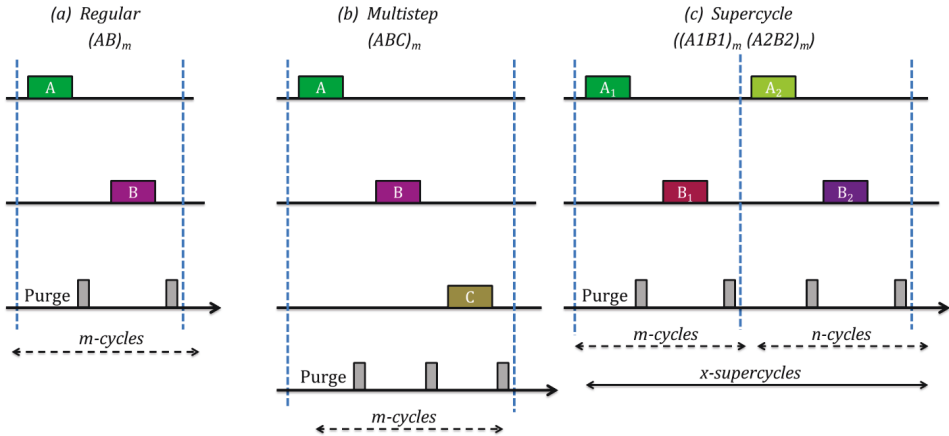


**Figure 2.5:** Schematic illustration of the (a) “Regular” ALD mode and more advanced ALD approaches: (b) the “Multistep” ALD mode (c) and the “Supercycle” ALD mode. Reprinted with permission of [57]

Here two regular ALD cycles  $A_1B_1$  and  $A_2B_2$  are combined sequentially, and the composition of the material is tuned by alteration the number of repetitions of the ALD cycles,  $m$  and  $n$  (shown in the subscript), respectively. As an example, Al doped zinc oxide films (ZnO: Al) were obtained by combining the ALD cycles of  $\text{Al}_2\text{O}_3$  and ZnO with different ratio depending upon the doping level [59]. In this work the ‘Supercycle’ approach was applied for the growth of the  $\text{Sr}_x\text{Ti}_y\text{O}_z$  thin films where the films’ stoichiometry was controlled by the repetitions of SrO and  $\text{TiO}_2$  ADL cycles [60]

## 2.4 Material properties

### 2.4.1. $\text{SrTiO}_3$

$\text{SrTiO}_3$  at room temperature exhibits an ideal cubic perovskite structure with a lattice parameter of about  $a = 3.905268 \text{ \AA}$  [61]. The unit cell of  $\text{SrTiO}_3$  contains Sr atoms positioned at the edges while the Ti atoms in the center of the cell occupy (1/2, 1/2, 1/2) positions. Each Ti atom is surrounded by six oxygen atoms that form an octahedral  $\text{TiO}_6$  cluster. In general the structure of  $\text{SrTiO}_3$  can be illustrated by corner-sharing  $\text{TiO}_6$  octahedra with Sr sitting in the spaces.  $\text{SrTiO}_3$  is an ionically bonded crystal, i.e., the valence electrons of the  $\text{Ti}3d$  and  $\text{Sr}5s$  orbitals are transferred to  $\text{O}2p$  orbital giving rise to the oxidation states being close to  $\text{Ti}^{4+}$ ,  $\text{Sr}^{2+}$  and  $\text{O}^{2-}$ . The extensively studied bipolar RS in epitaxial  $\text{SrTiO}_3$  thin film devices is basically attributed to an electric field- and temperature-enhanced drift of oxygen vacancies along filaments that induces a metal-to-insulator transition in the  $\text{SrTiO}_3$  material [10, 13, and 62]. The confined nature of the conductive filaments in single-crystalline  $\text{SrTiO}_3$  has been shown by Szot et al. using local-conductivity atomic force microscopy (LC-AFM) with nanometer resolution as shown in (Fig 2.6) [63]. In addition to the filamentary-type RS an area-dependent type of RS has been reported for epitaxial Fe-doped  $\text{SrTiO}_3$  films by Muenstermann et al.[64]. The corresponding  $I$ - $V$  switching curves reveal two main differences regarding the switching polarity and the electrode area scaling behavior. It should be noted that the RS polarity is defined for a ‘standard’ M/O/M’ configuration, when the voltage of the active electrode is displayed in the  $I$ - $V$  curve [13] and it shows no significant contact area dependence while the ‘homogeneous’ RS effect reported in [64] exhibits an ‘eightwise’ switching polarity and a clear pad size dependence of the conducting LRS state.



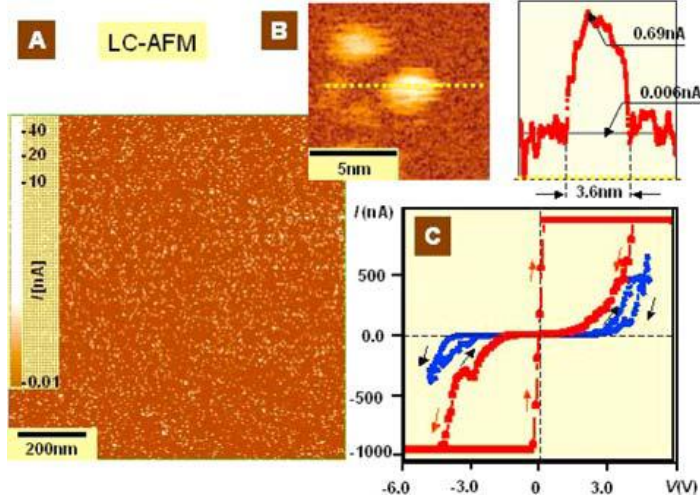


**Figure 2.6:** A local-conductivity atomic force microscopy (LC-AFM) scan of a  $\text{SrTiO}_3$  (10nm)/ $\text{SrRuO}_3$  layer stack contacted by a Pt/Ir LC-AFM tip. (A) Conductivity map at the micron scale and (B) at the nano scale and (C) I-V characteristics of the two conductive spots as shown in (B). Reprinted with the permission of [65]

According to Muenstermann et al. [64], both types of RS, filamentary and area switching, can coexist in the same epitaxial  $\text{SrTiO}_3$  thin film, depending on the local defect density in the active switching regime. From in-situ switching studies by means of photoemission electron microscopy and analytical transmission electron microscopy Bäumer et al [229] derived a qualitative model for eightwise switching in Nb:STO/STO/Pt structures which considers an oxygen exchange reaction at the  $\text{SrTiO}_3$ /Pt interface being responsible for the eightwise switching behavior. For the pulsed laser deposited (PLD)  $\text{SrTiO}_3$  films also effects on the RS behavior originating from growth induced structural defects and from variations in the cation stoichiometry were reported [66-67]. These studies on epitaxial  $\text{SrTiO}_3$  thin films already showed that the control of the density and the distribution of defects are of utmost importance for the fabrication of reproducible and scalable resistive switching devices. An obstacle for the application of epitaxial STO layers is that they are generally grown by high temperature PLD processes on single crystalline oxide substrates. Both requirements are not compatible with the high-density large-scale integration of up-to-date memory technologies.

### 2.4.2. $\text{Nb}_2\text{O}_5$

Niobium pentoxide is a group (V) transitional-metal oxide with a wide band gap. There are three relevant oxides in the Nb-O system,  $\text{Nb}_2\text{O}_5$ ,  $\text{NbO}_2$  and  $\text{NbO}$  as depicted in the phase diagram in Fig. 2.7 [180]. The electrical properties of the three oxides differ significantly. Two crystal structures are known for stoichiometric  $\text{Nb}_2\text{O}_5$ , a monoclinic structure called the  $\alpha$ -form and an orthorhombic structure named the  $\beta$ -form [181].  $\text{Nb}_2\text{O}_5$  is a wide band gap n-type semiconductor material with a gap of about 3.9 eV [68]. Due to its interesting dielectric properties  $\text{Nb}_2\text{O}_5$  is used as high permittivity insulating thin film capacitor material. It has also been investigated for the non-volatile type resistive switching random access memories.  $\text{Nb}_2\text{O}_5$  is one of the first transitional metal oxide materials for which bistable switching has been reported already in 1969 as shown in the Fig. 2.8 (a) [182]. In contrast, niobium dioxide ( $\text{NbO}_2$ ) is a narrow band gap semiconductor at room temperature that undergoes an insulator to metal phase transition (IMT) at about 800 °C [183].

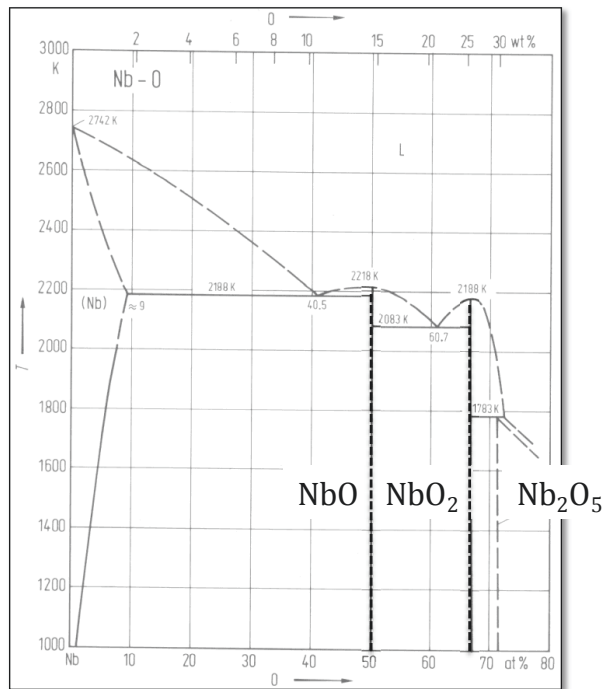


**Figure 2.7:** The phase diagram Nb-O from 0 to 80 at% oxygen. Reprinted with permission of [180]

The current-voltage characteristics in  $\text{NbO}_2$  based devices reveal an irregular behavior called threshold switching (TS) [120]. This effect is applied for bipolar select devices integrated into ReRAM arrays as will be discussed later in this thesis. Early studies on  $\text{NbO}_2$  thin film devices from the 1960's already report on a phenomenon called current-controlled negative differential resistance (NDR) that is shown in Fig. 2.8 (b). This effect which is closely related to threshold switching has been addressed to the insulator to metal phase transition in the early studies [120, 121]. The appearance of metallic conductivity is linked to a local temperature increase. Thus, the metallic phase disappears upon cooling which explains the volatile nature of threshold switching [118]. However, the interest in the threshold switching behavior of  $\text{NbO}_2$  thin films utilized for ReRAM select devices has brought up an alternative physical explanation for the observed current-voltage ( $I$ - $V$ ) characteristic.

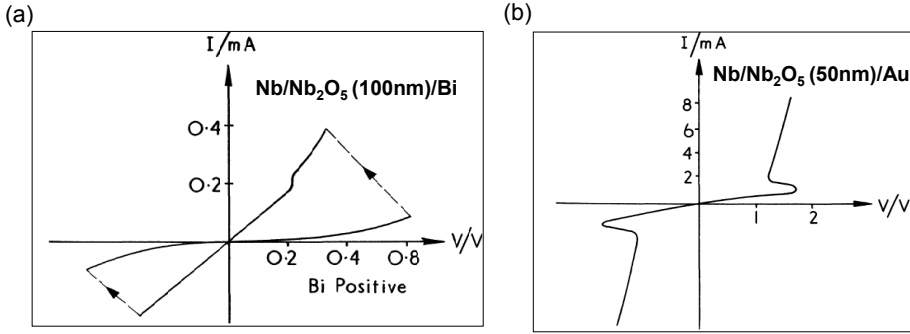


**Figure 2.8:** (a) The bistable switching in an Nb/100 nm  $\text{Nb}_2\text{O}_5$ /Bi capacitor stack [182] and (b) current-controlled negative differential resistance in the system Nb/50 nm  $\text{NbO}_2$ /Au. Reprinted with permission of [120]

The two models, (1) the insulator to metal transition (IMT) and (2) the electric field triggered thermal runaway (FTTR) will be summarized shortly in the next paragraph. In respect of the materials' selection made for the ALD processes studied thesis, unique properties of the Nb-O system made amorphous  $\text{Nb}_2\text{O}_5$  layers an interesting material to study crystallization and phase separation effect during the electroforming and switching process in respective nanoscaled devices. This will be discussed in detail in Chapters 6 and 7. As mentioned before in section (2.2) ReRAM passive cross bar arrays require select devices to practically address the write memory cells. However, selectors for bipolar resistive switching devices need to operate symmetrical with respect to the

polarity. One approach is the use of a select transistor, so called 1T1R cells, but this increases the occupied area of the ReRAM cell significantly beyond  $4F^2$ . Other concepts utilize complementary resistive switches (CRS, see section (2.2)) where two cells are antiseriably connected in a proper manner or bipolar type threshold devices based on  $\text{NbO}_2$  or  $\text{VO}_2$ . The feasibility of a  $\text{Pt}/\text{NbO}_2/\text{Pt}$  threshold-type selector combined with a  $\text{Pt}/\text{Nb}_2\text{O}_5/\text{Pt}$  RS memory device is shown in Fig. 2.9 (a), (b) [110]. In this study the two niobium oxide layers were deposited from reactive sputtering which allows for a good adjustment of the Nb/O stoichiometry but is not applicable for very thin layers or vertical structures necessary for high density intergration. A typical  $I$ - $V$  characteristic is shown in Fig. 2.9 (c) [110].

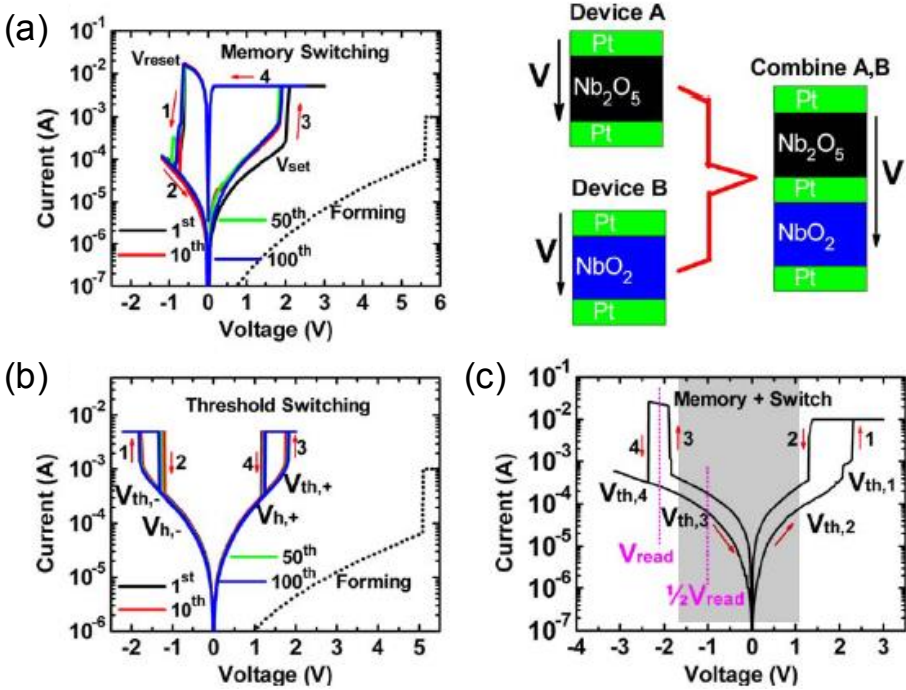


**Figure 2.9:** The schematics and operational representation of (a) bipolar two resistive switching in a  $\text{Pt}/\text{Nb}_2\text{O}_5/\text{Pt}$  memory cell and (b) threshold type switching in a  $\text{Pt}/\text{NbO}_2/\text{Pt}$  select cell. Diagram (c) shows the resulting  $I$ - $V$  characteristic which evolves for a serial connection of both types of cells, i.e.  $\text{Pt}/\text{NbO}_2/\text{Pt}$  and  $\text{Pt}/\text{Nb}_2\text{O}_5/\text{Pt}$  representing a combined threshold and bipolar resistive switching element, respectively. Reprinted with the permission of [110]

---

## 3. Integration of the Micro- and Nano-Crossbar Devices

---

In this chapter the fabrication procedures of the resistive switching cross bar devices are described in detail. The fabrication processes of the micro- and nanocrossbars, respectively, are divided into three main sections: thin film deposition, patterning and structuring. Additionally, the used electrical characterization methods will be described at the end of this chapter.

### 3.1 Thin film deposition techniques

In this section thin film deposition methods utilized for the fabrication of crossbar devices will be described. For high-end integration the precise and controlled deposition of thin films is a main prerequisite for processing of nanometer scale devices for resistive switching applications. The basic structural element of the VCM-type resistive switching cell is an M/O/M' stack which requires deposition of metal layers (M, M') as electrodes and a metal oxide (O) as the switching material. In this work oxide layers were deposited by means of plasma assisted atomic layer deposition (PE-ALD) for  $\text{Sr}_x\text{Ti}_y\text{O}_z$  and thermal ALD for  $\text{Nb}_2\text{O}_5$  whereas the metal deposition was performed by magnetron sputtering or thermal evaporation methods.

#### 3.1.1. Atomic layer deposition (ALD)

Atomic layer deposition (ALD) is a chemical vapor-phase technique for the deposition of ultrathin films. First publications on ALD appeared as 'molecular epitaxy' in the late 60's, and later named atomic layer epitaxy (ALE), mainly utilized for the growth of ZnS based thin film devices for the flat panel displays. [70, 71] The term 'ALE' is not used anymore today, because the main focus has been shifted from epitaxial growth towards thin film deposition of high permittivity dielectrics in the semiconductor industry [72]. The basic principle of ALD constitutes of the alternating sequencing of precursor and co-

reactant in the gas phase independently [56]. Thus the thin films are grown in a layer-by-layer type fashion due to the limited amount of precursor chemisorbed on, typically OH-terminated, surface sites in the precursor dose step. The reaction principle of ALD is illustrated by the example of  $\text{Al}_2\text{O}_3$  thin film growth shown in Fig. 3.1. Thermal ALD of  $\text{Al}_2\text{O}_3$  consists of an alternating delivery of  $\text{Al}(\text{CH}_3)_3$ , trimethylaluminum (TMA), as metal source precursor and  $\text{H}_2\text{O}$  vapor as a co-reactant. [69, 73, 74] In the first half of the ALD cycle, steps A and B in Fig. 3.1, the metal source precursor (TMA) absorbs on the surface, partly by physisorption, partly by chemisorption. Reactions with pre-existing surface sites ( $\text{OH}^-$ -groups) occur via ligand exchange. The  $(-\text{CH}_3)$  precursor ligands and hydroxyl groups on the surface of the substrate react and from Al-O chemical bonds releasing volatile byproducts in the form of  $\text{CH}_4$ . Hereafter, remaining physisorbed precursor and non-reacted precursor in the gas phase are purged and pumped out by using an inert gas, i.e., nitrogen or argon. Due to a finite number of active surface sites ( $-\text{OH}$ ) on the substrate the chemisorption of the TMA molecules is self-limited. Therefore, at the end of step B, the surface is saturated with chemisorbed molecules.

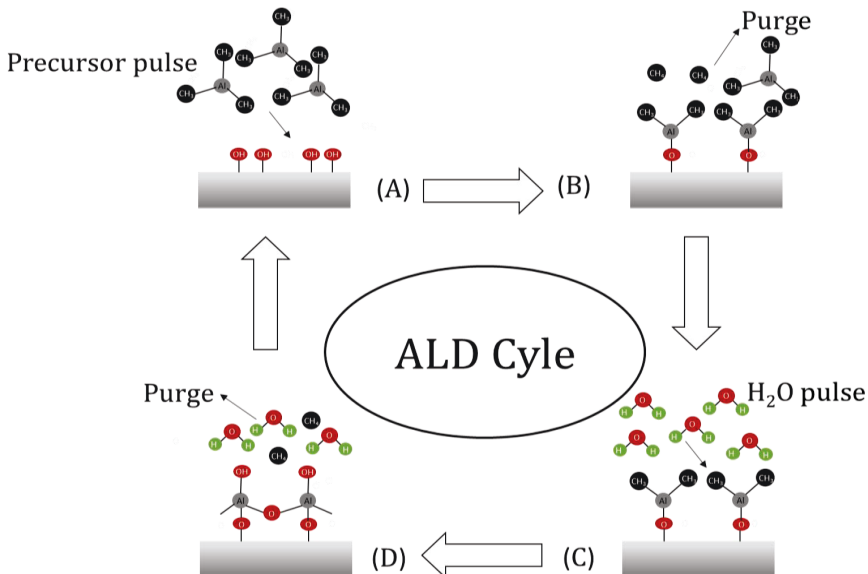


**Figure 3.1:** Schematic illustration of the regular ALD cycle process of  $\text{Al}_2\text{O}_3$  where the (A-B) steps involve the dosing of precursor (TMA) and purging, whereas the steps (C-D) engages the injection of water vapor as oxygen source, and a final purge step to remove all the non-reacted products [73]

In the second half of the ALD cycle (steps C and D shown in Fig. 3.1), the co-reactant, i.e.,  $\text{H}_2\text{O}$  molecules are injected and they react with the  $(-\text{CH}_3)$  of the chemisorbed TMA species. In this cycle,  $\text{CH}_4$  molecules are again produced as a by-product and the  $(-\text{CH}_3)$  ligands on the surface sites are replaced by the hydroxyl groups for the next ALD cycle. The second half of the ALD cycle is also self-limiting due to the limited number of surface active sites, i.e.,  $(-\text{CH}_3)$  ligands. Excess water molecules are purged and pumped out of the reaction chamber. In this way new surface active sites are created for the next ALD cycle. After each completed ALD cycle a submonolayer of material has been deposited. The regular increase in thickness which is obtained after each complete cycle (steps A to D) is called *growth-per-cycle* (GPC-value). ALD cycles are repeated to achieve the desired film thickness. This example demonstrates that ALD, in the ideal case, is characterized by chemisorption of precursor molecules on existing surface sites thus it follows the self-limiting growth mechanism. The surface controlled reaction, in contrast to the gas phase reaction in chemical vapor deposition (CVD), makes ALD advantageous over other deposition methods. Purge and pump steps are applied to inhibit any undesired reaction between precursor and co-reactant, i.e. a component of CVD. Therefore, especially for low growth temperatures ALD thin films generally offer very high quality, i.e., density, homogeneity and purity, combined with conformal and uniform coverage over large area as compared to other deposition techniques such as CVD and physical vapor deposition (PVD). ALD processes can also be differentiated based on the type of reactant activation during deposition, namely ‘thermal ALD’ and ‘plasma-assisted ALD’. In the case of a ‘thermal ALD’ process for a metal oxide typically  $\text{H}_2\text{O}$  (water) vapor,  $\text{O}_2$  (oxygen) or  $\text{O}_3$  (ozone) gas are utilized as the oxygen source. Usually, thermally driven ALD reactions require substrate temperatures in the range of 150 - 350 °C to ensure complete half reactions. In this work, the thermal ALD of the amorphous  $\text{Nb}_2\text{O}_5$  films was performed using  $\text{O}_3$  (ozone) as oxygen source. In the case of the ‘plasma-assisted ALD’ process highly reactive and energetic species are generated like for example in a direct or in an inductively coupled plasma source. These highly energetic species increase the chemical reaction rates at the surface of the substrate. This approach gives an opportunity for deposition of ALD thin films at low temperature [57]. In this work, the plasma assisted ALD of the amorphous  $\text{Sr}_x\text{Ti}_y\text{O}_z$  thin films was performed using a remote inductively coupled oxygen plasma ( $\text{O}_2$ -plasma) as oxygen source.



### 3.1.2. Plasma assisted ALD of $\text{Sr}_x\text{Ti}_y\text{O}_z$ thin films

$\text{Sr}_x\text{Ti}_y\text{O}_z$  thin films of thickness 12 nm and 15 nm with various cation compositions  $[\text{Sr}]/([\text{Sr}]+[\text{Ti}])$  of 0.57 (Sr-rich), 0.50 (stoichiometric) and 0.46 (Ti-rich) were deposited by means of plasma-assisted atomic layer deposition (short: PE-ALD) at 350°C in an Oxford Instruments' FlexAL<sup>TM</sup> ALD reactor. An image of instrument and a schematic view of the reactor used for depositions are shown in Figs. 3.2 (a), (b). The reactor is equipped with a load-lock chamber for loading and unloading the wafer without venting the whole reactor chamber. The load-lock and reactor chamber are connected to a turbo molecular pump which maintains the base pressure of the reactor chamber up to  $10^{-7}$  torr. The tool has a dedicated system of precursor delivery consisting of ALD valves placed in close vicinity to the reactor chamber. Furthermore the set-up is equipped with a remote inductively coupled plasma (ICP) source which supplies the reactor. Various gases, i.e., Ar, O<sub>2</sub>, N<sub>2</sub>, NH<sub>3</sub>, and SF<sub>6</sub> are available in the reactor chamber, however only remote O<sub>2</sub> plasma is used as the oxygen source for the performed depositions. The setup is also equipped with in-situ characterization tools like quadrupole mass spectrometer (QMS) and spectroscopic ellipsometer (SE). Platinum served as the bottom electrode in planar or bar-structured (micro and nano) configuration. The substrates' layer stack was (100) Si/SiO<sub>2</sub> (430nm)/Ti (5nm)/Pt (30nm). Cyclopentadienyl-based precursors from Air Liquid, namely, Ti-Star<sup>TM</sup>, which is the product name of (pentamethylcyclopenta-dienyl) tri-methoxy-titanium  $[\text{CpMe}_5\text{Ti}(\text{OMe})_3]$ , and Hyper-Sr<sup>TM</sup>, which defines bis(tri-isopropylcyclopentadienyl)-strontium with a 1,2-dimethoxy-ethane adduct  $[\text{Sr}(\text{iPr}_3\text{Cp})_2\text{DME}]$ , were used in sequence with an oxygen plasma as the co-reactant as shown in Fig. 3.3 (a), (b) respectively. The deposition of  $\text{Sr}_x\text{Ti}_y\text{O}_z$  was performed in "supercycle mode" of  $[\text{SrO}]$ - and  $[\text{TiO}_2]$ -ALD processes as described in section 2.3. The  $[\text{Sr}]/([\text{Sr}] + [\text{Ti}])$  ratio of the films were adjusted by tuning the  $[\text{SrO}]/[\text{TiO}_2]$  cycle ratio while the film thicknesses were controlled by the numbers of executed ALD supercycles, as depicted in Figure 2.5c. First Ti-Star<sup>TM</sup> is injected in a bubbling-type mode using argon as the carrier gas. The precursor supply step is followed by a purge and pump step. Second is the O<sub>2</sub> plasma step, again followed by a purge and pump step. The complete TiO<sub>2</sub> cycle is repeated several times. Subsequently, the second precursor, which is Hyper-Sr<sup>TM</sup>, is dosed and purged by Ar gas; again reactive oxygen species are provided during the O<sub>2</sub> plasma step and purged by Ar gas. The complete SrO cycle is also repeated several times. Further details to the growth process can be found in reference [75].

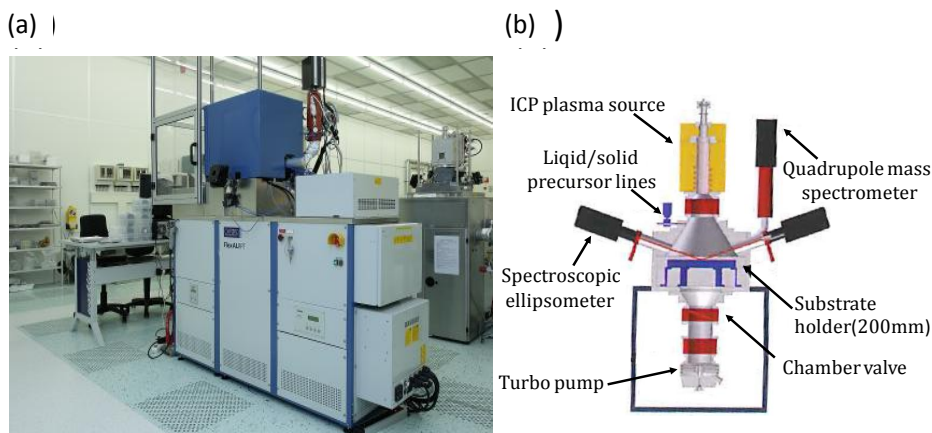


**Figure 3.2:** (a) The picture of the tool from Oxford Instruments' FlexALTM and (b) a schematic illustration of the reactor at the Technical University of Eindhoven, Netherlands. Reprinted with the permission of [188]

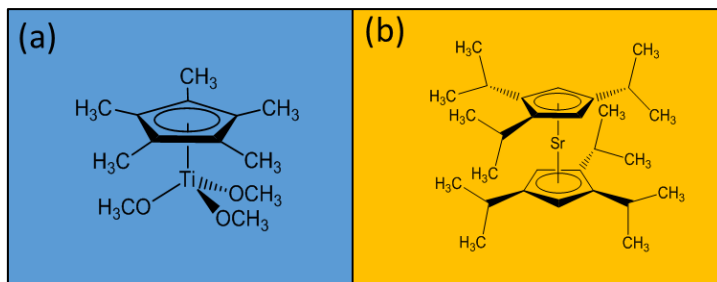


**Figure 3.3:** Cyclopentadienyl-based precursors used for the deposition of  $\text{Sr}_x\text{Ti}_y\text{O}_z$  thin films. (a) Ti-Star™, (pentamethylcyclopenta-dienyl) tri-methoxy-titanium,  $\text{CpMe}_5\text{Ti}(\text{OMe})_3$  as titanium source and (b) Hyper-Sr™, bis(tri-isopropylcyclopentadienyl)-strontium with a 1,2-dimethoxy-ethane adduct,  $\text{Sr}(\text{Pr}_3\text{Cp})_2\text{DME}$  as strontium source, respectively. Reprinted with the permission of [188]

### 3.1.3. Thermal ALD of $\text{Nb}_2\text{O}_5$ thin films

$\text{Nb}_2\text{O}_5$  thin films of  $\sim 10\text{nm}$  were grown in a commercially available flow-type hot-wall reactor of the type F-120 ALD reactor from ASM Microchemistry Ltd utilizing a thermal ALD process. The films were deposited on Pt coated Si/SiO<sub>2</sub> substrates, i.e. (100)

Si/SiO<sub>2</sub> (430nm)/Ti (5nm)/Pt (30nm), with the Pt layer being structured as a micron or nanometer wide bar to serve as the bottom electrode for the cross-bar resistive switching devices. The deposition of Nb<sub>2</sub>O<sub>5</sub> was performed in a “Regular ALD mode”, as described in section 2.3 (see figure 2.5 (a)). The image of the tool used for the Nb<sub>2</sub>O<sub>5</sub> thin films is shown in Fig. 3.4 (a). The deposition was performed at a reactor pressure of about 5-10 mbar. Ozone was used as oxygen source with a concentration of 100 g/m<sup>3</sup>, produced from O<sub>2</sub> (99.999%) in an ozone generator, i.e., Ozomatic modular HC Lab-Ozone by a Wedeco company. N<sub>2</sub> (>99.999%) generated by a Nitrox UHPN 3000-1 nitrogen generator used as carrier gas for precursor and also for the purging process. The thin films of Nb<sub>2</sub>O<sub>5</sub> were grown using an heteroleptic alkylamide-imide niobium precursor, i.e., 'BuN=Nb (NMe<sub>t</sub>)<sub>3</sub>, shown in Fig. 3.4 (b). The precursor was evaporated at 55 °C in the low temperature part of the F-120 system and feeded into the higher temperature deposition zone of the hot-wall flow-type F-120 ALD reactor. The film was deposited at a temperature of 275 °C with a growth rate of 0.5 Å per cycle. The injection was performed by choosing a 0.7/1.0/1.0/1.5s (pulse/purge) sequence for the Nb-precursor and for the ozone step, respectively. The ALD Nb<sub>2</sub>O<sub>5</sub> thin films were amorphous as grown, while a consecutive annealing step at a temperature of 600 °C for 5 min in air resulted in crystallization of the films into the orthorhombic Nb<sub>2</sub>O<sub>5</sub> structure. Detailed information to the growth process can be found in reference [76].

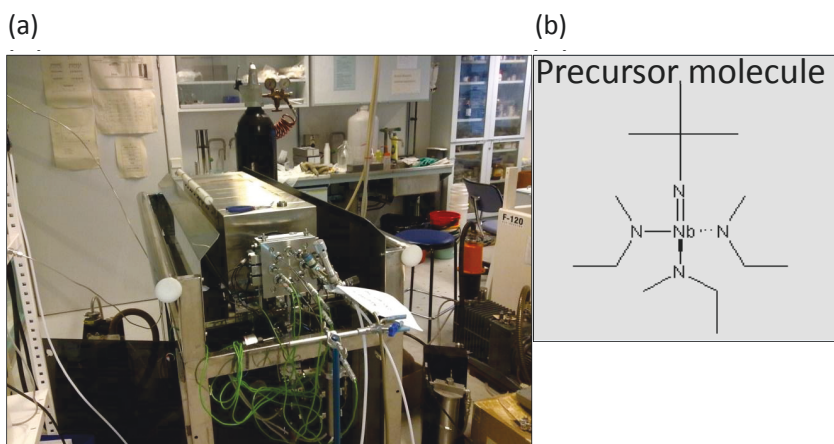


**Figure 3.4:** (a) The picture of ASM microchemistry hot-wall ALD reactor type F-120 at the University of Helsinki, Finland, which had been used for the deposition of the ALD Nb<sub>2</sub>O<sub>5</sub> thin films. (b) Two-dimensional picture of 'BuN=Nb (NMe<sub>t</sub>)<sub>3</sub> molecule utilized as niobium source in the thermal Nb<sub>2</sub>O<sub>5</sub> ALD process. Reprinted with the permission of [77]

### 3.1.4. Sputter deposition of metal layers

Sputter deposition is a physical vapor deposition (PVD) technique where electrically induced argon plasma is used to ablate material from the metal target which is subsequently redeposited on the substrate's surface. For parallel plate reactors the voltage is applied between the cathode, on which the target is mounted, and the anode, where the substrate is located. Generally, the anode with the substrate is at ground potential while the cathode with the metal target is connected to the power supply. Depending on the material or process either a radio frequency (RF) generator, typically at  $f = 13.56\text{MHz}$ , or a direct current (DC) voltage source are used as shown in Fig. 3.5 (a) and (b), respectively. For more detailed information the reader is referred to [177]. The plasma is created by the collisions of kinetically high energetic electrons with gas atoms leading to ionization of the inert gas (Ar) atoms. The ignition of the plasma process requires a gas pressure of about  $10^{-3}$  to 1 mbar in order to establish a constant ionization rate. The ionized  $\text{Ar}^+$  atoms are directed towards the cathode on which the target material is mounted.

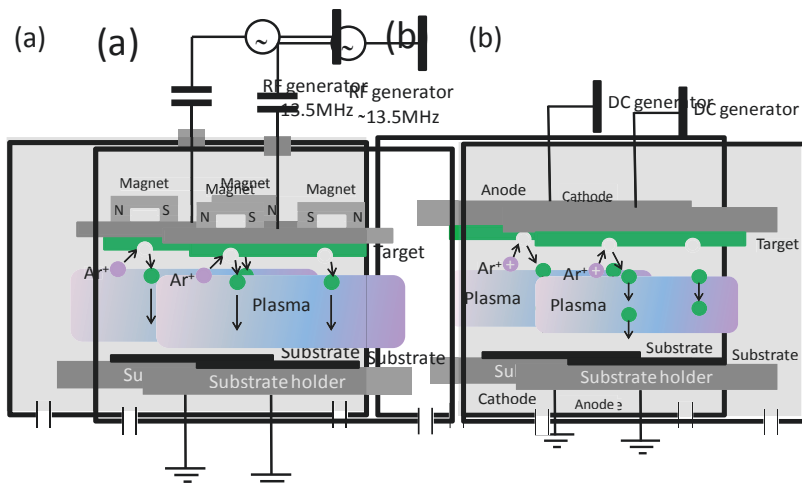


**Figure 3.5:** Schematic overview of (a) RF-source and (b) DC-source based physical vapor deposition or sputter tool. Reprinted with the permission [177]

The momentum transferred during the collisions of the  $\text{Ar}^+$ -ions with the metal atoms of the target cause an ablation of the target material and a transfer of metal ions into the vapor phase. The metal ions have a momentum pointing towards the substrate surface (as

well as towards the chamber walls). Metal ions are typically neutralized by electrons from the plasma before the metal atoms reach the sample's surface (as well as other surrounding surfaces). The sputter deposition technique is anisotropic in nature due to relatively high energy and momentum of the particles. Therefore a serious drawback of sputter deposition is an inhomogeneity of the film thickness close to edges due to shadowing of the 'beam' of metal ions or atoms. Therefore, sputtering is generally not suitable for conformal deposition and considered as non-ideal for additive processes [176]. In this work thin metal layers used for top as well bottom electrodes were deposited by sputtering. The titanium and platinum metal layers were deposited by DC sputtering from metal targets using argon as the sputtering gas. TiN films were deposited by RF sputtering from a TiN target using argon as sputtering gas. The complete list of sputter parameters is given in table 3.1. Both DC and RF sputtering processes were performed in a Univex 450C cluster tool from Oerlikon-Leybold Company. Different metal layers can be deposited in-situ with this machine that is equipped with several sputter chambers one for each target material which are connected to a transfer chamber.

**Table 3.1:** *Sputter deposition parameters for Ti, Pt and TiN metal layers utilized as top and bottom electrodes in the micro- and nano-crossbar structures fabricated in this study*

Sputter Parameters	Ti	Pt	TiN
Gas flow [sccm]	60 Ar	60 Ar	60 Ar
Power [W]	300	375	175
Pre Sputter[s]	180	20	120
Pressure[mbar]	$2.24 \times 10^{-2}$	$1.44 \times 10^{-2}$	$2.2 \times 10^{-2}$
Deposition rate[Å/s]	4.2	17.6	3.3

### 3.1.5. Thermal evaporation of metal films

Thermal evaporation was used to evaporate Ti and Pt metal for use as top electrode material. Thermal evaporation was done at room temperature under high vacuum (HV) at a pressure of about  $10^{-7}$  mbar. The UHV- conditions not only help to evaporate the low vapor pressure materials, but also enable a large mean free path of the evaporated atoms

which is a prerequisite for an undisturbed trajectory of the evaporated material to substrate. The undisturbed trajectory gives an advantage over the sputter deposition because poor step coverage is ensured by good directionality of deposition, making lift-off process feasible [176]. Usually thermal evaporation requires direct sublimation of material which is achieved either by thermal heating utilizing a resistively heated source or by an electron beam heated source. In the present work, the electron beam heated method is preferentially used for Ti and Pt evaporation. The schematic diagram of the electron beam evaporation system is shown in Fig. 3.6. Under (UHV) condition, high energy electrons are accelerated either by electron emitter or by electron gun and directed towards the water cooled crucible containing the material to be evaporated. The deposited material is cooled by water which is necessary to avoid melting and splashing of material. The evaporation rate of the material is monitored by using a quartz crystal next to the sample surface. The substrate is fixed in the opposite of the crucible. The major advantage of using electron beam evaporation is the low kinetic energy of the evaporated material which enables to avoid thin film surface damage caused when high energy particles hit the growing layer. Therefore the deposition of the Ti and Pt top electrodes on the  $\text{Nb}_2\text{O}_5$  thin films of the nanocrossbar devices was performed by electron beam evaporation.

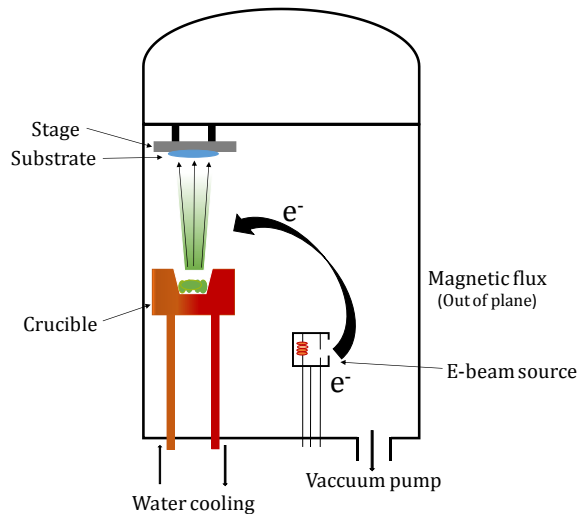


**Figure 3.6:** Schematic view of the electron beam evaporator chamber. An electron beam is used to evaporate the material which is then deposited on the substrate opposite to the crucible. Reprinted with the permission of [177]

## 3.2 Patterning techniques

Patterning of various material stacks with different feature sizes is essential in semiconductor industry even for the research and development of future electronic devices. For that purpose a technique called lithography is used as a very important pillar in semiconductor industry. Lithography is further divided into two main categories (i) photo mask based and (ii) mask less lithography technique. Photo mask based lithography is commonly called photolithography in which opaque fused silica masks are used to transfer the pattern onto the substrate. Generally, the pattern of the masks is transferred to the wafer by means of UV-light and the medium of transformation of patterns is called 'resist'. The resist is further divided into two main types, positive and negative tone resist depending upon the application. In the case of positive tone resist the area of resist which has been exposed to either light or charged particles is dissolved during development, where as for the negative tone resist exposed areas become cross linked and remain on the wafer after development. In this work the micrometer sized pattern were transferred by conventional photo lithography. In contrast, nanometer sized pattern were transferred by mask less lithography techniques known as e-beam lithography and nanoimprint lithography. The detailed information about the techniques and the processes will be discussed in this section.

### 3.2.1. Micro-crossbar patterning

The most common lithography technique which is used for micrometer scale patterning with very high throughput is known as photolithography. In this research work the structures with lateral dimensions of  $\sim 1\mu\text{m}$  are achieved by optical lithography using AZ 5214E, an image reversal photo resist, from *MicroChemicals* GmbH. This resist is capable of featuring both positive and negative process utilizing the same photo mask. This special feature of AZ5214E photo resist is due to the coexistence of a novolak resin and nepthahoquinone diazide as photoactive compound together in a single resist [178]. Fig 3.7 shows the corresponding negative and positive process steps. Initially for both processes the sample is cleaned with acetone to remove organic contaminants, and to the acetone is removed from surface by putting the samples into an isopropanol bath. In both steps the samples are given ultrasonic agitation for 5 minutes and then dried with  $\text{N}_2$  gas. Afterwards, the samples are put on a hot plate at  $120^\circ\text{C}$  for 3 minutes for removing any residuals of solvents and water. The photo-resist AZ 5214E is spin coated on the

substrates with 500 rpm for 5 seconds and subsequently with 4000 rpm for 30s. This spinning recipe results in a homogenous resist film of a thickness of approximately 15 $\mu$ m. Subsequently the samples are immediately put onto a hot plate for 5 minutes at 90 °C. During this baking step the most of the solvent evaporates while the resist molecules stay on the substrate surface [179]. For UV exposure an MA 6 mask aligner from Karl Süss GmbH was used. The optical system of the MA 6 is shown in Fig 3.8. It contains the exposure lamp of wave length  $\lambda = 356$  nm (I-line) of the mercury short arc lamp with 1000 W power mounted inside the ellipsoidal mirror exactly at its first focal point. The ellipsoidal mirror collects the radiations emitted by the lamp and focuses it to the second focal point. The radiations coming from the ellipsoidal mirror are collected by the cold light mirror which splits the radiation into non-used long wave lengths and the exposure light. The non-used radiation passes through the mirror and is absorbed in the heat sink. The useful wave length is reflected at 90° to the fly's eye lens. This lens disperses the light and sends it straight to the condenser lens. The condenser lens collimates the exposure light. Both fly's eye and condenser lenses are made of fused silica for all optical systems.

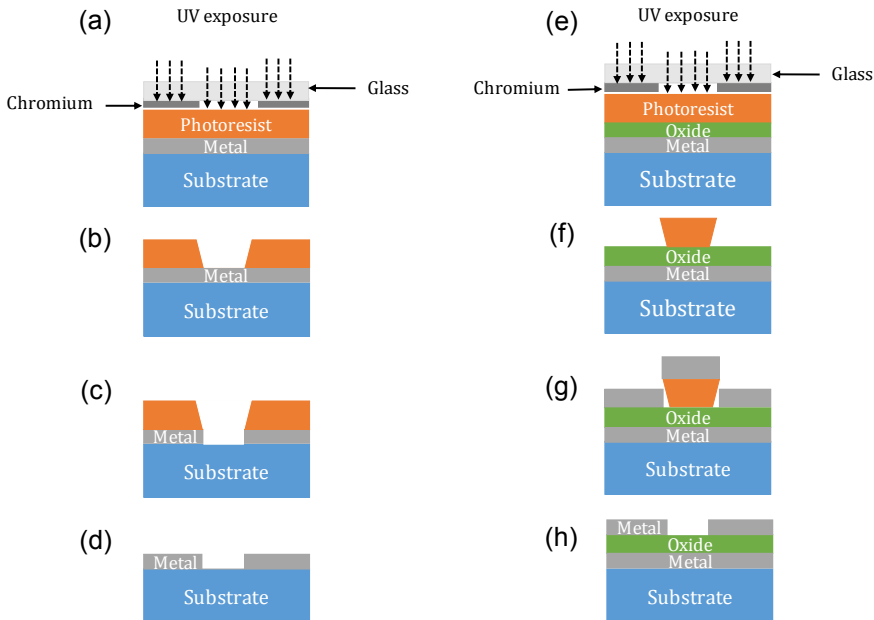


**Figure 3.7:** Photolithography processes (a)-(d) show the positive process (back etching process) and pictures (e) to (h) depict the negative process.



A set of filters sitting in front of the condenser lenses is used to select the more specific exposure wave lengths. All filters are made of quartz glass. The selected exposure light is passed through the integrated block containing two parallel lens plates with exactly defined distance to each other for good uniformity. The main purpose of the lens system is the reduction of diffraction. The subsequently well defined light hits the turning mirror which deflects the exposure light to the exposure area. At the final stage the deflected light passes through the front lens which also provides the collimation and further uniformity of the exposure beam. This lens is specific for each wave length and made of quartz glass. The schematic view of the exposure system of the MA6 mask aligner is shown in Fig. 3.8 (b). In photolithography processes there are three modes for transfer of a pattern from a mask to the substrate, (i) *contact mode* (ii) *proximity mode* and (iii) *projection mode lithography*. In *contact mode lithography*, the mask is brought in contact to the resist. The critical dimensions (CD) theoretically depend on the wave length ( $\lambda$ ) used for the resist exposure and the resist's thickness. The maximum attainable resolution for contact mode lithography is less than  $1\mu\text{m}$  by using MA 6 mask aligner but due to flawed contact between the mask and the resist and other reasons the maximum resolution is approximately  $1\mu\text{m}$ . The main disadvantage of contact mode lithography is the contamination and the corrosion of the mask due to the physical contact with the resist and stress due to pressure during the exposure. This drawback of the contact mode can be overcome by using the *proximity mode lithography* where a gap is introduced between the mask and the substrate. The disadvantages of the proximity mode lithography are a limited resolution and high costs. An advanced technique which doesn't suffer from the described disadvantages is the *projection mode lithography* which is the standard technique utilized in semiconductor industry despite of high cost and some diffraction issues. In this research work, proximity lithography has been utilized for the patterning of the micro-crossbar devices for  $\text{Sr}_x\text{Ti}_y\text{O}_z$  and  $\text{Nb}_2\text{O}_5$  devices. In the case of  $\text{Sr}_x\text{Ti}_y\text{O}_z$  as well as  $\text{Nb}_2\text{O}_5$  the Pt bottom electrodes were patterned by using the positive (additive) process as described in Fig. 3.7 (a)-(d). In the positive process (cf. Fig. 3.7 (a)-(d)) and in the negative process (cf. Fig. 3.7(e)-(h)) first the resist (AZ 5412E) was spin-coated on the Pt coated silicon substrate. After a soft bake at  $90^\circ\text{C}$  for 5 minutes the first exposure was performed which is a distinctive feature to distinguish the positive from the negative process. For the positive process the exposure was performed for 40 s with an intensity of  $2.4\text{ mW}/\text{cm}^2$  in constant power mode (350 W). After exposure the illuminated substrate was immersed into the developer AZ 326 for 60s. The developer removed the resist in

the exposed area and kept the resist in the unexposed regimes (see Fig. 3.7 (b)). Later the structuring of Pt was done by reactive ion beam etching (see Fig. 3.7 (c)). Afterwards, remaining unexposed resist was removed in acetone and isopropanol. In the case of the  $\text{Nb}_2\text{O}_5$  devices the top electrode metal lines of Pt and Ti/Pt were patterned by a positive process as well. For the  $\text{Sr}_x\text{Ti}_y\text{O}_z$  the top electrodes were patterned by negative process. For the negative process (cf. Fig. 3.7(e)-(h)), the first exposure time was significantly shorter, i.e., only 16s. Afterwards, an image reversal baking step at 120 °C for 40 s was performed. The short baking step helped to crosslink the resist molecules in the exposed area. Next the flood exposure step was carried out for 90 s without any mask to activate the photoactive compound in the unexposed area. Later, the substrate was immersed into the developer for 60 s. As a result the resist in the exposed area remained where as the resist in the unexposed area is dissolved by the AZ326 developer. During this process an undercut appears which is essential for the lift-off process (see Fig. 3.7(f)). The metal layer for top electrode, in the case of  $\text{Sr}_x\text{Ti}_y\text{O}_z$ , TiN, was deposited by sputtering (see Fig. 3.7(g)). The lift-off process was performed by putting the substrate into an acetone bath and drying with nitrogen (see Fig. 3.7(h)).

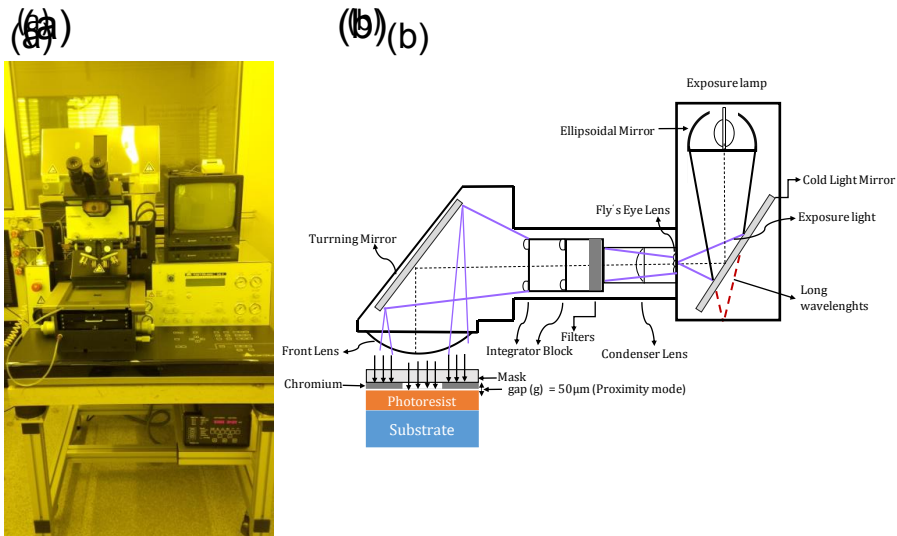


**Figure 3.8:** (a) The picture of the Mask aligner MA6 from Karl Süss used for UV exposure and (b) a schematic illustration of the exposure system of the MA6 mask aligner.

The summarized sequence of the **positive process** for micro-crossbar cell fabrication is as follows:

- ❖ Sputter deposition of Ti (5nm)/Pt (25nm) on 430 nm SiO<sub>2</sub> /Si wafer.
- ❖ Cleaning of Ti(5nm)/Pt(25nm) substrate by:
  - Acetone with Ultra sonic bath
  - Isopropanol with ultrasonic bath
  - Dry the substrate with N<sub>2</sub> gas
  - Piranha etch solution cleaning with (1:1, H<sub>2</sub>O<sub>2</sub>: H<sub>2</sub>SO<sub>4</sub>) for 10 minutes
  - O<sub>2</sub> plasma cleaning for 10 minutes at 300 W
- ❖ Spin coating of UV curable resist (AZ5412) at 4000 rmp for 1minute (see Fig. 3.7 (a))
- ❖ Soft bake at 90 °C for 5 minutes
- ❖ UV-Photolithography exposure for 40 s (see Fig. 3.7 (a))
- ❖ Development of resist after UV exposure for 1 minute and 20 s (see Fig. 3.7 (b))
- ❖ Removing of residual resist layer by O<sub>2</sub> plasma in the reactive ion beam etching (RIE) tool.
- ❖ Structuring of Ti(5nm)/Pt(25nm) by Ar etching using RIBE (see Fig. 3.7 (c))
- ❖ Resist striping after final structuring by EKC 890 (a resist stripper @ 80°C) (see Fig. 3.7 (d))
- ❖ Cleaning the substrate in DI water and dry with N<sub>2</sub>
- ❖ Final cleaning:
  - Acetone with Ultra sonic bath for 3 minutes
  - Isopropanol with ultrasonic bath for 3 minutes
  - O<sub>2</sub> plasma cleaning in a plasma etcher @ 300W for 30 minutes

The summarized flow of **negative process** for micro-crossbar cell fabrication is as follow:

- ❖ Sputter deposition of Ti (5nm)/Pt (25nm) on 430 nm SiO<sub>2</sub>/Si wafer.
- ❖ Cleaning of Ti(5nm)/Pt(25nm) substrate by:
  - Acetone with Ultra sonic bath
  - Isopropanol with ultrasonic bath
  - Dry the substrate with N<sub>2</sub> gas
  - Piranha etch solution cleaning with (1:1, H<sub>2</sub>O<sub>2</sub>: H<sub>2</sub>SO<sub>4</sub>) for 10 minutes
  - O<sub>2</sub> plasma cleaning for 10 minutes at 300 W
- ❖ Spin coating of UV curable resist (AZ5412) at 4000 rpm for 1 minute (see Fig. 3.7(e))
- ❖ Soft bake at 90 °C for 5 minutes
- ❖ UV-photolithography exposure process for 16 s (see Fig. 3.7 (e))
- ❖ Post exposure bake (PEB) after UV exposure for 40 s
- ❖ Flood UV exposure for 90 s without mask.
- ❖ Development of resist after flood exposure for 1 minute and 20 s (see Fig. 3.7 (f))
- ❖ Removing of residual resist layer by O<sub>2</sub> plasma in RIBE.
- ❖ Deposition of Ti(5nm)/Pt(25nm) by e-beam evaporation of TiN by RF sputtering as top electrodes (see Fig. 3.7 (g))
- ❖ Immersion of the substrate in acetone overnight heated @ 60° C (see Fig. 3.7 (h))
- ❖ Ultrasonic bath for 3 minutes in acetone and then isopropanol
- ❖ Dry the substrate with N<sub>2</sub> gas

Note: In the case of Sr<sub>x</sub>Ti<sub>y</sub>O<sub>z</sub> constituted devices both top as well bottom electrodes were made by combining positive and negative process whereas for Nb<sub>2</sub>O<sub>5</sub> the bottom and top electrodes were made by using applying only positive processes. The schematic image and SEM micrograph including high resolution image of the (1μm)<sup>2</sup> micro-crossbar device in the inset as shown in Fig. 3.9 (a), (b) and (c), respectively.

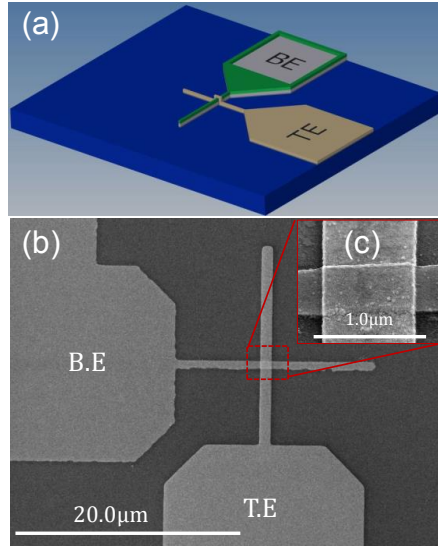


**Figure 3.9:** (a) Schematic overview of the micro-crossbar device. (b) Scanning electron microscopic picture of a fabricated micro-crossbar device showing the contact pads as well as the crossbars of top and bottom electrodes. (c) The inset shows the  $(1\mu\text{m})^2$  crosspoint with higher magnification.

### 3.2.2. Nano-crossbar patterning

The progressive down scaling in semiconductor's device size needs alternative patterning methods different from conventional optical lithography. Also the metal-insulator-metal structures for future resistive switching devices have to be characterized regarding their switching properties at reduced dimensions. For this purpose structures at the nanometer scale have to be fabricated. Due to the limited resolution, the optical lithography which has been described in the preceding section cannot provide nanometer size structures. The advanced optical lithography methods like immersion lithography with double patterning are already in use in the semiconductor industry for the sub-20 nm node. This type of optical method is not accessible for research studies due to its cost. At research level the laboratory needs some very economic technique for patterning even below 50 nm in lateral dimensions. For that purpose two methods were employed for patterning the nanocrossbar devices built from MIM (Metal-insulator-Metal) stacks. The bottom electrodes were patterned by using UV-Nanoimprint Lithography (UV-NIL) by means of a Nanonex-2000 tool and the top electrodes were patterned with a state of art Electron Beam Lithography (EBL) tool from Leica EBP 5000 from Vistec EBL GmbH.

### **3.2.3. Mask layout**

The mask layout used for the integration of bottom as well as top electrodes was introduced by Lentz et al. [184]. The size of the single die is (2cm × 2cm) which is shown in Fig 3.10. The die contains a total number of 72 blocks. Each block contains 25 crossbar devices arranged in rows and columns in a (5×5) array. Each column represents the same lateral size where as the dimension changes along the row. Each row contains crossbar structures of 5 different sizes, e.g., 100 nm, 80 nm, 60 nm, 40 nm and 20 nm. In total 360 devices of each size enable to obtain a sufficient statistics for the electrical characterization of the resistive switching behavior with respect to internal (thickness) and external (voltage, temperature) parameters.

### **3.2.4. Nanoimprint lithography (NIL)**

Nanoimprint lithography is a high resolution, low cost, high throughput mask less patterning technique which was introduced first time in 1995 by Stephen Y. Chou and co-workers [191, 193]. The basic principle of nanoimprint lithography (NIL) is based on utilization of stamp (mold), containing the desired nanostructure, pressing it physically by means of pressure onto a resist spin coated substrate. As a result of replication, the nanostructures were transferred onto the substrate. The imprinted resist acts as pattern transfer source which later develops through etching process for final structuring. In general NIL can be divided into two main categories: (1) thermal NIL and (2) UV- NIL. The first description on NIL reported by Stephan Chou in 1995 was about thermal NIL. In this technique the thermo plastic polymer PMMA was used as deformable resist. Being a very frequent and adaptable resist the PMMA can be spin-coated on substrates with very high uniformity and variable thickness depending on the spin rate. After spin-coating the thermo plastic resist, the master stamp is pressed mechanically with high pressure into the resist, while the temperature is raised up to values higher than the glass transition temperature ( $T_g$ ). These thermo plastic resist undergoes two different stages (1) hard elastic ( $T > T_g$ ) and (2) visco elastic ( $T < T_g$ ) during the imprint depending upon the temperature. Initially below the glass transition the resist is in hard elastic state which changes to viscoelastic state for  $T > T_g$ . The second kind of nanoimprint lithography is UV-NIL which was first investigated by Haisma et al. [194].

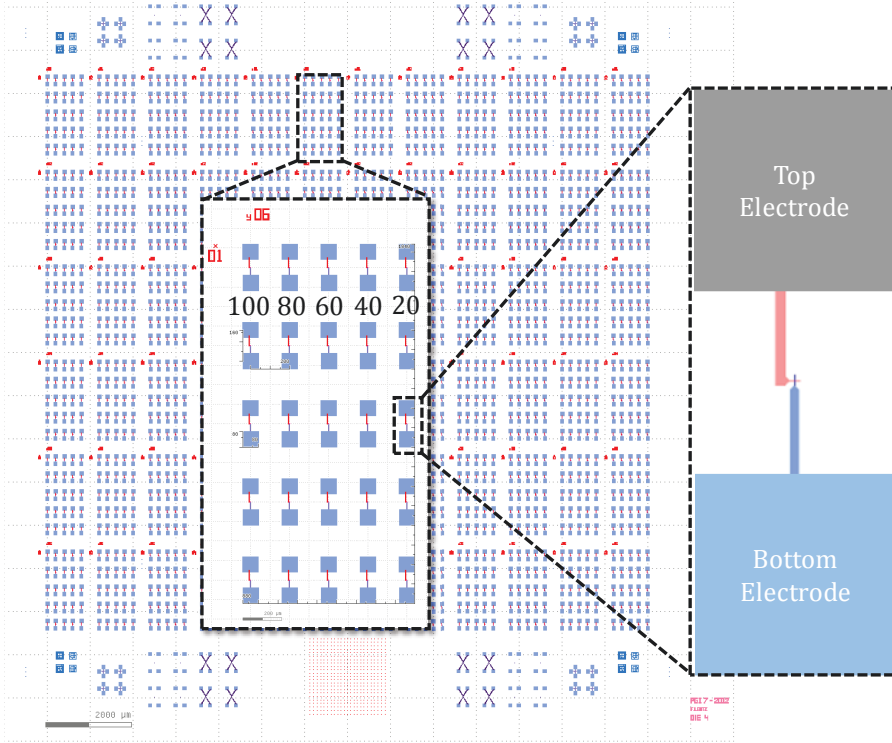


**Figure 3.10:** Mask layout of the (2 cm x 2 cm) single nano-crossbar devices with lateral dimensions ranging from 20 nm to 100 nm as shown in middle of the figure. The inset shows the configuration of top electrode (gray) and bottom electrode (light blue).

In UV-NIL, contrary to the thermal NIL, a low viscous and UV-curable resist is used which deforms at room temperature. Initially these resists are spin coated on the substrate and then a translucent mold made of quartz glass is pressed onto the substrate by mechanical pressure. After that the substrate with the pressed mold is exposed to UV light which cross links the monomer based UV resist forming oligomers. Once the process is completed the mold is devided from the substrate by mechanical force. To transfer the pattern of the mold, the first step is to remove the unwanted resist layer, called residual layer, by plasma etching to open the surface of layer for the final structuring. This needs subsequently a dry etching step. In this research work only an UV-NIL process was used for patterning the bottom electrode. For making bottom electrodes, a quartz wafer with diameter of 100 mm from plane Optic AG with a thickness of about 525 μm was used as mold. Later on, this quartz substrate was covered by a 15 nm thick Cr layer utilizing e-beam evaporation followed by PMMA (AR.P 679.02, 950K. 2) from All RESIST GmbH

after spinning @ 3000 rpm for 60 sec. As a result the resist thickness of 80 nm was obtained. Subsequently the nanostructures were patterned onto the mold by electron beam lithography (EBL). The detailed information of electron beam writing is described by Lentz et al. [184]. After EBL exposure the PMMA is developed by APP 600.5 developer from All RESIST GmbH for 40 s and then the substrate was put into the fresh acetone for 30 s and was blown by dry  $N_2$ . The EBL pattern after development of PMMA was transferred into glass mold. First the Cr layer was removed by ion beam etching using a RIBE tool with the help of (Ar) as a plasma source for 3 minutes with etching rate of 209 nm/min. Fig. 3.12 shows representative SEM images of the structured glass mold before removal of the complete Cr layer by chromium etchant process for getting contrast images during SEM. The structured Cr layer was later used as hard mask for etching the quartz mask against the  $CF_4$ . The trenched depth of  $SiO_2$  was estimated selectively between Cr and  $SiO_2$ . Resulting etch depth of  $SiO_2$  was obtained in the range of about ~150 nm. To remove the residual traces of PMMA resist the substrate was cleaned by acetone and isopropanol and dry with  $N_2$ .

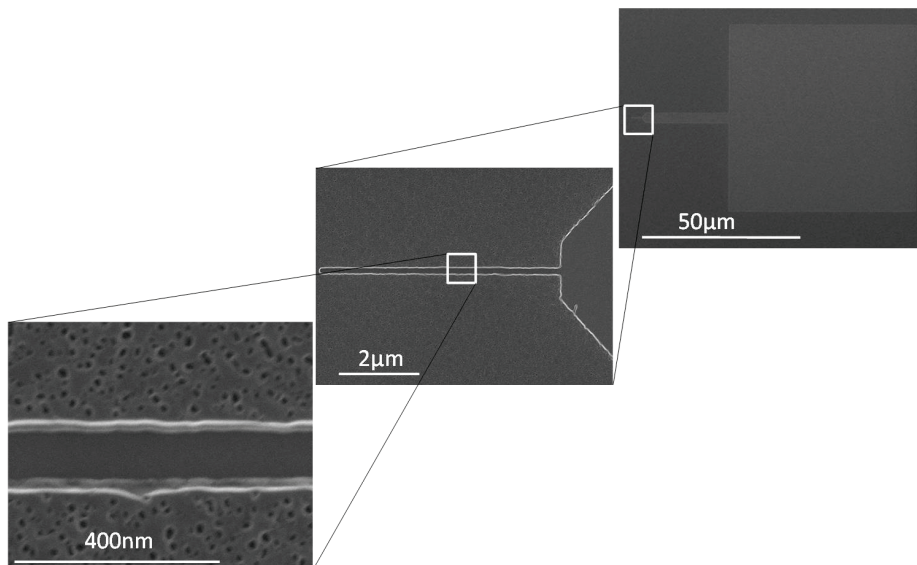


**Figure 3.11:** SEM micrographs of the nano structures on the glass mold after the EBL writing. The SEM images were taken before the removal of the complete Cr layer by chromium etchant process for providing high contrast images in the SEM.



Finally remaining Cr was removed by wet etch process by chromium etchant (MicroChemicals GmbH). In UV-NIL a crucial step is the separation of the mold from the substrate after imprint. To avoid any destruction an anti-sticking layer was employed by coating a self assembled monolayer (SAM). For that purpose well studied SAMs for SiO<sub>2</sub> are fluorinated silanes. In this research try chlorosilane molecules from ABCR were deposited by a vapor deposition technique. Before silanization the glass was cleaned by acetone and isopropanol flowed by piranha etch solution with 1:2 ratio for 10 minutes and then it was put into O<sub>2</sub> plasma cleaning @ 300W for 10 minutes. This process not only gave a clean surface but also helped to activate the surface active sites for the covalent attachment of silane molecules. The silanization was performed in desiccators by using 200μL of silane which is enough for 100 mm SiO<sub>2</sub> wafer at pressure of 45 mbar for 1 h. The attachment of silane molecules to the surface of SiO<sub>2</sub> was supported by silanol groups which turned the hydrophilic into hydrophobic surface. After silanization the UV-NIL was performed using the nanoimprint tool Nanonex 2000 shown in Fig 3.12 (a). The NX-2000 can imprint single wafers of a diameter of 100 mm. For imprinting structures, the system uses the air cushion technology for applying pressures up to 550psi on the mold sitting on the top of the substrate by pressing it in a process chamber as shown in Fig 3.12 (b) known as air cushion technology. The combined set of mold and substrate between two transparent foils was transferred into the imprinter process chamber (IPC) with the help of sample drawer. To remove any air between foils, substrate and mold, a vacuum was built up as shown schematically in the inset of Fig 3.11(c). The major advantage of the air cushion process over a parallel plate pressure press system is its uniformity for achieving a homogenous residual layer thickness. The UV-NIL resist mr-UV Cur 21 from Micro-resist technology GmbH was used as photo curable resist. The resist has already shown single digital nano fabrication potential by UV-NIL lithography with very good etch biasing potential against the nano structuring [195]. On top of that it is easy to remove after harsh dry etching processes due to nonexistence of inorganic contents. It is an augment advantage for removing the residual resist after final etching with simple O<sub>2</sub> plasma for final Pt nano structures. Before spinning the resist on the Pt substrate it was cleaned by piranha etch solution with (1:1, H<sub>2</sub>O<sub>2</sub>: H<sub>2</sub>SO<sub>4</sub>) for 5 min to remove any organic contamination and then put the substrate under O<sub>2</sub> plasma for 1 h at 600 W.

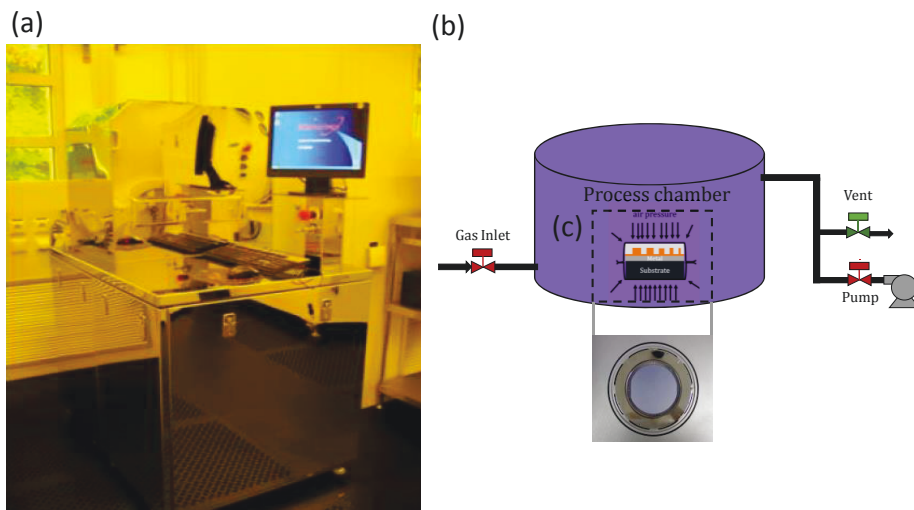


**Figure 3.12:** (a) Image of the NX-2000 NIL set up (b) the schematic diagram of the process chamber and (c) the substrate and mold air cushion set up.

The resist was spin-coated at 300 rpm for 60 s without any dilutions which resulted in 100 nm resist thickness after soft baked immediately at 80 °C for 60 s. After loading the wafer into the chamber, first the pressure was set for 20 s at 100 psi. This pre-imprint pressure not only helps to release any air between foils, substrate and mold but also a gentle press to avoid any sudden displacement of mold and substrate during the high pressure step. Afterwards a high pressure process at about 500 psi is supplied for 5 minutes to fill the cavities of mold with resist. After that the wafer was exposed to UV-light for 4 minutes. The over all process of UV-NIL was performed at room temperature. Corresponding SEM micrographs in Figs. 3.13(a), (c) show the UV-NIL resist patterns of ~100 nm, ~80 nm and, ~40 nm in design, respectively. After the UV-NIL imprint and before etching for the final Pt bottom electrodes structuring the structures look slightly bigger than the expected final structures. The SEM micrographs in Fig. 3.14 (a)-(c) depict the Pt structures after etching of the resists patterns described prior of the sizes ~100 nm, ~80 nm and, ~40 nm, respectively.

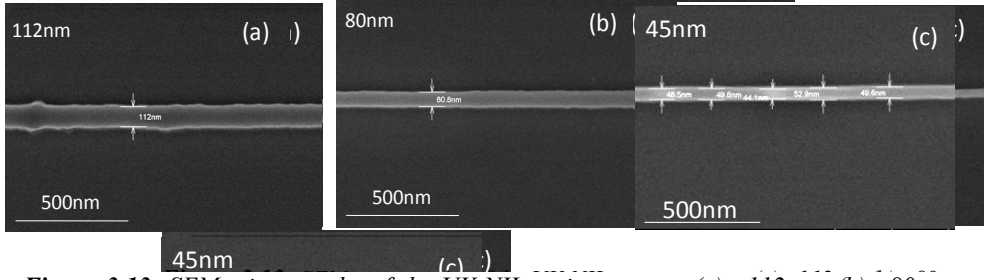


**Figure 3.13:** SEM micrographs of the UV-NIL resist patterns (a) ~112 nm (b) ~80 nm and (c) ~45 nm in design on the Pt substrate after the UV-NIL imprint and before etching. The structures after imprint look slightly bigger than the expected final structure.

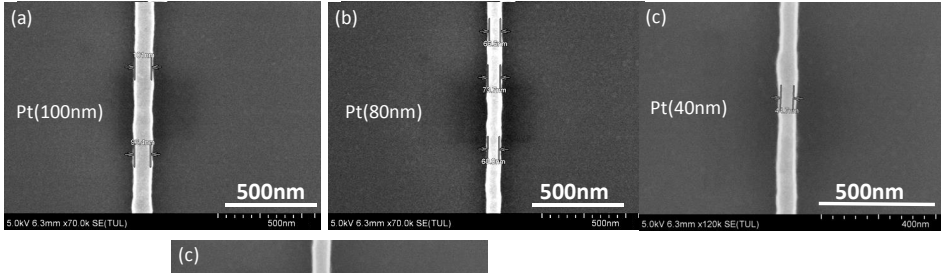


**Figure 3.14:** SEM micrographs of the UV-NIL resist patterns after reactive ion beam etching (RIBE) showing Pt nanostructures of (a) ~100 nm (b) ~80 nm and (c) ~40 nm. The structures after etching look analogous in structure and in design.

### 3.2.5. Electron beam lithography (EBL)

#### Top electrode fabrication

The top electrodes of MIM nano-crossbar devices were patterned by electron beam lithography (EBL). There were three major reasons for using the electron beam lithography.

- High resolution
- Absence of mask aligner capability in the NX 2000 tool
- NIL process only works for planarized substrates

The bottom electrode made by UV-NIL was in the range of 40 nm to 100 nm in lateral dimension. To have almost the same lateral dimension for top electrode the normal UV optical lithography cannot be used. The available lithography can structure minimum dimension of less (1 $\mu$ m) as has been mentioned in section 3.2.1. Therefore electron beam lithography (EBL) due to high resolution patterning is a good choice left at research level.

In EBL technique electrons are used to expose the electron beam sensitive resist at very short wave length. According to the De Broglie hypothesis, the wavelength associated with electrons is expressed as

$$\lambda = \frac{h}{p} = \frac{h}{m_e \cdot v} \quad (3.1)$$

In EBL the momentum of electrons accelerated by voltage ( $V_{acc}$ ) in EBL column is:

$$\begin{aligned} E_{kin} &= E_{el} \\ \Rightarrow \frac{1}{2} m_e v^2 &= e V_{acc} \end{aligned} \quad (3.2)$$

$$\Rightarrow m_e \cdot v = \sqrt{2 m_e e_0 V_{acc}} \quad (3.3)$$

By combining equation 3.2 and 3.3 we get the following expression:

$$\lambda = \frac{h}{\sqrt{2 m_e e_0 V_{acc}}} \quad (3.4)$$

Hence the resolution can be calculated as follows: For the used EBL system an acceleration voltage of  $V_{acc} = 50$  kV is used. In a non-relativistic approximation the wave length of the electron beam radiation is  $\lambda = 5.5$  pm. But still the attainable resolution is lower. It is evidenced that resolution of EBL is not limited by wave length but several other factors described by Nauenheim et al. [176]. The EBL system used in this work belongs to EBPG 5000 from Vestec GmbH as shown in Fig. 3.15 (a). The EBL column is schematically shown in Fig. 3.15 (b). Electrons are generated from a thermal field emission gun made from tungsten (W) as Schottky emitter (coated with  $ZrO_2$ ) with a radius of approximately  $\geq 1 \mu m$  located in the EBPG 5000 system at the top of the EBL column. The thermal extraction of electrons is achieved by heating the emitter up to  $1800^\circ C$  and an electric field is applied by putting a positive bias of about 6022 V on the extractor for the enhancement of thermally excited electrons to overcome the surface potential of the tungsten metal. After extraction the electron is focused by a Wehnelt cylinder and accelerated by gaining the kinetic energy from an applied electric field in respect to the anode. Subsequently, the electron beam on the way to the sample passes

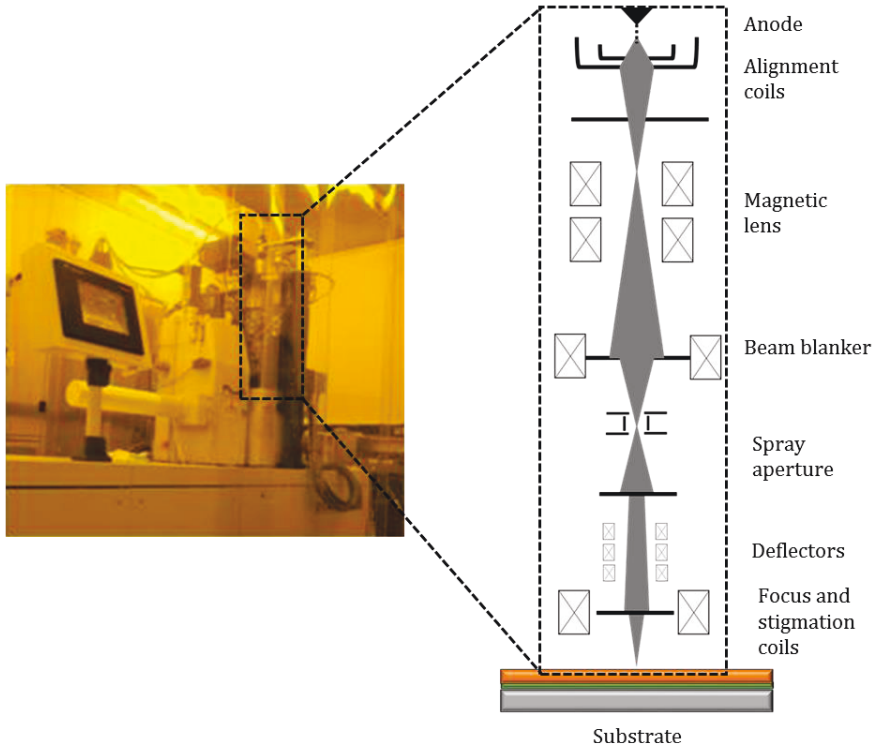


**Figure 3.15:** (a) The EBPG 5000 EBL tool from Vestec GmbH and (b) the schematic diagram of an EBL column system.

through several magnetic lenses, analogue a gun alignment. Furthermore the electron beam passes through two apertures, beam blanker and spray aperture. The beam blanker is situated at the focal point and is used to turn on and off the beam by deflecting the beam away from the optical axis. The spray aperture controls the strayed electrons. In front of the final lense different systems are used for focusing and stigmation the beam passing through the set PF defectors called upper main field, sub field and lower main field enabling a scanning the electron beam to get the final structures. Deflection of the beam always follows the CAD mask layout file containing the final design. The EBL system is a vector scan system. Therefore any patterning is divided into two main categories additive and subtractive. In both techniques the resist is structured using irradiation either by particles or photons. The additive patterning is performed by positive tone resist in which the irradiated area of the resist is removed after development. Whereas in the subtractive approach the resist in the exposed area becomes cross linked and one additional step called post exposure bake is needed while unexposed resist

dissolves in the developer. Subtractive patterning can only be performed by negative tone resist. Generally the additive process is called lift-off process and the subtractive process is known as back etching process. Special resist called image reversal resist could be used for both the subtractive and the additive processes. The additive process for the patterning of the top electrodes of nano-crossbar devices by EBL has been studied and employed in the former work of Nauenheim *et al* [176] and Lentz *et al* [184]. In the scope of this work for the first time the subtractive method for patterning of top electrode of single nano-crossbar devices was introduced. In contrast to the additive process, here the top electrode metal deposition is performed prior to resist coating. As a consequence, the interface between top electrode and switching material remains unaffected from contaminations. For subtractive patterning of the top electrode the resist from *Micochemical GmbH AZ nLoF 2020* was chosen as negative tone resist for EBL writing. Several publications have demonstrated the performance of AZ nLOF2020 resist for nanoscale fabrication down to 50 nm in lateral dimension [186]. The AZnLOF 2020 offers several advantages over other negative tone resists including a high thermal and chemical stability. The resist thickness plays a very important role in achieving small structures. Therefore the resist thickness against the spin rate was determined. For that reason resist of various concentrations was spin coated for 1 min at four spin speeds differing by about 1000 rpm. Fig. 3.16 shows the different resist thickness plotted against the spin speed. From the graphs it can be seen that for certain dilutions the resist thickness becomes saturated. The TE of the nano-crossbar structures fabricated in this work were patterned by means of a 180 nm thick resist layer obtained from AZnLOF2020 diluted in AZ ebr solvent in a ratio of 1:2 and spin coated for 60 s at 3000 rpm. The resist properties are investigated by varying the dose test, post exposure bake time.

The suitable EBL dose was determined by writing test patterns with variable doses. In reality the used EBL system has a circular shape electron beam spot with Gaussian beam intensity distribution. The resulting exposure dose can be calculated [184] by defining range, proper beam step size  $d_{step}$ , and beam current  $I_{beam}$  and step frequency  $f_{step}$  between two adjacent pixels for a square writing area

$$D = \frac{I_{beam}}{d_{step}^2 \cdot f_{step}} \quad (3.5)$$

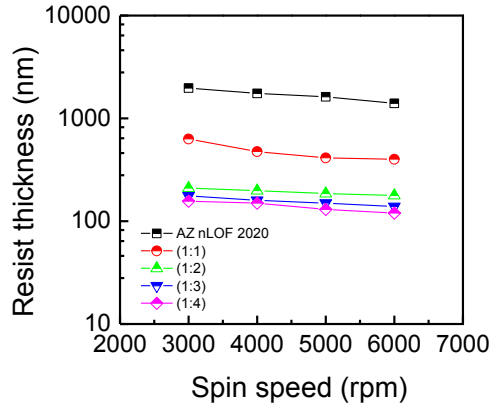


**Figure 3.16:** Properties of the AZnLOF2020 negative tone resist: film thickness dependence of the resist against spin speed for 60s for different concentrations.

Before employing the dose test the diluted resist ((nLoF 2020): (AZ ebr solvent) = 1:2), was spin coated on the Pt coated Si substrate with spin rate of 3000 rpm for 60s which spins the thickness of about 180 nm. After spinning the resist was pre baked at 110 °C for 60s on a hot plate before EBL exposure. This was realized with dose exposures ranging from 18 - 36  $\mu\text{C}/\text{cm}^2$  for 10 different doses by 100 kV<sub>acc</sub>. EBL current of 200 pA in the case of nanostructures was used. The larger microstructures (pad for external electrical connections) were written with fixed broader beam of 20 nA, 25  $\mu\text{C}/\text{cm}^2$ , and 50 nm (BSS). After EBL writing the sample was post exposure baked at 110 °C for 6 minutes and developed for 40 s in an aqueous solution of AZ 726 MIF, a tetramethyl ammonium hydro-oxide developer. Fig. 3.17 (a) shows the comparison between the line width in mask layout and the line width obtained on the substrate after different doses. A clear trend was found with respect to a decrease in the written line width as compared to the line width in the mask layout obtained for alower EBL exposure dose.

The trend is also evident from the sensitivity of AZ nLOF 2020 resist against different doses. From the sensitivity graph it could be seen that it is not possible to obtain 20 nm line structures from AZ nLOF2020 negative tone resist due to its resolution limit. The smallest double resist pattern obtained by using AZ nLOF2020 resist was 40 nm in lateral dimensions as shown in SEM images Fig. 3.17 (b).

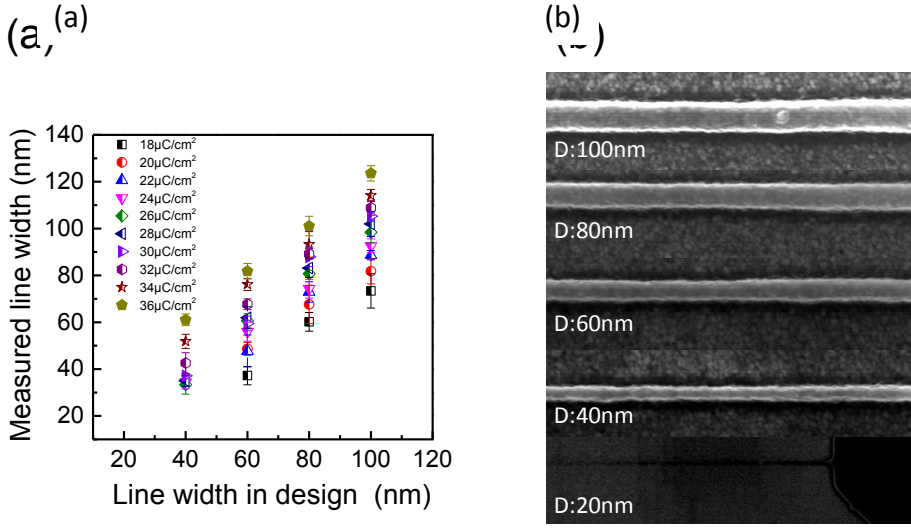


**Figure 3.17:** (a) The EBL dose sensitivities of AZnLOF2020 negative tone resist after EBL writing: measured line width against line widths in the mask layout, show a linear trend. i.e. the higher the EBL dose the larger will be the written line width. (b) SEM micrographs of resist lines written at an optimum dose of about  $32\mu\text{C}/\text{cm}^2$  (the maximum resolution achieved by the AZnLOF2020 negative tone resist).

The sensitivity graph also shows the direct relation between the EBL exposure dose and the achievable lateral dimensions. The larger the dose is, the larger are the written structures in comparison to the designed structures in the EBL mask layout. The post exposure bake (PEB) time effect after EBL writing on resist sensitivity has been investigated. The PEB test is performed for 180 nm thick resist layers. The samples were pre backed at 110 °C for 1 min before EBL writing. EBL exposure parameters and development time were kept the same as described in the case of dose test in the prior section. The PEB effect for the sample post baked for 3, 5, 6, 8, 10 and 12 minutes after EBL exposure showed that the longer the PEB time the larger will be the size of measured line width of resist as compared to the designed line width. After EBL writing with an exposure dose of  $32\mu\text{C}/\text{cm}^2$  samples with different post exposure baked times are developed for 40 s in an aqueous solution of AZ 726 MIF. Fig. 3.18 depicts the comparison between the line width in mask layout and the measured line width after different post exposure baked times.



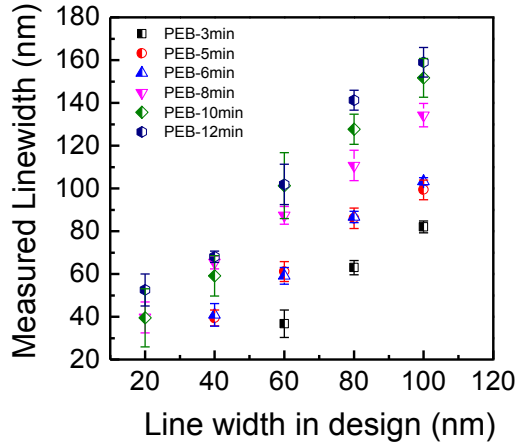


**Figure 3.18:** The PEB sensitivities of AZnLOF2020 negative tone resist after EBL writing for measured line widths against line widths in the mask layout show a linear trend, i.e., the higher the PEB time the larger will be the measured line width.

It is very well known for all chemically amplified (CA) resists such as AZ nLOF 2020 that the PEB time affects the extent of the deprotection reaction [187]. The higher the deprotection the higher will be the sensitivity. The best PEB time was six minutes for producing the final structures close to the design given in the mask layout. The 40 nm line was identified as the resolution limit of the AZ nLOF2020 negative tone resist due to high deprotection reaction rate for given PEB time. Unlikely electron beam lithography does not suffer from diffraction effects but electron optic aberration and more importantly scattering of electron in resist and substrate [190]. In this case the resist is not only exposed by the incident beam but also by an additional interaction of back scattered electrons. The electron scattering during EBL writing causes unwanted exposure called proximity effect. Many different schemes have been invented to minimize the proximity effect. In the case of uniform density and line width, this requires the adjustment of overall dose until the pattern comes out at appropriate size. Dose modulation is one of the most common techniques of proximity correction. Theoretically in dose modulation each and every individual shape in the pattern is allocated a dose in a way that the shape reproduces at its correct size. The calculations required to solve the shape-to-shape interactions are all computationally solved for the individual dose by the proximity correction tools. Although the actual effect of electron scattering is to increase the dose received by large areas, for practical reasons proximity correction is normally thought of

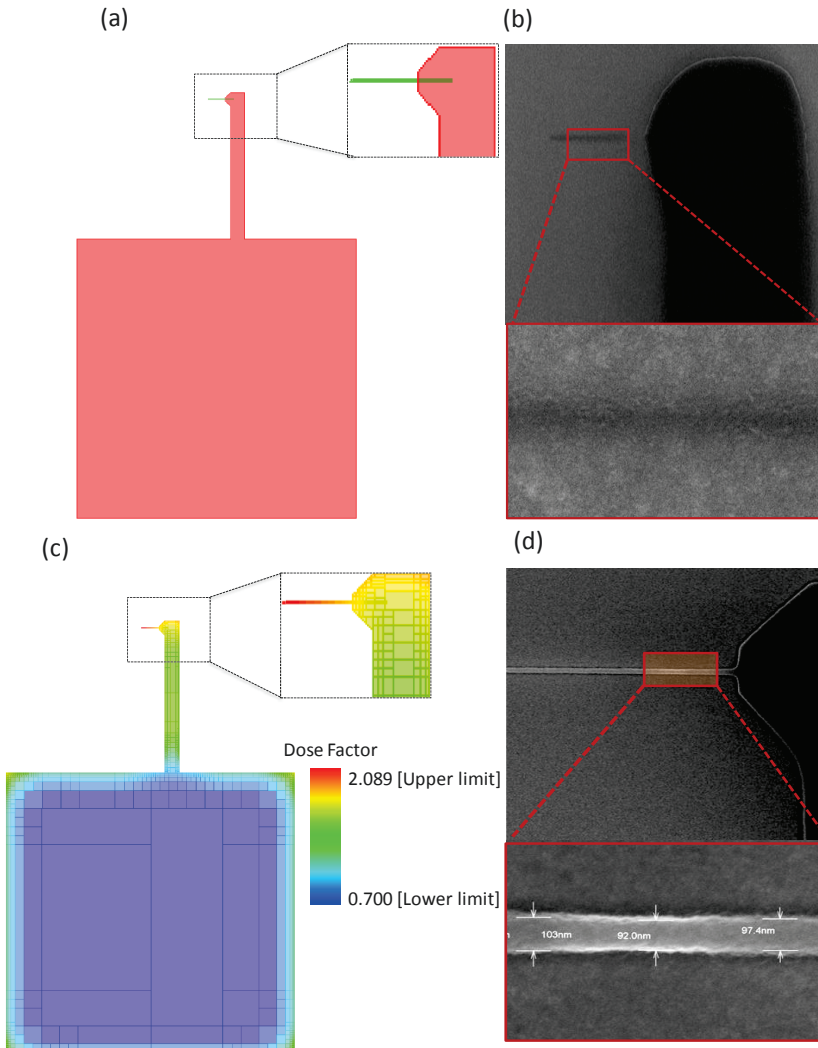


**Figure 3.19:** The simulated version of (a) structure and (b) SEM micrograph of the EBL written AZ nLOF2020 negative tone resist without proximity effect correction on the Pt substrate. It showed the missing nanostructures and deteriorated structures. While the simulated version of (c) after proximity correction by dose modulation the simulated version (a) structure and (b) SEM micrograph of the EBL written AZ nLOF2020 negative tone resist on the Pt substrate without any worsening.

in terms of the large areas receiving a base dose of unity, with smaller and/or isolated features receiving a larger dose to compensate. Fig. 3.19 (a) shows simulated structures obtained without proximity correction. The SEM micrographs in Fig. 3.19 (b) show the distorted structures. After proximity effect correction (PEC) the simulation (Fig. 3.19 (c))

was carried out to calculate the dose factor by using the resulting base dose both for nano (a wire) as well for micro structures (connecting pads). At the end after PEC SEM micrographs in Fig. 3.19 (d) show the corrected structures without distortion. The final structures look very similar to the structures in the mask layout without any obliteration. Figs. 3.20 (a) to (c) show the resist profile of the minimum feature size of the PEC corrected EBL written AZ nLOF2020 negative tone resist after proper PEB, after development and before RIBE.

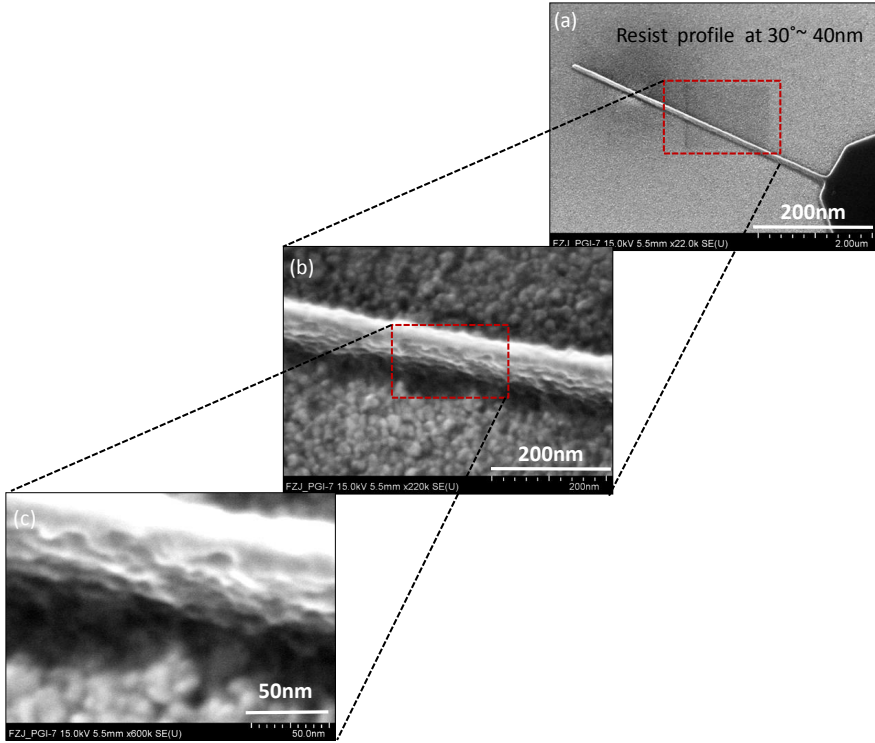


**Figure 3.20:** The resist profile of the AZ nLOF2020 negative tone resist after proper proximity effect corrections by dose modulations for nanocrossbar top electrodes.

In summary, the process flow of **bottom electrode structuring using UV-NIL** patterning is as follows:

- ❖ Sputter deposition of Ti (5nm)/Pt (25nm)  
on 100 mm Si wafer with thermally grown 430 nm SiO<sub>2</sub>.
- ❖ Cleaning of the Ti (5 nm)/Pt (25 nm) substrate:
  - With acetone in ultrasonic bath for 3min
  - With isopropanol in ultrasonic bath for 3min
  - Dry substrate with N<sub>2</sub> gas
  - Piranha etch solution with (1:1, H<sub>2</sub>O<sub>2</sub>: H<sub>2</sub>SO<sub>4</sub>) for 10 min
  - O<sub>2</sub> plasma cleaning for 10 min at 300W
- ❖ Spin UV-NIL resist (mr-uv Cur 21) at 300 rpm for 1min
- ❖ Soft bake at 80 °C for 60s
- ❖ UV-NIL imprint process
- ❖ Removing of residual layer of resist by O<sub>2</sub> based reactive ion beam etching
- ❖ Structuring of Ti (5 nm)/Pt (25 nm) after etching
- ❖ Resist striping after final structuring by EKC 890
- ❖ Cleaning the substrate in DI water and blowing with dry N<sub>2</sub>
- ❖ Final Cleaning:
  - With acetone in ultrasonic bath for 3min
  - With isopropanol in ultrasonic bath for 3min
  - O<sub>2</sub> plasma cleaning for 30 min at 300 W

In summary the process flow of **top electrodes** by EBL is as follows:

- ❖ Electron beam evaporation of Ti (5 nm)/Pt (25 nm) top electrode layer onto the ALD grown Nb<sub>2</sub>O<sub>5</sub> film covering the structured Pt bottom electrodes. Where as in the case of ALD grown STO the TiN top electrode layer was grown by sputtering.
- ❖ Cleaning of the structure with top electrode metal layer:
  - in acetone ultra sonic bath for 1 minute
  - in isopropanol ultrasonic bath for 1 minute
  - dry by N<sub>2</sub> gas
- ❖ Spin AZ nLOF 2020 negative tone resist with (1:2) dilution @ 3000 rpm for 1 minute
- ❖ Soft bake @ 110° C for 3 minutes
- ❖ EBL writing with PEC (proximity effect correction)
- ❖ Post exposure bake @ 110° C for 6 minutes
- ❖ Develop the resist in a developer AZ MIF 726 @ 40 s.
- ❖ Removing of residual layer of resist by O<sub>2</sub> plasma in the reactive ion beam etching tool
- ❖ Structuring of Ti(5nm)/Pt(25nm) and TiN as top electrodes by Ar<sup>+</sup> ions and CH<sub>4</sub>, respectively.
- ❖ Resist stripping after final structuring by RIBE in DMSO @ 120° C for 1h
- ❖ Washing the samples in DI water and blowing with N<sub>2</sub>
- ❖ Final Cleaning:
  - acetone ultra sonic bath for 1 minute
  - isopropanol ultrasonic bath for 1 minute
  - Dry with N<sub>2</sub>

The fabrication process-flow of the nanocrossbar ReRAM elements as shown schematically in Fig. 3.21 (a) is summarized below. The SEM micrographs of single nanocrossbar devices investigated for ReRAM applications of both ALD grown STO and Nb<sub>2</sub>O<sub>5</sub> with stack sequence are shown in Figs. 3.21 (b)-(c) and Fig. 3.21 (d)-(e), respectively.

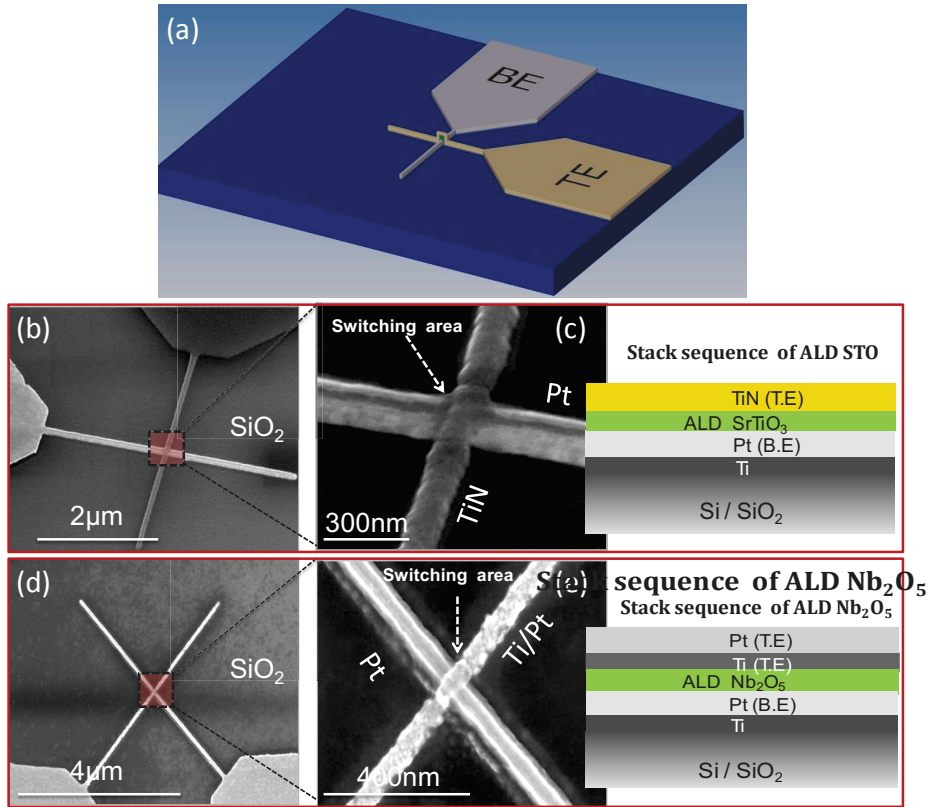


**Figure 3.21:** (a) Schematic diagram of a nanocrossbar device after final etching. The SEM micrograph of the nanocrossbar device (b-c) depicts Pt as a bottom and TiN as top electrode sandwiching the ALD grown 12 nm STO layer in between the cross point. The SEM images of the nano crossbar device (d-e) show Pt as a bottom and Ti/Pt as top electrode with ALD grown 10 nm  $\text{Nb}_2\text{O}_5$  in between. The left side of the frames shows the stack sequences of the electrically characterized devices for resistive switching applications.

### 3.3 Structuring

For structuring the crossbar devices an advanced dry etching process was performed with an Ionfab 300plus tool from Oxford Ion Fab Instruments as shown in Fig. 3.22. Various gasses like Ar,  $\text{O}_2$ , and  $\text{CF}_4$  can be used in the tool for etching of different materials (e.g., metals or oxides). This tool can perform both physical and chemical assisted etching. For example, Ar is used as a physical etching source where as  $\text{CF}_4$  or  $\text{O}_2$  are used for chemical assisted etching. The tool can handle up to 150 mm diameter wafers by using a transfer load-lock sytem into the process chamber which is held under HV condition ( $1\text{-}2 \cdot 10^{-6}$

mbar). Inside the chamber the wafer is mechanically clamped onto a rotating, temperature controlled chuck. The back side of chuck is cooled by fluid circulation from an external chiller. The chuck can be tilted from  $0^{\circ}$ - $90^{\circ}$  in relation with the beam which gives an opportunity for etching at different angles. The etching at different angles provides a chance of side wall trimming. For homogenous etching the chuck is kept at a rotation speed of 20 rpm. The plasma is created by inductively coupled plasma (ICP) source situated outside the reactor chamber. The energy for the generation of plasma is provided by time-varying electric currents through a coil and electromagnetic induction. The plasma ions are extracted and accelerated by a two stage grid, called inner grid and outer grid at potential  $V_a$  (accelerated voltage) and  $V_b$  (beam voltage). The beam voltage is measured between source and walls of the source. The beam voltage is kept slightly positive with respect to plasma whereas the acceleration voltage is kept negative with respect to ground potential to avoid any streaming of electrons back to the source. The overall total extraction potential of the ions can be defined as difference between beam voltage and acceleration voltage [184].

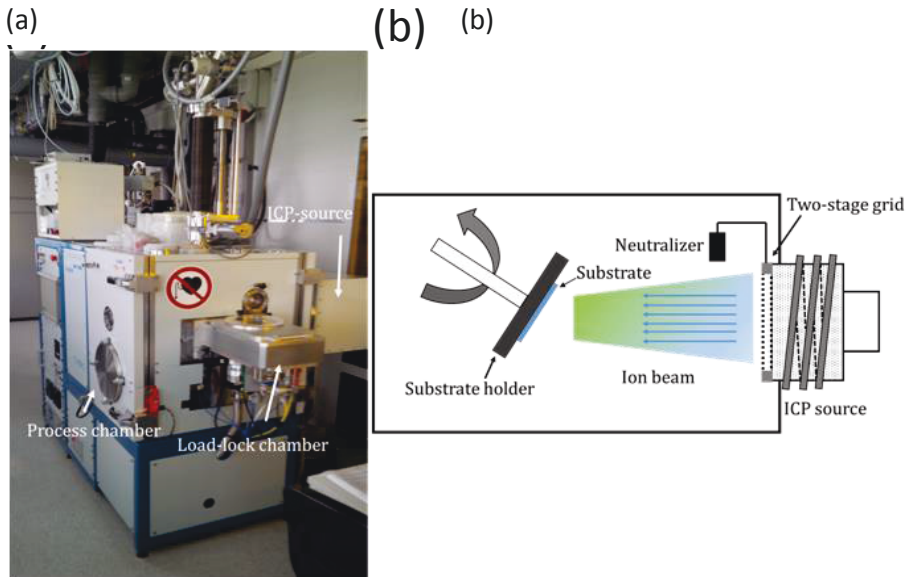


**Figure 3.22:** (a) Reactive ion beam etching (RIBE) tool Ionfab300plus from Oxford Instruments with process and load-lock chamber. The plasma source is situated outside the main chamber. In addition, a mass spectrometer is mounted on the top of the machine for determining the end point of the etching and enabling a determination of the etching rate of different materials. (b) Schematic drawing of the internal setup of the machine. [189]

**Table 3.2:** Reactive ion beam etching parameters and etch rates determined for the different materials utilized in the studied ReRAM devices.

Material	Pt	Ti	TiN	Nb <sub>2</sub> O <sub>5</sub>	STO
Process Gas	Ar	CH <sub>4</sub>	CH <sub>4</sub>	CH <sub>4</sub>	CH <sub>4</sub>
Etch rate (nm/min)	21	20	15	33	7

Due to encroaching of ions insulating surfaces could charge up and keep away the ions coming from the source due to which the etching characteristics could be changed. To avoid this situation neutralization is performed by producing strong plasma in a cylindrical metal cup inside the filament bridge (FBN) feeding electrons to the ion beam. Both parameters have linear impact on the etching rate of materials. In summary, RIBE (Reactive ion beam etching) offers a great potential for structuring of nanometer size devices. In this research work both nano and micro-crossbar structuring is performed by the RIBE system. There are two main tunable parameters due to which the etch characteristics could be changed: beam voltage and current. The inert metals (Pt) are etched by Ar plasma (physical etching) whereas all oxides and non-inert metals (TiN, Ti) are etched by CF<sub>4</sub> plasma. The etching parameters are given below in Table 3.2.

### 3.4 Characterization of thin films and devices

In this section a brief introduction of the methods used for thin films analysis and the electrical characterization of the resistive switching devices employed in this work will be described. The thin film methods include investigation of the structural, chemical, optical and morphological characteristics. The resistive switching properties of the devices were analyzed by means of continuous current-voltage (*I-V*) sweeps.

#### 3.4.1. Thin film characterization methods

The thin film characteristics of the atomic layer deposited binary oxide Nb<sub>2</sub>O<sub>5</sub> and ternary oxide Sr<sub>x</sub>Ti<sub>y</sub>O<sub>z</sub> required several thin film analytical methods to elucidate the chemical



impurities in the films, as well as compositional and structural properties depending upon the growth of the thin films. The chemical analysis was performed by x-ray photoemission spectroscopy (XPS). This analysis reveals the binding energies of core level electrons. In this work XPS analysis has been used mainly to determine the elemental composition of the plasma assisted ALD grown STO films, predominantly the cation ratio, i.e., the  $[Sr]/([Sr]+[Ti])$  ration, and the amount of contamination for example by carbon. The XPS analysis on thermally grown  $Nb_2O_5$  was performed to determine compositional information, such as the occurrence of an sub oxide like  $NbO_2$  during growth in addition to the carbon contamination. The optical dielectric properties and the thickness of the thin films were determined by using spectroscopic ellipsometry (SE). The ellipsometry is technique based on the polarization change of reflected or transmitted light in comparison to the incident beam using light in the UV-VIS range. In this research work, SE is used particularly for the determination of the thickness and the dielectric function of ALD grown STO thin films. The crystal structure of the thin films was analysed by X-ray diffraction (XRD). In XRD the constructive interference of elastically scattered X-rays from the thin films are examined. The condition for the interference is referred as *Bragg's law*. The crystal structures of the as-grown and annealed  $Nb_2O_5$  and STO @ 600° C under different atmospheres were analyzed by XRD. As grown ALD thin films are well known for their smoothness. The morphology and local features like grains, grain boundaries and conduction through these units of the thin films were investigated by using atomic force microscopy (AFM) and local conductive atomic force microscopy (LC-AFM), respectively. The atomic force microscopy is a scanning probe microscopy method based on the measurement of the ultra low force between tip and the surface of the examined thin film. The structural analysis of the thin films is limited at the nano scale. An alternative to that is a method called transmission electron microscopy (TEM) which uses electrons to reveal the structural properties of the materials. TEM not only gives the direct structural information but also enables to take diffraction patterns due to wave-particle nature of electrons. This special type of transmission electron microscopy (TEM) is known as scanning transmission electron microscopy (STEM) which helps for obtaining the nanodiffraction patterns of the material at nano scale. In this thesis STEM was used to study the nature of the ALD grown  $Nb_2O_5$  sandwiched into the nanocross bar devices after electrical stimulus by nanodiffraction analysis. At device level physical characterization is needed in process development of the ReRAM devices. It is very important to check the quality of the devices during the process development of the

ReRAM devices for each step like structuring, patterning and depositions etc. for this purpose scanning electron microscopy was used.

### **3.4.2. Electrical characterization methods**

The resistive switching characteristics of ALD grown micro as well as nano-crossbar devices were measured electrically by recording quasi-static current-voltage ( $I$ - $V$ ) curves. The electrical set-up employed for the ReRAM devices was based on a *B1500A Semiconductor parameter Analyzer* from Agilent Technologies. The Semiconductor Parameter Analyzer tends four source measurement units (SMU's). The input impedance of the analyzer is in the range of tera ohm ( $1\text{T}\Omega$ ). The nano-sized crossbar devices exhibited initially very high resistive states as compared to microcross bar devices. Hence, the demands are very high resolution and very accurate instruments. The two (SMU's) out of four have very high resolution (SMU's) in the range of  $1\text{fA}$  for voltages as low as  $0.5\mu\text{V}$ . In the case of the quasi-static resistive switching analysis of the ReRAM crossbar devices an accurate limitation of the current overshoot during electroforming as well as switching is required. The overshooting of currents not only can cause permanent breakdown in the oxide films but can also cause electrode damaging resulting in a strong variability of the switching voltage. The Semiconductor Parameter Analyzer provides an active control over current compliance. The  $I$ - $V$  hysteresis is measured by applying voltage ramps to the sample where the voltage is increased or decreased in steps.

---

## 4. Material Properties of ALD grown $\text{Sr}_x\text{Ti}_y\text{O}_z$ Films

---

This chapter is devoted to the material properties of ALD grown strontium titanate,  $\text{Sr}_x\text{Ti}_y\text{O}_z$  (STO), thin films with various cation stoichiometries deposited by plasma-assisted atomic layer deposition (ALD) using cyclopentadienyl-based metal precursors and oxygen plasma as counter-reactant. The chemical, optical as well as morphological properties are investigated to evaluate later on the compositional impact on the resistive switching properties of MIM' type micro - as well nano-crossbar devices.

### 4.1 Chemical and physical properties of ALD $\text{Sr}_x\text{Ti}_y\text{O}_z$

By means of spectroscopic ellipsometry (SE) and X-ray photoelectron spectroscopy (XPS) the thickness and chemical composition of as-deposited STO films on planar Si/SiO<sub>2</sub>/Pt structures were analyzed. Further description about the ways of characterization applied to comparable STO films grown on different substrates is given in references [75, 78-79]. Table 4.1 comprises of the properties of the STO films which were used in this study. It is noteworthy here that the planar Pt layers were deposited exactly in the same manner as the Pt bottom electrodes of the crossbar structures in order to assure identical ALD growth behavior of the STO films. Films of three compositions were studied, Ti-rich STO, stoichiometric STO, and Sr-rich STO with [Sr]/ ([Sr]+[Ti]) ratios of 0.46, 0.50, and 0.57, respectively. Crystallization of the as-deposited amorphous films was induced by means of an additional rapid thermal annealing (RTA) step at 600°C performed after ALD growth. Due to densification the films' thickness decreased to about 0.90 % of the value obtained before annealing. Attention was paid to the effect of non-stoichiometry of the as-deposited ALD grown amorphous STO layers on the microstructural evolution and homogeneity of the annealed thin films. Although variations of the cation composition in the as-deposited amorphous films can be easily managed by the choice of the ALD subcycle ratio, composition-induced effects on the films' crystallization behavior might result in different microstructures for films of various compositions after annealing.

**Table 4.1:** Influence of the  $(\text{SrO})/(\text{TiO}_2)$  ALD cycle ratio on the elemental composition of about 30 nm and 15 nm thick amorphous STO films. The composition, i.e., the  $[\text{Sr}]/([\text{Sr}]+[\text{Ti}])$  ratio, was determined by SE and cross-checked by XPS. The relative errors in the  $[\text{Sr}]/([\text{Sr}]+[\text{Ti}])$  ratios from SE and XPS are  $\pm 0.03$  and  $\pm 0.02$  respectively.

STO composition	$(\text{SrO})/(\text{TiO}_2)$ ALD cycle ratio	$[\text{Sr}]/([\text{Sr}]+[\text{Ti}])$ ratio from SE	$[\text{Sr}]/([\text{Sr}]+[\text{Ti}])$ ratio from XPS
Ti-rich	1:4	0.46	0.46
Stoichiometric	1:3	0.50	0.50
Sr-rich	1:2	0.57	0.58

In high quality, dislocation-free  $\text{SrTiO}_3$  single crystals solubility limit for cation excess is very narrow for both regimes, i.e., SrO or  $\text{TiO}_2$  enrichment. Witek *et al.* [80] found for  $\text{SrTiO}_3$  ceramics that an Ti excess of only 0.5 at% is sufficient to start segregation of  $\text{TiO}_2$  typically in the triple points. Depending on the oxygen partial pressure of the annealing atmosphere, not only  $\text{TiO}_2$  but also various titanium suboxides might form. [81] As a consequence of deviations from the ideal  $\text{SrTiO}_3$  stoichiometry, intergrowth of SrO layers or  $\text{TiO}_2$  layers into the perovskite-type  $\text{SrTiO}_3$  structure might occur. The intergrowth leads to the formation of either Ruddlesden-Popper type-phases for the Sr-rich STO material, i.e.,  $\text{Sr}_{n+1}\text{Ti}_n\text{O}_{3n+1}$  [82-83], or Magnéli type-phases for the Ti-rich STO films, i.e.,  $(\text{Ti}_n\text{O}_{2n-1})^*(\text{SrTiO}_3)$  [84-86]. For standard ALD- and annealing temperatures the mean free path of cations is limited, and therefore in the STO thin films an ordered-fashion-type intergrowth might only happen on a local scale leading to micro-regions of slightly different composition [83]. The incorporation of cations in excess of the stoichiometric  $\text{SrTiO}_3$  composition has been investigated for different ALD STO thin films due to the potential application as high- $k$  material [87]. Clima *et al.* [88] and Popovici *et al.* [89] studied the crystallization behavior of Sr-rich STO films grown by thermal ALD from  $\text{Sr}(\text{tBu}_3\text{Cp})_2$  and  $\text{Ti}(\text{OMe})_4$ . After RTA (rapid thermal annealing) at 600 °C the films showed perovskite related reflections in XRD whereas the peaks of the Sr-rich STO film are slightly shifted towards lower angle as compared to the stoichiometric STO film. This ‘metastable crystalline’ state was transferred into a Ruddlesden-Popper (RP)-type crystalline structure,  $\text{SrO}(\text{SrTiO}_3)_n$ , after annealing at about 1000°C [88]. A similar observation was reported by Shibuya *et al.* [90] for PLD grown  $\text{Sr}_2\text{TiO}_4$  films which show a distribution of extended defects and a regular RP-phase structure depending on

the growth temperature. Local imperfections and inhomogeneities in the thin film structure and morphology can play a significant role in the resistive switching behavior of oxide devices. Hence, the micro-structural properties of the 600°C annealed ALD STO thin films were carefully analysed. The chemical composition and the thickness of as-deposited STO films on planar Si/SiO<sub>2</sub>/Pt structures were characterized by means of spectroscopic ellipsometry (SE) and X-ray photoelectron spectroscopy (XPS). Further details on the characterization methods applied to comparable STO films grown on different substrates have been reported in references [75, 78-79].

#### **4.1.1. Chemical properties of ALD grown $\text{Sr}_x\text{Ti}_y\text{O}_z$**

The information regarding composition was determined from X-ray photoelectron spectroscopy (XPS) data taken with a Thermo Scientific K-Alpha spectrometer using monochromatic Al K $\alpha$  X-ray radiation ( $h\nu = 1486.6$  eV). Charge correction was performed by setting the C1s signal at a binding energy of 284.8 eV [91]. The binding energies of Ti 2p<sub>3/2</sub> of  $\sim 458.5$  eV, and of Sr 3d<sub>5/2</sub> of  $\sim 133.3$  eV found for all three samples of various compositions are in good agreement to bulk reference data [92]. For the 12 nm thick STO films annealed at 600 °C detailed photoelectron spectra taken for the Sr 3d, Ti 2p, and O 1s signals are shown in Fig. 4.1(a), (b) and (c) respectively. For a comparison of the chemical states of the constitutive cations in the stoichiometric, Ti-rich and Sr-rich STO films, the photoelectron spectra for the Ti 2p and Sr 3d signals were normalized to the maximum intensity of the Ti 2p<sub>3/2</sub> and Sr 3d<sub>5/2</sub> lines, respectively. The normalized pattern is given in Figs. 4.2. Generally the thin film signals reveal a broadening as compared to single crystal reference data indicating a higher degree of lattice disorder. However a qualitative analysis of the Ti 2p lines (see Fig. 4.2 (a)) indicates the same valence states and FWHM values for all three STO compositions. The Sr 3d lines (cf. Fig. 4.2 (b)) of the stoichiometric and the Ti-rich STO film are nearly identical, while for the Sr-rich STO a broadening of the respective peaks towards higher binding energies is observed, indicating the formation of a Sr-carbonate compound in the near-surface region. The O 1s signals in Fig. 4.1 (c) show two characteristics, a broader shoulder originating from carbonly-adsorbates on the surface and the O 1s peak at  $\sim 529.8$  eV attributed to SrTiO<sub>3</sub>. Comparing the height of the contributions qualitatively, one finds that the intensity ratio of surface oxygen to bulk oxygen increases with increasing  $[\text{Sr}]/([\text{Sr}]+[\text{Ti}])$  content.

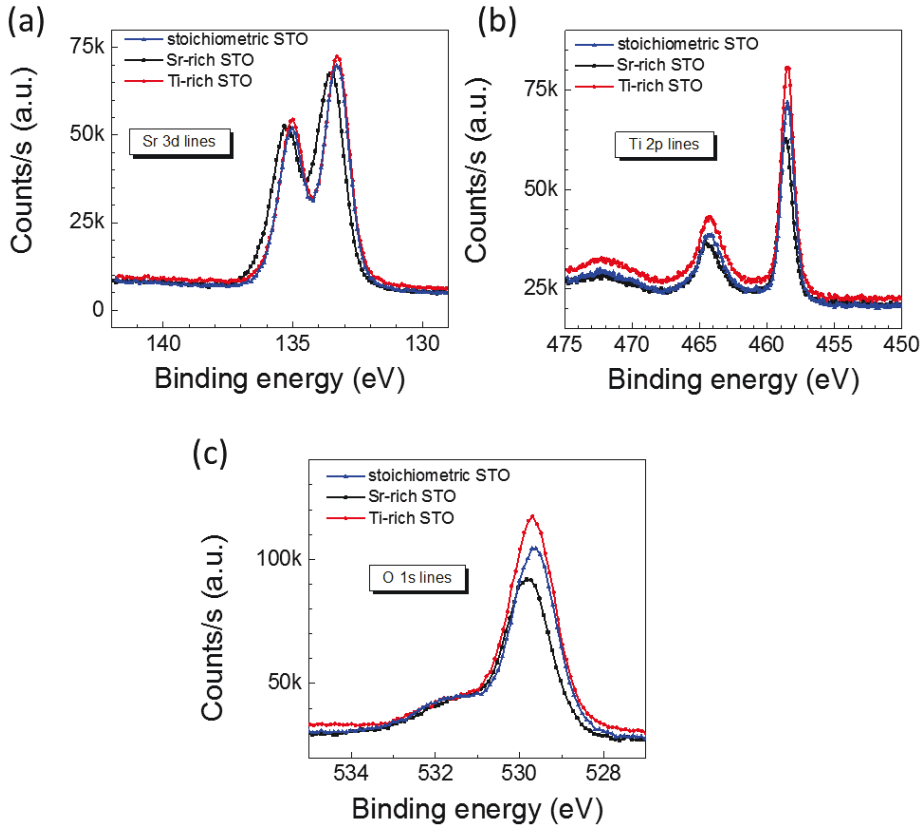


**Figure 4.1:** X-ray photoelectron spectra taken for the 12 nm thick STO films with different  $[\text{Sr}]/([\text{Sr}]+[\text{Ti}])$  compositions according to Table 4.1 and indexed by the color code. The detail spectra show the (a) Sr  $3d_{5/2}$  lines, (b) Ti  $2p_{3/2}$  lines and (c), the O  $1s$  lines. All films were grown on planar Pt/Si substrates and annealed at  $600^\circ\text{C}$  in nitrogen for 5 min, analog to the crossbar structures. Reprinted with the permission of [60]

The formation of a strontium carbonate compound on the surface of the Sr-rich STO film agrees with a microscopic model of an intergrowth of SrO and  $\text{SrTiO}_3$  layers in the Sr-rich STO films (0.57), where SrO in the near surface region will react to form  $\text{SrCO}_3$  based compounds [231]. The XPS data of the  $600^\circ\text{C}$  annealed STO films can be consistently interpreted under the assumption of SrO intergrowth in the Sr-rich STO films. Although defined signals originating from  $\text{TiO}_{2-x}$  intergrowth in the Ti-rich STO films were not found, the broadening of the Ti 2p lines might indicate additional Ti oxidation states.

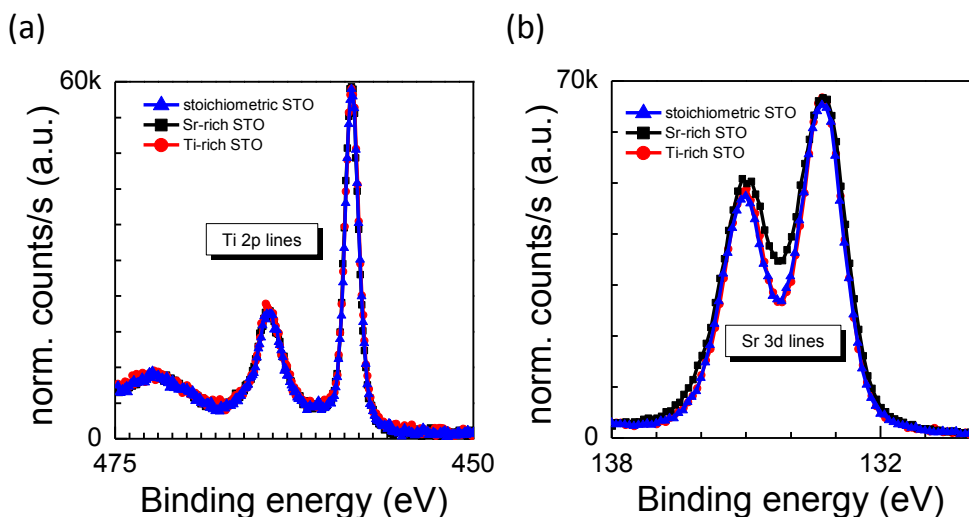


**Figure 4.2:** A comparative analysis of the chemical states of the constitutive cations in the stoichiometric, Ti-rich and Sr-rich STO films showing the photoelectron spectra for the (a) Ti 2p and (b) Sr 3d signals normalized to the maximum intensity of the Ti 2p<sub>3/2</sub> and Sr 3d<sub>5/2</sub>. Reprinted with the permission of [60]

#### 4.1.2. Optical properties of ALD grown $\text{Sr}_x\text{Ti}_y\text{O}_z$

Spectroscopic ellipsometry was used to determine the  $[\text{Sr}]/([\text{Sr}]+[\text{Ti}])$  ratios of the ALD grown  $\text{Sr}_x\text{Ti}_y\text{O}_z$  thin films on the basis of an SE optical constant library [75]. Comparison of the  $[\text{Sr}]/([\text{Sr}]+[\text{Ti}])$  ratios of the as-deposited  $\text{Sr}_x\text{Ti}_y\text{O}_z$  films determined from SE and XPS as listed in Table 4.1 reveals excellent agreement between the different methods. In addition to the chemical analysis, SE was also utilized to determine the dielectric optical functions of the STO layers as a function of the composition as well as of the annealing treatment. Figures 4.3 (a) to (d) show the real and imaginary parts ( $\epsilon_1$  and  $\epsilon_2$ ) of the determined dielectric functions of about 30 nm thick  $\text{Sr}_x\text{Ti}_y\text{O}_z$  films in the as-deposited state (a and b) and after RTA treatment at 650° C for 10 minutes (c and d). For the as-deposited  $\text{Sr}_x\text{Ti}_y\text{O}_z$  films (cf. Fig. 4.3 (a), (b)) the dielectric function shows an increase in magnitude of both  $\epsilon_1$  and  $\epsilon_2$  with increasing Ti-content, which is in agreement with previous results [75]. For the 650 °C-RTA processed films (cf. Fig. 4.3 (c), (d)) a change in the dielectric function ( $\epsilon_1$  and  $\epsilon_2$ ) of the stoichiometric ( $[\text{Sr}]/([\text{Sr}]+[\text{Ti}]) = 0.50$ ) and the Sr-rich (0.57) film is observed. In contrast no remarkable changes in the dielectric function between as-grown and annealed quality are visible for the Ti-rich film (0.46).



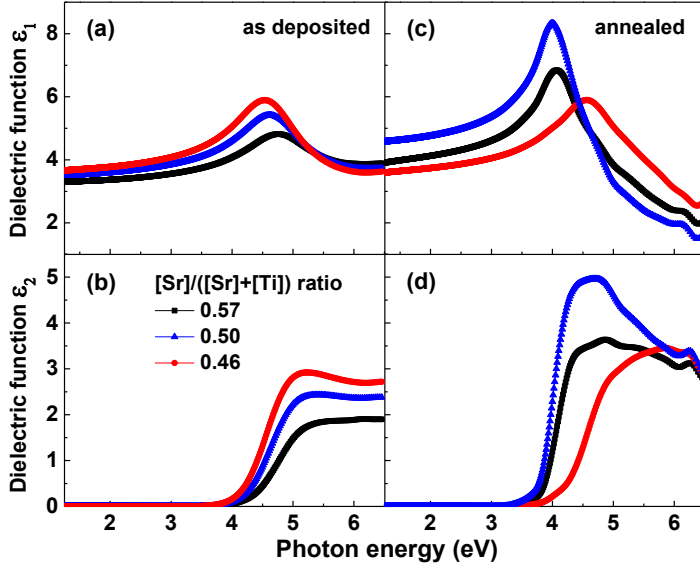


**Figure 4.3:** Optical dielectric functions ( $\epsilon_1$  and  $\epsilon_2$ ) of the stoichiometry series of about 30 nm thick  $\text{Sr}_x\text{Ti}_y\text{O}_z$  thin films grown at 350 °C on Pt coated Si substrate by plasma-assisted ALD (a,b) and after annealing at 600°C for 10 min in  $\text{N}_2$  (c,d). Reprinted with the permission of [102]

The changes in dielectric function are attributed to crystallization of the respective  $\text{Sr}_x\text{Ti}_y\text{O}_z$  films into the perovskite structure. We note here that the stoichiometric and Sr-rich films were fully crystallized while the Ti-rich STO film remained amorphous or exhibited only partial crystallization [75]. The optical constants of the films have been determined from the dielectric function values through the relations:

$$\epsilon_1 = n^2 - k^2 \text{ and } \epsilon_2 = 2nk, \quad (4.1)$$

here  $n$  is the refractive index and  $k$  is the extinction coefficient.

The band gap values  $E_g$  of as-deposited and annealed films, both  $\sim 30$  nm thick were determined from the plot  $(ah\nu n)^{1/2}$  versus  $h\nu$ , shown in Fig. 4.4 (a-b), respectively, where  $h\nu$  is the energy of incident photons and  $\alpha$  is the absorption coefficient. Fitting the linear parts of these curves by a straight line enables an approximate determination of the band gap values from the intercepts of these lines with the horizontal axis. The band gap value for a (100)  $\text{SrTiO}_3$  single crystal purchased from Crystal GmbH, Berlin, Germany was determined as a reference.

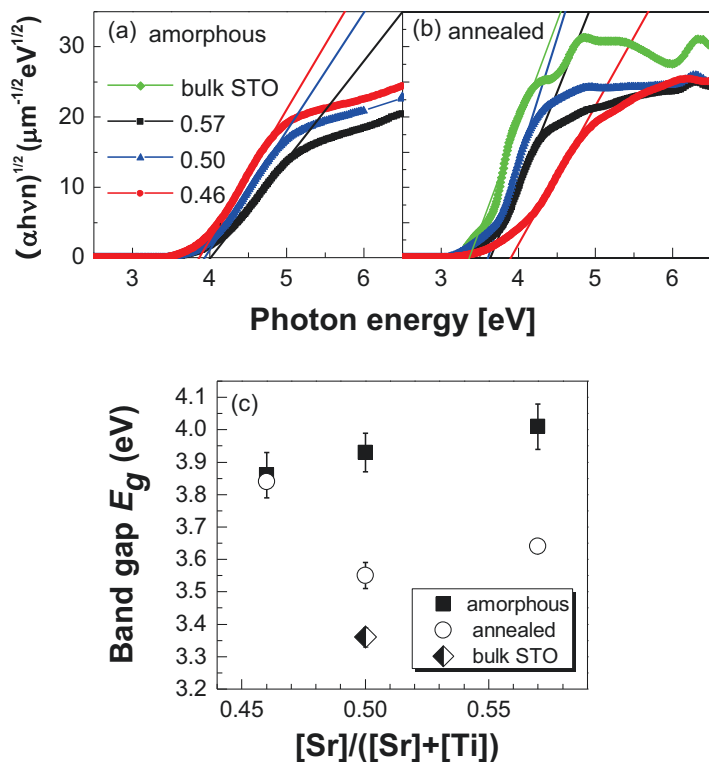


**Figure 4.4:** Determination and values of the optical band gap  $E_g$  of (a) as deposited (amorphous) and (b) 650°C annealed films as a function of the  $\text{Sr}_x\text{Ti}_y\text{O}_z$  stoichiometry. Data point of a  $\text{SrTiO}_3$  single crystal is added as a reference. Reprinted with the permission of [102]

The band gap values for as-deposited and annealed STO films and the STO single crystal are given in Fig. 4.4 (c). The band gap values of the as-deposited amorphous STO films increase with increasing Sr-content as previously reported [75]. For the annealed Ti-rich STO film no remarkable change compared to the as-grown state was recorded in agreement with the fact that this film remained amorphous after 650 °C anneal. Due to the crystallization in the perovskite phase the stoichiometric and Sr-rich STO film showed a decrease in the band gap after the RTA step. Also for the crystallized films an increased Sr-content resulted in a higher band gap. The band gap values obtained for the crystallized films were higher than the bulk value 3.35 eV (see Fig. 4.4(c)). Higher band gap values for nanocrystalline STO thin films compared to the bulk value have been reported in the literature [93-94]. The ‘optical shift of the band gap’-effect has been attributed to quantum-size effects due to the nanoscale crystallites’ dimension [95- 96].

## **4.2 Crystallization behavior of ALD grown $\text{Sr}_x\text{Ti}_y\text{O}_z$ films**

For crystallization of the layers into the perovskite structure a post-deposition rapid thermal annealing (RTA) of the films at 600 °C in nitrogen atmosphere was performed. The structural properties of the annealed films grown on planar Pt substrates were analyzed by means of grazing-incidence X-ray diffractometry (GI-XRD) using a Panalytical X'Pert PRO MRD system with  $\text{Cu K}_\alpha$  radiation. Fig. 4.5 shows the GI-XRD spectra of the 12 nm thick  $\text{Sr}_x\text{Ti}_y\text{O}_z$  films with three different compositions. The spectra clearly disclose that regardless of the nonstoichiometry, all STO films appeared to crystallize into the metastable perovskite phase. The observations can be compared to the previous reports on the micro-structural evolution of annealed ALD STO films [75, 87, 89, and 98]. For the metastable crystalline Sr-rich STO films it is suggested that the excess SrO could be distributed randomly and in a disordered manner in the  $\text{SrTiO}_3$  matrix. This picture might be valid for the metastable crystalline STO thin films of different stoichiometry investigated in this study.

## **4.3 Morphologies of ALD grown $\text{Sr}_x\text{Ti}_y\text{O}_z$ films**

Additionally, the morphology of the annealed films was studied by scanning electron microscopy (SEM) using a Hitachi SU 8000 system. Plasma-assisted ALD STO thin films after annealing at 600 °C were analyzed with respect to the different compositions and film thickness in terms of microstructure and the morphology. The thin film crystallization is controlled by the kinetics of nucleation and grain growth. This study was performed on similar STO films deposited on  $\text{Si}_3\text{N}_4$  membranes utilized as 'transparent' thin film supports for transmission electron microscopy (TEM) [79]. The performed TEM investigations revealed that the crystallization of the films yielded transrotational perovskite-type crystals. In particular, the regular small-grain morphology of the crystalline Sr-rich STO films was imputed to a high nucleation probability at the onset of crystallization process.

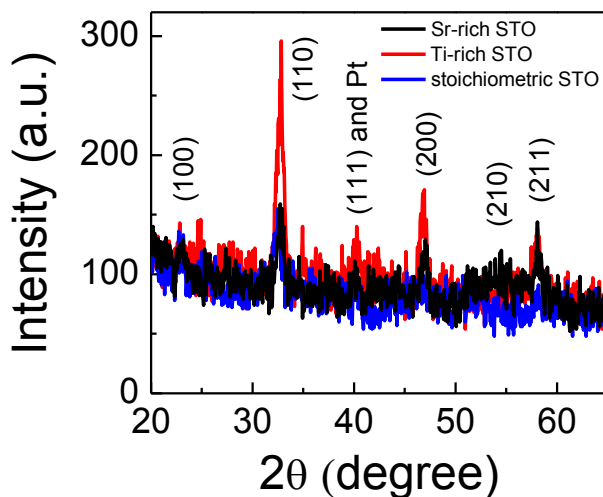


**Figure 4.5:** GI-XRD scans for the structural characterization of 12 nm thick STO films with different  $[\text{Sr}]/([\text{Sr}]+[\text{Ti}])$  compositions according to Table 2. The films were grown on planar Pt/Si substrates and annealed at 600° C in nitrogen for 5 min, analog to the crossbar structures. Reprinted with the permission of [60]

In addition, the important influences of STO composition and annealing temperature on the final grain size, the tendency for cracking and the formation of voids has been demonstrated. After annealing at 600 °C in nitrogen for about 5 min (for STO films of 12 nm thickness) and 10 min (for 15 nm), microstructural characterizations were performed on STO thin films deposited on planar Si/Pt substrates. In Figure 4.6 shows plan-view high resolution SEM top view micrographs of the annealed STO thin films. The pictures are arranged from left to right with respect to a decreasing Sr-content, in particular Sr-rich STO (0.57), stoichiometric STO (0.50), and Ti-rich STO (0.46). The graphs of the 15 nm thick STO films are shown in Figs. 4.6 (a) to (c) and those of the 12 nm films are given in Figs. 4.6 (d) to (e). The Sr-rich and the stoichiometric composition both show a comparable surface morphology for the films of different thickness, while grain boundaries are more apparent in the 15 nm thick as compared to 12 nm thick films. The Sr-rich STO films (c.f. Fig. 4.6 (a) and (d)) exhibit a finer grained structure with a more uniform morphology if compared to the stoichiometric STO films shown in Fig. 4.6 (b) and (e) where grid-patterns formed by small cracks developed at the grain boundaries upon crystallization and densification (see also [79]). These types of micro-cracks seem less apparent for the Sr-rich films. This observation is consistent with previous a TEM

study [79] which describes an increased nucleation density resulting in a higher density of smaller grains for the Sr-rich films as compared to the stoichiometric STO films. In addition to the described topological issues, regimes of different contrast with a lateral extension of about 100 nm – 500 nm are revealed in the SEM micrographs (see Fig. 4.6(c) and (f)). This observation is especially pronounced for the Ti-rich STO films which show a different surface morphology altogether. Regarding previous crystallization studies [79], the difference in morphology was explained by a locally incomplete crystallization process. Additional AFM pictures shown in Figures 4.7 (a) to (c) reveal a complementary view. While the Sr-rich and stoichiometric STO thin film samples show very smooth surface morphologies, a patch like structure is obtained for the Ti-rich STO sample. Comparing Fig. 4.7 (c) with Fig. 4.6 (e) revealed that the regions of brighter contrast in the SEM picture exhibit an average thickness which is reduced by about 10 % compared to the surrounding darker regions. The thickness reduction is attributed to a local densification induced by the temperature anneal. Additionally, the inhomogeneity is attributed to a locally inhomogeneous stoichiometry of the Ti-rich STO films leading to crystallization in the regime of Ti-excess while the surrounding STO film stays in the amorphous phase. The different shapes of the crystallites between the films of 12 nm and 15 nm in thickness might relate to a thickness effect on the crystallization or to slight differences in composition. The reduced thickness is relevant to a densification process due to the crystallization. It has been shown that Ti-rich STO thin films require more thermal budget to induce crystallization compared to stoichiometric and Sr-rich films [79]. Hence, minor differences in composition can lead to significant modifications in the crystallization behavior of the Ti-rich films.

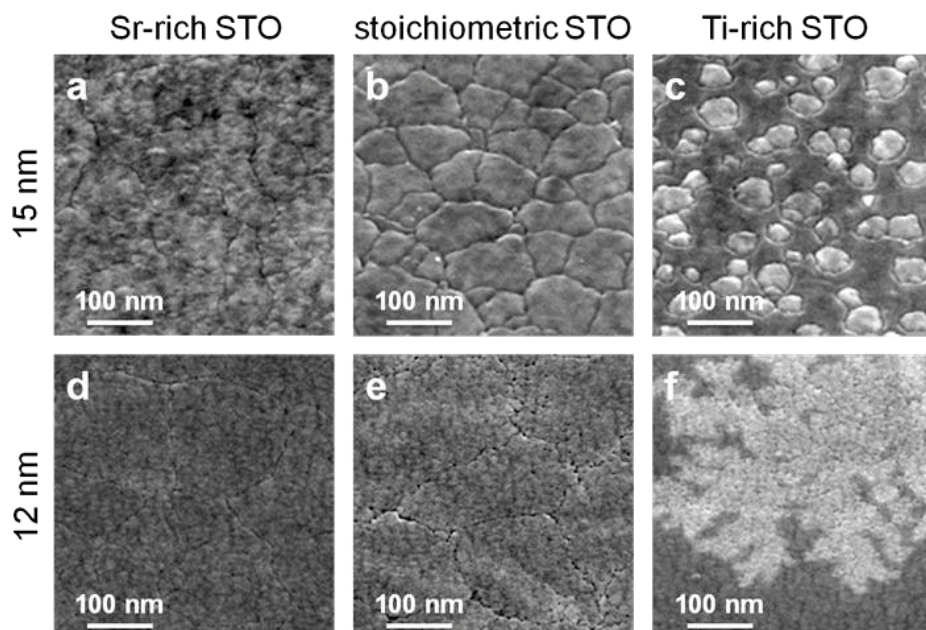


**Figure 4.6:** SEM top view micrographs of STO thin films of different  $[\text{Sr}]/([\text{Sr}]+[\text{Ti}])$  compositions grown on planar Si/Pt substrates and annealed at 600 °C in nitrogen; (a-c) 15 nm films annealed for 10 min, (d-f) 12 nm films annealed for 5 min; the STO compositions are arranged from the left to the right, i.e., Sr-rich (a,d), stoichiometric (b,e), and Ti-rich (c,f). Reprinted with the permission of [60]

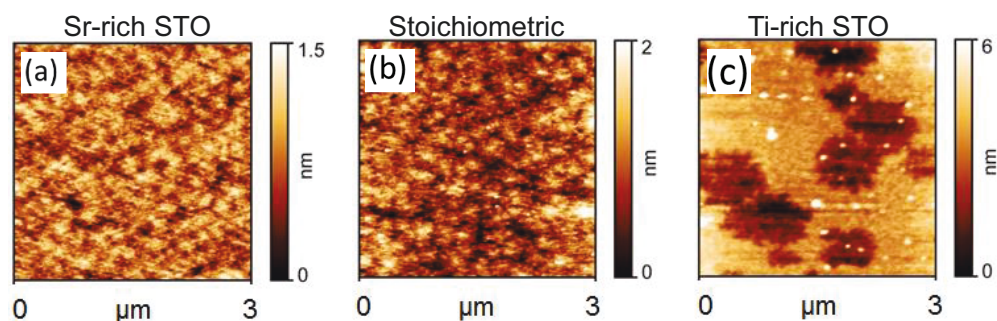


**Figure 4.7:** AFM pictures showing the topography of the 12 nm STO thin films grown on planar Si/Pt substrates and annealed for 5 mins at 600 °C under nitrogen atmosphere; the different STO compositions (a) Sr-rich (b) stoichiometric and (c) Ti-rich shows significant difference in the films' morphology. Reprinted with the permission of [60]

## **4.4 Summary**

In this chapter, the optical, chemical and morphological properties of  $\text{Sr}_x\text{Ti}_y\text{O}_z$  thin films deposited by means of plasma-assisted ALD on Pt-coated Si-substrates are presented. A pronounced effect of the local cation composition ( $[\text{Sr}] / ([\text{Sr}] + [\text{Ti}])$ ) of the as-deposited films on the respective microstructure after annealing under nitrogen at 600–650 °C is revealed. In addition, the influence of the composition on the optical, chemical and physical properties of the films in the amorphous and the polycrystalline states is discussed.

## 5. Resistive Switching Behavior of the $\text{Sr}_x\text{Ti}_y\text{O}_z$ Films

---

This chapter is assigned to the resistive switching (RS) properties of ALD grown strontium titanate ( $\text{Sr}_x\text{Ti}_y\text{O}_z$ ) thin film cells. Metal-STO-metal structures prepared from industrial compatible processes have been investigated focusing on the effects of composition, microstructure and device size. Metastable perovskite-type STO films were deposited on sputtered Pt substrates utilizing plasma-assisted atomic layer deposition (ALD) from cyclopentadienyl-based metal precursors and oxygen plasma at 350 °C, and a subsequent annealing at 600 °C in nitrogen. Two different film thicknesses of 15 nm and 12 nm with three different compositions ( $[\text{Sr}]/([\text{Sr}]+[\text{Ti}])$ ) of 0.57 (Sr-rich STO), 0.50 (stoichiometric STO) and 0.46 (Ti-rich STO) were integrated into crossbar structures with sizes ranging from 100  $\mu\text{m}^2$  to 0.01  $\mu\text{m}^2$  and with a stack sequence given as Pt (bottom electrode) / STO / TiN (top electrode). Nano-structural characterizations disclosed a clear effect of the composition of the as-deposited STO films on their crystallization behavior and thus on the final microstructures. Local current maps obtained by local-conductivity atomic force microscopy (LC-AFM) were in good agreement with local changes of the films' microstructures depending on the composition of the  $\text{Sr}_x\text{Ti}_y\text{O}_z$  thin films after ex-situ annealing.

### 5.1 Electrical properties of crossbar cells in the initial state

The effect of the  $[\text{Sr}]/([\text{Sr}]+[\text{Ti}])$  composition on the dielectric properties of MOM based devices obtained from 15 nm thick films annealed at 600°C has been investigated in a study reported in detail in reference [102]. Mean values of the capacitance density were about 50 fF/ $\mu\text{m}^2$ , 25 fF/ $\mu\text{m}^2$ , and 10 fF/ $\mu\text{m}^2$  for the stoichiometric, the Sr-rich and the Ti-rich STO composition, respectively. Considering the identical device geometry and film thickness the differences were addressed to the different microstructures and different bulk properties of the STO layers. The high effective dielectric permittivity of  $\epsilon_{\text{eff}} \approx 85$  calculated for the stoichiometric STO material was attributed to a higher degree of crystallization in the stoichiometric STO film as compared to nanocrystalline Sr-rich STO



( $\epsilon_{\text{eff}} \approx 42$ ) and partly amorphous Ti-rich STO film ( $\epsilon_{\text{eff}} \approx 17$ ). In addition to the dielectric properties of the STO thin film devices, the initial leakage behavior of micro- and nano-crossbar devices containing STO thin films of different compositions were analysed by means of current-voltage characteristics measured on pristine cells. Figures 5.1(a) and (b) show representative  $I$ - $V$  curves of the pristine Pt/STO/TiN cells where the voltage signal was always applied to the TiN top electrode. The voltage range was restricted  $\pm 2.0$  V in order to avoid an unwanted electroforming of the MOM devices. The asymmetry of the  $I$ - $V$  curves is attributed to the different Schottky barriers of the STO films in contact with the TiN top electrode compared to the Pt bottom electrode. Typically, the STO cells reveal an electroforming into the OFF state for a positive voltage applied to the TiN top electrode, inducing a soft breakdown at the Pt (BE) Schottky barrier. Because the electroforming is observed for positive polarity of the voltage applied to the TiN top electrode, the leakage currents are compared for the positive polarity. The initial leakage current values were analysed for statistical ensembles consisting of about 30 devices for each sample. The resulting cumulative distribution functions (CDF) of the leakage currents are shown in Figures 5.1 (c) and (d) for the micro- and nano-sized crossbar cells, respectively. Addressing the huge difference in the initial leakage current values, the representative data are taken at +1.0 V for the stoichiometric and Ti-rich STO samples and at +2.0 V for the more insulating Sr-rich STO devices. In the following sections the leakage current characteristics as a function of the composition will be separately discussed for the micro- and nano-crossbar structures built from 15 nm and 12 nm thick STO films, respectively.

### 5.1.1. Micro-crossbar devices

Fig. 5.1(a) shows the  $I$ - $V$  plots for micro-crossbar cells of about  $1 \times 1 \mu\text{m}^2$  size made from the Sr-rich, stoichiometric, and Ti-rich STO films of about 15 nm thickness annealed at 600°C for 10 min. The current values show a slight asymmetry with respect to the voltage polarity which is attributed to the difference in the work functions of the respective electrode metals, Pt and TiN, thus giving rise to different Schottky barrier heights of the respective metal/STO interface. Although well-defined data for ALD STO/metal interfaces are not available from the literature, the ALD  $\text{HfO}_2$ /metal system might serve as a reference here. For these interfaces effective metal work functions of about 5.15 eV for Pt [99] and  $(4.56 \pm 0.35)$  eV for TiN [100] in contact to ALD  $\text{HfO}_2$  have been determined revealing a difference in the barrier heights of roughly 0.5 eV. From the 50%

values of the CDF functions Fig. 5.1 (c) mean initial resistances of the micro-crossbar devices were determined being about 5 G $\Omega$  for Sr-rich STO (at + 2.0 V), 4 M $\Omega$  for Ti-rich STO and 25 k $\Omega$  for the stoichiometric STO (at +1.0 V). The surprisingly low resistance of the device from stoichiometric STO contradicts the findings reported by other groups [87, 101]. For this study, the finding might be attributed to the formation of micro-cracks in the 15 nm thick annealed  $\text{SrTiO}_3$  films which cause an increased current flow. The insulating behavior of the Sr-rich STO devices is in line with the regular dense morphology of the fine-grained films and with the slightly increased band gap found for the Sr-rich STO [102].

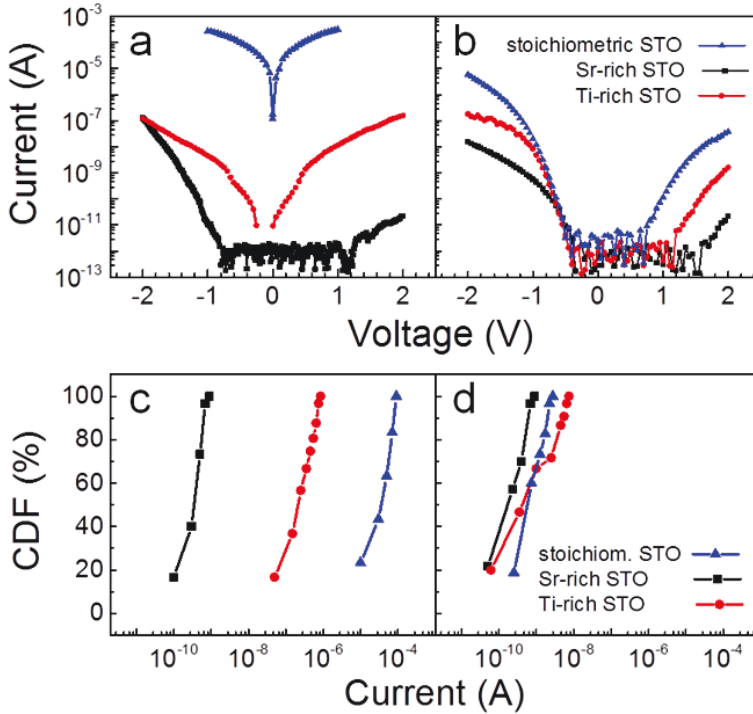


**Figure 5.1:** Current-voltage ( $I$ - $V$ ) characteristics as a function of the STO composition (see Table 4.1) of Pt/STO/TiN devices in pristine state measured at 25 °C with the voltage applied to the TiN top electrode. (a) Micro-crossbar devices of 1.0  $\mu\text{m}^2$  size made from 15 nm thick polycrystalline STO films, and (b) 0.01  $\mu\text{m}^2$  size nano-crossbar structures with 12 nm thick STO integrated. Respective cumulative distribution functions (CDF) showing the leakage current variations of the (c) micro-crossbar and (d) nano-crossbar devices. The leakage current value was determined at + 2.0 V for the Sr-rich STO films and at + 1.0 V for the stoichiometric and Ti-rich STO films. Reprinted from [60]

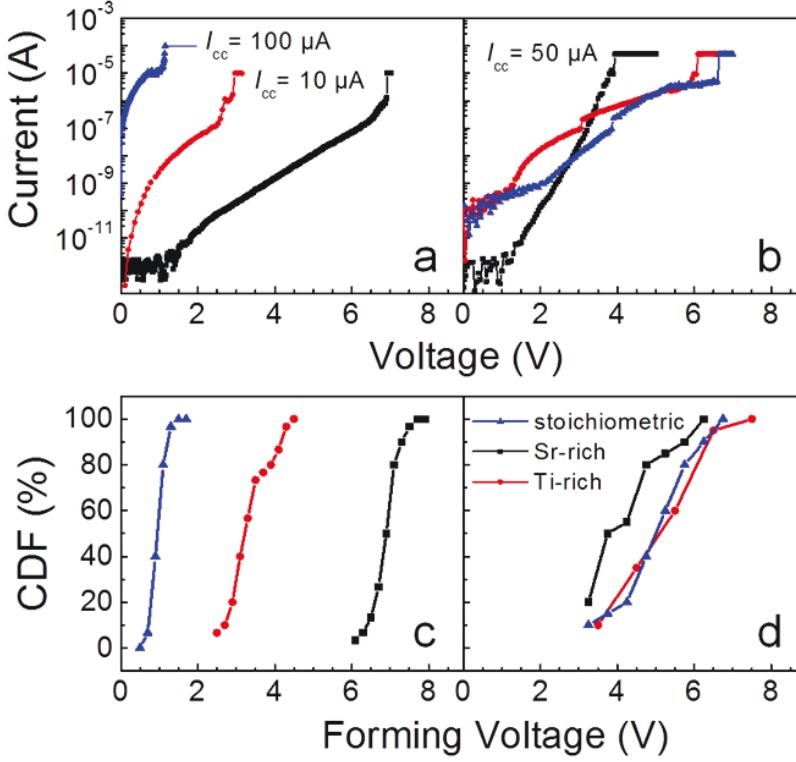
### 5.1.2. Nano-crossbar devices

Figure 5.1 (b) shows the  $I$ - $V$  plots for the nano-crossbar devices of  $0.01\ \mu\text{m}^2$  size built from 12 nm thick STO films of different compositions which were annealed at  $600^\circ\text{C}$  for 5 min. For the small pad sizes the current-resolution of the setup of about 1 pA was easily reached at low voltages. The leakage current data of these polycrystalline STO films at higher voltages are in reasonable agreement with results reported for high- $k$  STO thin films [87, 101]. It is observed that the leakage current for the stoichiometric STO films of 12 nm thickness was considerably reduced as compared to the 15 nm thick film (see Fig. 5.1 (a)). This behavior can be attributed to the difference in the films' microstructures. The SEM micrographs in Fig. 4.6 (b) and (e) clearly indicate that micro-cracks are more apparent in the 15 nm as compared to the 12 nm STO film. This might result from the variation of the film thickness, the slightly different annealing times, or both. From the comparison it is concluded that the enhanced current flow in the devices containing stoichiometric STO films is mainly along nano- or micro- cracks rather than along grain boundaries.

A statistical analysis of the mean leakage currents of the STO nano-crossbar devices is given in Fig. 5.1 (d). The data for the Sr-rich and stoichiometric STO devices are based on a yield of insulating devices of  $> 90\%$ . Thus the mean resistance values of about a few 10 G $\Omega$  for Sr-rich STO and a few G $\Omega$  for the stoichiometric STO devices can be regarded as solid representative values. In contrast, the Ti-rich STO nano-crossbar devices show a rather large spread in their initial resistance values ranging from about several G $\Omega$  to values in the range of 100 M $\Omega$ . Therefore the CDF of the leakage current of the Ti-rich STO nano-crossbar devices is described by a type of bimodal distribution (see Fig. 5.1 (d)). This result of the statistical evaluation of about 30 devices is in good agreement with the local conductivity distribution measured on the 12 nm Ti-rich STO film by means of LC-AFM using the AFM-tip as the nano top electrode (see Fig. 5.8(g)). This comparison can be interpreted in the way that for the case of the partly crystallized 12 nm Ti-rich STO films the nano-crossbar devices might include either an area of crystalline or of amorphous material resulting in a lower or higher value for the initial resistance, respectively. Therefore the resistive switching study which is described in the following was performed only on devices which were formed into the ON state by a positive voltage signal and which were successfully reset to the OFF state by a negative voltage applied to the top electrode.

## 5.2 Electro-forming of the crossbar devices

The voltage controlled electro-forming process [103] of the Pt/STO/TiN diodes was performed by applying a positive voltage ramp to the TiN (used as top electrode, TE) with the Pt (bottom electrode, BE) grounded. For protection of the device from hard breakdown a current compliance  $I_{CC}$  for the electroforming procedure was set with values between 10  $\mu A$  and 100  $\mu A$ , depending on the leakage current behavior of the investigated cell. Representative  $I$ - $V$  electroforming curves for devices of different STO compositions and for two different pad sizes, explicitly 1.0  $\mu m^2$  and 0.01  $\mu m^2$ , are shown in Figs. 5.2 (a) and (b), respectively. The electro-forming voltage  $V_{EF}$  is the voltage at which the abrupt increase in current, the soft breakdown, occurred. Thus, the initially insulating MOM structure changed into a higher conducting state, representing voltage-induced electroforming into the ON state. Application of a voltage ramp of opposite polarity resulted in a partial recovery of a high resistivity, thus the device was reset into the OFF state. The micro- crossbar devices from STO films of various compositions (see Fig. 5.2 (a)) show a clear trend of decreasing electroforming voltage with increasing leakage current of the MOM structure. This trend was not explicitly repeated in the electro-forming behavior of the nano-crossbar devices (Fig. 5.2 (b)), which nevertheless reproduce well the  $I$ - $V$  curves of the pristine devices for voltages of about +2.0 V (see Fig. 5.1(b)). This observation is owed to differences in the conduction mechanisms at high fields for the devices built from STO thin films of different compositions and microstructures. To summarize, various Pt/STO/TiN devices were electro-formed into the ON state when a voltage ramp of positive polarity was applied to the TiN TE, equaling a negative voltage polarity at the Pt (BE) Schottky electrode. If the samples were afterwards polarized with a negative voltage of about -3.0 V, the high current through the devices was reduced significantly; the devices were reset into a higher resistance state. For each STO thin film sample statistical analysis was performed for an average of 30 devices formed into the ON state with respect to the electroforming and later with respect to the RS behavior. Figs 5.2 (c) and (d) show the cumulative probability plots of the electro-forming voltages ( $V_{EF}$ ) as a function of the STO composition for 1.0  $\mu m^2$  devices with 15 nm thick STO and 0.01  $\mu m^2$  cells with 12 nm thick STO. For the micro-crossbar cells Fig. 5.2 (c) a clear dependency of the films composition on the value of  $V_{EF}$  is found, with very little variation in  $V_{EF}$  for equivalent devices.



**Fig. 5.2:** Representative electro-forming  $I$ - $V$  curves for the (a) micro-crossbar ( $1.0 \mu\text{m}^2$ , 15 nm STO) and (b) nano-crossbar ( $0.01 \mu\text{m}^2$ , 12 nm STO) Pt/STO/TiN devices. A positive voltage ramp applied to the TiN top electrode initiated a soft-breakdown event while the devices were protected by a current compliance  $I_{cc}$ . Each cumulative distribution function (CDF) was derived from thirty electroformed (c) micro- and (d) nano-crossbar devices. Reprinted with the permission of [60]

The mean values were for Sr-rich STO  $V_{EF} = 7.0 \pm 1.0$  V, for Ti-rich STO  $V_{EF} = 3.5 \pm 1.0$  V, and for stoichiometric STO  $V_{EF} = 1.0 \pm 0.5$  V. The electro-forming voltages are higher for devices with lower initial leakage currents. In contrast, for the nano-crossbar devices a similar effect of the different STO composition on the electro-forming voltage was not seen (compare Fig. 5.2 (d)). However, if compared to the micro-crossbars the device-to-device variations in electroforming voltage increased considerably as demonstrated by the non-steep CDF-characteristics in Fig. 5.2(d). Mean values of the nano-crossbar devices determined for the various compositions were for Sr-rich STO  $V_{EF} = 4.5 \pm 1.5$  V, and for stoichiometric and Ti-rich STO  $V_{EF} = 5.0 \pm 2.0$  V.

Considering the LC-AFM current maps (see Fig. 5.8), this larger variation of the  $V_{\text{EF}}$  values for the nanocross bar structures might be due to a device scenario where the contact pad size approaches the lateral dimensions of the local conductivity changes of the thin films. This ‘lateral parameter’ can be either the grain size, the distance between small cracks for the Sr-rich and stoichiometric STO films, or the distance between the grains for the Ti-rich STO films. This is in good agreement with the dimensions of the local changes observed in LC-AFM. The apparent changes in the CDF-characteristics of  $V_{\text{EF}}$  see Figs. 5.2 (c), (d) which are observed upon changing the crossbar size from ‘micro’ to ‘nano’, we can determinemight indicate a characteristic length of about a few 100 nm being the distance between local weak spots in the annealed STO thin films. In summary, the electro-forming voltage of Pt/STO/TiN devices is influenced by the STO composition in two different ways. Intrinsically the change of the material’s stoichiometry affects the conduction mechanism in the STO film and, extrinsically it affects the thin film’s microstructure and morphology.

### 5.3 Resistive switching of the crossbar devices

After the electroforming and reset procedures, all devices studied exhibited bipolar-type resistive switching (RS) behavior. Exemplary, Figs. 5.3 (a), (b) and (c) show the quasi-static  $I$ - $V$  sweeps obtained for representative Pt/STO/TiN nano-crossbar structures with STO films of different compositions. The nano-crossbar devices could be stably switched at a current compliance of  $I_{\text{CC}} = 50 \mu\text{A}$  with a resistance ratio of  $R_{\text{off}}/R_{\text{on}} > 10$ , fulfilling the requirement for ReRAM operation [10]. In addition, Fig. 5.3 (d) shows the endurance plot for the Ti-rich STO nano-crossbar device obtained from the repetition of 1000 quasistatic switching cycles. At a read voltage of  $V_{\text{read}} = + 0.3 \text{ V}$  the mean resistance values are 15 k $\Omega$  for the low resistance state (LRS, or ON state) and  $> 3 \text{ M}\Omega$  for the high resistance state (HRS, or OFF state). The micro-crossbar devices showed similar RS characteristics although higher  $I_{\text{CC}}$  values were required. For discussing the polarity dependence in respect of a switching model, the  $I$ - $V$  hysteresis needs to be referred to the voltage signal at the active switching interface, which for the crossbar cells is the Pt/STO interface. It should be noticed that the  $I$ - $V$  curves shown in Fig. 5.3 (a) to (c) the current is plotted against the voltage signal applied to the TiN top electrode.

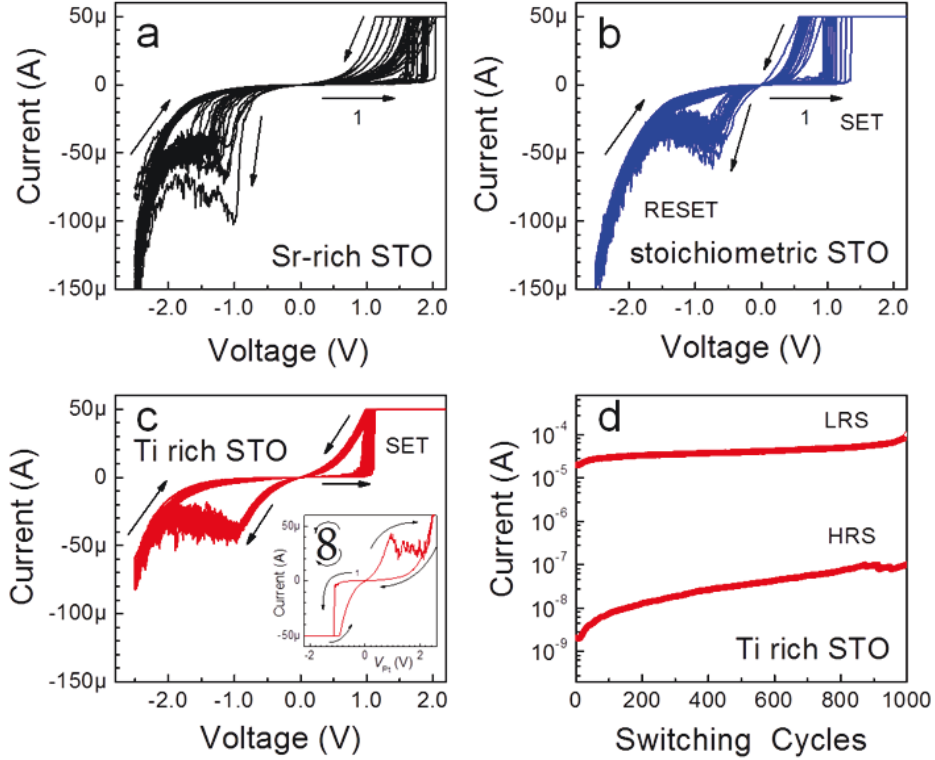


**Figure 5.3:** (a-c)  $I$ - $V$  hysteresis of nano-crossbar Pt/STO/TiN devices of  $0.01 \mu\text{m}^2$  size with 12 nm polycrystalline STO thin films of different compositions listed in Table 4.1. The voltage signal was applied to the TiN top electrode. All devices reveal stable VCM-type bipolar RS at a current compliance of  $50 \mu\text{A}$ . The inset in (c) shows the ‘counter-eight-wise’ RS with respect to the actively switching Pt/STO contact. (d) Endurance plot over 1000 quasistatic switching cycles ( $I_{cc} = 100 \mu\text{A}$ ) for a Pt/Ti-rich STO/TiN device for  $V_{read} = +0.3 \text{ V}$ . Reprinted with the permission of [60]

Therefore, the inset in (Fig. 5.3(c)) shows the corresponding  $I$ - $V_{\text{Pt}}$  switching curve with the voltage  $V_{\text{Pt}}$  applied to the Pt electrode given on the abscissa. From this plot it is clear that the Pt/STO/TiN crossbar devices exhibit a typical ‘counter-eightwise (c8w)’ bipolar behavior which is characteristic for filamentary-type switching valence change memories [5, 13, 64,]. All the Pt/STO/TiN crossbar devices measured in this study showed the same c8w switching polarity. A conspicuous difference in the continuous  $I$ - $V$  characteristics of the different STO samples appears in the non-linearity of the LRS current response. While the  $I$ - $V$  nonlinearity for the LRS of the stoichiometric and the Ti-rich STO devices (see (Figs. 5.3 (b) and (c))) is rather comparable, the Sr-rich STO nano-crossbar cell reveal an LRS characteristic of an enhanced  $I$ - $V$  nonlinearity (see Fig. 5.3 (a)). A quantitative

value for the LRS-nonlinearity is in general defined by the non-linearity factor NL which is calculated from the reset characteristic of the continuous  $I$ - $V$  curve according to  $\text{NL} = |I(V_{\text{reset}})|/|I(V_{\text{reset}}/2)|$ . By this definition nonlinearity factors are calculated for the LRS of the STO nano-crossbar structures. From the curves we calculated values of the NL-factor of about 18 for the Sr-rich STO device which is significantly larger than the values of about 6.5 and 4 calculated for the stoichiometric and Ti-rich STO films, respectively. For comparison, a value of  $\text{NL} = 2$  equals an ohmic LRS state.

### 5.3.1. Set and reset-voltages

The RS characteristics of the various STO devices have been interpreted in a statistical manner for two device sizes, i.e.  $1.0 \mu\text{m}^2$  and  $0.01 \mu\text{m}^2$ , and three STO compositions, i.e.  $[\text{Sr}]/([\text{Sr}]+[\text{Ti}])$  ratios of 0.57 (Sr-rich), 0.50 (stoichiometric) and 0.46 (Ti-rich). Characteristic values of the  $I$ - $V$  hysteresis (see Figs. 5.3 (a) and (c)) to be discussed are: 1) the set-voltage  $V_{\text{set}}$ , determined as the voltage where the current compliance is reached during the (abrupt) set-process, 2) the reset-voltage  $V_{\text{reset}}$ , determined as the voltage where the negative current reaches a local maximum during reset-process and 3) the resistance values  $R_{\text{ON}}$  (LRS) and  $R_{\text{OFF}}$  (HRS) determined at a read voltage  $V_{\text{read}} = +0.3 \text{ V}$ . The variation of the data determined from about 20 devices and 30 switching cycles per device is described by means of the cumulative distribution function (CDF). Fig. 5.4 interprets the CDF of the set- and reset-voltages of the STO based RS devices for (a) the  $1.0 \mu\text{m}^2$  micro-crossbars, and (b) the  $0.01 \mu\text{m}^2$  nano-crossbars. The three various STO compositions are again encoded by colors. The micro-crossbar cells reveal rather narrow distributions of the switching voltages and quite symmetric values for  $V_{\text{set}}$  and  $V_{\text{reset}}$ , as compared to the nano-crossbar devices. For the Ti-rich STO mean values were  $V_{\text{set}} \approx 0.85 \pm 0.1 \text{ V}$  and  $|V_{\text{reset}}| \approx 0.65 \pm 0.15 \text{ V}$ , and for the Sr-rich STO we obtain  $V_{\text{set}} \approx 1.0 \pm 0.15 \text{ V}$  and  $|V_{\text{reset}}| \approx 0.9 \pm 0.1 \text{ V}$ . In contrast, the switching voltages of the stoichiometric STO cells are nearly symmetric with absolute values of  $V_{\text{set}} \approx |V_{\text{reset}}| \approx (0.9 \pm 0.1) \text{ V}$ . The micro-crossbar devices with non-stoichiometric STO films show a slightly larger set-voltage compared to the value of the reset-voltage. Interestingly, the switching voltages of the different micro-crossbar devices are very close in contrast to the forming voltages which differ significantly for the various STO compositions (see Fig. 5.2(c)). In addition, it is found that the stoichiometric STO devices with the highest leakage current in the initial state (see Fig. 5.2(a)) show a nearly forming-free RS behavior, i.e.  $V_{\text{EF}} \approx V_{\text{set}} \approx 1 \text{ V}$ .



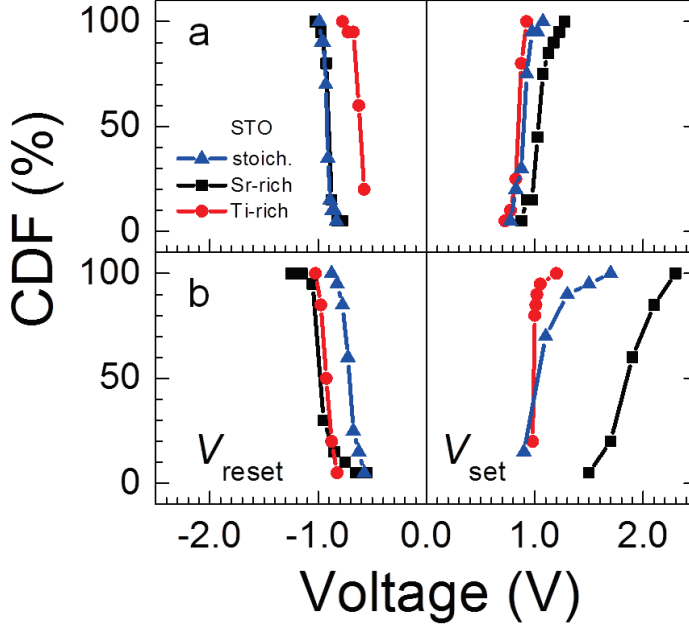


**Figure 5.4:** Cumulative distribution functions of the set- and reset-voltages of the quasistatic  $I$ - $V$  hystereses for (a) micro-crossbar ( $1 \mu\text{m}^2$  size, 15 nm thick STO) and (b) nano-crossbar ( $0.01 \mu\text{m}^2$  size, 12 nm thick STO) Pt/STO/TiN devices of different compositions listed in Table 4.1. Reprinted with the permission of [60]

A relationship between higher initial leakage and lower forming voltage has also been observed for  $\text{HfO}_2$ -based RS devices [104]. From the correlation of morphological and LC-AFM studies we assume that the RS switching in the polycrystalline STO films might dominantly appear at weak points like, for example, the observed micro-cracks. This brings up the question whether the RS in the ALD STO based devices is a filamentary-type phenomenon or somehow relates to the density of micro-cracks in the thin films. This point will be further discussed at the end of the section. Generally, for the nano-crossbar cells shown in (Fig. 5.4(b)) the set-voltages  $|V_{\text{set}}|$  were higher than the corresponding  $|V_{\text{reset}}|$  reset-voltages. Here, the Ti-rich STO films show the most symmetric RS curves with  $V_{\text{set}} \approx 1.0 \pm 0.15$  V and  $|V_{\text{reset}}| \approx 0.95 \pm 0.1$  V. In comparison, the stoichiometric STO devices with  $V_{\text{set}} \approx 1.1 \pm 0.4$  V and  $|V_{\text{reset}}| \approx 0.7 \pm 0.15$  V, and the Sr-rich STO with  $V_{\text{set}} \approx 1.9 \pm 0.4$  V and  $|V_{\text{reset}}| \approx 1.0 \pm 0.2$  V exhibit a significant asymmetry in the RS behavior. The higher set-voltage of the Sr-rich STO nano-crossbar might indicate that setting these devices into the highly conductive ON-state is more difficult to achieve than in case of the Ti-rich and stoichiometric STO devices.

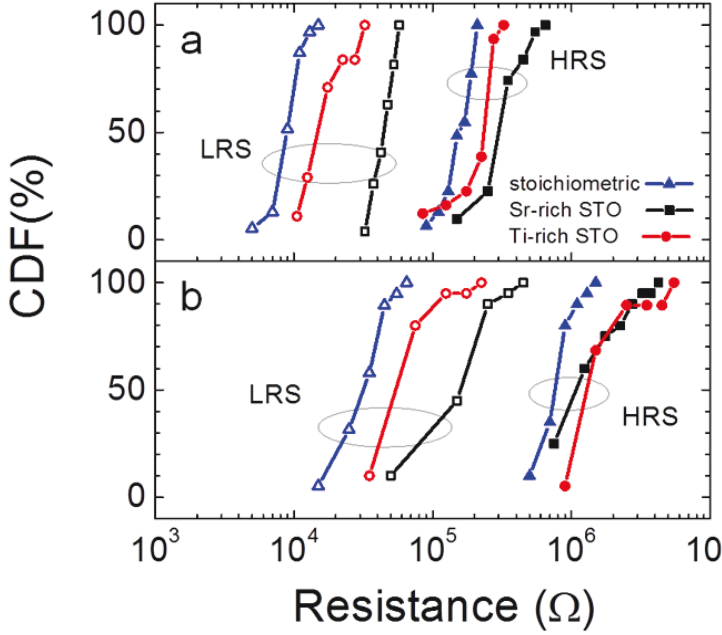


**Figure 5.5:** Cumulative distribution functions of the resistance values derived from the quasistatic  $I$ - $V$  hysteresis for (a) micro-crossbar ( $1 \mu\text{m}^2$  size, 15 nm thick STO) and (b) nano-crossbar ( $0.01 \mu\text{m}^2$  size, 12 nm thick STO) Pt/STO/TiN devices of different compositions (see Table 4.1). Reprinted with the permission of [60]

Notable for the nano-crossbars are the quite broad distributions of the set-voltages observed for all three STO compositions. In addition, the RS voltages of the nano-crossbar devices are significantly lower than the respective forming voltages of about +5.0 V (see Fig. 5.2(d)). The trend of an increase of the set- and reset-voltages with decreasing size of the RS devices has also been reported for  $\text{HfO}_2$ -based RS devices by Chen *et al.*[105], who addressed this effect to the lower total number of defects in the smaller devices compared to the larger ones. This scenario might also apply to the STO based RS devices in this study. Interestingly, the trend regarding the influence of the  $[\text{Sr}]/([\text{Sr}]+[\text{Ti}])$  composition on the switching voltages is obtained for the micro- and nano-crossbar cells, i.e. an increase of the mean switching voltage with increasing Sr-content in the STO thin films. However, the stoichiometry effect is more apparent in the nano-crossbar cells which were electroformed at comparable voltages.

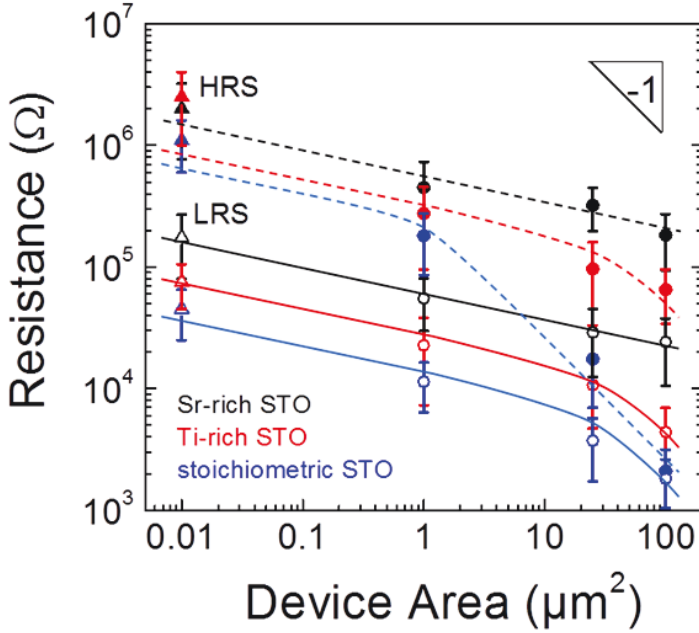
### 5.3.2. ON- and OFF- resistance states

Figure 5.5 interprets the CDF plots of the ON-state (LRS) and OFF-state (HRS) resistance values for the STO based RS devices as determined from the continuous  $I$ - $V$  switching cycles at a read voltage of  $V_{\text{read}} = +0.3$  V. Again, the three STO compositions are encoded by colors and the data for the micro- and nano-crossbars are shown in Figs. 5.5 (a) and (b), respectively. General trends which can be identified are, first, that smaller devices exhibit higher LRS- and HRS-values, and second, that the difference of the resistance values as a function of the  $[\text{Sr}]/([\text{Sr}]+[\text{Ti}])$  composition is larger for the LRS values as compared to the HRS values. In addition, for each device size, the stoichiometric STO cells show the lowest resistance values in ON- and OFF-state compared to the values of the non-stoichiometric STO devices, while generally an increase in the resistance ratio ( $R_{\text{OFF}}/R_{\text{ON}}$ ) with decreasing device size is observed.

### 5.3.3. Area dependence

To assess the influence of the device size, the area dependency of the resistance values for devices of different STO compositions has been analyzed. The graph in Fig. 5.6 comprises mean values of the HRS (filled symbols) and the LRS (open symbols) for four different device sizes, i.e.  $0.01 \mu\text{m}^2$ ,  $1 \mu\text{m}^2$ ,  $25 \mu\text{m}^2$ , and  $100 \mu\text{m}^2$ . The different STO compositions are again encoded by colors. Despite the different film thicknesses, a consistent trend in the resistance values as a function of the device size is obtained for the devices of different STO compositions. The micro-crossbar devices ( $> 1 \mu\text{m}^2$ ) were fabricated from STO films of about 15 nm thickness, while for the nano-crossbar devices ( $0.01 \mu\text{m}^2$ ) films of about 12 nm were integrated. The area-dependency can be explained as follows: the Sr-rich STO devices (black) show a very weak area dependency for the LRS and HRS values which change roughly by a factor of ten when the cell area is varied by a factor of  $10^4$ . A resistance ratio  $\frac{R_{\text{OFF}}^{\text{Sr-STO}}}{R_{\text{ON}}^{\text{Sr-STO}}} = 10$  independent of the device area was determined which is addressed to the highly insulating properties behavior of the annealed Sr-rich STO thin films. The HRS values of the Ti-rich STO reveal an enhanced dependency on the cell area which is attributed the higher leakage currents becoming significant for larger devices. Thus a mean resistance ratio  $\frac{R_{\text{OFF}}^{\text{Ti-STO}}}{R_{\text{ON}}^{\text{Ti-STO}}} = 20$  is obtained for the smaller devices. The Ti-rich STO devices also show a weak area-dependency of the LRS similar to that of the Sr-rich STO devices, while the value is reduced to about one

third,  $\frac{R_{ON}^{Ti-STO}}{R_{ON}^{Sto-STO}} = 0.3$ . For small area cells ( $< 1 \mu m^2$ ) the stoichiometric STO devices show a weak area dependence for the LRS and HRS values with a resistance ratio  $\frac{R_{OFF}^{Sto-STO}}{R_{ON}^{Sto-STO}} = 25$ , while for device sizes  $> 1 \mu m^2$  the HRS values show a strong area dependence with a proportionality factor of approximately one. This clearly indicates that the effect of leakage current through the micro-cracks dominates the total current for large pad sizes. Thus for large stoichiometric STO devices any RS effect is completely obscured by the high leakage current contribution from the non-switching area of the device. As a result, reliable information on the compositional effect of the ALD STO films on the RS properties can only be obtained from device structures of reasonably small area.



**Figure 5.6:** Area dependency of the resistance states of the Pt/STO/TiN devices determined at  $V_{read} = +0.3$  V from stable, quasistatic  $I$ - $V$  hysteresis. The colors encode the films composition, Sr-rich (black), Ti-rich (red), and stoichiometric STO (blue) values (see Table 4.1), resistance values of HRS and LRS are given in open and filled symbols, respectively. The symbols stand for the different structures, circles for micro- and triangles for nano-crossbars. The slope of (-1) is plotted for easy identification of area-scaling. Reprinted with the permission of [60]

In LRS, all STO devices of the three compositions show a considerably weak area-dependency of their resistance values. The area-dependency of the HRS values demonstrates the significant effect of the films microstructure and morphology on the RS properties. If effects originating from a parallel leakage current path are considered it can be concluded that the resistive switching behavior of the Pt/STO/TiN devices after electroforming is described by an area-independent VCM-type filamentary mechanism. Additionally, an effect of the STO thin film composition is observed, predominantly for the LRS values. Considering devices of the same size, smaller than  $10 \mu m^2$ , the ON-state resistance values increase from stoichiometric to Ti-rich to Sr-rich STO films resulting in a ratio of the LRS values of about  $\frac{R_{ON}^{Sr-STO}}{R_{ON}^{Stoi-STO}} = 6$ . Although the HRS states of the smaller devices are not too much affected by an area dependent leakage current parallel to the filament current, the dependence of the HRS states on the composition of the STO films is less pronounced, i.e.,  $\frac{R_{OFF}^{Sr-STO}}{R_{OFF}^{Stoi-STO}} \sim 2$ . In total, the highest resistance ratio  $R_{OFF}/R_{ON}$  of about 25 was obtained for stoichiometric STO and the lowest value of about 10 for the Sr-rich STO films. The lowest values of LRS were found for the stoichiometric STO films, while Sr- or Ti-excess nonstoichiometries typically result in higher  $R_{ON}$  values. This picture is more apparent for the Sr-rich STO than for the Ti-rich devices.

While micro-structural effects (e.g. micro-cracks and grain sizes) dominate the resistance states for larger cell areas, the HRS states of the nano-crossbar cells might still be affected by varying defect densities in the films induced by differences in the films crystallization behavior. In addition to the significant influence of the STO thin films microstructure on the RS characteristics of respective Pt/STO/TiN devices also a composition effect was observed. However, the LRS values of the Pt/STO/TiN devices show a reproducible tendency with variation of the STO film composition:  $R_{ON}^{Sr-STO} > R_{ON}^{Ti-STO} > R_{ON}^{Stoi-STO}$ , for different device sizes, film thicknesses and microstructures. This finding might show a compositional dependence of the local defect states of the conducting filaments RS devices from polycrystalline ALD STO thin films with various  $([Sr]/([Sr] + [Ti]))$  contents.

## 5.4 Local-conductivity probed by LC-AFM

Local-conductivity atomic force microscopy (LC-AFM) and morphological atomic force microscopy (AFM) studies were performed in order to analyze local conducting paths along grains and grain boundaries. So, the films' surface topography was recorded in parallel to a laterally resolved current mapping for the 12 nm thick STO films annealed for 5 min. at 600 °C. The measurements were made under ultra-high vacuum (UHV) conditions at 200 °C while a constant voltage was applied to the sample via a conducting Pt/Ir-coated AFM tip. The corresponding current maps shown in Figs. 5.7 (d) to (f) reveal an inhomogeneous distribution of differently conducting regimes. The corresponding AFM pictures shown in Figs. 5.7 (a) to (c) reveal distinct topographical differences between the three samples. The surface of the Sr-rich (a) and the stoichiometric (b) STO film are rather flat and consist of grains separated by grain boundaries. Although the averaged conductivity of the Sr-rich sample (see Fig. 5.7 (d)) was significantly lower as this of the stoichiometric STO (see Fig. 5.7 (e)), both films reveal conducting paths along grain boundaries. Minor cracks in the stoichiometric STO film which appear in the topography map (Fig. 5.7 (b)) as darker lines show up as slightly brighter lines in the LC-AFM map (Fig. 5.7 (e)). For each individual case the degree by which the nano- or microcracks contribute to the total leakage current of a particular device might depend on the dimensions of the cracks. Results on local leakage non-uniformity in ALD STO thin films have also been reported by Menou *et al.*[87] who attributed the higher leakage paths to micro-cracks in their films as well. The corresponding current map of the Ti-rich STO film shown in Fig. 5.7 (f) shows that the thinner areas of the material (see Fig. 5.7 (c)) exhibit increased conductivity indicating that semiconducting phases are formed locally. The topography map of the partly crystallized Ti-rich STO film ( $([\text{Sr}]/([\text{Sr}] + [\text{Ti}]) = 0.46)$  in Fig. 5.7 (c) completely differs from the other STO compositions. One might observe the remarkable accordance between the AFM, LC-AFM and SEM images with respect to the areas of reduced film thickness in Fig. 5.7 (c) and these with enhanced conductivity in Fig. 5.7 (f). Hence, these regimes might be described by being large crystal plates of Ti-rich STO phase embedded in an insulating matrix of amorphous material. The appearance of partial crystallization is in qualitative agreement with the results of a recently performed TEM study [79], while slight variations in the film growth might arise from the different substrates.

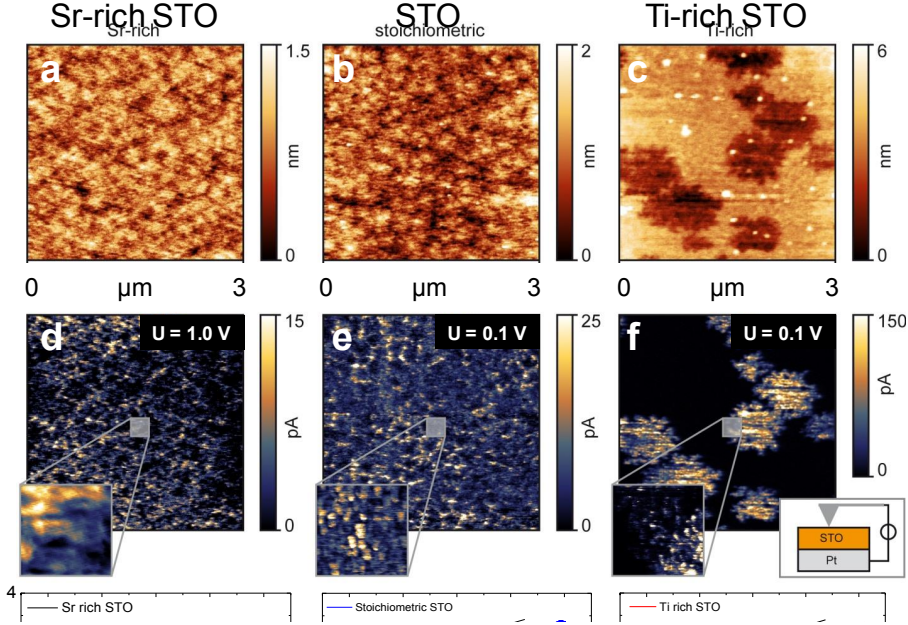


**Figure 5.7:** (a-c) AFM and (d-f) LC-AFM pictures showing the topography and the corresponding current maps, respectively, of the 12 nm STO thin films grown on planar Si/Pt substrates and annealed at 600 °C in  $\text{N}_2$  for 5 mins. The STO compositions are arranged from the left to the right Sr-rich (a, d), stoichiometric (b, e), and Ti-rich (c, f). The LC-AFM measurements were performed at 200°C under UHV conditions with the voltage applied to the AFM tip. Reprinted with the permission of [60]

The LC-AFM results clearly describe local inhomogeneous current spots which are related to the thin films' microstructure being influenced by the films' composition as the result of a stoichiometry-affected nucleation and crystallization behavior. Thus, in order to analyze the electrical properties of the RS devices accurately, both, the influences of the  $[\text{Sr}]/([\text{Sr}]+[\text{Ti}])$  composition and of the microstructure of the ALD STO thin films after annealing have to be considered. For the nano-crossbar devices with the pad size approaching the grain size (or patch size) one would expect a statistical variation in the electrical data. Whereas the electrical properties of the micro-crossbar structures present average thin film properties. Crossbar contacts of about 100 nm size might either sandwich a single grain or two grains with a grain boundary in between. Alternatively for the Ti-rich STO films the contacts could either sandwich the amorphous, less conducting matrix or a semiconducting crystalline regime. It should be noted that the above mentioned micro-structural phenomena particularly appear on a length scale of a few hundred nanometers. In addition, the presence of a current inhomogeneity on the smaller

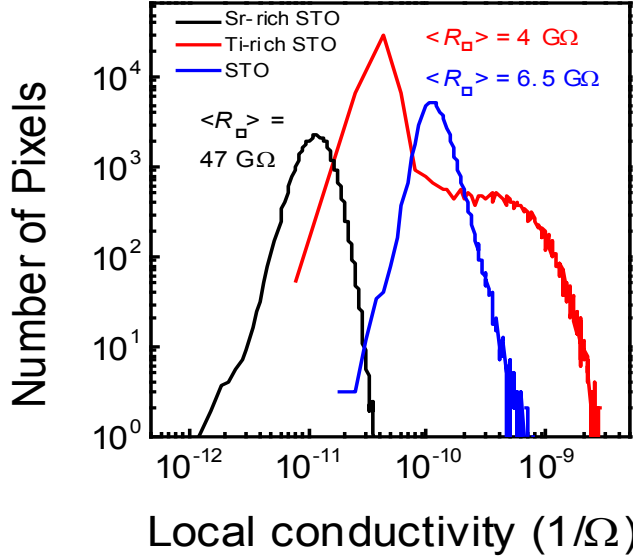


**Figure 5.8:** Histogram of the local conductivity values shown in pictures 5.7 (d-f). Average resistance values  $\langle R_{\square} \rangle$  refer to the measured areas of  $(3 \times 3) \mu\text{m}^2$ . Reprinted with the permission of [60]

scale could be observed by LC-AFM at higher resolution. The grains of the Sr-rich and stoichiometric STO films (see Fig. 5.7 (d) and (e)) revealed additional local conductivity spots with a diameter of 10 nm to 30 nm inside the grains. This observation correlates with the evidence of voids with diameter of a few nanometers within single STO grains found by TEM in our previous study [79]. Since the stoichiometry range of  $\text{SrTiO}_3$  is very narrow, a phase separation in non-stoichiometric parts could also result. So, one possible explanation of the locally varying conductivity observed by LC-AFM could be that in the investigated Ti-rich STO thin films  $\text{TiO}_x$ -phases with  $x < 2$  [106] were present and influence the local conductivity.

In the histogram in Fig. 5.8, the distribution of the local conductivity as measured by the LC-AFM scans in Figs. 5.7 (d) and (f) over an area of  $3 \times 3 \mu\text{m}^2$  is shown. For a semi-quantitative discussion of the mean thin film resistance values  $\langle R_{\square} \rangle$  the number of pixels is plotted logarithmically versus the local conductivity calculated from the measured current and the applied voltage,  $\sigma_{\text{loc}} = I_{\text{loc}} / V_{\text{tip}}$ . It is seen that the average conductivity of the Sr-rich STO film is the lowest ( $\langle R_{\square} \rangle = 47 \text{ G}\Omega$ ) although a relatively high voltage of  $\pm 1.0 \text{ V}$  was applied to the sample, whereas for the stoichiometric STO film a higher



average conductivity was determined ( $\langle R_{\square} \rangle = 6.5 \text{ G}\Omega$ ) at a lower applied voltage of  $\pm 0.1 \text{ V}$ . The Sr-rich and the stoichiometric STO thin film both exhibit comparable uni-modal conductivity distributions indicating that the distribution of conducting grains is similar in both cases despite of the fact that the films show overall different conductivity. The width of the local conductivity distribution in the histogram is the highest for the Ti-rich STO sample due to the inhomogeneous distribution of conducting regions, while the mean value of the thin film resistance  $\langle R_{\square} \rangle = 4 \text{ G}\Omega$  is only slightly smaller than the value of the stoichiometric STO film. The histogram of the Ti-rich STO film instead shows a bi-modal distribution relating to the two regions with different local conductivities. However, a large part of the scanned area revealed a low local conductivity resulting in the appearance of the maximum peak in the histogram, while the highly conducting areas in Fig. 5. 7(f) is reflected in the tail of the distribution appearing at higher conductivities.

## **5.5 Summary**

In this study, we investigated the resistive switching properties of ALD derived  $\text{SrTiO}_3$  thin films of various compositions. The films were grown on platinum coated silicon substrates at  $350^\circ\text{C}$  by using oxygen plasma and a subsequent ex-situ annealing at  $600^\circ\text{C}$  under  $\text{N}_2$  atmosphere.  $\text{SrTiO}_3$  thin films of two different thickness, i.e.  $15 \text{ nm}$  and  $12 \text{ nm}$ , and with three different compositions  $[\text{Sr}]/([\text{Sr}]+[\text{Ti}])$  of  $0.57$  (Sr-rich),  $0.50$  (stoichiometric), and  $0.46$  (Ti-rich) were integrated into crossbar-devices with lateral dimensions varied from several micro meters to  $100 \text{ nano meters}$ . The effect of the ALD STO cation composition on the crystallization behavior and, thus, on the resulting morphologies revealed a significant impact on the electrical properties of Pt/STO/TiN crossbar devices. Local defects in the film's microstructure dominantly affect the electrical properties of the pristine Pt/STO/TiN cells, i.e., the leakage current behavior and the soft-breakdown or electroforming voltages. The HRS values of cells of sizes  $>1 \times 1 \mu\text{m}^2$  are affected by the superimposed residual conductivity through the whole cell. The polarity dependence of the resistive switching curves and the area-independent LRS values serve as an indirect proof of VCM-type filamentary resistive switching controlling the RS behavior of the Pt/ALD-STO/TiN devices under study. Once the microstructural effects of the polycrystalline thin films have been assessed by measuring the local conductivity, a clear effect of the STO composition on the RS behavior was observed.

## 6. Material and Electrical Properties of ALD Nb<sub>2</sub>O<sub>5</sub>

---

In this chapter the structural and morphological analysis and the quasi-static electrical characterization of Nb<sub>2</sub>O<sub>5</sub> thin films grown by a thermal ALD process will be described. The first part deals with the analysis of as-deposited amorphous as well as annealed crystalline Nb<sub>2</sub>O<sub>5</sub> thin films on planar, non-structured Si/SiO<sub>2</sub>/Ti/Pt substrates. The substrate material is identical to the Pt bottom electrodes, which are utilized in micro-crossbar structures. These devices are discussed in the second part, which is dedicated to the quasi-static electrical characterization of the resistive switching behavior of as-deposited Nb<sub>2</sub>O<sub>5</sub> thin films integrated into microcross bar devices with lateral dimensions of  $1 \times 1 \mu\text{m}^2$ . The thin film growth parameters and the fabrication process flow of microcross bar devices have been described in chapter 3. To further understand the electrical properties of the Nb<sub>2</sub>O<sub>5</sub> thin films at a local scale additionally local conductivity atomic force microscopy (LC-AFM) was utilized.

### 6.1 Thin film properties of ALD grown Nb<sub>2</sub>O<sub>5</sub>

Knowledge of the structure, composition and morphology of the utilized thin films is a key parameter for the realization of a desired resistive switching behavior and for a detailed physical understanding of the switching process. In this section the composition of ALD grown Nb<sub>2</sub>O<sub>5</sub> analysed by XPS, the morphological information obtained by AFM and SEM, and the structure obtained from GI-XRD scans will be described.

#### 6.1.1. Chemical properties

The chemical nature of as-deposited niobium oxide films grown on planar Si/SiO<sub>2</sub>/Ti/Pt substrates was obtained by means of X-ray photoelectron spectroscopy (XPS) measurements performed at different temperatures. A PHI 5600 spectrometer from Physical Electronics equipped with a monochromatized Al-K <sub>$\alpha$</sub>  radiation source was used. During the analysis the vacuum was maintained on a  $10^{-9}$  mbar level (UHV conditions) even at high temperatures. The photoelectrons were collected at an angle of  $45^\circ$  to the

sample surface. As shown in Fig. 6.1, the measured spectra of the Nb 3d core line were examined by peak fitting after subtraction of the background signal using the Shirley method. At room temperature the spectrum of the Nb 3d line shows one doublet due to spin-orbit coupling. The spectrum is characteristic for Nb<sub>2</sub>O<sub>5</sub> and Nb 3d core level can be well fitted assuming niobium in the Nb<sup>5+</sup> chemical state. This means that the ALD Nb<sub>2</sub>O<sub>5</sub> films were stoichiometric as-grown. Heating the films under UHV conditions, an additional peak appears at lower binding energy indicating the appearance of an additional doublet coming from reduced Nb states that start to appear at 200 °C. The intensity of these peaks increases with increasing temperature. This evolution of additional valences upon heating at reduced pressure is consistent with an overall reduction tendency of the material, which has already been reported by Nowak *et al.* [107]. For the measurement performed at 600°C under UHV conditions signatures of an additional doublet at even lower binding energy could be detected associated with the small peak at 206.8 eV. These signatures are attributed to a lower Nb oxidation state, i.e. NbO<sub>x</sub> with  $x < 2.5$ . Similar results were reported by Jung *et al.* [108]. Comparing the results obtained for the amorphous ALD grown Nb<sub>2</sub>O<sub>5</sub> thin films in this study with the results of the careful study by Nowak *et al.* [107] a clear difference becomes apparent concerning the intensity ratio of Nb<sup>4+</sup> / Nb<sup>5+</sup> peaks for the different thin films studied. The results indicate that the reduction process in the ALD Nb<sub>2</sub>O<sub>5</sub> thin films might be slower than for the amorphous Nb<sub>2</sub>O<sub>5</sub> thin films obtained from oxidation of sputtered Nb metal. For the ALD Nb<sub>2</sub>O<sub>5</sub> thin film, the Nb 3d doublet characteristic of Nb<sub>2</sub>O<sub>5</sub> is obtained up to temperatures 600°C, whereas at 600 °C the spectrum of the films formed by oxidation of Nb metal differs completely from the Nb<sub>2</sub>O<sub>5</sub> reference. The latter is attributed to NbO<sub>x</sub> complexes, which indicate no well-defined Nb oxidation states.

Although a detailed analysis of the Nb oxidation states is far beyond the scope of this qualitative study, three important results on the chemical nature of the amorphous ALD Nb<sub>2</sub>O<sub>5</sub> films can be derived. First, the composition of the ALD grown niobium oxide films is equivalent to Nb<sub>2</sub>O<sub>5</sub>, and, second, a vacuum anneal at 600 °C causes a near-surface reduction of the material. Third, the reduction process in the amorphous ALD Nb<sub>2</sub>O<sub>5</sub> films is much slower than in the amorphous Nb<sub>2</sub>O<sub>5</sub> films obtained from oxidation of sputtered Nb metal films [107], even though both processes were performed at comparable temperatures of 275 °C and 300 °C, respectively.

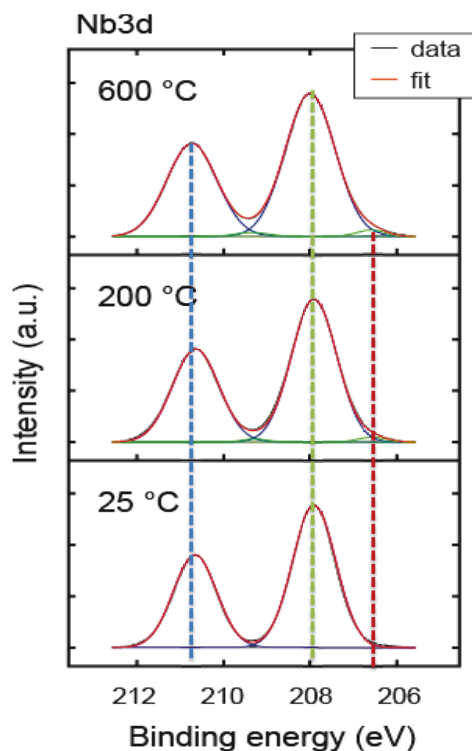


**Figure 6.1:** Results of fitting the photoemission spectra, i.e. the Nb 3d doublet for an amorphous as-deposited ALD Nb<sub>2</sub>O<sub>5</sub> film obtained at selected temperatures, e.g., 25 °C, 200 °C and 600 °C.

Thus, the enthalpy of oxygen migration might vary for different qualities of amorphous thin films even if the stoichiometry in the amorphous state is equivalent. Complementary techniques are required that might close this gap of chemi-structural information.

### 6.1.2. Morphological and structural properties

For the physical description of resistive switching devices the morphology of the oxide thin films that are sandwiched between top and bottom electrode is of high importance. The morphology was studied for ALD grown ~10 nm thick Nb<sub>2</sub>O<sub>5</sub> films deposited on planar Si/SiO<sub>2</sub>/Ti/Pt substrates at 275 °C by using (<sup>t</sup>BuN=Nb (NMeEt)<sub>3</sub>) as a Nb-precursor and ozone as oxygen source. AFM measurements were performed for obtaining quantitative data of the surface roughness and SEM (scanning electron microscopy) micrographs provided the thin film morphology in the form of top-down view.

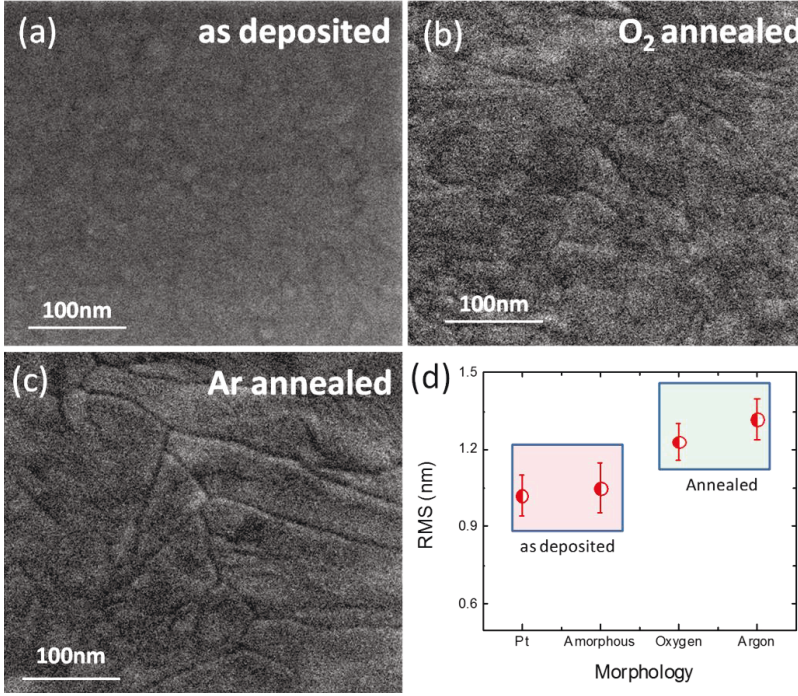


**Figure 6.2:** SEM top view images of 10 nm thick  $\text{Nb}_2\text{O}_5$  films grown on Si/SiO<sub>2</sub>/Ti/Pt substrates by means of a thermal ALD process: (a) as-deposited, (b)  $\text{O}_2$  annealed, and (c) Ar annealed at 600 °C for 5 minutes. (d) Comparison of the rms roughness values of the Pt substrate and the surfaces of the different films (a) to (c), respectively.

The grainy structures that can be seen in the SEM micrograph in Fig. 6.2 (a) for an as-deposited  $\text{Nb}_2\text{O}_5$  appears to be due to the Pt grains rather than thin films. In the CMOS compatible fabrication process of ReRAM devices there is one key parameter that can strongly affect the resistive switching behavior, this is the spike annealing process, a thermal step, which is normally used in CMOS technology to activate dopants and remove defects. Hence it is of high importance to know the influence of annealing on the surface morphology. Therefore amorphous  $\text{Nb}_2\text{O}_5$  thin films were annealed after the deposition and the film morphologies were compared by using SEM. The films became crystalline after annealing at 600 °C for 5 min in oxygen as well as in argon atmosphere, see Fig. 6.2 (b) and (c), respectively. A clear difference in the morphology can be seen with respect to microstructures and grains between the amorphous and the differently annealed  $\text{Nb}_2\text{O}_5$  thin films noting that the surface roughness of the  $\text{Nb}_2\text{O}_5$  films has been increased after crystallization. The measurements performed on the films deposited on Si/SiO<sub>2</sub>/Ti/Pt substrate show means roughness RMS values measured by AFM of about

( $1.04 \pm 0.60$ ) nm as compared to the substrate's RMS value of about ( $1.01 \pm 0.4$ ) nm. Hence it can be concluded that the main contribution to the RMS value comes from the substrate roughness. The RMS-values are plotted in Fig. 6.2 (d) for both, deposited and annealed films; the substrate again is Si/SiO<sub>2</sub>/Ti/Pt. After annealing the RMS values increased to 0.7 nm. The Ar annealed films exhibit slightly higher surface roughness (RMS) values as compared to O<sub>2</sub> annealed samples.

The structural properties of as-deposited  $\text{Nb}_2\text{O}_5$  thin films grown by ALD on Pt coated silicon substrates were analyzed by means of GI-XRD using an X'Pert MRD system from Panalytical company. For the as-grown 10 nm  $\text{Nb}_2\text{O}_5$  film no peaks were observed in the GI-XRD the peaks of the black curve in Fig. 6.3 are attributed to (111) and (200) peaks of the Pt layer (BE) and assigned with black dots. Thus it can be concluded that the as-deposited ALD  $\text{Nb}_2\text{O}_5$  thin film exhibits an amorphous structure. Additional, as-grown  $\text{Nb}_2\text{O}_5$  films were annealed by RTA ex-situ under two different environments namely O<sub>2</sub> and Ar at 600 °C for 5 min. at this temperature the films crystallized into an orthorhombic phase irrespective of the atmosphere as can be seen from the peaks indicated in the GI-XRD scans by grey squares as shown in Fig.6.3. Similar crystallization temperatures were reported by other groups [76,157].

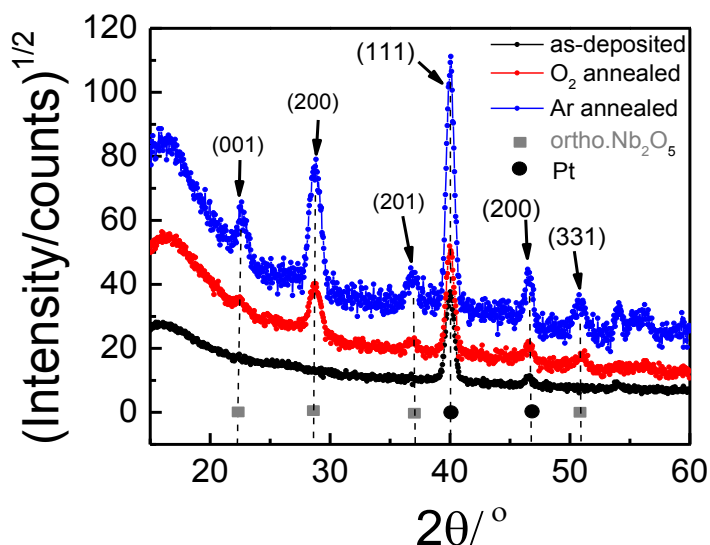


**Figure 6.3:** Structural characterization by means of GI-XRD scans taken for 10 nm thick  $\text{Nb}_2\text{O}_5$  films grown by ALD on planar Pt/Si substrates comparing as-deposited films, and films annealed at 600 °C in O<sub>2</sub> and Ar for 5 minutes, respectively.

## **6.2 Local conductivity of Nb<sub>2</sub>O<sub>5</sub> probed by LC-AFM**

In order to gain an insight into the resistive switching behavior on the microscopic scale, local conductivity measurements by atomic force microscopy (AFM) were performed. For this purpose a JEOL system equipped with a Pt-Ir tip was used. Using local-conductivity atomic force microscopy (LC-AFM), the electronic transport properties of the surface were investigated as a function of the temperature under vacuum conditions. As shown in Fig 6.4(a) - (c) the current map measured while scanning the surface with the AFM tip at room temperature revealed an inhomogeneous structure related to conducting grains. The structure of these grains corresponds to those observed in the topography maps Fig 6.4 (e) - (g), respectively. Since the films were deposited on a polycrystalline Pt layer, it is concluded that the grainy structure of this underlying Pt electrode determines the morphology and conductivity measured by scanning the surface of the topmost Nb<sub>2</sub>O<sub>5</sub> layer. For increasing temperature, the overall conductivity increases following an Arrhenius law with activation energy of about 0.4 eV as can be seen in Fig. 6.5(a). Regarding the current maps exemplarily shown for the measurements obtained at 100 °C and 175 °C in Fig. 6.4 (b) and (c), respectively, it becomes obvious that the inhomogeneous structure is more pronounced at room temperature and gets slightly diminished at higher temperatures. This indicates that a reasonable Schottky barrier exists at the Pt/Nb<sub>2</sub>O<sub>5</sub> interface which might explain the exponential current increase within the regimes attributed to the core of the Pt grains. However, the diminishing contrast in the lateral structure of the LC-AFM pictures obtained at higher temperature might hint towards an increasing conductivity of the niobium oxide itself. To analyse the distribution of the current measured in each scan consisting of 256 x 256 pixels and additionally its evolution with temperature, histograms were calculated which are shown in Fig. 6.5(b) as log-log plots. The current distributions are relatively broad spanning one or two orders of magnitude revealing a high degree of heterogeneity of the surface conductivity. With increasing temperature the maximum of the distributions is shifted to higher current values due to the thermal activation of electronic transport near the surface. In order to investigate the possibility of modifying the films by electrical gradients on the nanoscale, an electro-degradation experiment was performed. The results are shown in Fig. 6.6. At first, an area of 200 nm x 200 nm was scanned while a voltage of -6 V was permanently applied to the tip resulting in a current flow of 10 - 100 µA. After this 'writing'-procedure, a 'reading' scan with a voltage of 1 mV was performed.

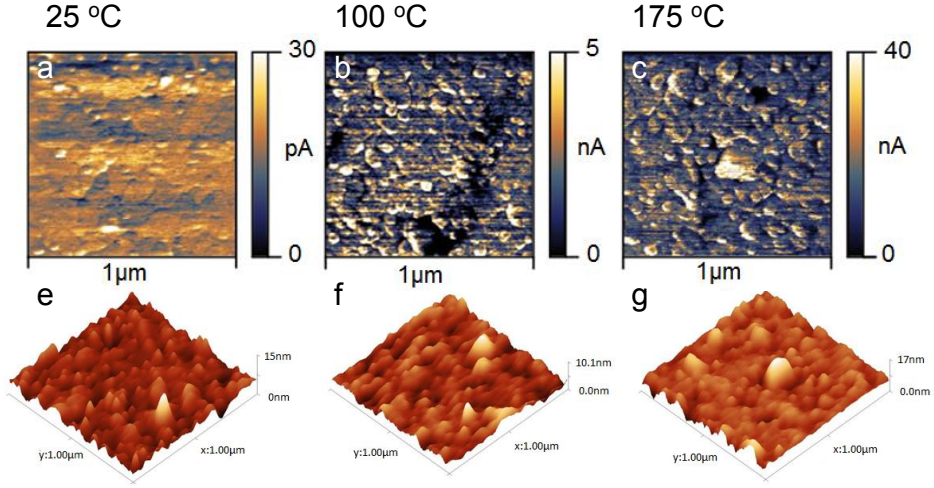


**Figure 6.4:** (a-c) Current maps obtained by LC-AFM at different temperatures on the amorphous film using a voltage of 1 V. (e-f) 3D illustrations of topography maps of the films obtained in contact mode corresponding to the different temperatures.

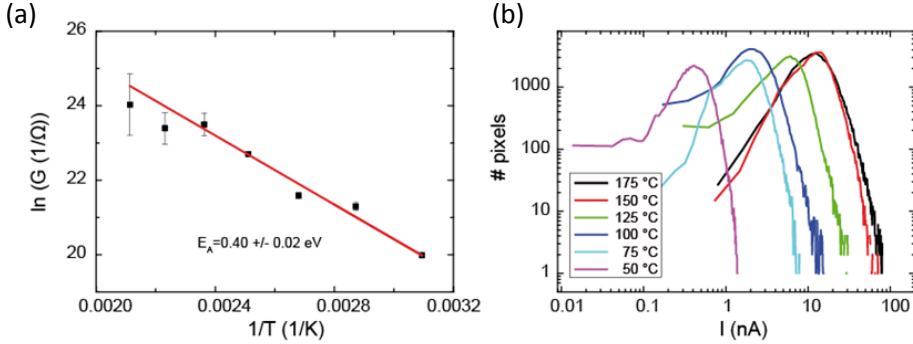


**Figure 6.5:** (a) Arrhenius plot of the local conductance as calculated from the current maps obtained for different temperatures (cf. Fig. 6.4). (b) Histograms of the local current values determined for the different temperatures

The topography map in Fig. 6.6 (a) reveals that a cone (see Fig. 6.6 (c)) with a height of more than 60 nm had evolved. Since the height of this cone is much larger than the initial film thickness of 10 nm, this result demonstrates that under extreme conditions ionic movement can play a significant role. Regarding the current maps shown in Fig. 6.6 (b) and (c), which were measured simultaneously with the topography, it can be seen that in



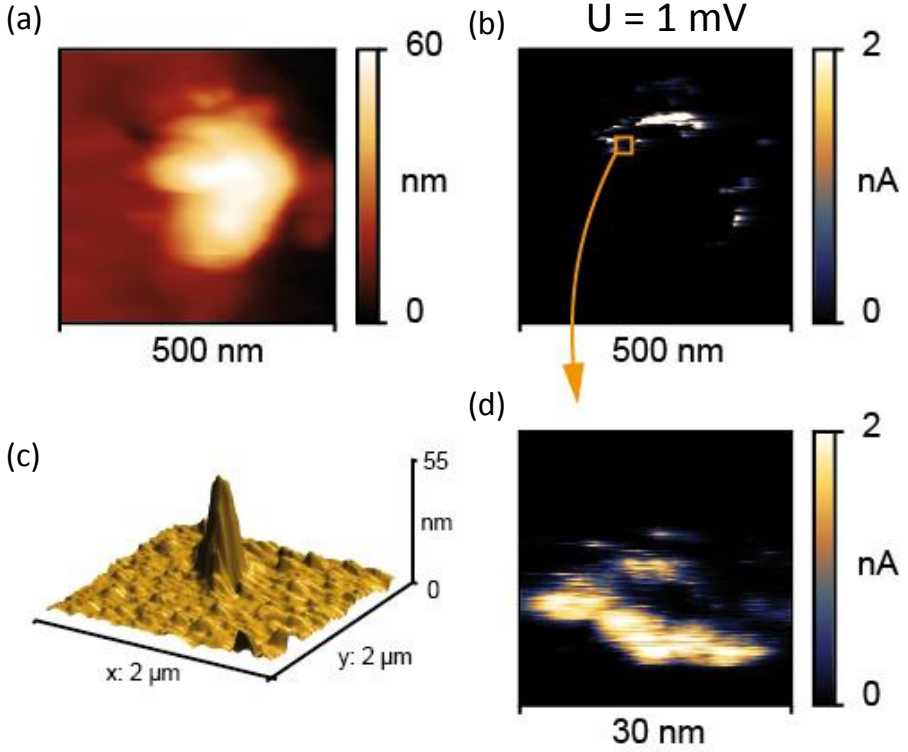


**Figure 6.6:** (a) AFM topography and (b, c) local conductivity (LC) maps of the  $\text{NbO}_x$  film after electrodegradation with a voltage of  $-6\text{ V}$ . (b) LC map obtained with the bias voltage of  $1.0\text{ mV}$  for the same area as shown in (a). (c) Structural deformation after electrodegradation (d) Current map with increased resolution for the area marked in (b).

some regions of the cone, the conductivity was distinctly increased. In comparison to the pristine film, the local conductance of the surface was higher by a factor of about  $10^6$ . This is attributed to an indication that a local insulator-metal transition took place during the electro-degradation, this means, and ‘writing’ process. This measurement indicates that ionic movements leading to the formation of metallic conducting filaments by phase transformations may occur. This finding is particularly interesting since it is assumed that gradients applied during electroforming of a resistive switching device are comparable.

### 6.3 Resistive switching in $\text{Nb}_2\text{O}_5$ micro-crossbar devices

In order to study resistive switching behavior, the ALD grown  $\text{Nb}_2\text{O}_5$  thin films were integrated into single micro-crossbar devices with lateral dimensions of about  $1 \times 1 \mu\text{m}^2$  as illustrated in Fig. 6.7. The thermal ALD process for the 10 nm thick  $\text{Nb}_2\text{O}_5$  layer was as described in section 3.1.3. MIM cross point devices were built with a stack sequence of Pt (30 nm, BE)/ $\text{Nb}_2\text{O}_5$  (10 nm)/M (10 nm)/Pt (25 nm). All electrical measurements were performed on a Süss Microtech PA-200 probe station with an Agilent B1500A semiconductor analyzer which allows controlling different parameters such as slew rate and the current compliance. For reasons of compatibility between resistive switching characteristics, the voltage was always applied to the top electrode (TE). The electrical characterization of the devices for resistive switching application was performed in a standardized way described as follows. The electro-forming procedure for initializing resistive switching behavior was executed by using a voltage controlled  $I$ - $V$  sweep mode

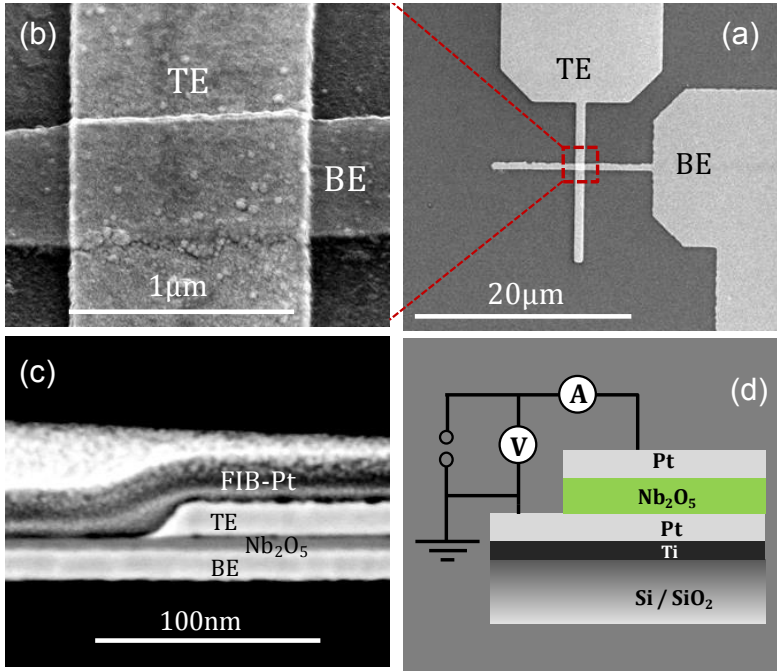


**Figure 6.7:** (a) SEM micrograph of a micro-crossbar device with close overview of (b) the crossbar structure. (c) FIB-SEM micrograph of a cross section showing the micro-crossbar Pt (BE)/ $\text{Nb}_2\text{O}_5$ /Pt (TE) structure. (d) Schematic of stack and electrical measurement setup of the Pt (BE)/ $\text{Nb}_2\text{O}_5$ /Pt (TE) devices.

of positive polarity giving a current compliance. The subsequent RESET  $I$ - $V$  sweep was performed with negative voltage. After successful electro-forming and RESET process, VCM-type bipolar resistive switching behavior was recorded for optimized parameters allowing a reasonable stable  $I$ - $V$  hysteresis to be obtained. For every device under test the parameters were defined by an optimum current compliance for the SET process, this is, the transition from high resistance state (HRS-state) to low resistance state (LRS-state), and an optimum voltage for the RESET process, this is, the transition from LRS to HRS.

### 6.3.1. ALD Nb<sub>2</sub>O<sub>5</sub> films in symmetric Pt micro-crossbar structures

The electrical properties of 10 nm ALD Nb<sub>2</sub>O<sub>5</sub> integrated into a system with symmetric electrode configuration, this means, Pt (30 nm)/Nb<sub>2</sub>O<sub>5</sub> (10 nm)/Pt (25 nm), were studied as a reference. For these devices, both top and bottom electrode interface form Schottky-type contacts for the high work function metal, i.e., Pt ( $\Phi \approx 5.1$  eV), being in contact with an insulating material (as-grown), i.e., Nb<sub>2</sub>O<sub>5</sub> ( $E_g \approx 3.9$  eV) [68]. Electro-forming is a controlled soft break down process of the insulating resistive switching layer which brings the devices into ON-state. It is considered as a prerequisite for the stable switching process of devices under a VCM-type bipolar mechanism. During electro-forming process, typically a reduction of the device resistance of about several orders of magnitude is observed. The decrement in the resistance is basically addressed due to the formation of a conductive filament setting the device from the initial OFF-state into the ON-state [109]. A suitable current compliance was set in order to avoid a hard destructive breakdown of the devices. The electro-forming characteristics of the Pt/Nb<sub>2</sub>O<sub>5</sub>/Pt devices are shown in Fig. 6.8 (a). The forming procedure was performed with a positive voltage applied on the top Pt electrode by increasing the applied voltage at a slew rate of 166 mV/s until the current compliance was reached. A proper value of the compliance current  $I_{CC} = 50$   $\mu$ A was set for every sample individually in order to achieve a stable resistive switching behavior. The device was formed at forming voltage of about  $V_F = +4.2$  V and switched to low-resistance state (LRS). After successful electroforming, the negative polarity was applied on the top electrode to RESET the device to distinguish between the soft breakdown (electro-forming) and hard break down (complete breakdown). For this a negative voltage of about  $V = -2.5$  V was applied with same slew rate of about 16 mV/s. During the RESET process the device switches back to high resistive state (HRS) as is shown in Fig 6.8 (b). After successful electro-forming and subsequent RESET procedure the Pt/Nb<sub>2</sub>O<sub>5</sub>/Pt crossbar cells revealed bipolar type

resistive switching behavior as shown in Fig. 6.8 (c). The SET operation was obtained for positive voltage and the RESET operation for negative voltage applied to the top electrode. For the SET process a current compliance of about  $I_{CC} = 500 \mu\text{A}$  and a positive voltage of  $V = +5.0 \text{ V}$  were chosen, while the negative RESET stop bias was limited to  $V = -2.5 \text{ V}$  and no current compliance was defined, as the RESET process was found to be self-limiting. From the  $I$ - $V$  curves in Fig. 6.8 (c) taken for a compliance current of  $500 \mu\text{A}$  SET and RESET voltages are determined as  $V_{SET} = +3.7 \text{ V}$  and  $V_{RESET} = -1.5 \text{ V}$ , respectively. The LRS exhibits a linear ohmic-like  $I$ - $V$  behavior, and the resistance values at  $V_{read} = -0.2 \text{ V}$  were about  $1.7 \text{ M}\Omega$  and  $3.4 \text{ k}\Omega$  for HRS and LRS, respectively. This equals a memory window of about 500.

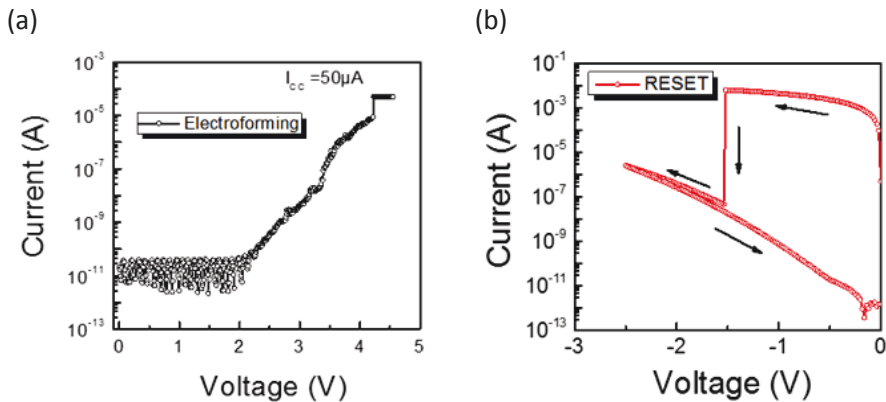


**Fig 6.9 :** (a) Voltage controlled electrod (c) on top electrode of ALD grown 10nm Nb<sub>2</sub>O<sub>5</sub> rods (b) RESET by applying negative polarity

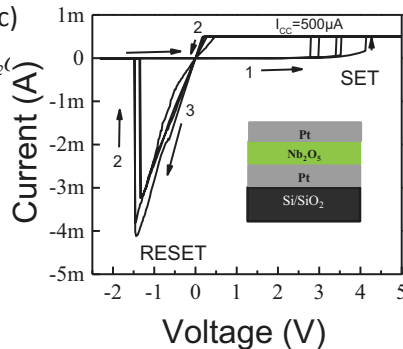


**Figure 6.8:** *I-V characteristics of ALD grown  $\sim 10$  nm  $\text{Nb}_2\text{O}_5$  thin film integrated into  $1 \times 1 \mu\text{m}^2$  single micro-crossbar devices with stack arrangement of  $\text{Pt}/\text{Nb}_2\text{O}_5/\text{Pt}$ . (a) Voltage controlled electroforming performed by applying a positive voltage to the top electrode. (b) A subsequent RESET was achieved by applying negative voltage to the top electrode. (c) Bipolar resistive switching.*

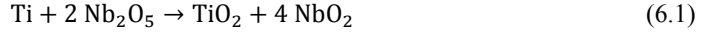
A comparable type of abrupt BRS behaviour with asymmetric values of the SET and RESET voltage, a linear LRS and a high  $R_{OFF}/R_{ON}$  ratio has also been reported for a Pt/Nb<sub>2</sub>O<sub>5</sub>/Pt cell built from a 30 nm thick, sputtered and oxidized Nb films [110]. In contrast to the results given in ref. [110] for the Pt/ALD Nb<sub>2</sub>O<sub>5</sub>/Pt cells in this study the SET voltage is found to be very close to the forming voltage (cf. Fig. 6.8 (a) and (c)), giving rise to a rather limited cycling endurance for this ‘hard’ switching event.

### 6.3.2. ALD Nb<sub>2</sub>O<sub>5</sub> in micro-crossbars with asymmetric electrodes

Different kinds of switching characteristics were perceived after inserting as deposited Nb<sub>2</sub>O<sub>5</sub> thin films in between micron scale asymmetric electrodes. Alongside bipolar resistive switching characteristics as mentioned in the previous section the use of Ti as a top electrode (TE) material with varied layer thickness in combination with Pt as a bottom electrode (BE) produced explicitly additional interesting resistive switching characteristics. The ALD grown  $\sim 10$  nm Nb<sub>2</sub>O<sub>5</sub> films were deposited on micro structured Pt bottom electrodes. After deposition of the film, (Ti/Pt) top electrodes with three different Ti layer thicknesses, this is, 2 nm, 5 nm and 10 nm, covered by a Pt capping layer were deposited and structured. In general, resistive switching can be divided into two main categories with respect to storage class: non-volatile memory switching (short: MS) and volatile threshold switching (short: TS). The non-volatile MS is further being divided into unipolar and bipolar resistive switching relating on the polarity dependence [31,155]. The bipolar resistive switching ‘1MS’-routine of as deposited Nb<sub>2</sub>O<sub>5</sub> has already been reported in the previous subsection as well as in literature [156,157]. The bipolar resistive memory switching (1MS) of Nb<sub>2</sub>O<sub>5</sub> enables two resistance states, HRS and LRS acting as ‘0’ and ‘1’, respectively [10]. One of both is always present at zero bias. For the further discussion, the respective switching voltages of the BRS-type memristive SET and RESET processes are named “ $V_{MS, SET}$ ” and “ $V_{MS, RESET}$ ”, respectively. The representative  $I$ - $V$  sweep is shown schematically in Fig. 6.9 (a) for VCM-type Nb<sub>2</sub>O<sub>5</sub> ReRAM devices, as reported in [158]. The device with only 2 nm of Ti layer thickness from this study showed an  $I$ - $V$  characteristic which resembles simple BRS behavior (cf. Fig. 6.9 (b)). The parameters for a compliance current of 500  $\mu$ A are  $V_{SET} = +2.5$  V,  $V_{RESET} = -0.65$  V with resistance values of about 1.3 M $\Omega$  for HRS and 7.8 k $\Omega$  for LRS giving rise to resistance ratio of roughly 170 at  $V_{read} = -0.2$  V. The switching voltages, currents and the memory window are found to be reduced compared to the symmetric cell (see section 6.3.1). When the thickness of the Ti OEL (oxygen exchange

layer) was increased from 2 nm to 5nm a dramatic change in the switching behavior was observed. The measured  $I$ - $V$  characteristic of the Pt/Nb<sub>2</sub>O<sub>5</sub>/Ti (5 nm)/Pt stack shown in Fig. 6.9 (d) is understood as resulting from superimposed  $I$ - $V$  characteristics of both 1TS and 1MS-type like being reported for Pt/Nb<sub>2</sub>O<sub>5</sub>/NbO<sub>2</sub>/Pt cells (see Fig. 6.9 (c)). Note that similar type of  $I$ - $V$  characteristics are reported for serially added Nb<sub>2</sub>O<sub>5</sub> based 1MS and NbO<sub>2</sub> based 1TS threshold switching devices [110, 53, and 164]. In (1MS+1TS) type devices the 1MS element must be connected in series to the 1TS element as portrayed schematically in Fig. 6.9 (c) sandwiched between top and bottom electrodes.

An open question arises for the cells prepared in this study because no 1TS layer has been deliberately added to the Pt/Nb<sub>2</sub>O<sub>5</sub>/Ti (5 nm)/Pt stack. Therefore, the conditions for the stability of Nb<sub>2</sub>O<sub>5</sub> aside of Ti metal are discussed based on the Ellingham phase diagram [224]. This allows determining stable compositions of oxides for a given system, e.g., NbO<sub>x</sub> - TiO<sub>x</sub>, which might in detail, represent the Nb<sub>2</sub>O<sub>5</sub>/Ti interface. For a homogeneously mixed system at thermodynamic equilibrium, that is, without additional driving forces like e.g. the electric field in the case of resistive switching, the Ellingham diagram allows to discuss possible stability scenarios balancing the Gibbs free energy change ( $\Delta G$ ) for each oxidation reaction as a function of the temperature. Thus, for the studied system the most interesting reaction is given as:



The total Gibbs free energy change is expressed as:

$$\Delta G_r = v_2 \Delta G_2^\circ - v_1 \Delta G_1^\circ \quad (6.2)$$

Here  $\Delta G_1^\circ$  and  $\Delta G_2^\circ$ , and  $v_1$  and  $v_2$  are the differences in values of Gibbs enthalpy of the involved oxides of the different species and the number of moles participating in the reaction, respectively. According to the values tabulated for the respective metal oxide species, from equation (6.2), the value of  $\Delta G_r$  is calculated to about  $-316.25 \left( \frac{\text{kJ}}{\text{mol}(\text{O}_2)} \right) @ T = 298.05 \text{ K}$  or  $-3.278 \text{ eV}$ . Since  $\Delta G_r < 0$ , the reaction given in equation (6.1) should always proceed towards the products predicting the formation of TiO<sub>2</sub> and NbO<sub>2</sub> in thermal equilibrium. From this a certain probability is deduced that NbO<sub>2</sub> might form at the Ti-Nb<sub>2</sub>O<sub>5</sub> interface under ambient conditions. This consideration can explain the (1TS+1MS) behavior observed in the Pt/Nb<sub>2</sub>O<sub>5</sub>/Ti (5 nm)/Pt system. When the Ti layer thickness in the Pt/Nb<sub>2</sub>O<sub>5</sub> (10 nm)/Ti/Pt stack sequence was

further increased from 5 nm to 10 nm, only 1TS-type pure threshold switching  $I$ - $V$  characteristics were obtained as shown in Figure 6.9 (f). It is a well-known phenomenon that increasing the layer thickness of the reactive metal electrode tends to increase the reduction of the switching oxide material due to redox reaction [15]. Applying the same argumentation as before for the Pt/Nb<sub>2</sub>O<sub>5</sub>/Ti (10 nm)/Pt before (cf. equations 6.1 and 6.2) it is assumed that the intended increase of Ti layer thickness further enhances the tendency for and the amount of NbO<sub>2</sub> formed. If the remaining amount of memristive switching Nb<sub>2</sub>O<sub>5</sub> phase is too small, pure TS-type switching might dominate the measured  $I$ - $V$  curve. Beside considerations on thermodynamic stability the comparison of  $I$ - $V$  curves plotted in Figure 6.9 (e) and (f) might give further evidence for this assumption. The volatile threshold switching (TS) involves two resistance states, namely a metallic-like “TS<sub>on</sub>-state” and insulating “TS<sub>off</sub>-state”. In volatile switching cells, the device upholds only one resistance state that is the TS<sub>off</sub>-state close to zero bias voltage. Owing to this, TS-type cells are also called “mono-stable switching devices” because only one resistance state is maintained above and below the assured bias [159-160]. The transition from insulating TS<sub>off</sub>-state to metallic TS<sub>on</sub>-state occurs at a certain threshold voltage  $V_{TS_{on}}$  during ramping up the applied bias whereas the reverse process happens at the voltage  $V_{TS_{off}}$  during ramping down of same applied bias for both positive and negative polarities [161, 53-54]. For typical 1TS-type switching the  $I$ - $V$  sweeps should be symmetrical with respect to the voltage polarity as shown in Fig. 6.9(e) for the Pt/NbO<sub>2</sub>/Pt cells. In the literature from before 2015 the 1TS behavior observed for NbO<sub>2</sub> – based thin films devices is (by default) attributed to the insulator to metal transition (IMT) that appears in NbO<sub>2</sub> at a transition temperature of  $T_{IMT} = 1180$  K. The temperature induced phase transition from a low-temperature insulating to a high temperature metallic state in NbO<sub>2</sub> is identified as Mott-Peierls transition [225,226]. Applying this IMT-model, the 1TS effect is being explained as a result of localized electrically induced Joule heating inducing IMT in the NbO<sub>2</sub> filament [162-163,129]. In this study devices with a stack structure of Pt/Nb<sub>2</sub>O<sub>5</sub>/Ti (10 nm)/Pt also showed reproducible 1TS-type switching after an electro-forming and first RESET process. Fig. 6.9(f) shows characteristic  $I$ - $V$  curves for applied voltages of -1.5 V → +1.5 V and a current compliance of about  $I_{CC} = 500$  μA. By reaching a critical voltage of about  $V_{TS_{on}(+)} = +1.0$  V a sudden current jump is observed while the device switches from the TS<sub>off</sub>-state to the TS<sub>on</sub>-state that is remained until the voltage is reduced again to a value of  $V_{TS_{off}(+)} = +80$  mV which brings the device into insulating TS<sub>off</sub>-state again.

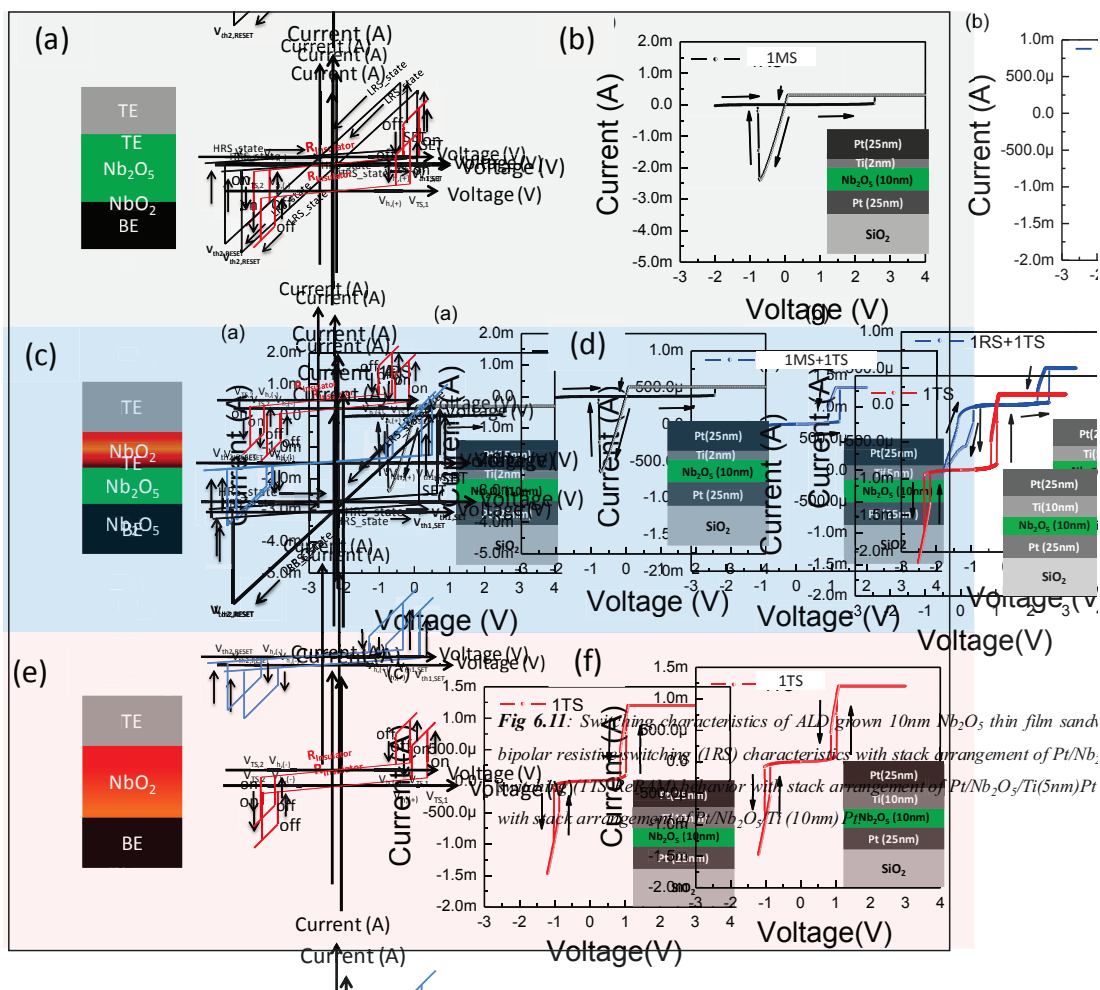


**Figure 6.9:** Schematic (left column) and measured (right column) switching characteristics of ALD grown 10 nm amorphous  $\text{Nb}_2\text{O}_5$  thin films integrated into  $(1\ \mu\text{m})^2$  micro-crossbar devices. The left column (a, c, e) shows a variation of the niobium oxide phase from bipolar MS for  $\text{Nb}_2\text{O}_5$  to pure TS for  $\text{NbO}_2$ , reproduced from reference [110]. The left column (b, d, f) shows experimental data of this study obtained for  $\text{Pt}/\text{Nb}_2\text{O}_5/\text{Ti}/\text{Pt}$  cells with different thickness of the Ti oxygen exchange layer (OEL) chosen as top electrode material, these are, 2 nm, 5 nm, and 10 nm, respectively. The comparison shows an amazingly interesting analogy between the corresponding  $I$ - $V$  curves.



The same characteristic is observed for negative polarity with the critical voltage signals being about  $V_{TS\_on, (-)} = -1.0$  V until the voltage reached back to  $V_{TS\_off, (-)} = -80$  mV. The overall observed ITS behavior is comprised as: reaching at the critical threshold voltages ( $|V_{TS\_on, +}| = |V_{TS\_on, (-)}|$ ) during rise of the applied voltage turns the threshold device from insulating to conducting state. Vice versa, decreasing the amplitude of the applied voltage below a critical value ( $|V_{TS\_off, (+)}| = |V_{TS\_off, (-)}|$ ) the device is switched back to the insulating TS\_off-state. Explanations proposed in the literature mostly attribute this behavior to a current induced Joule heating and accompanying IMT effect in the NbO<sub>2</sub>-based threshold devices. However, a recently proposed purely electronic effect based on a Poole-Frenkel type conduction mechanism enables a complete simulation of the ITS behavior in contrast to the IMT model [202].

## 6.4 Summary

In summary, Nb<sub>2</sub>O<sub>5</sub> thin films grown by thermal atomic layer deposition on planar substrates were studied with respect to composition, surface morphology and the crystal structures. The chemical and physical characterization showed that as-grown films were made from stoichiometric Nb<sub>2</sub>O<sub>5</sub> material with an amorphous structure. It has been demonstrated that the electrical properties of devices consisting of as grown Nb<sub>2</sub>O<sub>5</sub> thin films can be tuned by replacing the accessed top electrodes from inert Pt to non-inert Ti electrode material. By this means the  $I$ - $V$  hystereses could be changed from a pure bipolar VCM-type resistive switching to a threshold-type switching when the thickness of the Ti oxygen exchange layer was increased from 2 nm to 10 nm, respectively. In the literature, threshold-type switching behavior is reported for NbO<sub>2</sub>-based selector devices. Here, for the studied Pt/Nb<sub>2</sub>O<sub>5</sub>/Ti/Pt micro-crossbar cells a phase transformation during the electroforming process is proposed. This is in line with the stability of the compounds given by the Ellingham diagram predicting a reduction of Nb<sub>2</sub>O<sub>5</sub> to NbO<sub>2</sub> and oxidation of titanium metal to titanium oxide. This type of a local reduction process if happening for example during electroforming at the Ti (TE) might open up possibilities for tailoring the switching characteristics by proper device engineering.

## 7. Resistive Switching of Nb<sub>2</sub>O<sub>5</sub> Nano-Crossbar Cells

This chapter describes the electrical characteristics of nano-crossbar devices obtained from integration of ALD Nb<sub>2</sub>O<sub>5</sub> thin films. As-deposited amorphous Nb<sub>2</sub>O<sub>5</sub> thin films of 10 nm thickness were stacked into a cross junction between a Pt bottom and a Ti/Pt top electrode defining a cell size of 110×110 nm<sup>2</sup> to 55×55 nm<sup>2</sup>. The detailed process flow of the fabrication is described in Chapter 3 (see section 3.2.3). The resulting stack sequence from bottom to top is given by Si/SiO<sub>2</sub>/5 nm Ti/25 nm Pt/10 nm Nb<sub>2</sub>O<sub>5</sub>/5 nm Ti/25 nm Pt. A schematic figure as well as SEM micrographs of the nanocrossbar device and junction together with a TEM cross section picture is shown in Figure 7.1.

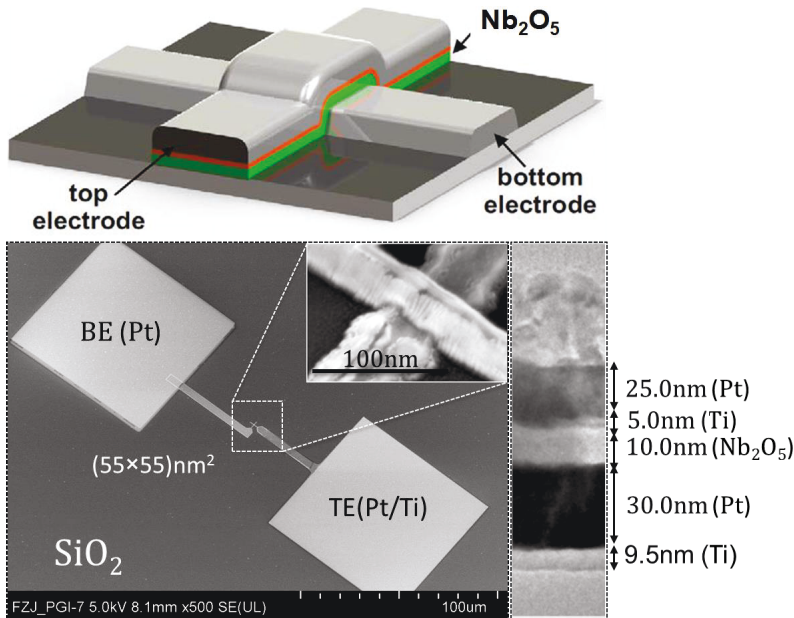


**Figure.7.1:** The schematic diagram of a single nanocross bar device and a top view SEM micrograph of a Pt/Nb<sub>2</sub>O<sub>5</sub>/Ti/Pt nano-crossbar device. The inset shows a higher magnification SEM image of the 55×55 nm<sup>2</sup> junction and a cross sectional TEM picture of the device cross section.

As has been shown in Chapter 6 for micron-size devices, this layer stack is interesting due to the coexistence of threshold and memory switching functionality. In nano-crossbar devices the effect of parasitic leakage current can be significantly reduced in comparison to micro-crossbar cells. This allows a more systematic study of the (1TS+1MS) mechanism and the possible transition between two types of switching, that is, 1TS and 1MS. Additionally, a discussion by means of an empirical model will be performed and results of nanoscale analysis obtained on a device after threshold switching will be shown. By this means the physical origin of combined threshold and memory switching found in the Pt/Nb<sub>2</sub>O<sub>5</sub>/Ti/Pt cells will be deliberated.

## 7.1 Threshold switching triggered by an electric field

Threshold switching devices show an instantaneous resistance change upon increasing the applied voltage as shown in Fig. 7.2. Following the IMT model, the sudden jump in the conductivity appears when the temperature in the filament reaches the phase transition temperature from insulator to metal  $T_{\text{IMT}}$ . In other words, the device switches into the TS<sub>on</sub>-state if the intrinsic temperature exceeds  $T_{\text{IMT}}$  due to Joule heating. For years the IMT model has been widely accepted for the explanation of the threshold switching event, although it faces two major conflicts. The first one is the huge difference in electrical power required for switching the threshold function ON and OFF, respectively. As one can easily see from Fig. 7.2 the electrical power for switching off is significantly higher than the power calculated for the switching on point:  $P_{\text{TS, OFF}} \gg P_{\text{TS, ON}}$ . In contrast, for an IMT effect where the critical temperature is defined by Joule heating, both, on and off switching, are expected to happen at comparable electrical power:  $P_{\text{IMT, OFF}} \approx P_{\text{IMT, ON}}$ . From this the question arises how the very slim and small opening of the typical threshold  $I$ - $V$  hysteresis of NbO<sub>2</sub> as shown in Fig. 7.2 can be explained by means of an IMT. In other words, the threshold onset event happens when the filament regime reaches a certain temperature due to electrical heating equivalent to  $P_{\text{TS, ON}}$ . However, when the voltage is reduced from high values towards zero it is found that the threshold devices switches to the OFF-state for a power significantly larger than  $P_{\text{TS, ON}}$ , this means,  $P_{\text{TS, ON}}$  is not sufficient to keep the TS in its ON-state. Further the small opening of threshold switching loop shows that the switching happens nearly at same voltage when ramping up or down which is an indication that the threshold switching in NbO<sub>2</sub> is voltage controlled

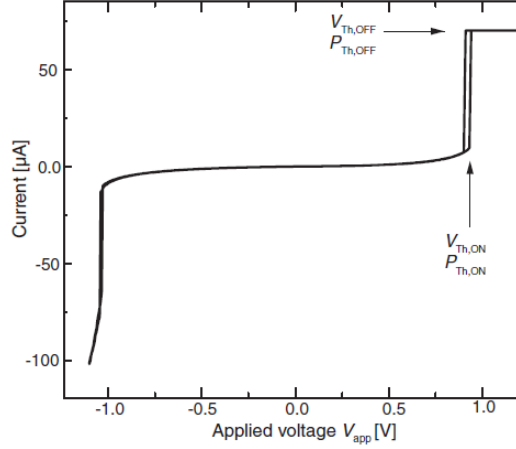


**Figure 7.2:** Measured volatile threshold switching  $I$ - $V$  characteristics of NbO<sub>2</sub>-based (ITS+IMS) nano-crossbar structure of  $80 \times 80 \text{ nm}^2$ . Reprinted from [202]

rather than power controlled [202-203]. The second concern regarding the IMT model is that the measured change in the current at the IMT phase transition of NbO<sub>2</sub> at 1080 K comes out to be lower than factor of 10 [203-205]. In contrast, the jump in current for threshold switching NbO<sub>2</sub> based devices has been reported to reach values of up to 100. [226] In the recent work of Funck *et.al.* [202] an axisymmetric 2D multidimensional simulation model named electric field triggered thermal run away (FTTR) model was presented for the simulation of threshold switching in NbO<sub>2</sub>. The model successfully reproduces the experimental results obtained on 10 nm thick ALD grown Nb<sub>2</sub>O<sub>5</sub> films integrated into nano-crossbar devices as also used in this thesis and answers the questions which are raised in contradiction of the IMT model. According to the FTTR model the combination of moderate temperature and intrinsic polaron hopping based on Pool Frenkel (PF) like barrier lowering as described in equation 7.1 causes the threshold type switching in NbO<sub>2</sub> [202]. The physical origin of the switching is based on the self-acceleration process of carrier generation and Joule heating that leads to a thermal run away process. The conductivity in the threshold regime is described by:

$$\sigma_{Th} = \sigma_0 \exp \left[ -\frac{\Delta W_A - \beta \sqrt{E}}{k_B T} \right] = \sigma_0 \exp \left[ -\frac{\Delta W_A}{k_B T} \right] \exp \left[ -\frac{\beta \sqrt{E}}{k_B T} \right] \quad (7.1)$$

where  $\sigma_0$  is the conductivity prefactor,  $\Delta W_A$  the activation energy,  $k_B$  Boltzmann constant,  $T$  temperature,  $E$  the electric field,  $\beta$  the pre factor.

Fig. 7.3 (a) shows the axisymmetric 2D simulated temperature distribution inside the filament area. The FTTR-based 2D model reproduces the threshold switching  $I$ - $V$  sweep  $\text{NbO}_2$  based (1TS+IMS) cells considerably well as seen from Fig. 7.3 (b). Therefore for the further discussion the FTTR model will be utilized for explaining the 1TS or 1TS+IMS characteristics measured for the devices in this study.

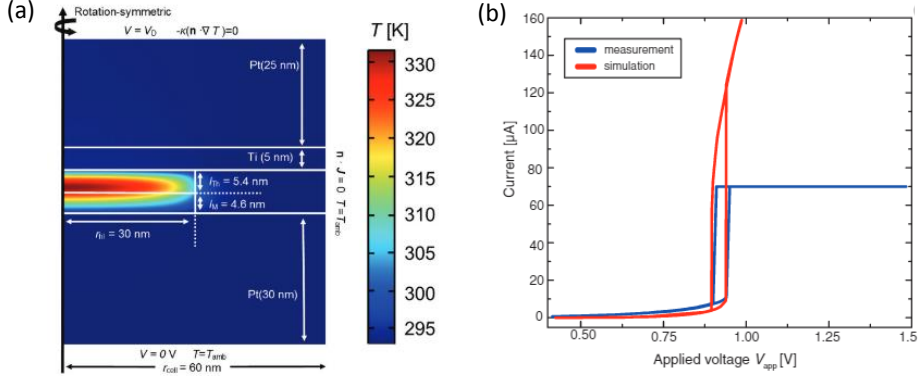


**Figure 7.3:** (a) Axisymmetric 2D simulation geometry of the (1TS+IMS) structure with boundary conditions given in the picture. The color code depicts the temperature distribution within the cell for the  $TS_{off}$  - state at the threshold voltage  $V_{TS, on}$ . (b) Simulated threshold  $I$ - $V$  curve using the FTTR model in comparison to the measured data obtained for a 1TS+IMS structure with the memory in the LRS. Reprinted with permission of [202]

## 7.2 Threshold and memory type (1TS+1MS) switching

### 7.2.1. Initial Leakage, Electro-forming and RESET process

Fig. 7.4 (a) shows a representative  $I$ - $V$  plot of the initial leakage current characteristics of nano-crossbar device in its pristine state with a lateral dimension of  $55 \times 55 \text{ nm}^2$  built from a 10 nm amorphous ALD  $\text{Nb}_2\text{O}_5$  layer. The applied voltage was limited to  $\pm 2.0 \text{ V}$  in order to avoid electro-forming of the cell. Asymmetric diode-like leakage behavior was observed due to the asymmetric electrode configuration. The effective metal work functions of Ti ( $\Phi \approx 4.33 \text{ eV}$ ) which serves as oxygen exchange layer at TE and Pt ( $\Phi \approx 5.15 \text{ eV}$ ) that is used as the BE in contact to the ALD  $\text{Nb}_2\text{O}_5$  layer cause a barrier offset of roughly  $0.82 \text{ eV}$  (see also [112]).

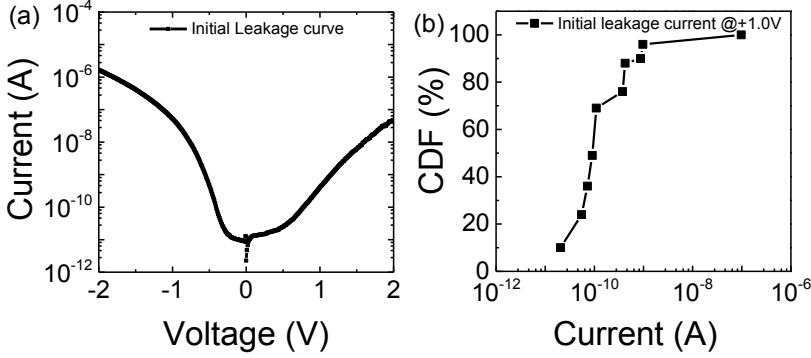


**Figure 7.4:** (a) Initial  $I$ - $V$  characteristics of the as-deposited amorphous ALD  $\text{Nb}_2\text{O}_5$  in  $\text{Pt}/\text{Nb}_2\text{O}_5/\text{Ti}/\text{Pt}$  nanocross bar device of  $(55 \text{ nm})^2$  size in pristine state measured under ambient conditions with voltage applied to the Ti TE. (b) The CDF plot represents the initial leakage current variation measured at  $+1.0 \text{ V}$  for 50 devices.

The leakage current data determined at  $1.0 \text{ V}$  from about 50 devices with the same lateral dimensions are presented as cumulative distribution function (CDF) plot in Fig. 7.4 (b). From this a mean value of the initial leakage current at  $+1.0 \text{ V}$  of less than  $1 \cdot 10^{-9} \text{ A}$  is determined. This reasonable insulation resistance of the cells in the giga-Ohm range indicates the highly homogeneous and dense film quality achieved from the ALD process. A mean initial resistance of the nanocross bar devices from the 50 % values of the CDF plot was found to be in the range of  $10 \text{ G}\Omega$  at  $+1.0 \text{ V}$ .

The device configuration of  $\text{Pt}(\text{BE})/\text{Nb}_2\text{O}_5/\text{Ti}/\text{Pt}(\text{TE})$ , where the switching oxide film ( $\text{Nb}_2\text{O}_5$ ) with a band gap of  $\sim 3.9 \text{ eV}$  is sandwiched between different electrodes can be described as asymmetric. Due to the high metal work function the Pt interface forms a Schottky-type contact whereas the low metal work function Ti forms an Ohmic-type contact to the oxide [68]. For valence change mechanism (VCM)-type resistive switching devices, the  $\text{Pt}/\text{Nb}_2\text{O}_5$  interface is described as inert active (switching) electrode (AE) whereas the  $\text{Nb}_2\text{O}_5/\text{Ti}$  interface is named as an ohmic counter electrode or electrochemical active electrode (OE or EAE) with high oxygen affinity and low metal work function. The electro-forming process prior to the regular resistive switching that depends on the applied polarity with respect to the top or bottom electrode brings devices into the LRS-state (forming into the ON-state) or HRS-state (forming into the OFF-state), respectively [109]. Fig.7.5 (a) shows a representative positive voltage-controlled electro-forming curve accomplished from the initially high resistive device by applying a positive

voltage to the Ti/Pt (TE) with respect to Pt (BE) as a ground. This type of electro-forming process which brought the initially high resistive devices ( $\sim 10 \text{ G}\Omega$ ) into the low resistance state ( $\sim 100 \text{ k}\Omega$ ) yielded the best results in terms of a stable switching behavior. Initially due to the high resistance, a suitable compliance current has to be set in order to prevent the device from a ‘hard’ destructive breakdown. A typical electro-forming  $I$ - $V$  sweep shown in Fig. 7.5 (a) was achieved by applying a positive forming voltage of  $V_F = +4.0 \text{ V}$  to the top electrode, with a proper value of  $I_{CC} = 10 \mu\text{A}$  for the compliance current. During electro-forming, typically a reduction of the device resistance of about several orders of magnitude is observed. The decrement of the initial high resistance of the device is basically addressed to the formation of a conductive filament, this is, a reduced sub-oxide of the switching oxide material, by setting the device from the initially high resistive state to low resistance state [109,113]. In general the forming voltage is always higher than the absolute switching voltages. The electro-forming method has been assumed to cause a significant increase in the local temperature [114] which, vice versa, leads to an acceleration of the forming procedure and may also induce morphological changes [115-117]. Applying a positive voltage signal to the top electrode of the nano-crossbar devices initiates a local reduction of Nb<sub>2</sub>O<sub>5</sub> and a drift of O<sup>2-</sup> ions towards the anode thereby oxidizing partly the Ti top electrode. Hence the electro reduction process consequently leaves oxygen vacancies  $V_O^{\bullet\bullet}$  behind which drift towards the cathode (bottom electrode, Pt). According to the filamentary resistive switching model, as assumed in this work, an oxygen deficient (NbO<sub>2</sub>/Nb<sub>2</sub>O<sub>5-x</sub>) filament is formed consisting of an n-type conducting oxide called the ‘plug’ (NbO<sub>2</sub>) and the potential barrier called the ‘disc’ (Nb<sub>2</sub>O<sub>5-x</sub>). This process can also enhance not only oxygen vacancies but also enhanced the Nb vacancies in Nb<sub>2</sub>O<sub>5</sub> [108]. As a result of the electro-forming process a gradient of oxide thin layers is always present between top and bottom electrodes such as Pt (BE)/Nb<sub>2</sub>O<sub>5-x</sub>/NbO<sub>2</sub>/Ti/Pt (TE). The statistical analysis and variation in the electro-forming voltages from device to device is shown in Fig. 7.5 (b) by the cumulative distribution function (CDF). A very steep CDF characteristic has been recorded out of 50 devices of cross junction area of  $55 \times 55 \text{ nm}^2$ . Conventionally in VCM based resistive switching processes, electro-formed devices are in LRS. To ensure that there is no permanent electrical breakdown in the switching material rather than successful electro-forming process the devices are brought into HRS. For that purpose negative polarity was applied on the top electrode with respect to bottom electrode.

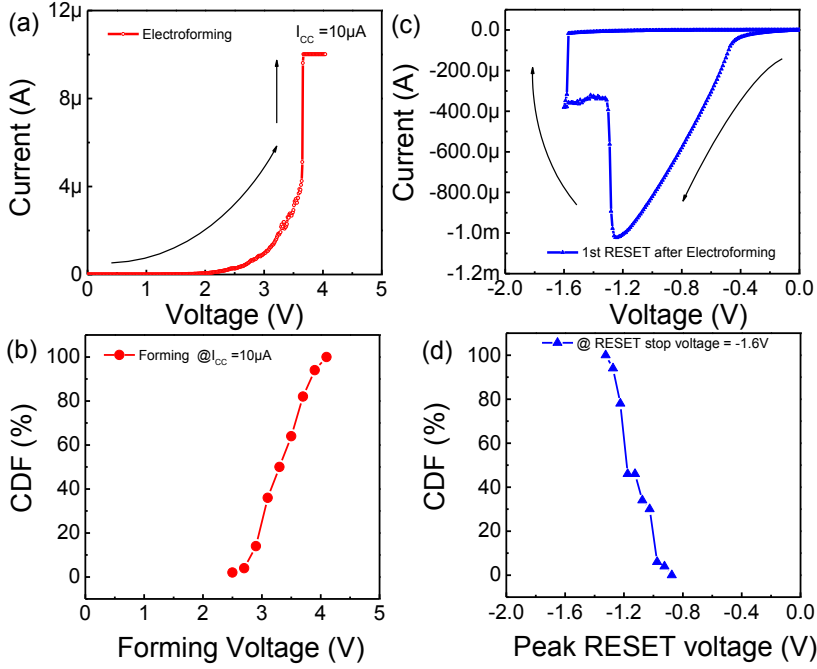


**Figure 7.5:** (a) A representative electro-forming I-V curve of an as deposited ALD grown  $\text{Nb}_2\text{O}_5$  based Pt/ $\text{Nb}_2\text{O}_5$ /Ti/Pt nano-crossbar device of  $55 \times 55 \text{ nm}^2$  obtained with positive voltage ramp on the Ti/Pt TE, (b) CDF of the forming voltage of 50 formed devices and (c) the most representative 1<sup>st</sup> RESET I-V characteristics after successful electroforming process with negative voltage on the Ti/Pt TE, (d) CDF plot represents the peak RESET voltage under applied voltage of about -1.6 V on Ti/Pt TE for 50 successfully electro-formed devices.

As it has been described earlier the electro-forming process leads to the formation of oxygen deficient filament (reduction) and leaves oxygen vacancies behind in the oxide layer. By applying negative polarity on the top electrode with respect to bottom electrode the filament is re-oxidized and the HRS of the device is reached which is not as high as the pristine state. The process of bringing the device back into the HRS after electro-forming process is called RESET process which has been already described in chapter 2. Fig. 7.5 (c) shows the representative RESET process curve of the electro-formed device. The RESET stop biasing was always chosen  $V_{\text{RESET\_stop}} = -1.6 \text{ V}$  which resulted in successful RESET after electro-forming and brought the devices from the 100 k $\Omega$  range to the 1.5 M $\Omega$  range without any current compliance applied. The statistical analysis in the form of CDF has been plotted and is shown in Fig. 7.5 (d) for the peak RESET stop voltages for about 50 formed devices.



### 7.2.2. Basic switching operation of (1TS+1MS) devices

After the electro-forming and RESET procedure the devices typically revealed combined threshold and memory switching characteristics as shown in Fig. 7.6. The corresponding semilogarithmic  $I$ - $V$  curve is shown in the inset of Fig. 7.6. The combination of both threshold and memory switching is abbreviated as (1TS+1MS) in which 1TS and 1MS stand for threshold and memory switching, respectively. Due to its high nonlinearity the main function of the ‘1TS’ element is to constitute as a selector in a passive ReRAM crossbar array to block the parasitic currents known as sneak path currents ( $I_{sneak}$ ). The threshold switching characteristics are achieved by the direct integration of a 1TS element with a memristive (1MS) cell, for example NbO<sub>2</sub> – based cell combined with Nb<sub>2</sub>O<sub>5</sub> device. Here, as will be shown, the threshold element is created during the electroforming procedure of the memristive element resulting in a (NbO<sub>2</sub>/Nb<sub>2</sub>O<sub>5-x</sub>) structure having both threshold and memory switching functions after electro-forming and RESET process. As grown Nb<sub>2</sub>O<sub>5</sub> layers are stoichiometric at room temperature according to the XPS analysis (cf. Fig. 6.1). No indication of NbO<sub>2</sub> was observed except for vacuum anneal at higher temperature of about 400-600 °C [126]. Therefore any possible formation of NbO<sub>2</sub> is attributed to the ‘high current’ electro-forming and subsequent RESET process. It is assumed that a threshold switching NbO<sub>2</sub>-region is located close to the Ti/Pt top electrode. Its real existence confirmed by nanodiffraction analysis will be discussed in section 7.7. Further a thin Nb<sub>2</sub>O<sub>5-x</sub> region close to the Pt bottom electrode should enable the memristor functionality [202]. With this, the representative  $I$ - $V$  curve in Fig. 7.6 can be understood in the following manner. Initially, after electro-forming and 1<sup>st</sup> RESET process the oxygen deficient filament comprised of Nb<sub>2</sub>O<sub>5-x</sub> oxide layer near to bottom electrode interface (called *disc*) is in its OFF-state and moreover the NbO<sub>2</sub> (TS)-filament is insulating for low electric field. The overall hybrid is considered in (1TS+1MS)<sub>OFF\_state</sub> indicated by state ① in Fig. 7.6. Increasing the positive voltage applied to the (Ti/Pt) top electrode above the threshold voltage ( $V_{MS\_on} > V_{appl} > V_{TS\_on, (+)}$ ) of NbO<sub>2</sub> which is assumed to be less than the memristor SET voltage,  $V_{MS\_on}$  of the Nb<sub>2</sub>O<sub>5-x</sub>, the NbO<sub>2</sub> plug switches from its OFF-state to its ON-state. With increasing voltage, the SET voltage of the memristive element is reached, this is the memory switches to the ON-state at  $V_{th, 1} = V_{MS\_on} = +1.35$  V and the total current is just limited by the current compliance of  $I_{CC} = +100$   $\mu$ A.

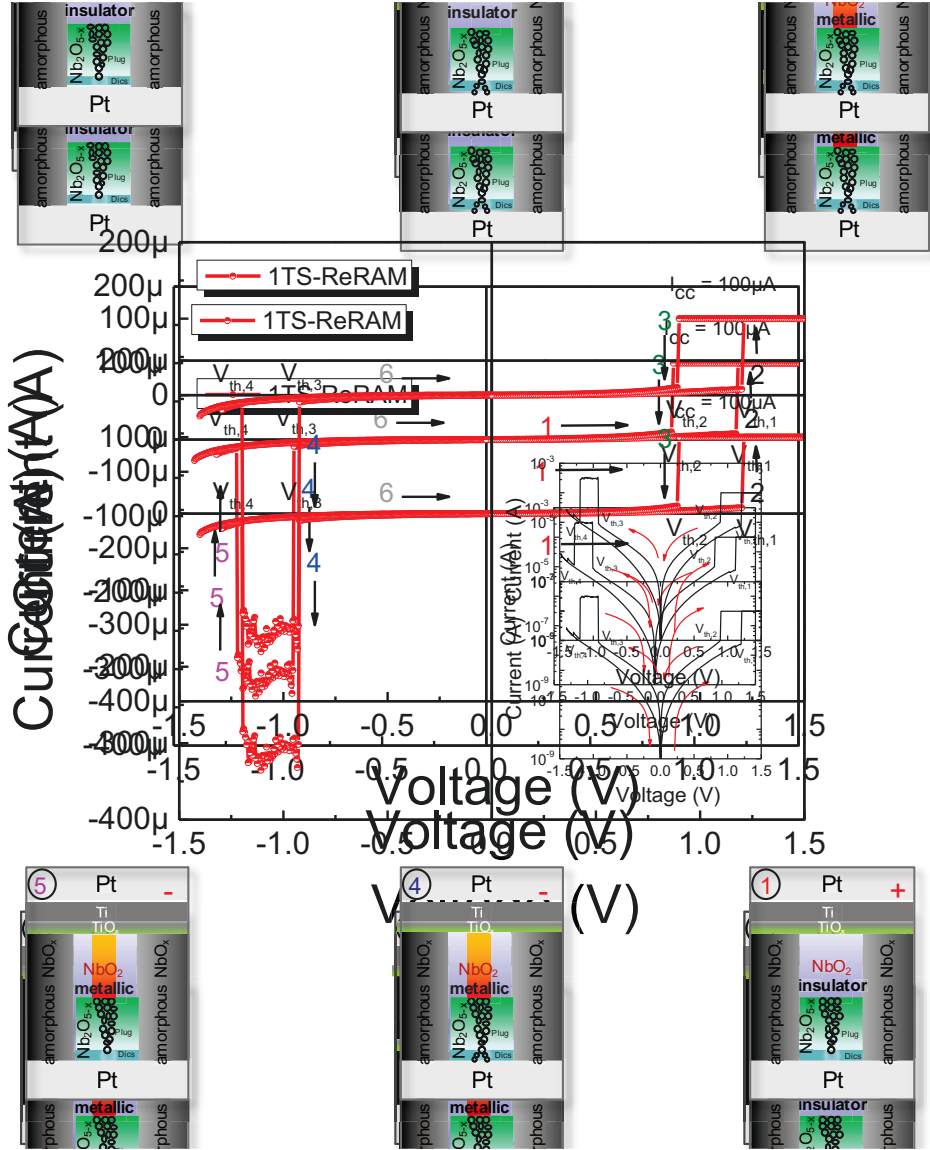


**Figure 7.6:** The mechanism and the schematic illustration of the switching sweep of (1TS+ 1MS) of the ALD grown single layered  $\text{Nb}_2\text{O}_5$  on Pt/ $\text{Nb}_2\text{O}_5$ /Ti/Pt nanocross bar device of size  $55 \times 55 \text{ nm}^2$  after electro-forming and 1<sup>st</sup> RESET process at a certain current compliance of  $I_{cc} = 100 \mu\text{A}$  showing the switching direction and the different steps involved during the switching.

The microscopical mechanism might involve oxygen vacancies attracted towards the disc (Nb<sub>2</sub>O<sub>5-x</sub>) and by this causing a significant decrease in the potential barrier between filament and bottom electrode as a consequence of a local reduction process. As a result of this, the plug state changes from 1MS<sub>HRS</sub> to 1MS<sub>LRS</sub> and the hybrid device turns into (1TS+1MS)<sub>ON\_state</sub> ②. During the descending of the applied voltage and reaching at voltage  $V_{th, 2} = V_{TS\_off, (+)} = +0.85$  V, state ③ the conductivity of the (NbO<sub>2</sub>) threshold element changes from ON-state to OFF-state while the oxygen deficient memory regime (Nb<sub>2</sub>O<sub>5-x</sub>) stays in its ON-state. The full device stays in this TS<sub>OFF</sub>-state until the applied negative voltage approaches to  $V_{applied} = V_{TS\_on, (-)}$  less than the  $V_{MS, RESET}$  on the top electrode (Ti/Pt). The hybrid device suddenly jumps to 1TS1MS<sub>ON\_state</sub> when the negative voltage passes the threshold voltage  $V_{th, 3} = V_{TS\_on, (-)} = -0.89$  V required for transition of the plug (NbO<sub>2</sub>) from 1TS<sub>off\_state</sub> to 1TS<sub>on\_state</sub>. So the overall status of the hybrid device again changes to (1TS+1MS)<sub>ON\_state</sub> ④. But when the hybrid device passes the threshold voltage  $V_{th, 4} = V_{MS, RESET} = -1.25$  V, the voltage necessary for RESET the 1MS, the hybrid device is turned into the (1TS+1MS)<sub>OFF\_state</sub> ⑤. Upon reaching at state ⑥ both plug and disc are in OFF-state which means 1TS is in OFF-state and 1MS is in HRS-state like it was the situation in ①, the starting point. This type of coexisting phenomenon has already been reported but for intentionally stacked bilayer materials like for example. (NbO<sub>2</sub>/Nb<sub>2</sub>O<sub>5</sub>), (TiO<sub>2</sub>/Ti<sub>4</sub>O<sub>7</sub>) and (TiO<sub>2</sub>/VO<sub>2</sub>) type systems [110, 24, 39-41].

The emerging of both (1TS) and (1MS) has great potential towards the ReRAM high density arrays to resolve the sneak path issues [131-132]. In order to investigate the technological potential of the hybrid devices further, statistical analysis was performed. The CDF plot in Fig.7.7 shows a steep distribution of the threshold voltages i.e.  $V_{+th,1}$ ,  $V_{+th,2}$ ,  $V_{-th,3}$ ,  $V_{-th,4}$  of the 55×55 nm<sup>2</sup> nano-crossbar device of size of 50 quasi-static cycles for the applied voltage range of +1.5 V to -1.5 V. The reduced leakage current in the low voltage range of ±1.5 V makes these types of hybrid devices very interesting for future high density crossbar memory array structures to avoid the sneak path issues during LRS due to high nonlinearity. The existence of both 1TS (volatile switching) and 1MS (non-volatile switching) together in a single layer switching material makes this interesting as a selector and memory material by performing a suitable device engineering. The steep threshold switching voltage distributions due to the intrinsically built in 'S-NDR' make these types of devices interesting for high density cross bar memory and logic application. [111]

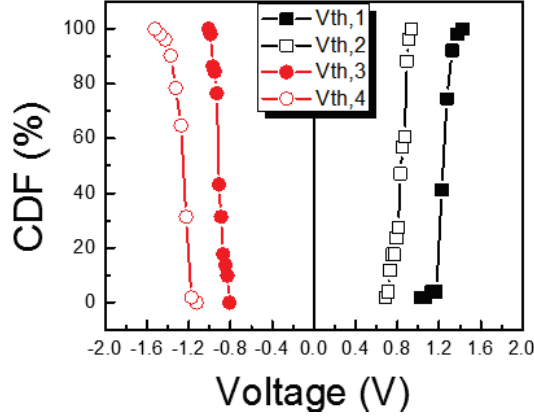


**Figure 7.7:** The CDF (%) plot of the (1TS+1MS) threshold switching voltages of the Pt/ALD  $\text{Nb}_2\text{O}_5$ /Ti/Pt nano-crossbar device of size  $55 \times 55 \text{ nm}^2$ .

### 7.3 Analysis of combined (1TS+1MS) switching

To understand the electrical characteristics of the combined or hybrid-type (1TS+1MS) switching in more detail, an equivalent circuit model is proposed. This is realized by two resistors in series as shown in Fig 7.8 (a), where one resistor represents the threshold (plug) and the other one the memory (disc) as described in the prior section 7.2. In VCM-type resistive switching cells the memory resistance depends on the RESET stop  $V_{\text{RESET-stop}}$  voltages. By the definition of the threshold selector, the resistance of  $1\text{TS}_{\text{off\_state}}$  is always higher than the resistance of  $1\text{MS}_{\text{LRS\_state}}$ . In this section, the switching operation of (1TS+1MS) devices is analyzed with respect to threshold voltage and memory window obtained from voltage and current controlled  $I$ - $V$  schemes. The current controlled scheme is implemented by controlling the current compliance  $I_{\text{CC}}$  during the SET process while the voltage controlled scheme is achieved by controlling the RESET stop biasing during RESET process.

#### 7.3.1. Voltage controlled switching

Figures 7.8 (b) and (c) exemplify the linear and semi-log presentations of  $I$ - $V$  characteristics of (1TS+1MS) switching obtained for different RESET stop voltages (e.g. -1.1 V, -1.2 V, -1.3 V, -1.4 V, -1.5 V, and -1.6 V). The voltage sweeps with  $V_{\text{RESET}}$  variation were always performed with a maximum applied positive voltage of +2 V on the

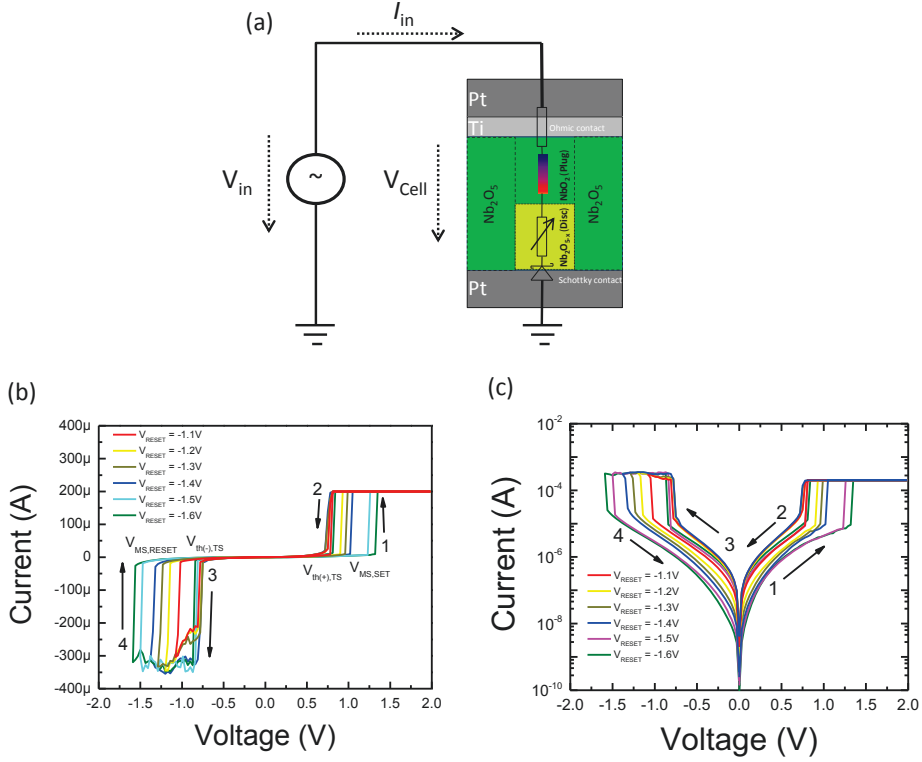


**Figure 7.8:** (a) The two serial resistor model where one of the resistors is the ITS threshold switch known as plug and the second one is the variable resistor due to different reset stop voltages and called memory switch 1MS (disc). The chart (b) represents linear and (c) semi-log presentations of I-V sweeps of the (ITS+1MS) cells after electro-forming and 1<sup>st</sup> reset process. The reset during switching is performed at different reset stop voltages of -1.1 V, -1.2 V, -1.3 V, -1.4 V, -1.5 V, and -1.6 V.

top electrode and for a fixed current compliance of 200  $\mu\text{A}$ . The parameters  $V_{MS, SET}$ ,  $I_{MS, SET}$  and  $R_{MS, on}$  depend clearly on the RESET stop voltage as shown in Fig. 7.9 (a) and (c). The plot of the switching power  $P_{MS, on}$ , necessary to set the threshold to on and the memory into LRS, as a function of the reset stop voltage is shown in Fig. 7.9 (b). The graph shows a saturation of the  $P_{MS, on}$  value at about 9  $\mu\text{W}$  for low reset stop voltages between -1.0 V and -1.4 V whereas the  $P_{MS, on}$  values decrease to about 2  $\mu\text{W}$  for a reset stop voltage of about -2.0 V. In contrast, the voltages  $V_{TS, off, (+)}$  and  $V_{TS, on, (-)}$  are discovered to be independent of the reset stop biasing with both amplitudes being in the range of 0.8 to 0.9 V (see Fig. 7.9 (d)). Hence switching voltage, current and power are functions of the reset stop voltage. Likewise the device under test shows different

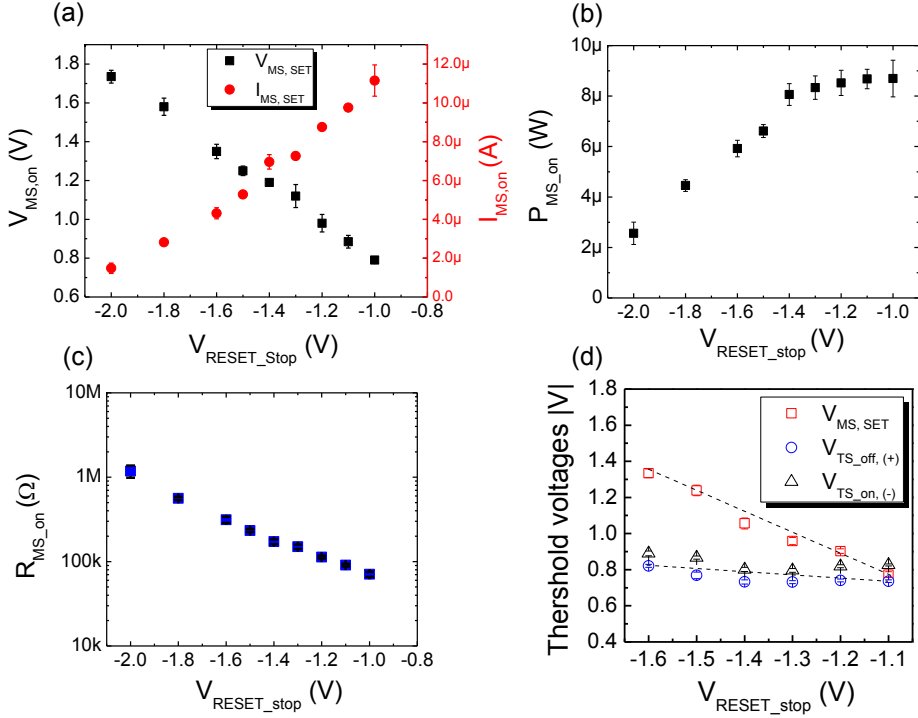


**Figure 7.9:** (a) Voltage and current necessary to SET the (ITS+IMS) devices into the on-state;  $V_{\text{MS\_on}}$ ,  $I_{\text{MS\_on}}$  showing opposite trends against the RESET stop biasing. (b)  $P_{\text{MS\_on}}$  of the memory switching is showing a linear trend with respect to REST stop biasing whereas (c)  $R_{\text{MS\_on}}$  resistance depicts linear correlation and (d) the threshold switching ITS voltages are independent of the reset stop biasing.

memory HRS ( $\text{MS}_{\text{HRS}}$ ) but rather constant and stable LRS ( $\text{MS}_{\text{LRS}}$ ) values against variations of the reset stop biasing. This is a precondition for multilevel switching which will be discussed in chapter 8 [133]. Considering that the  $\text{Pt}/\text{NbO}_x/\text{Ti}/\text{Pt}$  cell is characterized by a signature of a separated two phase system, i.e. threshold-type switching  $\text{NbO}_2$  and memristive-type switching  $\text{Nb}_2\text{O}_5$ , the device behavior can be understood from drift-/diffusion processes of oxygen vacancies and oxygen ions, respectively, locally affected by Joule heating [134-135]. It is assumed that recombination of oxygen vacancies and oxygen ions cause the rupture of conductive filament between disc and the plug. By increasing the reset stop biasing the electric field and the localized Joule heating effect are further increased which enhances the diffusion of oxygen ions [136-137], increases the recombination process with oxygen vacancies and increases the potential barrier (disc) in front of the active electrode (Pt) [138-140]. This increases the barrier height for electronic current and favours the Schottky emission mode dominates at

the interface over the electric field model. To overcome this Schottky barrier the device needs higher switching voltage. In the combined threshold and memory switching event the threshold voltages are independent of the RESET stop biasing and the switching mechanism is dominantly governed by FTTR model [202].

### 7.3.2. Extraction of the threshold (1TS) switching

Pure threshold switching happens when the memory switching element remains in its MS<sub>LRS</sub> state during the switching sweep. The memory (1MS) and threshold (1TS) switching states in hybrid devices can be deduced from quasi-static  $I$ - $V$  analysis. In Fig. 7.10 (a-red curve), the (1TS+1MS) device was SET by applying the positive voltage of about +2 V on the top electrode with current compliance of 200  $\mu$ A after the successful RESET process (not shown in the graph). The device showed the (1TS+1MS) switching characteristics. Similarly, if a negative voltage of about -1.6 V ( $V_{RESET\_stop} > V_{TS\_on, (-)}$ ) was applied after successful SET process (not shown in the graph) the device again established the (1TS+1MS) behavior as shown in Fig. 7.10 (b-red curve). But when the device was put under positive applied bias after SET process consecutively ('SET after SET') the (1TS+1MS) device only showed a small and slim opened 1TS  $I$ - $V$  sweep (Fig. 7.10 (a, black curve)). The reason behind this characteristics has been described in the prior section where it has been shown that after SET process the memory element 1MS stays in 1MS<sub>LRS</sub> but the 1TS converts into 1TS<sub>on</sub> at +850 mV and switched back into off state at TS<sub>off</sub>= +830 mV. In the second case when a negative voltage  $V_{RESET\_stop} = V_{TS\_on, (-)}$  = -940 mV was applied after the 1<sup>st</sup> reset, i.e., 'RESET after RESET' process, the device stays in the 1MS<sub>LRS</sub> as depicted in Fig. 7.10 (b-black curve). Apparently, by fine tuning of electrical parameters the memory element can be suppressed for positive as well as negative polarities and only 1TS switching is obtained even without any current compliance as shown in Fig. 7.10 (c). For the 1TS switching behavior it has been observed that the absolute SET voltage of threshold devices  $|V_{TS\_on}|$  is larger than the absolute off-switching threshold voltage  $|V_{TS\_off}|$ , in other words,  $|V_{TS\_on}| > |V_{TS\_off}|$ . In contrast,  $V_{TS\_on, (+)} = V_{TS\_on, (-)}$  and correspondingly  $V_{TS\_off, (+)} = V_{TS\_off, (-)}$  as shown in Fig. 7.11 (a). The same holds for the resistance values, i.e.  $R_{TS\_on}$  and  $R_{TS\_off}$  depicted in Fig. 7.11 (c). On the other hand the currents  $I_{TS\_on}$  and  $I_{TS\_off}$  showed an opposite behavior

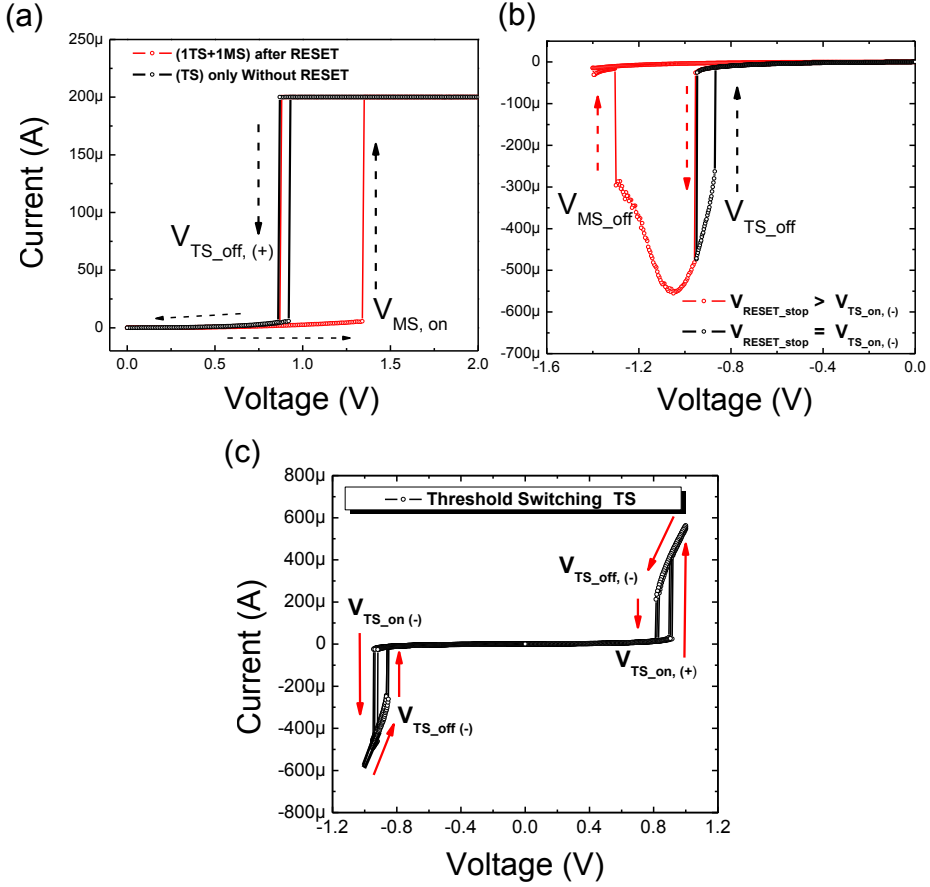


**Figure 7.10:** Extraction of I-V sweeps of 1TS from hybrid switching (ITS+IMS) behavior for single nano-crossbar devices. (a) curve after successful reset (red curve) and without reset process (black), 'SET after SET' process of IMS switching, (black curve) (b) after successful SET with  $V_{\text{RESET\_stop}} > V_{\text{TS\_on, (-)}}$  (red curve) and without SET process, 'RESET after RESET' process with  $V_{\text{RESET\_stop}} < V_{\text{TS\_on, (-)}}$ , (black curve) (c) stable 1TS switching sweep for both positive as well as negative polarities.

compared to the threshold voltages that is an abrupt decrease at voltages  $|V_{\text{TS, on}}|$  and  $|V_{\text{TS, off}}|$  as shown in Fig. 7.11 (b). Similarly the power at which the threshold switch is turned-on into the conducting state and turned-off into the insulating state, obeys the relation  $|P_{\text{TS, off}}| > |P_{\text{TS, on}}|$ .

Exactly this difference in the power values that is characteristic for the studied  $\text{NbO}_2$ -based threshold-type devices is inconsistent with the IMT based threshold model



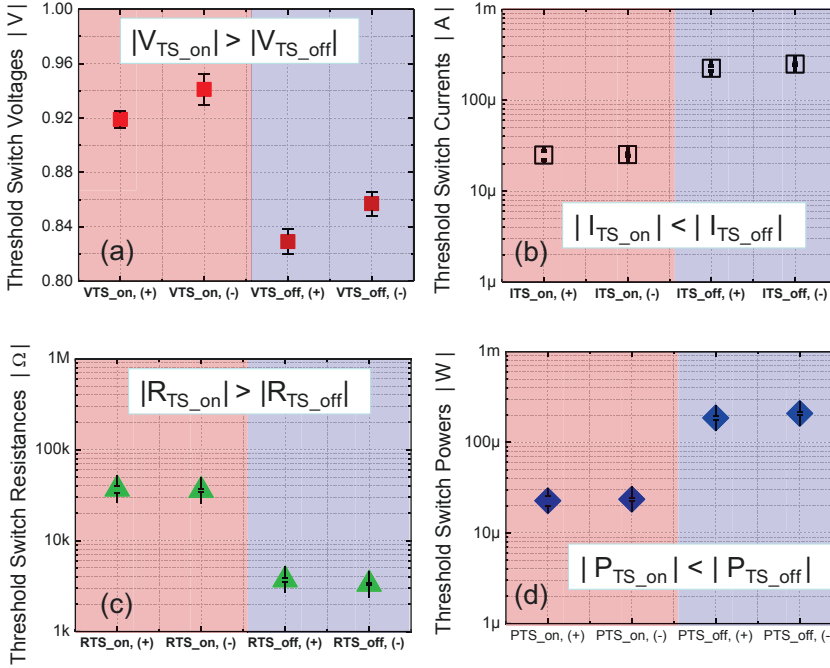


**Figure 7.11:** The statistical analysis of on- and off-states in  $\text{NbO}_2$  – based ITS switching devices: (a) threshold voltages (b) threshold currents (c) threshold resistance and (d) threshold switching power values.

proposed in previous studies. This led to the proposal of an alternative threshold switching ‘mechanism’ (see Fig. 7.11 (d)). This model is based on an electronic field triggered thermal runaway (FTTR) effect [202] which considers the combination of moderate Joule heating and Poole Frenkle (PF) conduction mechanisms as responsible for the threshold switching behavior of  $\text{NbO}_2$  thin films rather than the formerly assumed IMT effect.

### 7.3.3. SPICE simulation based on (1TS+1MS) devices

Figure 7.12 (a) depicts the equivalent circuit used in the SPICE simulation. The device model is marked by a question mark. As discussed in the previous section 7.2, a serial connection of a 1TS and 1MS element is considered as a good approximation for the  $\text{NbO}_x$  device. In Fig. 7.12 (b) the resulting circuit model consisting of a non-volatile switching element (IMS, Fig. 7.12 (c)) and a volatile switching element (ITS, Fig. 7.12 (d)) is shown. Both models are implemented using hysteretic switching elements and

non-linear current sources which are available in SPICE OPUS as basic building blocks [196].

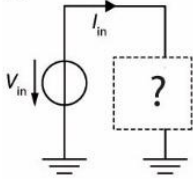
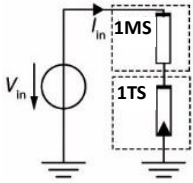
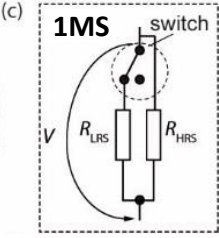
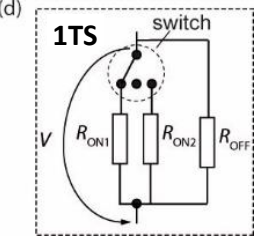
In SPICE OPUS, a voltage-controlled switching (model-type ‘SW’), which is a four terminal device, can be used for this purpose. By selecting the same voltage nodes for the control and for the actual switch, a two terminal device can be emulated. For simulation, an appropriate hysteretic switch model is needed. In the ‘SW’- model four parameters need to be defined: the offset voltage ( $VT$ ), the hysteresis voltage ( $VH$ ), the resistance when the switch is closed ( $R_{ON}$ ) and the resistance when the switch is open ( $R_{OFF}$ ). For the model the following definition is given:  $R_{ON} = R_{LRS}$  and  $R_{OFF} = R_{HRS}$ . The hysteresis voltage  $VH$  can be calculated from the arithmetic average of  $|V_{SET}|$  and  $|V_{RESET}|$  [197]:

$$VH = \frac{|V_{SET}| + |V_{RESET}|}{2} \quad (7.2)$$

If  $|V_{SET}| = |V_{RESET}|$ , a non-zero offset voltage  $VT$  is needed to shift the actual threshold values to  $V_{SET}$  and  $V_{RESET}$ , respectively.  $VT$  is calculated like [197]

$$VT = \frac{|V_{SET}| - |V_{RESET}|}{2} \quad (7.3)$$

The threshold voltages and curve shapes are fitted to match the measured data as shown in Fig. 7.13. The simulation proves that a series connection of a 1TS and a 1MS element is a valid approach to explain the observed characteristics. Moreover, independent simulations of the 1TS behavior (see Fig. 7.13 (b)) and the 1MS behavior (see Fig. 7.13 (c)) are also enabled from the experimental data. One should note that the parameters extracted from the fitting of the simple devices shown in Fig. 7.13 (b) and (c), respectively, differ considerable from those used in the SPICE model (see Fig. 7.12, left column). This is due to the abrupt switching model used for the 1MS SPICE simulation which doesn’t reproduce the gradual reset process correctly (see Fig. 7.13 (c))

Device types	Parameters and equations
<p>(a)</p>  <p>(b)</p>  <p>(c)</p>  <p>(d)</p> 	<p><b>(1MS+1TS) hybrid Switching</b></p> <p><b>1MS</b></p> <p>LRS: <math>I = V / (2500 \text{ Ohm})</math></p> <p>HRS: <math>I = 1.755 \mu\text{A} \times \sinh(V \times 1.788 \text{ V}^{-1})</math></p> <p>Switch LRS branch: <math>V_T = 0.2 \text{ V}</math> <math>V_H = 1.15 \text{ V}</math></p> <p><b>1TS</b></p> <p>ON1: <math>I = V / (1000 \text{ Ohm})</math> [Current deviced by 1RS anyway]</p> <p>ON2: <math>I = V / (1000 \text{ Ohm})</math> [Current deviced by 1RS anyway]</p> <p>OFF: <math>I = 0.8102 \mu\text{A} \times \sinh(V \times 3.846 \text{ V}^{-1})</math></p> <p>Switch ON1 positive branch: <math>V_T = 0.5 \text{ V}</math> <math>V_H = -0.28</math> (controlled by V)</p> <p>Switch ON2 negative branch: <math>V_T = 0.5 \text{ V}</math> <math>V_H = -0.4</math> (controlled by -V)</p> <p><b>1MS Memory switching</b></p> <p>LRS: <math>I = 0.715 \mu\text{A} \times \sinh(V \times 7.165 \text{ V}^{-1})</math></p> <p>HRS: <math>I = 1.46 \mu\text{A} \times \sinh(V \times 1.788 \text{ V}^{-1})</math> for <math>V &gt; 0</math></p> <p><math>0.6529 \mu\text{A} \times \sinh(V \times 2.6 \text{ V}^{-1}) + 3.077 \text{e-}18 \times \sinh(V \times 18 \text{ V}^{-1})</math> for <math>V &lt; 0</math></p> <p>Switch LRS path: <math>V_T = 0.47 \text{ V}</math> <math>V_H = 1.45 \text{ V}</math></p> <p><b>1TS Threshold switching</b></p> <p>ON1: <math>I = -0.00432 \times V^2 + 0.009719 \times V - 0.004852</math> for <math>V &gt; 0</math></p> <p>ON2: <math>I = 0.003315 \times V^2 + 0.007668 \times V + 0.003773</math> for <math>V &lt; 0</math></p> <p>OFF: <math>I = 0.6428 \mu\text{A} \times \sinh(V \times 4.508 \text{ V}^{-1})</math></p> <p>Switch ON1 positive branch: <math>V_T = 0.875 \text{ V}</math> <math>V_H = -0.04</math> (controlled by V)</p> <p>Switch ON2 negative branch: <math>V_T = 0.8375 \text{ V}</math> <math>V_H = 0.0425</math> (controlled by -V)</p>

**Figure 7.12:** Left side column: (a) Equivalent circuit model for arbitrary devices. (b) Equivalent circuit model for (1TS+1MS). (c) SPICE model of 1MS. (d) SPICE model of 1TS. Right side column: Equation and parameters used to simulate the 1TS+1MS, 1MS and 1TS devices.

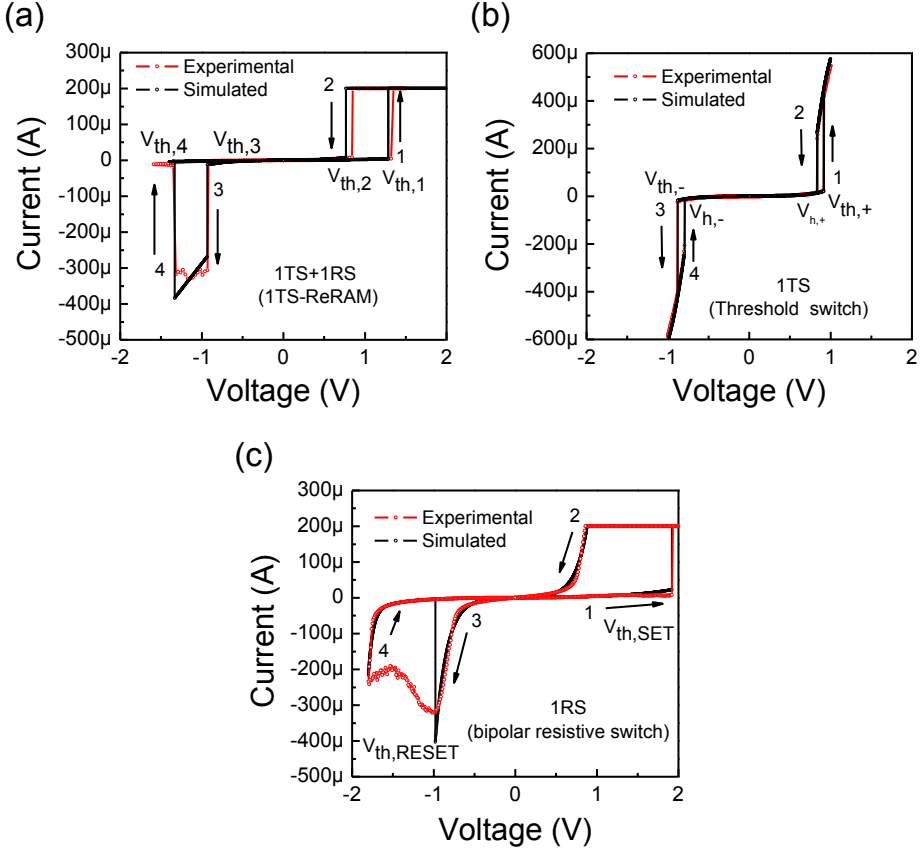


**Figure 7.13:** Measured ( $I$ - $V$ ) sweeps of the  $\text{Pt}/\text{NbO}_x/\text{Ti}/\text{Pt}$  nanocrossbar devices (red curves) and simulation results obtained from the SPICE model (black curves) for different states of the switching device. The arrows indicate the cycling direction for the voltage signal applied to the (Ti/Pt) electrode. (a) ( $I$ - $V$ ) curve representing the possible (1TS+1RS) characteristic at  $I_{CC} = 200 \mu\text{A}$ ; (b) ( $I$ - $V$ ) curve for a typical 1TS switching behaviour (with 1RS staying the LRS); and (c) ( $I$ - $V$ ) curve for a typical 1RS switching behaviour.

#### 7.3.4. Current-controlled negative differential resistance (CC-NDR)

Current controlled negative differential resistance (CC-NDR), also known as S-NDR due to the S-like shape of the current-voltage characteristics, was observed in TS-type switching  $\text{NbO}_x$  based devices if an additional resistor was put in series with the switching cell. As it is discussed in the monography of Dearnaley [118] several physical phenomena can cause a CC-NDR behavior, like for example Joule heating, semi-permanent space charge limited distribution and phase change or atomic rearrangement of

the host insulator. The current-controlled negative differential resistance effects was initially found in chalcogenide semiconductors and has already been reported in the 1960's for electro-formed NbO<sub>2</sub> devices [199-122]. Electroforming-induced threshold switching has been reported for Nb<sub>2</sub>O<sub>5</sub> based thin film devices as well. These authors addressed this to an effect of sub-oxide formation, namely NbO<sub>2</sub> [108, 126]. The co-occurrence of S-type NDR and memristive behavior has been reported so far for a couple of intentionally grown bilayer structures involving NbO<sub>x</sub> [54,110,127,128]. The NDR behavior of NbO<sub>2</sub>-based thin film devices has been explained by a model considering the temperature-controlled growth and shrinkage of the radius of the metallic phase of an IMT-type filament. The model explains in the metal-Nb<sub>2</sub>O<sub>5</sub>-metal stack after electroforming step the behavior of the IMT filament. At the threshold voltage  $V_{TS\_on}$ , first, a small conducting channel is formed in the centre of the filament due to Joule heating, while the strength of the IMT filament depends on the amount of heat caused by the current flow through the filament. The resistance of the device is therefore mainly determined by the radius of the conducting part of the filament. The gradual increment in the applied voltage permits a higher current flow through the conductive filament which increases the conducting path of the filament. The enlargement of the conducting channel in the filament leads to a lower overall resistance. This explains the change in the resistance before and after change in the current at a given variation of the applied voltage which is described by

$$\Delta R_i = \frac{\Delta U_i}{\Delta I_i} \quad (7.4)$$

This expression provides a conceivable explanation of the negative differential resistance, where a smaller resistance is attained for a higher current. The difference in the voltage must be negative  $\Delta U_i < 0$  with increasing current,  $\Delta I_i > 0$ , because of the decreasing resistance. This model is purely based on the IMT approach. In contrast, in the FTTR-model an additional serial resistance has to be added to the (1TS+1MS) in order to obtain CC-NDR behavior. The equivalent circuit shown in the Fig 7.14 (a) contains the serial resistance and the (1TS+1MS) cell. In consequence, the applied voltage  $V_{app}$  is different from the voltage over the (1TS+1MS) device defined as  $V_D$ . The overall requirement is that the resistance decreases for an increasing current and henceforth for a rising temperature. The resulting resistance change must be sufficient to lower the voltage drop  $V_D$  across the cell irrespective of a rise of  $V_{app}$ . The remaining voltage drops at the additional serial resistance. As given in equation 7.4 the voltage difference must be

negative for negative values of the resistance change. Therefore, the combination of Joule heating and current flow through the filament gives rise to the CC-NDR effect. To observe NDR-type behavior it is important that the series resistor fits to the (1TS+IMS) element. If this resistor is chosen too large, the CC-NDR behavior would be suppressed due a too low total current.

CC-NDR occurs in NbO<sub>2</sub> when during threshold switching the device turns from its high resistance 1TS<sub>off\_state</sub> to the low resistance state 1TS<sub>on\_state</sub>. Fig.7.14 (b) shows a current voltage curve obtained by putting a serial resistance of 2.2 k $\Omega$  in addition to the device under test to measure the CC-NDR behavior in the 10 nm thick amorphous Nb<sub>2</sub>O<sub>5</sub>-based single nano-crossbar devices of 55  $\times$  55 nm<sup>2</sup>. The memory resistance is set to 4 k $\Omega$  which is the 1MS<sub>LRS</sub> of the (1TS+IMS) cell. After successful electro-forming and RESET process an S-type NDR  $I$ - $V$  behavior was observed for a maximum applied voltage of  $V_{app}$  = +1.2 V at a step voltage of 5 mV and a hold time of 10 ms without any current compliance.

After switching into 1TS<sub>on</sub> the device enters into the regime controlled by the metallic phase and exhibiting an unstable positive feedback effect due to the formation of a metallic conducting filament [130]. Joule heating and therefore the current are the reason

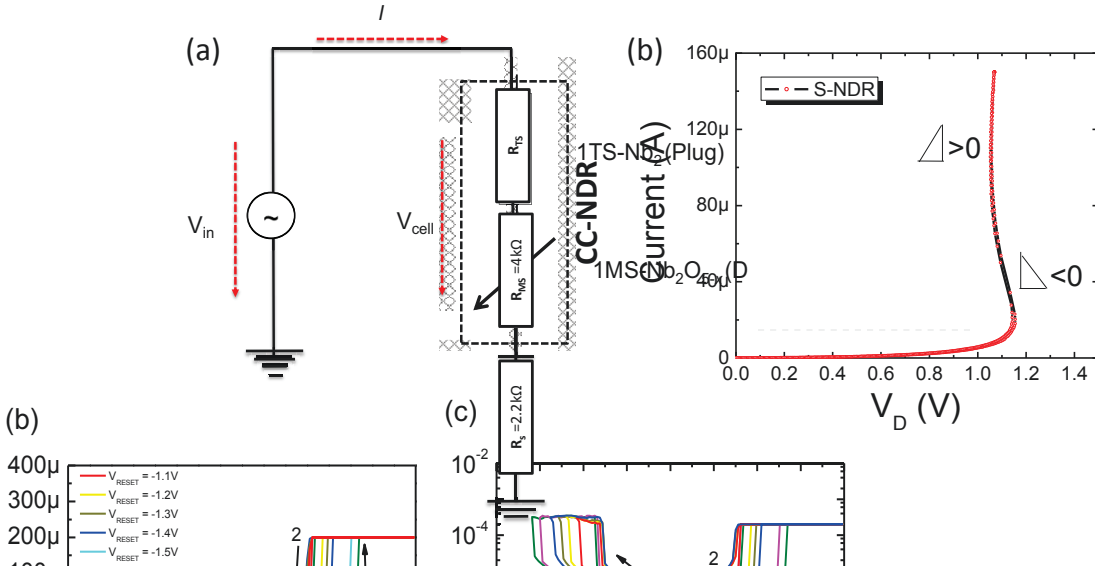


**Figure 7.14:** (a) A schematic of the electrical equivalent circuit diagram of the CC-NDR set up and (b) measured CC-NDR ( $I$ - $V$ ) curve simulated by the thermal runaway model (FTTR) assuming a serial resistance of 2.2 k $\Omega$ . The decrease of resistance with increasing current is caused by Joule heating.

for the resistance fall according to FTTR model.  $T_{MT}$  of the plug (NbO<sub>2</sub>) shows a lower increase. On the other hand very low serial resistance enables a very fast increase in temperature of the plug by the thermal runaway. The sudden jump in switching based on the thermal runaway confines the resistance states due to a slower heat up. At the point when the thermal runaway occurs the increase of current in the process is slowed down by the serial resistance.

### 7.3.5. Current Controlled Switching

Figures 7.15 (a) and (b) illustrate the linear and semi log  $I$ - $V$  graphs of (1TS+1MS) switching characteristics under different current compliances, this is, 100  $\mu$ A, 150  $\mu$ A, 200  $\mu$ A, 250  $\mu$ A, 300  $\mu$ A, 400  $\mu$ A, and 450  $\mu$ A. The voltage signal was changed in steps of 5 mV at a hold time of 10 ms between amplitudes  $V_{applied} = +2$  V and  $V_{RESET\_stop} = -1.6$  V applied to the top electrode. The  $55 \times 55$  nm<sup>2</sup> Nb<sub>2</sub>O<sub>5</sub> device demonstrates the typical (1TS+1MS) switching behavior for all current compliances. The  $V_{MS\_on}$  and  $I_{MS\_on}$  (1MS switching into on state) are discovered to be independent of the value of the given current compliance as clearly demonstrated in Fig. 7.16 (a). This is an indication that the (1TS+1MS) phenomenon is driven by the electric field rather than by the electric power in accordance with the FTTR model [202]. All switching relevant voltages,  $V_{MS\_SET}$  and  $V_{MS\_RESET}$  (1MS memory switching at  $V_{th\ 1, SET} < V_{th\ 4, RESET}$ ) as well as  $V_{TS\_off,(+)}$  and  $V_{TS\_off,(-)}$  (1TS threshold switch voltages at  $V_{th\ 2, TS}$  and  $V_{th\ 3, TS}$ ) are found to be rather independent of the current compliance values applied during SET, see Fig. 7.16 (c). Although device states programmed by different current compliances share similar  $I_{MS\_HRS}$  or  $I_{MS\_off}$  there is a quite a consistent trend for the  $I_{MS\_LRS}$  against different current compliances at  $V_{read} = -1.0$  V as shown in Fig. 7.16 (b). An increase of the current compliance by a factor of four results in an increase of the  $I_{off\_state}$  at least by one order of magnitude. This induces an increase of the memory window for higher current compliances. It is assumed that during SET process oxygen vacancies move from oxygen deficient part of filament Nb<sub>2</sub>O<sub>5-x</sub> (plug) and are attracted towards the disc as has been described in section. 7.3. The controllable factor in the case of current controlled  $I_{CC}$  resistive switching is the density of oxygen vacancies  $V_{\bullet\bullet}^{\bullet}$  [141]. Upon increasing the current compliance  $I_{CC}$  the device starts switching at a critical electric field and the conductive filament starts to enlarge until and unless it reaches to the applied current compliance.

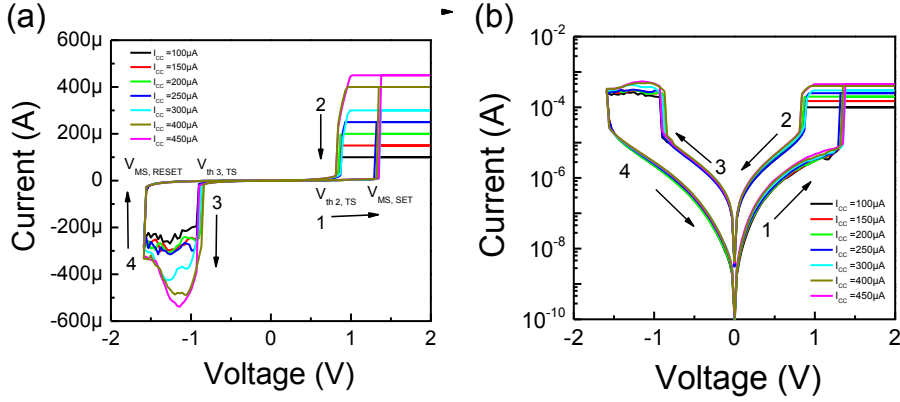


**Figure 7.15:** (a) Linear and (b) semi (log I-V) sweeps of the (ITS+IMS) cells after electro-forming and RESET process at different current compliances  $I_{CC}$  varied between 100  $\mu\text{A}$  and 400  $\mu\text{A}$ , in steps of 50  $\mu\text{A}$  of single crossbar areas of about  $55 \times 55 \text{ nm}^2$ .

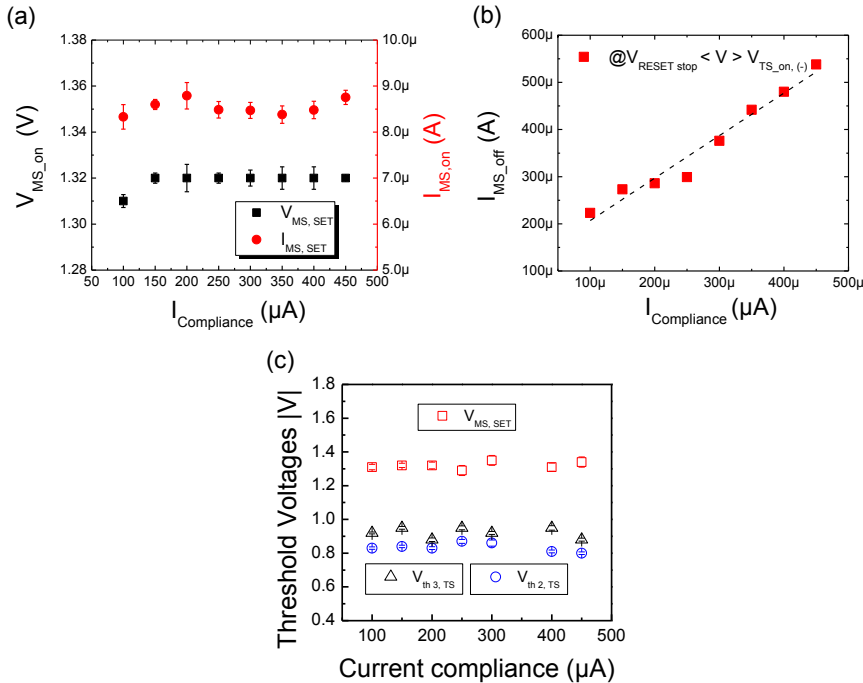


**Figure 7.16:** Characteristic voltages for the (ITS+IMS) curves shown in Fig. 7.15; (a)  $V_{MS, on}$ ,  $I_{MS, on}$  showing no trends against different current compliances whereas (b)  $I_{MS, off}$  showing linear correlation with respect to different current compliances and (c) the threshold switching ITS voltages are independent of the current compliance values.



## 7.4 Area dependency

The effect of the device size on (1TS+1MS) devices was evaluated by varying the area of the cross-point junction for the ALD grown  $\sim 10$  nm thick Nb<sub>2</sub>O<sub>5</sub> based devices and determining the dependence on the switching voltages and resistance values. The graph in Fig. 7.17 (a) encompasses the semi (log  $I$ - $V$ ) switching sweeps of four different device sizes, i.e.,  $0.00302 \mu\text{m}^2$ ,  $0.00502 \mu\text{m}^2$ ,  $0.0081 \mu\text{m}^2$ , and  $0.0144 \mu\text{m}^2$ . For all measurements the conditions are kept same for the cause of comparison, i.e.,  $V_{\text{appl}} = +2$  V,  $V_{\text{RESET\_stop}} = -1.6$  V and  $I_{\text{CC}} = 200 \mu\text{A}$ . As demonstrated in Fig. 7.17 (b) no significant effect of the area variation can be observed on the threshold switching voltages ( $V_{\text{th } 2, \text{TS}}$  (green dots) and  $V_{\text{th } 3, \text{TS}}$  (blue dots)) as well as on the memory switching voltages ( $V_{\text{th } 1, \text{SET}}$  (red dots) and  $V_{\text{th } 4, \text{RESET}}$  (black dots)) of the (1TS+1MS) devices. Devices with all different areas switched approximately at the same voltages independent of switching

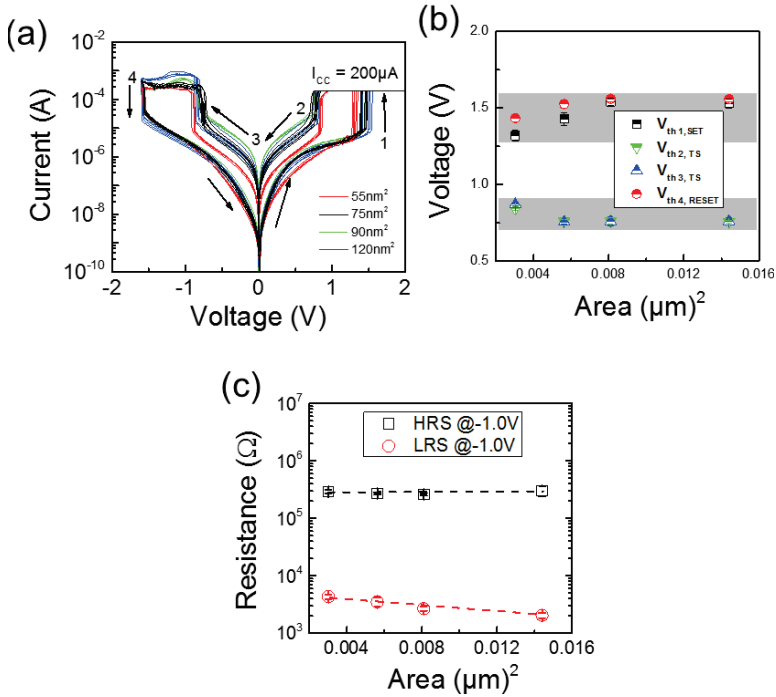


**Figure 7.17:** (a) The  $I$ - $V$  sweeps of the (1TS+1MS) cells of different crossbar areas of about  $0.00302 \mu\text{m}^2$ ,  $0.00502 \mu\text{m}^2$ ,  $0.0081 \mu\text{m}^2$ , and  $0.0144 \mu\text{m}^2$  after electro-forming and RESET process at current compliance of  $I_{\text{CC}} = 200 \mu\text{A}$ . (b) Area dependence of the switching voltages and (c) of the resistance values,  $R_{\text{OFF}}$  and  $R_{\text{ON}}$

area. The variations in the switching voltages against device area are addressed as total number of defects in the switching films [30]. The very slight variations in the switching voltages with respect to device area in Nb<sub>2</sub>O<sub>5</sub> thin film is an indication of low number of defects due to the high quality of the film. Fig. 7.17 (c) comprises the mean values of HRS (black symbols) and LRS (red symbols) for the four different device areas at read voltage of  $V_{read} = -1.0$  V of the single Nb<sub>2</sub>O<sub>5</sub> based nano-crossbar devices. Rather constant resistance values are obtained for all device areas. The resistance ratio  $R_{OFF}/R_{ON} \sim 65$  independent of device area is an indication of filamentary-type resistance switching.

## 7.5 Nanodiffraction of a Nb<sub>2</sub>O<sub>5</sub> nano-crossbar device

To investigate the structural impact of external electrical stimuli, electron nanodiffraction analysis has been carried out on a focused ion beam (FIB) lamella cut from a Pt/Nb<sub>2</sub>O<sub>5</sub>/Ti/Pt nano-crossbar device of lateral dimension of about 90×90 nm<sup>2</sup>. The analysis presented in this section was performed by Manuel Bornhöft at the Ernst Ruska Centre of Forschungszentrum Juelich GmbH and RWTH Aachen University. As has been described in section 7.1.1 the as built Pt/amorphous Nb<sub>2</sub>O<sub>5</sub>/Ti/Pt cells are initially highly insulating, while an electro-forming and subsequent reset process brings the devices into the (1TS+1MS) resistive switching state. This modification in the resistance is governed by the formation of the conductive filament associated with physical changes in the structures of the switching materials [146]. It is generally accepted that the enhanced conductivity after electroforming is caused by the formation of a metallic conducting filament built from the metal oxide host material either by a high density of oxygen vacancies or by the formation of new oxygen-deficient phases [147-151]. For the cells based on ALD grown amorphous Nb<sub>2</sub>O<sub>5</sub> thin films the filament formation during electroforming and reset is proposed to be accompanied by phase formation and phase separation in order to enable the proposed switching mechanism described in section 7.2.2. In detail, the coexistence of memristive 1MS and threshold switching 1TS might indicate the existence of a layer of reduced Nb<sub>2</sub>O<sub>5</sub>, i.e., Nb<sub>2</sub>O<sub>5-x</sub> (disc/ memristive switching part) and a layer of NbO<sub>2</sub> (plug/ threshold switching part). The FIB lamella was specially cut around a nano-crossbar cell that has been electro-formed and RESET by applying voltages of  $V_F = +3.0$  V and  $V_{RESET\_stop} = -1.6$  V, respectively, to the Ti/Pt top electrode, as shown in Fig. 7.18 (a), (b).

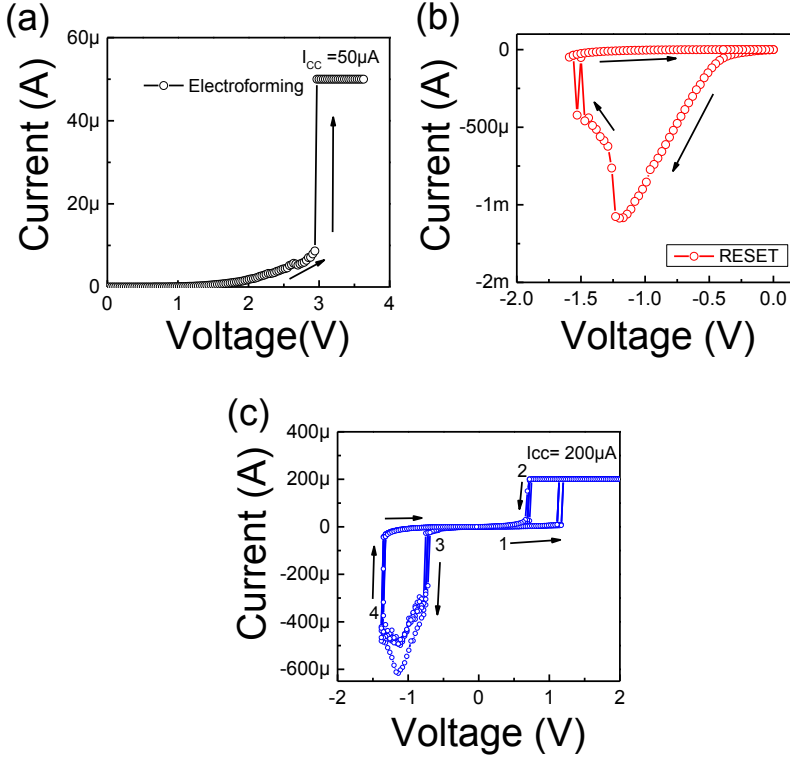


**Figure 7.18:** The electrical properties of the FIB cut Pt/Nb<sub>2</sub>O<sub>5</sub>/Ti/Pt nano-crossbar device of size  $\sim 90 \times 90 \text{ nm}^2$  later characterized by transmission electron diffraction; (a) positive polarity electroforming into the ON-state, (b) 1<sup>st</sup> RESET and (c) (I-V) sweep revealing the (1TS+1MS) behavior measured for  $I_{CC} = 200 \mu A$ .

Subsequently, the device is switched quasi- static with a current compliance of  $I_{CC} = 200 \mu A$  (see Fig. 7.18(c)) by applying  $V_{appl} = +1.2 \text{ V}$  and  $V_{RESET\_stop} = -1.6 \text{ V}$ , respectively. The exact device which showed the characteristic (1TS+1MS)-type switching was cut from the wafer and was investigated by nanodiffraction to uncover the origin behind this co-occurrence of (1MS+1TS) behavior.

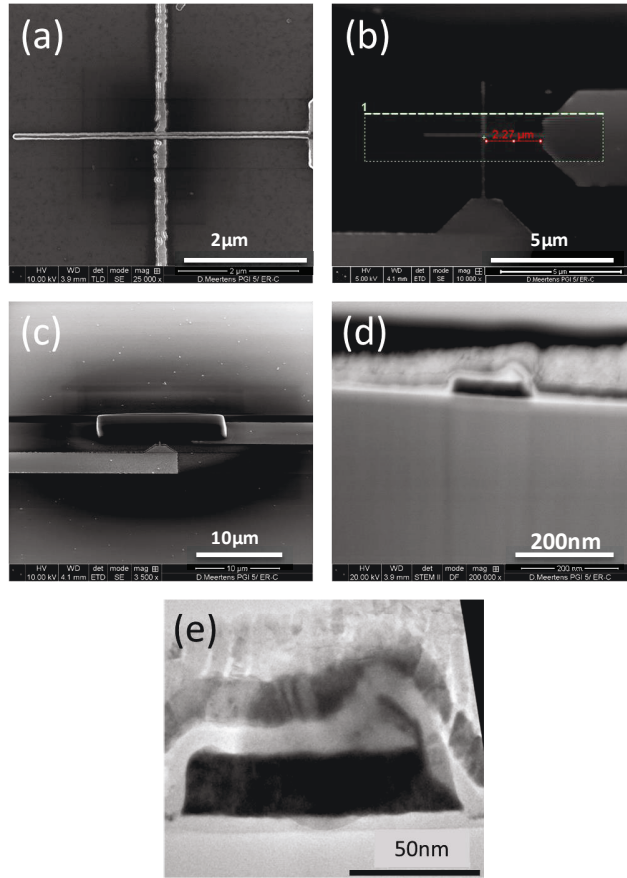


**Figure 7.19:** FIB cut preparation performed before the nanodiffraction: (a) Selection of the nano-crossbar device of  $90 \times 90 \text{ nm}^2$  in size after electroforming and switching; (b) determination of the to be prepared area along the top electrode before cutting (c) deposition of amorphous carbon followed by Pt deposition in close proximity to the prepared area for drilling the holes; (d) the STEM lamella is polished and thinned to the interesting area for investigation; (e) TEM image of the final intended cross section.

The FIB-cutting was performed by Mrs. D. Meertens from Ernst Ruska Center for Electron Microscopy at the Forschungszentrum Jülich (ER-C). For cross-sectional STEM (scanning transmission electron microscope) a very thin lamella is needed. For this purpose a lamella was cut of the bulk along the top electrode Ti/Pt line of the crossbar device by FIB using Ga<sup>+</sup> ions. During the FIB preparation SEM images were acquired by a FEI Helios Nanolab 400s instrument using accelerating voltage of 30kV in dual beam configuration.

The FIB-cut process is shown in Fig. 7.19 and the steps are as follow:

- ❖ Identification of the appropriate electroformed and switched nano-crossbar device of size  $\sim 90 \times 90 \text{ nm}^2$  by SEM, Fig. 7.19 (a)
- ❖ Marking of the cutting area along the top electrode Ti/Pt of the nano-crossbar device before starting the FIB-cutting, Fig. 7.19 (b)
- ❖ Deposition of the first amorphous carbon layer on the area that needs to be inspected by cross-sectional STEM and immediately after Pt deposition to avoid the damages during Ga<sup>+</sup> ion milling, Fig. 7.19 (c)
- ❖ Polishing and thinning the lamella for achieving close proximity of the interesting area for investigation, Fig. 7.19 (d)
- ❖ TEM image of the FIB-cut device after final polishing, Fig. 7.19 (e)

### **7.5.1. Nanodiffraction analysis**

After preparing the FIB-cut the TEM lamella is studied by scanning transmission electron microscopy for nanodiffraction analysis. Nanodiffraction is used to get nanometer scale information of the phase of materials. For the STEM technique the dedicated FEI (Company) Titan transmission electron microscope (TEM) is used in microprobe mode. In this mode there is no aberration correction and small convergence angles are possible to achieve a parallel beam. This enables the collection of “normal “diffraction” patterns. In this technique the sample is investigated by a coherent and parallel electron probe in the nanometer scale.

This is in contrast to the normal STEM, which is executed with a convergent beam. The coherent and parallel illumination enables us to image the diffraction patterns of probe size around 2 nm with a convergence angle of around 0.35 mrad (angle given by the machine, not measured). The annular dark field (DF) detector in microprobe mode is calibrated on a gold cross grating. The CCD camera is calibrated by a silicon  $\langle 111 \rangle$  sample. Si lamella with  $[111]$  zone axis was used as a standard for the diffraction pattern. After calibrations for nanodiffraction analysis four different areas of interest of a nanocross bar device are chosen for the cause of comparison between the analyses as shown in Fig. 7.20. The cross sectional images of the device obtained by using the TEM detector are marked by numbers 1, 2, 3 and 4. The inset in Fig.7.20 shows the TEM cross sectional image of the nanocross bar device with the stack sequence. Out of four areas,

area\_1 covers the  $\text{Nb}_2\text{O}_5$  on  $\text{SiO}_2$  ( $\text{SiO}_2/\text{Nb}_2\text{O}_5$ ) surface in a certain distance from the bottom electrode (electrically non-treated area of the device). In contrast, areas 2 to 4 contain the  $\text{Nb}_2\text{O}_5$  film on top of the Pt bottom electrode ( $\text{Pt}/\text{Nb}_2\text{O}_5$ ) (electrically treated area sandwiched between top and bottom electrode). All analyzed areas are marked by red rectangular boxes as shown in the upper picture of Fig.7.20.

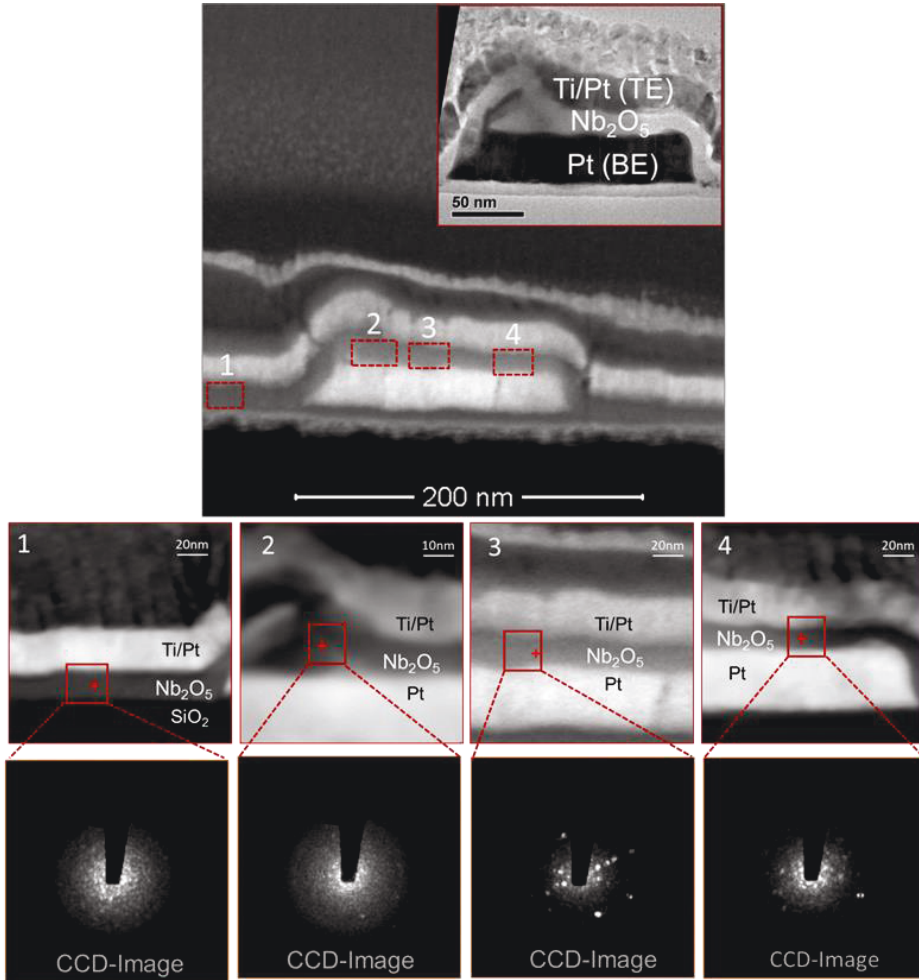


**Figure 7.20:** Top row shows the FIB cross section with STEM image in the inset of the  $90 \times 90 \text{ nm}^2$  single crossbar device after electrical treatment. The middle row depicts from 1-4 the different areas under investigation and the bottom row shows the selected area diffraction of the corresponding areas.

In area\_1 the Nb<sub>2</sub>O<sub>5</sub> film grown on SiO<sub>2</sub> appears to be amorphous as shown by the diffraction pattern obtained by CCD below the figure of area\_1. Likewise, in area\_2 and area\_4 the Nb<sub>2</sub>O<sub>5</sub> film appears to be amorphous even though these areas are parts of the switched cross-point area. Interestingly, the nanodiffraction pattern taken from area\_3 revealed diffraction spots originating from crystalline oxide material. The crystalline phase is analysed from a Fourier transform of the reflection spots shown in Fig.7.21 where the red dots mark the reflexes of a crystalline phase. This crystalline phase most likely appears to be tetragonal NbO<sub>2</sub> measured along <110> direction which is confirmed by the interatomic distance of about ~ 3.42 Å along the string between Nb-Nb [152-154]. After nanodiffraction analysis it could be assumed that the appearance of threshold switching along with bipolar switching is due to the existence of a small area of NbO<sub>2</sub> after electro-forming.

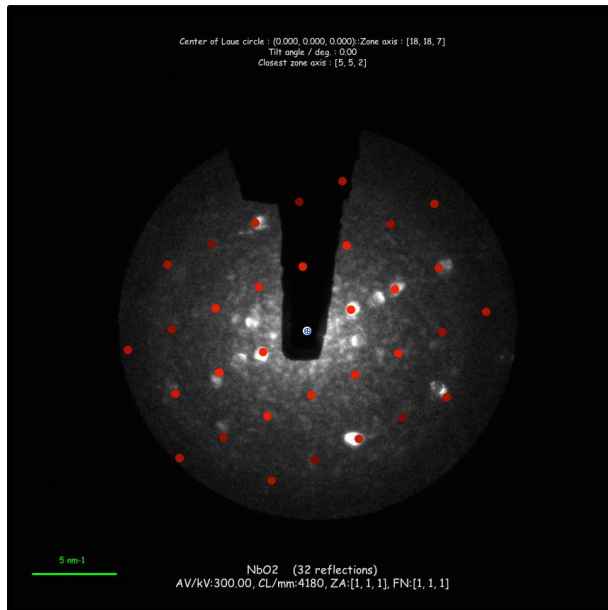


**Figure 7.21:** The CCD image of the STEM after nanodiffraction analysis shows the crystal structure of the NbO<sub>2</sub>. After detailed analysis and fitting, the NbO<sub>2</sub> nanocrystals found to be tetragonal in nature.

## 7.6 Summary

In this chapter as grown ALD grown Nb<sub>2</sub>O<sub>5</sub> were integrated into nanocross bar devices sandwiched between asymmetric electrodes (Pt as BE and Ti/Pt as TE) for further investigation of the electrical properties of the material. Thus after successful electro-forming and reset process which is necessary for resistive switching operation, a combined threshold- and bipolar-type resistive switching (1TS+1MS) was observed. The coexisting of both threshold and bipolar switching phenomenon in a single thin film of Nb<sub>2</sub>O<sub>5</sub> was interpreted by the proposal of a certain volume of NbO<sub>2</sub> which is a threshold-type switching material and Nb<sub>2</sub>O<sub>5-x</sub> which is an n-type semiconductor material that shows memristive behavior. As grown ALD Nb<sub>2</sub>O<sub>5</sub> thin films were reported stoichiometric in the prior chapter. Therefore, it is assumed that phases of lower oxygen to niobium content were created during the electro-forming and 1<sup>st</sup> reset process. Hence the combination of electrical stimuli and local heating enabled the change of the stoichiometry during the electro-forming. This presumably led to the local formation of NbO<sub>2</sub> phase as a consequence of local oxidation and reduction (redox) process in Pt/Nb<sub>2</sub>O<sub>5</sub>/Ti/Pt stack as was confirmed by nanodiffraction analysis. After electro-forming the *I-V* characteristics under both positive and negative polarities at different regimes of switching were illustrated by considering both sub oxides being electrically in series. The switching in NbO<sub>2</sub>/Nb<sub>2</sub>O<sub>5-x</sub> stack follows the FTTR model in which the combination of moderate temperature and intrinsic polaron hopping based on Pool Frenkel (PF) like barrier lowering caused threshold and memory type switching. The current and voltage dependences of the (1TS+1MS) curves and the area-independency of the switching behavior are interpreted as a direct proof for VCM-type filamentary resistive switching taking place in the Pt/Nb<sub>2</sub>O<sub>5</sub>/Ti/Pt devices.



---

---

## 8. Applications of (1TS+1MS)-type Nb<sub>2</sub>O<sub>5</sub> Devices

---

This chapter deals with the application of the ALD Nb<sub>2</sub>O<sub>5</sub> based crossbar devices. Amorphous Nb<sub>2</sub>O<sub>5</sub> thin films of about 10 nm thickness were integrated into nano-crossbar devices with lateral dimensions to 55×55 nm<sup>2</sup>. Using these cells with stack sequence of Pt/Nb<sub>2</sub>O<sub>5</sub>/Ti/Pt, the switching operation of such (1TS+1MS)-type device is studied in respect of properties required for passive crossbar array-based non-volatile applications.

### 8.1 Write and read operations of (1TS+1MS) devices

For the (1TS+1MS) type devices, the write operation is similar to the bipolar-type resistive switching devices, while the read operation is different. Basically for the read-out of the memory window, a level read scheme is used which is explained below.

#### 1.1 Write operation

From the quasi-static  $I$ - $V$  characteristics of Pt/Nb<sub>2</sub>O<sub>5</sub>/Ti/Pt nanocross bar cell of 55×55 nm<sup>2</sup> a procedure can be presumed which permits the use of these hybrid type devices as storage memory cells. All the possible memory states of the hybrid-type devices constituting from voltage divider configurations are summarized in table 8.1. As listed in the table, state (1MS<sub>LRS</sub> + 1TS<sub>off\_on</sub>) is assigned as storing state '1' and state (1MS<sub>HRS</sub> + 1TS<sub>off\_off</sub>) to '0'. Writing these two states requires voltages of  $V_{write\_0} < V_{th, 4}$  and  $V_{write\_1} > V_{th, 2}$  for 'write 0' and 'write 1', respectively. In Fig. 8.1, the required write voltage levels essential for writing the device to '0' and '1', respectively, are marked. For the device under test, the exact values are  $V_{write\_0} = -1.40$  V and  $V_{write\_1} = +1.49$  V. At low voltages the overall resistance of the (1TS+1MS)-type cells is always high; whatever the storage state of the device is, i.e. '0' or '1'. For voltages  $|V_{app}| < 0.6$  V the relation holds:

$$R_{(1TS+1MS)} \approx R_{1TS, off\_state} \quad (8.1)$$

---

## 2.1 Read operation

For read-out of the memory states of the hybrid-type (1TS+1MS) device, a different read scheme is needed as compared to single bipolar resistive switching cells. This is due to the intended fact that the (1TS+1MS) devices are always in their high resistive state at read voltage. For bipolar resistive switching devices with this clear resistance window the respective states are usually read at small read voltage either for positive or negative polarity. Unlike the bipolar resistive switching devices, the state of the hybrid-type (1TS+1MS) can only be read if the threshold element is in the on-state (1TS<sub>on-state</sub>). This defines the read voltage regimes of the (1TS+1MS) cell which, according to Fig. 8.1, are defined as  $V_{th,2} < V_{read} < V_{th,1}$  or  $V_{th,3} < V_{read} < V_{th,4}$  for positive as well as for negative polarity, respectively. For the exact Pt/Nb<sub>2</sub>O<sub>5</sub>/Ti/Pt of nanocross bar device shown in Fig. 8.1 the actual resistance values at  $V_{read} = -1.2$  V are  $R_{HRS} = 352.9$  k $\Omega$  (green dot) and  $R_{LRS} = 3.8$  k $\Omega$  (blue dot). This provides a sufficient memory window of about  $\frac{R_{HRS}}{R_{LRS}} = 91$ .

The switching stability of the (1TS+1MS) device was tested by a voltage pulsed switching mode as shown in Fig. 8.2 (a). In the pulsing regime the 55×55 nm<sup>2</sup> Pt/Nb<sub>2</sub>O<sub>5</sub>/Ti/Pt nano-crossbar device showed stable switching for at least 30×10<sup>3</sup> pulses with a memory window ( $R_{off}/R_{on}$ ) of about 75 which allows a stable ReRAM memory operation. The pulse length of 200  $\mu$ s was applied for  $V_{SET-Pulse} = +2$  V and  $V_{RESET-Pulse} = -1.6$  V with a current compliance of about 200  $\mu$ A and the signal applied to the top electrode. The applied pulse scheme is given below in Fig. 8.2 (a). The state of the device was read by applying a negative read out pulse of  $V_{read-Pulse} = -1$  V after every  $V_{SET-Pulse}$  and  $V_{RESET-Pulse}$ , respectively. The read out of the (1TS+1MS) device was found to be non-destructive for voltages in the regime  $V_{th3,TS} < V_{read-Pulse} < V_{th4,RESET}$  estimated from quasi-static  $I$ - $V$  curves. In case, if  $V_{read-out Pulse}$  is larger than the  $V_{th4,RESET}$ , the device always tends to switch-off, no matter about the state of the device after  $V_{SET Pulse}$  described in the next section. Additionally, externally triggered variations in the 1MS HRS and LRS could be observed which make the (1TS+1MS) cells applicable for multi-level resistive switching applications [143-145] as shown in Fig. 8.3. An increase in the RESET stop biasing from -1.1 V to -1.6 V results in an increased 1MS<sub>HRS</sub> by at least one order of magnitude as shown in Fig. 8.3 (a). In contrast, increasing in the current compliance (see Fig. 8.3 (b)) results in a change from a smaller to a larger conductive filament diameter which manifests in a lower 1MS<sub>LRS</sub> state [142].

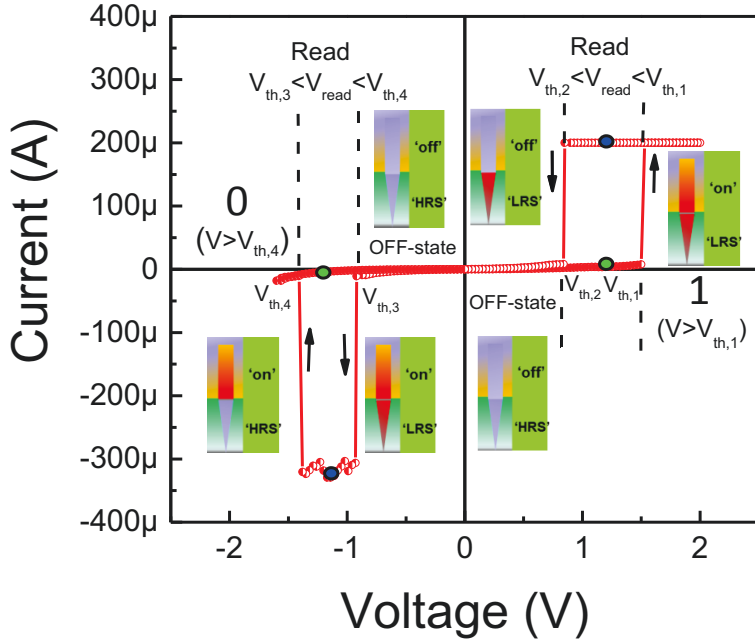


**Figure 8.1:** *I-V sweep of the (ITS+1MS) device depicting the possible read and write voltage levels. The arrows indicate the direction of switching and possible memory and volatile states with respect to the voltage applied on the top electrode.*

**Table 8.1:** *Possible states of the (ITS+1MS) hybrid-type Pt/Nb<sub>2</sub>O<sub>5</sub>/Ti/Pt device*

Over all device status	Memory element (IMS)	Threshold switch (ITS)	(ITS+IMS)
High	HRS	Metal	OFF
High	LRS	Insulator	OFF
High	HRS	Insulator	0
Low	LRS	Metal	1

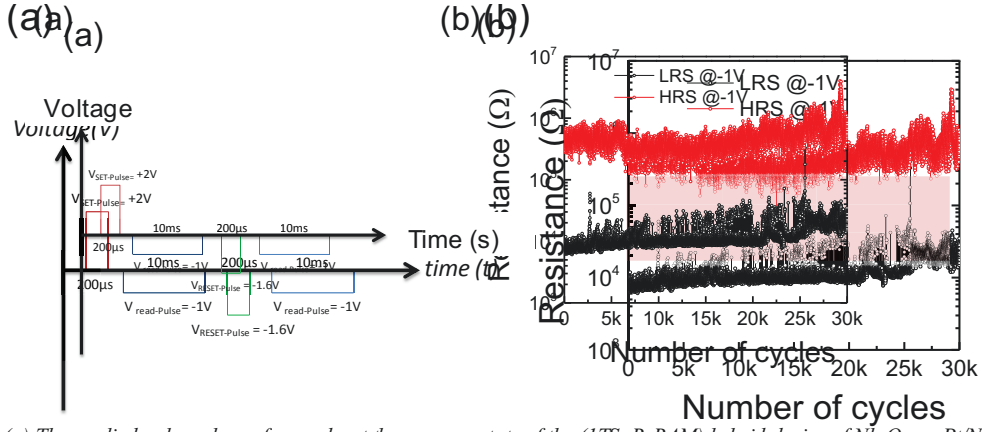


**Fig. 8.6:** (a) The applied pulse scheme for read-out the memory state of the (1TS\_ReRAM) hybrid device of Nb<sub>2</sub>O<sub>5</sub> on Pt/Nb<sub>2</sub>O<sub>5</sub>/Ti/Pt

**Figure 8.2:** (a) The applied pulse scheme for read-out the memory state of a (1TS+1MS) hybrid device of Pt/Nb<sub>2</sub>O<sub>5</sub>/Ti/Pt 55×55 nm<sup>2</sup> nano-crossbar device. (b) A representative endurance measurement of the (1TS+1MS) cell read @ -1.0 V showing cycling stability up to 30×10<sup>3</sup>.

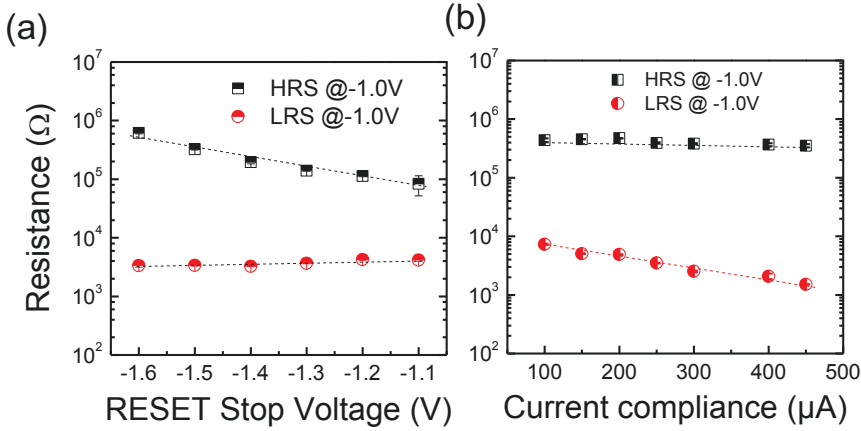


**Figure 8.3:** Variation of HRS and LRS values as a function of (a) the RESET stop voltage and (b) the current compliance. HRS and LRS values vary by about 1 order of magnitude for variation (a) and (b), respectively.

## 8.2 LRS-non-linearity in (1TS+1MS) nano-crossbar devices

Redox-based resistive switching memories (ReRAM) are considered highly attractive candidates for realization of future ultra high dense passive crossbar memories to satisfy the demands of increasing memory density [165,166]. However, the building of large-scale ReRAM arrays could lead to sneak path currents (unwanted parasitic currents) that cause read failures for a particular cell [167]. To overcome this issue, a selector device is required that introduces selectivity by its highly non-linear current voltage characteristic. The approach guaranteeing highest integration density is the combination of a bipolar rectifying selector device, such as tunneling diode or Schottky diode, together the memory device in the same crossbar junction [51,168-170]. An issue for the mentioned types of devices is about the current density requirements for the bipolar rectifying selectors. Therefore, alternative selector-less approaches are also discussed comprising complementary resistive switching (CRS) devices and ReRAM devices offering an intrinsic non-linearity or threshold switching behavior [171-175, 49, 53]. The sneak-current reduction is essential for the built-up of passive crossbar arrays from RERAM devices and for this purpose a high non-linearity of the current in LRS is decisive for the final size of the addressable crossbar array. Fig. 8.4 (a) shows a cross bar arrays which is

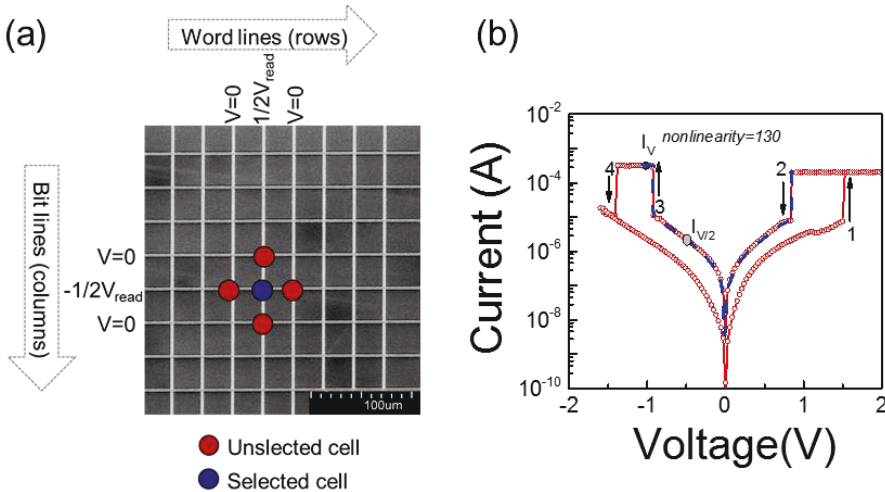


**Figure 8.4:** (a) Schematic illustration showing the half-select scheme for a crossbar array for selected and unselected cells. (b) The switching loop of a Pt/Nb<sub>2</sub>O<sub>5</sub>/Ti/Pt 55×55 nm<sup>2</sup> crossbar device, showing high nonlinearity of the I-V behavior in LRS.

---

utilized to discuss of the integration potential of the (1TS+1MS) Nb<sub>2</sub>O<sub>5</sub>-based cells fabricated in this work. Fig. 8.4 (b) shows a characteristic semi-log  $I$ - $V$  switching loop obtained by applying +2 V to the top electrode and -1.6 V to the bottom electrodes for a compliance current of 200  $\mu$ A. Quantitatively, the non-linearity can be defined as the ratio of the current level at voltage  $V$  to the one for  $V/2$  (or  $V/3$ ), adopted from [175], whereas  $V$  could be the read or write voltage. Hence the quantitative expression for the non-linearity factor  $NL$  is written as:

$$NL: = \frac{I_V}{I_{V/2}} \quad \text{or} \quad (8.2)$$

$$NL: = \frac{I_V}{I_{V/3}}$$

First, we consider the non-linearity scheme of half-select. Definition (8.2) yields a non-linearity factor of about 130 for the (1TS+1MS) Nb<sub>2</sub>O<sub>5</sub>-based device under test. This value is higher as  $NL$  values of IMT-based devices described in earlier reports [175]. The importance of the  $I_{V/2}$  value is illustrated in Fig 8.4 (a). For a half-read or -write scheme a signal of  $V/2$  is applied to the word line and a signal  $-V/2$  to the bit line of the selected cell shown by the blue dot. In total, the voltage drop across the cell is equal to  $V$ . Parallel to the selected cell, the unselected cells (red dots) which share the same row and column electrodes also experience a voltage drop of  $V/2$ . These unselected cells are usually called half-selected cells in crossbar arrays and sneak currents are unintentionally flowing through these half-selected cells which are a big obstacle for the practical size of the crossbar arrays. In the Pt/Nb<sub>2</sub>O<sub>5</sub>/Ti/Pt nano-crossbar devices the current levels detected at  $V_{read} = -1.0$  V and  $V/2_{read} = -0.5$  V were -307  $\mu$ A and -2.3  $\mu$ A, respectively, resulting in a value of the  $NL$ -factor of about 130. This inherent non-linearity could enable passive crossbar-array integration with up to approximately 1000 rows and columns. To test the leakage current stability at half read out voltage  $V_{read-out}/2 = -0.5$  V the device was switched in pulse mode with the same scheme as described in section 8.2. The currents of half-read-out and full read out at  $V = -1$  V are compared for a switching performed at  $V_{SET-Pulse} = +2$  V and  $V_{RESET-Pulse} = -1.6$  V for a pulse length of 200  $\mu$ s. A clear leakage current suppression in the range of two orders of magnitude for the LRS state of the device was found for half read out voltage as compared to full read out voltage, as shown in Fig. 8.5.

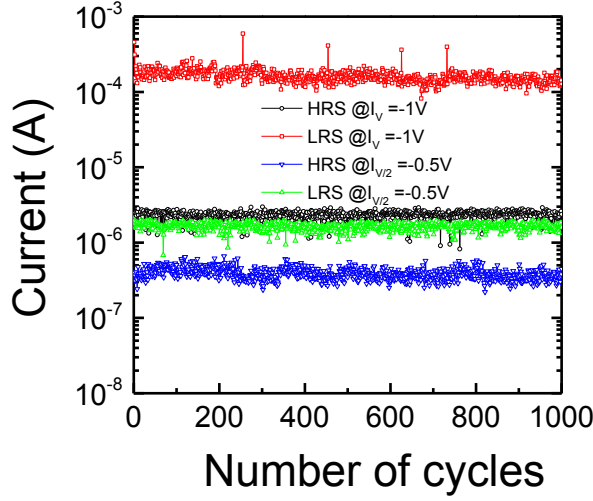


**Figure 8.5:** The full read out signal measured at  $-1\text{ V}$  compared to the half read at  $-0.5\text{ V}$  showing the memory window and the suppression of the leakage in LRS. Hence the LRS is found to be approximately equal to the HRS of the  $\text{Pt/Nb}_2\text{O}_5/\text{Ti/Pt } 55 \times 55\text{ nm}^2$  crossbar device demonstrating the huge  $I$ - $V$  nonlinearity of the LRS.

### 8.3 Constraints for (1TS+1MS)-based crossbar-arrays

The major advantage of a (1TS+1MS) type device over the single bipolar type resistive switching devices is the inhibition of sneak paths as described in the section 8.2. Therefore these devices have potential for integration into larger passive crossbar arrays. The major benefit of using the (1TS+1MS) elements/cells ensues due to the fact the cells are always in high resistive state under low voltages. Let us now consider a worst case scenario, in which a crossbar array stores the identical type of information and for read out operation the cell in the middle of the array has to be addressed. Fig. 8.6 depicts the sketch of a passive crossbar array to illustrate this property. In Case\_1 the cell of interest is in the '0' state (marked as blue cell) while in Case\_2 the cell is in the LRS state (marked as green cell). A low resistive state (LRS) can only be detected if the '1' state has been there prior to the application of the read out voltage, as described in the section 8.2.2. Thus, a large current is only present when reading a '1' state (thick red line in Case\_2) as compared to reading a '0' state due to the fact that  $\text{1MS}_{\text{LRS state}}$  and  $\text{1TS}_{\text{on state}}$  (metallic) for the hybrid type (1TS+1MS) based crossbar arrays are present. Since all non-accessed cells in the crossbar array are either in the '0' state or in the '1' state (marked as blue



cells), in which are highly resistive, sneak path currents are reduced (thin red line). The difference of currents between Case\_1 and Case\_2 is large which makes the state recognition rather straight forward compared to crossbar arrays built from normal BRS-based cells. However, (1TS+1MS) based crossbar arrays has one important restraint, which is the voltage scheme needed to prevent non-accessed cells from switching. For (1TS+1MS) it is important that voltages at all non-accessed cells are limited to values below the threshold voltage  $V_{th, 1}$  and  $V_{th, 3}$ , respectively. To achieve this  $1/3V$  voltage scheme is needed for the write operation. This results from the fact that a voltage larger than  $V_{th, 1}$  is needed for the write-operation. For the level read, either a  $1/2V$  voltage scheme or a  $1/3V$  scheme can be applied. As in the case of symmetrical 1RS elements, a  $1/2V$  voltage scheme is also applicable for the write operation but with very low voltage margins [197]. If all non-accessed cells have the same resistance (which is HRS\_state) the voltage drop at each cell is  $1/3V$  and hence no switching occurs at those cells. Thus, non-accessed rows and columns can remain on floating potential.

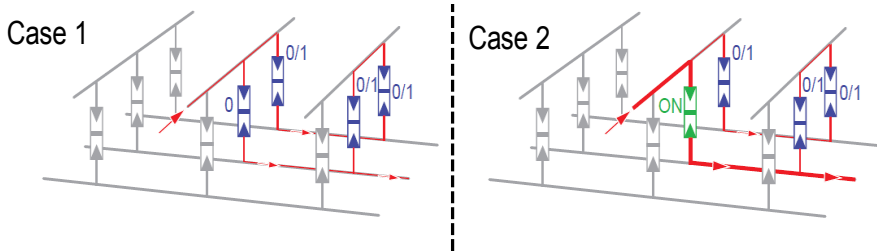


**Figure 8.6:** Sneak current pathes in (1TS+1MS)-based arrays. The cell in the middle is either in state '0' (Case 1) or in state '1'/'0' (Case 2). Reprinted with the permission [197]

---

## 8.4 Achievable size for a (1TS+1MS) based crossbar array

The major advantage of using the (1TS+1MS) cells in passive cross bar arrays is their capability for the prevention of sneak paths issues as has been described in the prior section. To understand this issue let us consider a passive crossbar which stores the same digital information (worst case pattern) made of (1TS+1MS) based cells. When reading the word (one row) the assessable normalized read voltage margin  $\Delta V/V_{pu}$  is an important parameter.  $\Delta V$  means the change in  $V_{out}$  sensed at the pull-up resistor  $R_{pu}$ , where  $V_{pu}$  is the supply voltage. The output voltage  $V_{out}$  results from the voltage divider with a cell which is defined by  $R_{1TS+1MS}$ . Let us consider an array consisting of  $N$  columns and  $M$  rows. For simplification it is considered  $N = M$  in the calculations. For a better contrast, an array is considered that keeps the same digital information, known as worst-case pattern, represented by a high-resistive element being surrounded by low-resistive elements. This means for (1TS+1MS) cells at worst, only those cells that are in one column are in LRS if reading a complete word. For those types of patterns the corresponding circuit model can be simplified to a four resistor matrix as shown in Fig. 8.7 with  $N$  = number of columns and  $M$  = number of rows. One element/cell (the upper left) is considered to be toggled between state '0' and state 'ON', respectively. For (1TS+1MS) based arrays this means  $R_{(1TS+1MS)} = R_{state\_0or1}$  or  $R_{(1TS+1MS)} = R_{ON}$ . For all  $(N - 1)$  non-considered elements, the column which is read is then assumed to be low-resistive, represented by the lower left element. Similarly, all  $(M - 1)$  elements in the row of the considered element are represented by the upper right element. The lower right element represents all other  $(N - 1) \cdot (M - 1)$  matrix elements which are high-resistive. In contrast to BRS arrays as described by Linn *et al.* [197], only these cells in the accessed column can be low-resistive (state 'ON'), whereby all other cells are high-resistive ( $R_{state\_0or1}$ ). For the minimum output voltage swing, the output voltage  $V_{out}$  for both storage states must be considered. All bit lines are pulled up, which was found to be advantageous for reading [197]. The equivalent circuit model of such a (1TS+1MS) based crossbar array is shown in Fig. 8.8 (a), which can be simplified to Fig. 8.8 (b) when considering reading the upper left element  $R_{1TS+1MS}$ . The derivation is done for a (1TS+1MS) array based on the BRS as described in [197], but due to the same structure, results can be directly re-allocated to (1TS+1MS) arrays. In the first calculation step, a star-mesh transformation is required, ensuing in the circuit model shown in Fig. 8.8 (c).

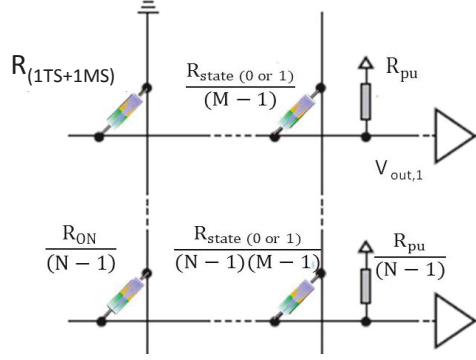


**Figure 8.7:** Reduced (1TS+1MS) based crossbar array cut down into a four resistor matrix with  $N$  columns and  $M$  rows. Reprinted with the permission [197]

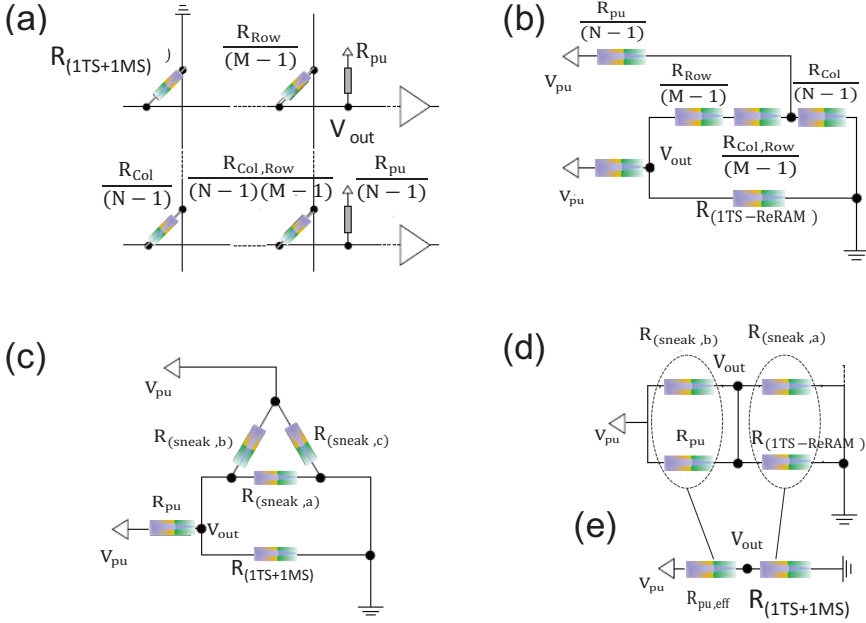


**Figure 8.8:** (a) Equivalent (1TS+1MS) based array for the worst-case scenario. (b) The circuit can be amended for circuit analysis. (c) New circuit representation after star-mesh transformation. (d) By reshuffling of elements, circuit analysis is cut down. (e) For simplified equivalent circuit, parallel resistances are combined. Reprinted with the permission [197]

The detailed calculations for  $R_{\text{sneak},a}$  and  $R_{\text{sneak},b}$  can be found in [197], while  $R_{\text{sneak},c}$  is not needed for the calculation. For calculation of  $V_{\text{out}}$  the resistances of the parallel resistors  $R_{\text{sneak},a}$  and  $R_{1\text{TS}+1\text{MS}}$  as well as  $R_{\text{sneak},b}$  and  $R_{\text{pu}}$  are desirable (compare Fig. 8.8 (c), (d), (e)):

$$R_{1\text{TS}+1\text{MS}} = \frac{R_{\text{sneak},a} \cdot R_{1\text{TS}+1\text{MS}}}{R_{\text{sneak},a} + R_{1\text{TS}+1\text{MS}}} \quad (8.3)$$

$$R_{\text{pu,eff}} = \frac{R_{\text{sneak},b} \cdot R_{\text{pu}}}{R_{\text{sneak},b} + R_{\text{pu}}} \quad (8.4)$$

The corresponding voltage divider for (1TS+1MS) leads to the following expression:

$$V_{\text{out}} = \frac{R_{1\text{TS}+1\text{MS},\text{sense}}}{R_{1\text{TS}+1\text{MS},\text{sense}} + R_{\text{pu,eff}}} \cdot V_{\text{pu}} \quad (8.5)$$

The normalized voltage swing for (1TS+1MS) based passive crossbar can then be calculated:

$$\frac{\Delta V_{\text{out}}}{V_{\text{pu}}} = \frac{R_{\text{state}_0,\text{sense}}}{R_{\text{state}_0,\text{sense}} + R_{\text{pu,eff}}} - \frac{R_{\text{ON},\text{sense}}}{R_{\text{ON},\text{sense}} + R_{\text{pu,eff}}} \quad (8.6)$$

To calculate the minimum possible normalized voltage swing, two different worst-case scenarios are considered for (1TS+1MS) based arrays. For  $R_{1\text{TS}+1\text{MS}} = R_{\text{state}_0}$  all other elements are in '1' state for reading state '0'. This corresponds to  $R_{\text{Row}} = R_{\text{Col, Row}} = R_{\text{state}_1}$  and  $R_{\text{Col}} = R_{\text{ON}}$  (Fig. 8.8 a). In the worst-case for reading an element in 'ON' state ( $R_{1\text{TS\_ReRAM}} = R_{\text{ON}}$ ), all other elements are in state '0'. In Fig. 8.8 (a), this corresponds to  $R_{\text{Row}} = R_{\text{Col}} = R_{\text{Col, Row}} = R_{\text{state}_0}/3$ . So, since patterns are different for reading  $R_{\text{state}_0}$  and  $R_{\text{ON}}$ ,  $R_{\text{sneak},a}$  (see equation (8.3)) and  $R_{\text{sneak},b}$  (see equation (8.4)) differ, too. Therefore, one has to deal with two different effective pull-up resistances  $R_{\text{pu, eff, state}_0}$  and  $R_{\text{pu, eff, ON}}$  which are state-dependent, accordingly. The non-accessed cells in the columns can either be in state '0' or state '1', but have no effect on the voltage swing. The minimum normalized voltage swing for (1TS+1MS) based passive crossbar can be calculated using:

$$\frac{\Delta V_{\text{out}}}{V_{\text{pu}}} = \frac{R_{\text{state}_0,\text{sense}}}{R_{\text{state}_0,\text{sense}} + R_{\text{pu,eff,state}_0}} - \frac{R_{\text{ON},\text{sense}}}{R_{\text{ON},\text{sense}} + R_{\text{pu,eff,ON}}} \quad (8.7)$$

The voltage margin, and with this the maximum array size, depends strongly on the non-linearity factor. In Fig. 8.9 (a) the non-linearity is extracted from  $I$ - $V$  sweeps of the Pt/Nb<sub>2</sub>O<sub>5</sub>/Ti/Pt single nano-crossbar device of about 55×55 nm<sup>2</sup>. For the level read, a 1/3V scheme is applied for reading a (1TS+1MS) cell. For a rule of thumb ( $R_{\text{state}_0}/R_{\text{ON}})/3$

is the figure of merit for (1TS+1MS) type devices which gives  $10^3$  for minimum normalized voltage swing by assuming  $(0.1 \cdot \frac{\Delta V_{out}}{V_{pu}})$  as minimum voltage margin shown in Fig. 8.9 (b).

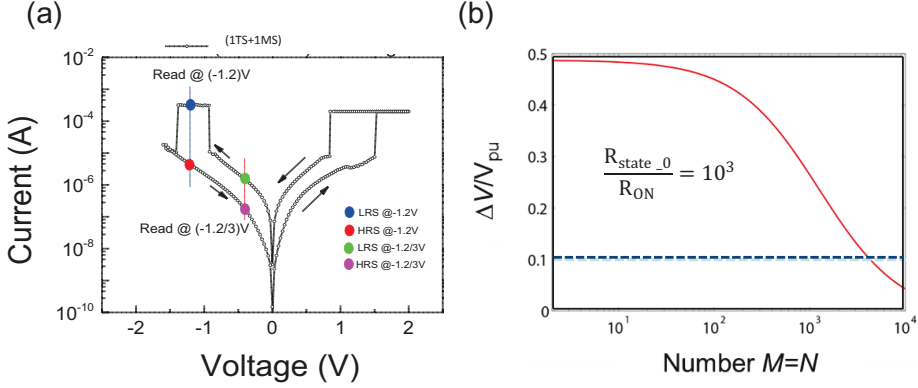


**Figure 8.9:** (I-V) sweep of a (1TS+1MS) based single crossbar device used for the reading at the 1/3V scheme. (b) Minimum normalized voltage swing assuming the  $(0.1 \cdot \frac{\Delta V_{out}}{V_{pu}})$  minimum voltage margin for the (1TS+1MS) cell with  $N$  columns and  $M$  rows, where  $M=N$ .

## 8.5 Summary

In this chapter the applicability of (1TS+1MS) cells towards the non-volatile memory applications was described. The read and write schemes of (1TS+1MS) memory cells based on  $\text{Nb}_2\text{O}_5$  for different threshold switching voltages for negative and positive polarities were discussed. Implementations of (1TS+1MS) cells into high-density  $4F^2$  passive crossbar arrays were described, focusing on the addressing of defined cells residing inside high-density crossbar arrays. Issues of LRS non-linearity are discussed with respect to reading the cells at one half or one third read schemes. The possible crossbar array which could be realized by using (1TS+1MS) cells was computed by assessing a normalized read voltage margin  $\Delta V/V_{pu}$ . The maximum size was found in the range of  $10^3$  for equal numbers of rows and columns.

---

## 9. Summary and Outlook

---

This chapter summarizes the results obtained for resistance switching memory devices built from sub-10 nm thin atomic layer deposited ternary ( $\text{Sr}_x\text{Ti}_y\text{O}_z$ ) and binary ( $\text{Nb}_2\text{O}_5$ ) oxide thin films. The focus of the work was on the evaluation of the effect of the cation ratio in the ternary oxide  $\text{Sr}_x\text{Ti}_y\text{O}_z$  grown by supercycle control during atomic layer deposition and of the cation to anion ratio in the binary oxide  $\text{Nb}_2\text{O}_5$  including the stability of the as-deposited amorphous  $\text{Nb}_2\text{O}_5$  phase under influence of high electric field and high current during electroforming and resistive switching cycles.

### 9.1 Resistive switching in ALD grown $\text{Sr}_x\text{Ti}_y\text{O}_z$ thin films

The resistive switching properties of Pt/STO/TiN devices from plasma assisted ALD grown  $\text{Sr}_{1+x}\text{Ti}_{1+y}\text{O}_{3+(x+2y)}$  thin films of various compositions by using the supercycle ALD process were investigated. Metastable perovskite-type STO films were grown on Pt coated silicon substrates by ALD at 350 °C using cyclopentadienyl-based metal precursors and oxygen plasma as the respective sources, followed by a subsequent annealing at 600°C in  $\text{N}_2$ . STO films of 15 nm and 12 nm thickness and with three different compositions ( $[\text{Sr}]/([\text{Sr}]+[\text{Ti}])$ ) of 0.57 (Sr-rich), 0.50 (stoichiometric) and 0.46 (Ti-rich) were integrated into crossbar-devices with lateral dimensions varied from  $(10 \times 10) \mu\text{m}^2$  to  $(100 \times 100) \text{nm}^2$ . Nano-structural characterizations by means of SEM and LC-AFM methods revealed a significant influence of the STO cation composition on the crystallization behavior and, thus, on the resulting morphologies of the ALD films. Local defects in the films' microstructure dominantly affect the leakage current behavior of pristine MOM cells and their soft-breakdown or electroforming voltages. For cell sizes larger than  $1 \mu\text{m}^2$  the HRS state of the switching filament is affected by residual conductivity of non-filamentary cell area. The polarity dependence of the RS curves and the area-independent LRS values serve as a direct proof of VCM-type filamentary resistive switching taking place at the Pt/STO interface of the countereigthwise switching Pt/STO/TiN devices. Once the microstructural effects of

---

the polycrystalline thin films have been assessed, a clear effect of the STO composition on the RS behavior was observed. Nanocross bar devices from stoichiometric STO films could be switched at lowest voltages of about 1.0 V between the lowest LRS of  $R_{ON} \approx 40$  k $\Omega$ , and reasonable HRS values of  $R_{OFF} \approx 1$  M $\Omega$  determined at +0.3 V. Non-stoichiometry in the ALD STO films, either Ti- or Sr-excess, both predominantly increase the  $R_{ON}$  values, i.e. result in LRS of lower conductance.

## 9.2 Resistive switching in ALD grown Nb<sub>2</sub>O<sub>5</sub> thin films

The resistive switching properties of Nb<sub>2</sub>O<sub>5</sub> based devices obtained from thermal ALD providing stoichiometric Nb<sub>2</sub>O<sub>5</sub> thin films were interrogated. The ALD Nb<sub>2</sub>O<sub>5</sub> thin films of about 10 nm were grown from a <sup>t</sup>BuN=Nb (NMe<sub>t</sub>)<sub>3</sub> precursor which was evaporated at 55 °C into a hot-wall flow type F-120 ALD reactor. Ozone (O<sub>3</sub>) was used as an oxygen source with a concentration of 100 g/m<sup>3</sup>. The structural and chemical analysis of as grown thin film Nb<sub>2</sub>O<sub>5</sub> on planar Si/SiO<sub>2</sub>/Ti/Pt substrate revealed that the films were amorphous. The films become reduced after heating up to 600 °C in vacuum. The crystallization temperature of the thin films in O<sub>2</sub> and Ar atmosphere was found to be in the range of 600 °C and the crystallization was into orthorhombic phase. No extra peak related to any second phase beside Nb<sub>2</sub>O<sub>5</sub> was observed in XRD analysis showing that as-grown films were of stoichiometric composition. However, a reduction to non-stoichiometric NbO<sub>x</sub> phase was enabled by high temperature vacuum anneal at 600 °C. Local conductive atomic force microscopy (LC-AFM) measurements revealed the electronic transport properties of the NbO<sub>x</sub> film after vacuum annealing. The current map measured while scanning the surface with the AFM tip at room temperature exposed that grains were conductive in nature rather than the grain boundaries. Additionally, the films were integrated into micro- as well nano-crossbar devices for resistive switching applications. At the first glance the resistive switching properties were investigated for both symmetric (Pt/Nb<sub>2</sub>O<sub>5</sub>/Pt) and asymmetric (Pt/Nb<sub>2</sub>O<sub>5</sub>/Ti/Pt) electrode combinations. In the first case (symmetric electrodes) the devices showed initially very high resistive (*I-V*) characteristics. The devices were electroformed ( $\sim +4$  V) by applying the positive polarity on top electrode and then RESET with ( $\sim -2.5$  V). A high voltage bipolar resistive switching was observed with very low potential stability. To mitigate such high voltage and high currents the Ti metal layer as top electrode was introduced to act as an oxygen exchange layer. The insertion of a thinner Ti layer ( $\sim 2$  nm) in comparison of  $\sim 10$  nm

---

Nb<sub>2</sub>O<sub>5</sub> devices showed high power resistive switching but comparatively lower than for the symmetric electrode stack. The further insertion of Ti layer (~5nm) gave a completely different electrical picture. The devices showed another feature called threshold switching in combination with bipolar resistive switching. In the case of nano crossbar devices a minimum feature size of approximately (55 nm)<sup>2</sup> was investigated with stack sequence of Pt/Nb<sub>2</sub>O<sub>5</sub> (10nm) /Ti (5nm)/Pt. The combination introduced the resistive switch and threshold switch (1TS+1MS) in a single oxide layered nano-crossbar MIM device. These crossbar devices showed a diode-like (*I-V*) characteristic in initial state which subsequently required electroforming and RESET process. After electroforming and successful RESET steps the devices showed S-type NDR (negative differential resistance) characteristics. The volatile-type bidirectional threshold switching (1TS) emerged with non-volatile-type memory switching (1MS) were predominantly observed in these type of devices. To understand the root cause of the combined threshold and resistive switch, analytically, the nano crossbar device of approximately 90×90 nm<sup>2</sup> was investigated after successful (1TS+1MS) switching by STEM (scanning transmission electron microscope) in nanodiffraction mode. The nanodiffraction analysis revealed the formation of a non-stoichiometric phase known as NbO<sub>2</sub> in form of tetragonal fashion. The NbO<sub>2</sub> is well known for insulator to metal transformation at 800°C. The mechanism of both threshold and memory switching in a single layer was explained imperially by considering both Nb<sub>2</sub>O<sub>5-x</sub> after reduction and NbO<sub>2</sub> due to Ti layer in series. The intrinsic Joule heating effect promotes phase separation and crystallization of tetragonal NbO<sub>2</sub> phase under certain conditions during the electroforming and reset steps. The NbO<sub>2</sub> plug formed locally enables selector functions to be integrated into the Nb<sub>2</sub>O<sub>x-5</sub> based bipolar redox-type resistive switching cell. Area independent resistive switching characteristics support a filamentary-type resistive switching behavior. The device under test for different current compliances and RESET stop biasing showed the potential for multilevel resistive switching in combination with threshold switching. Furthermore, an outlook towards the separation and toggling between “TS” and “MS” is provided and a possible destructive and non-destructive (1TS+1MS) read-out procedure is briefly discussed for memory applications. A very promising use of the (1TS+1MS) devices for passive cross bar arrays is the sneak path suppression through the non-accessed cells. The (1TS+1MS) showed very high potential for large number of cross bar arrays up to a limit of about  $M=N$  (*Rows= Columns*) ~ 1000 each.



---

In total, it is shown that the material control during ALD growth as well as during electroforming and 1<sup>st</sup> reset step is decisive to reproducibly obtain the desired film quality. The importance of cation stoichiometry as well as phase separation has been demonstrated.

## 9.3 Outlook

An important prerequisite for the future non-volatile memory technology is the enabling of fast read and write operations. For STO based cells of three different composition ( $[\text{Sr}]/([\text{Sr}]+[\text{Ti}])$  of 0.57 (Sr-rich), 0.50 (stoichiometric) and 0.46 (Ti-rich) integrated in crossbar devices the differences in switching kinetics and SET and RESET processes for different pulse lengths ranging from  $\mu\text{s}$  to ns need to be analysed for a deeper understanding. The advanced switching performance of stoichiometric STO against the non-stoichiometric (Sr or Ti rich STO) needs to be tested for nano-second pulses.

A threshold supported resistive switching element (1TS+1MS) utilizing amorphous  $\text{Nb}_2\text{O}_5$  thin films grown by ALD with excellent switching properties was found. The quasi-static analysis showed very promising results with reduced leakage current in the ON state. However, fast switching pulse experiments need to be done to evaluate the performance of the niobium oxide based (1TS+1MS) devices for future emerging memory applications. In addition, electrical characterisations should be performed under non-ambient conditions and for cells integrated into 3D via-hole type devices. These devices might conserve the heat locally enabling an enhanced long term stability and minimizing the drive current for the insulator to metal transition. It has been observed that accurate tuning of the electrical stimuli during electroforming and resistive switching facilitates the control of a fraction of volatile threshold and non-volatile memory switching niobium oxide phases in the crossbar cells. The volatile threshold switching alone can be used as a flip flop switch which could be a strong candidate for the replacement of high volume SRAM cells. The extension of finite element simulations for real devices will lead to a better understanding of the (1TS+1MS) devices which will enable to set-up design rules for optimized (1TS+1MS) device stacks.

## Bibliography

---

1. G. E. Moore. Cramming more components onto integrated circuits. *Electronics*, 38 (1965).
2. ITRS. The International Technology Roadmap for Semiconductors. - ITRS 2012 Edition. (2012).
3. R. Waser, R. Dittmann, M. Salina, M. Wuttig. The role of defects in resistively switching chalcogenides. *Int. J. Mat. Res.* Vol. 101, pp. 182-198 (2009)
4. J. J. Yang and R. S. Williams. Memristive Devices in Computing System. *Nat. Nanotechnol.*, Vol. 8, pp. 13-24 (2013)
5. D. S. Jeong, R. Thomas, R. S. Katiyar, J. F. Scott, H. Kohlstedt, A. Petraru; C. S. Hwang. Emerging memories: Resistive switching mechanisms and current status. *Rep. Prog. Phys.*, Vol. 75, pp. 76502/1- (2012).
6. ITRS-The International Technology Roadmap for Semiconductors. Edition 2012. <http://www.itrs.net/> (2012).
7. S. Yu, B. Gao, Z. Fang, H. Yu, J.F. Kang, and H.-S. P. Wong. A Low Energy Oxide-Based Electronic Synaptic Device for Neuromorphic Visual Systems with Tolerance to Device Variation. *Advanced Materials*, 25, 1774--1779 (2013).
8. R. Bruchhaus, R. Muenstermann, T. Menke, C. Hermes, F. Lentz, R. Weng, R. Dittmann, and R. Waser. Bipolar resistive switching in oxides: Mechanisms and scaling. *Current Applied Physics*, 11, E75-E78 (2011).
9. H.D. Lee, S.G. Kim, K. Cho, H. Hwang, H. Choi, J. Lee, S.H. Lee, H.J. Lee, J. Suh, S. Chung, Y.S. Kim, K.S. Kim, W.S. Nam, J.T. Cheong, J.T. Kim, S. Chae, E. Hwang, S. N. Park, Y.S. Sohn, C.G. Lee, H.S. Shin, K.J. Lee, K. Hong, H.G. Jeong, K.M. Rho, Y.K. Kim, S. Chung, J. Nickel, J.J. Yang, H.S. Cho, F. Perner, R.S. Williams, J.H. Lee: S.K. Park, and S. Hong. Integration of 4F2 selector-less crossbar array 2Mb ReRAM based on transition metal oxides for high density memory applications. *Digest of Technical Papers - Symposium on VLSI Technology*, *Digest of Technical Papers - Symposium on VLSI Technology*, 151-152 (2012).

10. R. Waser and M. Aono, 'Nanoionics-based resistive switching memories' *Nature Materials*, 6, 833-840 (2007).
11. K. Gopalakrishnan, R. S. Shenoy, C. T. Rettner, K. Virwani, D. S. Bethune, R. M. Shelby, G. W. Burr, A. Kellock, R. S. King, K. Nguyen, A. N. Bowers, M. Jurich, B. Jackson, A. M. Friz, T. Topuria, P. M. Rice, and B. N. Kurdi, 'Highly-Scalable Novel Access Device based on Mixed Ionic Electronic Conduction (MIEC) Materials for High Density Phase Change Memory (PCM) Arrays' *Symposium on VLSI Technology (VLSIT)*, Honolulu, HI, 2010 *Symposium On Vlsi Technology*, Tech. Dig., 205-206 (2010).
12. I. Valov, R. Waser, J. R. Jameson, and M. N. Kozicki, 'Electrochemical metallization memories-fundamentals, applications, prospects' *Nanotechnology*, 22, 254003/1-22 (2011).
13. R. Waser, R. Bruchhaus, and S. Menzel, 'Nanoelectronics and Information Technology (3rd edition)' *Wiley-VCH*, 683-710 (2012).
14. Y. Chen, B. Govoreanu, L. Goux, R. Degraeve, A. Fantini, G. Kar, D. Wouters, G. Groeseneken, J. Kittl, M. Jurczak, and L. Altimime, 'Balancing SET/RESET Pulse for >1010 Endurance in HfO<sub>2</sub> 1T1R Bipolar RRAM' *IEEE Transactions on Electron Devices*, 59, 3243-3249 (2012).
15. S. Stille, C. Lenser, R. Dittmann, A. Koehl, I. Krug, R. Muenstermann, J. Perlich, C. M. Schneider, U. Klemradt, and R. Waser, 'Detection of filament formation in forming-free resistive switching SrTiO<sub>3</sub> devices with Ti top electrodes' *Applied Physics Letters*, 100, 223503/1-4 (2012).
16. B. J. Choi, D. S. Jeong, S. K. Kim, C. Rohde, S. Choi, J. H. Oh, H. J. Kim, C. S. Hwang, K. Szot, R. Waser, B. Reichenberg, and S. Tiedke, 'Resistive switching mechanism of TiO<sub>2</sub> thin films grown by atomic-layer deposition' *Journal of Applied Physics*, USA, 98, 33715-1-10 (2005).
17. Ch. Walczyk, Ch. Wenger, R. Sohal, M. Lukosius, A. Fox, J. Dabrowski, D. Wolanski, B. Tillack, H.-J. Muessig, and T. Schroeder, 'Pulse-induced low power resistive switching in HfO<sub>2</sub> metal-insulator-metal diodes for nonvolatile memory applications' *J. Appl. Phys.* 105, 114103 (2009).
18. T. Sakamoto, K. Lister, N. Banno, T. Hasegawa, K. Terabe, and M. Aono, 'Electronic transport in Ta<sub>2</sub>O<sub>5</sub> resistive switch' *Applied Physics Letters*, 91, 92110/1-3 (2007).
19. Y. Li, S. Long, M. Zhang, Q. Liu, L. Shao, S. Zhang, Y. Wang, Q. Zuo, S. Liu, and M. Liu, 'Resistive Switching Properties of Au/ZrO(2)/Ag Structure for Low-Voltage Nonvolatile Memory Applications' *IEEE Electron Device Letters*, 31, 117-119 (2010).

20. S. Spiga, A. Lamperti, C. Wiemer, M. Perego, E. Cianci, G. Tallarida, H. L. Lu, M. Alia, F. G. Volpe, and M. Fanciulli. Resistance switching in amorphous and crystalline binary oxides grown by electron beam evaporation and atomic layer deposition. *Microelectronic Engineering*, 85, 2414-2419 (2008).
21. Y. Watanabe, J. G. Bednorz, A. Bietsch, Gerber-Ch, D. Widmer, A. Beck, and S. J. Wind. Current-driven insulator-conductor transition and nonvolatile memory in chromium-doped SrTiO<sub>3</sub> single crystals. *Applied Physics Letters*, USA, 78, 3738-40 (2001).
22. Chih-Yang Lin, Chen-Yu Wu, Chung-Yi Wu, Chenming Hu, and Tseung-Yuen Tseng. Bistable resistive switching in Al<sub>2</sub>O<sub>3</sub> memory thin films. *Journal of the Electrochemical Society*, 154, 189-192 (2007).
23. C. Schindler, S. C. P. Thermadam, R. Waser, and M. N. Kozicki. Bipolar and unipolar resistive switching in Cu-doped SiO<sub>2</sub>. *IEEE Transactions on Electron Devices*, 54, 2762-2768 (2007).
24. I. Kaerkaenen, A. Shkabko, M. Heikkila, J. Niinisto, M. Ritala, M. Leskela, S. Hoffmann-Eifert, and R. Waser. Study of atomic layer deposited ZrO<sub>2</sub> and ZrO<sub>2</sub>/TiO<sub>2</sub> films for resistive switching application. *Physica Status Solidi a-Applications and Materials Science*, 211, 301-309 (2014).
25. Sang. Chul. Oh, Ho. Yong. Jung, and Heon. Lee. Effect of the top electrode materials on the resistive switching characteristics of TiO<sub>2</sub> thin film. *Journal of Applied Physics*, 109, 124511/1- (2011).
26. Ying. Li, Gaoyang. Zhao, Jian. Su, Erfeng. Shen and Yang. Ren. Top electrode effects on resistive switching behavior in CuO thin films. *Applied Physics A: Materials Science and Processing*, 104, 1069-1073 (2011).
27. S.-Y. Wang, D.-Y. Lee, T.-Y. Tseng, and C.-Y. Lin. Effects of Ti top electrode thickness on the resistive switching behaviors of rf-sputtered ZrO<sub>2</sub> memory films. *Applied Physics Letters*, 95, 112904 (2009).
28. D. S. Jeong, H. Schroeder, and R. Waser. Coexistence of bipolar and unipolar resistive switching behaviors in a Pt/TiO<sub>2</sub>/Pt stack. *Electrochemical and Solid State Letters*, 10, G51-G53 (2007).
29. X. Sun, G. Li, X. Zhang, L. Ding, and W. Zhang. Coexistence of the bipolar and unipolar resistive switching behaviours in Au/SrTiO<sub>3</sub>/Pt cells. *Journal of Physics D-Applied Physics*, 44, 125404/1-5 (2011).
30. T. Yanagida, K. Nagashima, K. Oka, M. Kanai, A. Klamchuen, B.H. Park, and T. Kawai. Scaling Effect on Unipolar and Bipolar Resistive Switching of Metal Oxides. *Scientific reports*, 3 (2013).

31. R. Waser, R. Dittmann, G. Staikov, and K. Szot. Redox-Based Resistive Switching Memories - Nanoionic Mechanisms, Prospects, and Challenges. *Advanced Materials*, 21, 2632-2663 (2009).
32. M. Kund, G. Beitel, C. U. Pinnow, T. Roehr, J. Schumann, R. Symanczyk, K. D. Ufert, and G. Mueller. Conductive bridging RAM (CBRAM): an emerging non-volatile memory technology scalable to sub 20nm. *Electron Devices Meeting, 2005. IEDM Technical Digest. IEEE International, IEDM Tech. Dig.*, 754 - 757 (2005).
33. Z. Wei, T. Takagi, Y. Kanzawa, Y. Katoh, T. Ninomiya, K. Kawai, S. Muraoka, S. Mitani, K. Katayama, S. Fujii, R. Miyanaga, Y. Kawashima, T. Mikawa, K. Shimakawa, and K. Aono. Retention model for high-density ReRAM. *2012 4th IEEE International Memory Workshop, IMW 2012, 2012 4th IEEE International Memory Workshop, IMW 2012* (2012).
34. M. N. Kozicki, M. Park, and M. Mitkova. Nanoscale memory elements based on solid-state electrolytes. *IEEE Transactions on Nanotechnology, USA*, 4, 331-338 (2005).
35. Myoung-Jae Lee, Chang Bum Lee, Dongsoo Lee, Seung Ryul Lee, Man Chang, Ji Hyun Hur, Young-Bae Kim, Chang-Jung Kim, David H. Seo, Sunae Seo, U-In Chung, In-Kyeong Yoo, and Kinam Kim. A fast, high-endurance and scalable non-volatile memory device made from asymmetric Ta<sub>2</sub>O<sub>5-x</sub>/TaO<sub>2-x</sub> bilayer structures. *Nature Materials*, 625-630 (2011).
36. B. Govoreanu, G. S. Kar, Y-Y. Chen, V. Paraschiv, S. Kubicek, A. Fantini, I. P. Radu, L. Goux, S. Clima, R. Degraeve, N. Jossart, O. Richard, T. Vandeweyer, K. Seo, P. Hendrickx, G. Pourtois, H. Bender, L. Altimime, D. J. Wouters, J. A. Kittl, and M. Jurczak. 10x10nm<sup>2</sup> Hf/HfO<sub>x</sub> Crossbar Resistive RAM with Excellent Performance, Reliability and Low-Energy Operation. *2011 IEEE International Electron Devices Meeting - IEDM '11, IEDM Tech. Dig.*, S31.6 (2011).
37. M. Meier, R. Rosezin, S. Gilles, A. Rüdiger, C. Kügeler, and R. Waser. A multilayer RRAM nanoarchitecture with resistively switching Ag-doped spin-on glass. *Proceedings of 10th International Conference on Ultimate Integration on Silicon, March 18-20, Aachen, Proceedings of 10th International Conference on Ultimate Integration on Silicon*, 143-146 (2009).
38. J. J. Yang, D. B. Strukov, and D. R. Stewart. Memristive devices for computing. *Nature Nanotechnology*, 8, 13-24 (2013).
39. M. Di Ventra and Y. V. Pershin. The parallel approach. *Nature Physics*, 9, 200-202 (2013).

40. J. Borghetti, G. S. Snider, P. J. Kuekes, J. J. Yang, D. R. Stewart, and R. S. Williams. ‘Memristive’ switches enable ‘stateful’ logic operations via material implication. *Nature*, 464, 873-876 (2010).
41. E. Linn, R. Rosezin, S. Tappertzhofen, U. Böttger, and R. Waser. Beyond von Neumann-logic operations in passive crossbar arrays alongside memory operations. *Nanotechnology*, 23, 305205/1-6 (2012).
42. Myoung. -. Jae. Lee, Sun. I. Kim, Chang. B. Lee, Huaxiang. Yin, Seung. -. Eon. Ahn, BoS. Kang, Ki. H. Kim, Jae. C. Park, Chang. J. Kim, Ihun. Song, Sang. W. Kim, Genrikh. Stefanovich, Jung. H. Lee, Seok. J. Chung, Yeo.n. H. Kim, and Youngsoo. Park. Low-Temperature-Grown Transition Metal Oxide Based Storage Materials and Oxide Transistors for High-Density Non-volatile Memory. *Advanced Functional Materials*, 19, 1587-1593 (2009).
43. K. H. Kim, S. Gaba, D. Wheeler, J. M. Cruz-Albrecht, T. Hussain, N. Srinivasa, and W. Lu. A Functional Hybrid Memristor Crossbar-Array/CMOS System for Data Storage and Neuromorphic Applications. *Nano Letters*, 12, 389-395 (2012).
44. I. G. Baek, C. J. Park, H. Ju, D. J. Seong, H. S. Ahn, J. H. Kim, M. K. Yang, S. H. Song, E. M. Kim, S. O. Park, C. H. Park, C. W. Song, G. T. Jeong, S. Choi, H. K. Kang, and C. Chung. Realization of Vertical Resistive Memory (VRRAM) using cost effective 3D Process. 2011 Ieee International Electron Devices Meeting (iedm) (2011).
45. H.-Y. Chen, S. Yu, B. Gao, P. Huang, J. Kang, and H.-S. P. Wong. HfOx based vertical resistive random access memory for cost-effective 3D cross-point architecture without cell selector. 2012 Ieee International Electron Devices Meeting (iedm 2012), 20.7 (4 pp.)-20.7 (4 (2012).
46. T.-Y. Liu, T. H. Yan, R. Scheuerlein, Y. Chen, J. K. Lee, G. Balakrishnan, G. Yee, H. Zhang, A. Yap, J. Ouyang, T. Sasaki, S. Addepalli, A. Al-Shamma, C.-Y. Chen, M. Gupta, G. Hilton, S. Joshi, A. Kathuria, V. Lai, D. Masiwal, M. Matsumoto, A. Nigam, A. Pai, J. Pakhale, C. H. Siau, X. Wu, R. Yin, L. Peng, J. Y. Kang, S. Huynh, H. Wang, N. Nagel, Y. Tanaka, M. Higashitani, T. Minvielle, C. Gorla, T. Tsukamoto, T. Yamaguchi, M. Okajima, T. Okamura, S. Takase, T. Hara, H. Inoue, L. Fasoli, M. Mofidi, R. Shrivastava, and K. Quader. A 130.7mm 2 2-layer 32Gb ReRAM memory device in 24nm technology. *Proceedings of the IEEE International Solid-State Circuits Conference (ISSCC 2013)*, 210-211 (2013).
47. S. Yu, H.-Y. Chen, B. Gao, J. Kang, and H.-S. P. Wong. HfOx-Based Vertical Resistive Switching Random Access Memory Suitable for Bit-Cost-Effective Three-Dimensional Cross-Point Architecture.. *Acs Nano*, 7, 2320-5 (2013).

48. S. Yu, H.-Y. Chen, Y. Deng, B. Gao, Z. Jiang, J. Kang, and H.-S. P. Wong. 3D vertical RRAM - Scaling limit analysis and demonstration of 3D array operation. 2013 Symposium on Vlsi Technology, T158-9 (2013).
49. E. Linn, R. Rosezin, C. Kuegeler, and R. Waser. Complementary Resistive Switches for Passive Nanocrossbar Memories. *Nature Materials*, 9, 403-406 (2010).
50. J. Liang and H.-S. P. Wong. Cross-Point Memory Array without Cell Selectors—Device Characteristics and Data Storage Pattern Dependencies. *IEEE Transactions on Electron Devices*, 57, 2531 - 2538 (2010).
51. Sungho Kim, Jiantao Zhou, Kuk-Hwan Kim, and Wei Lu. Crossbar RRAM Arrays: Selector Device Requirements during Read Operation. *Electron Devices, IEEE Transactions on*, 61, 1369-1376 (2014).
52. A. Chen. A Comprehensive Crossbar Array Model with Solutions for Line Resistance and Nonlinear Device Characteristics. *IEEE Transactions on Electron Devices*, 60, 1318 - 1326 (2013).
53. X. Liu, S. M. Sadaf, M. Son, J. Shin, J. Park, J. Lee, S. Park, and H. Hwang. Diode-less bilayer oxide ( $\text{WO}_x - \text{NbO}_x$ ) device for cross-point resistive memory applications. *Nanotechnology*, 22, 475702/1-7 (2011).
54. M. D. Pickett, G. Medeiros-Ribeiro, and R. S. Williams. A scalable neuristor built with Mott memristors. *Nature Materials*, 12, 114-117 (2013).
55. Z. Zhang, Y. Wu, H.-S. P. Wong and S. S. Wong. Nanometer-Scale  $\text{HfO}_x$  RRAM. *IEEE Electron Device Letters*, 34, 1005-7 (2013).
56. S. M. George. Atomic Layer Deposition: An Overview. *Chemical Reviews*, 110, 111-131 (2010).
57. H. B. Profijt, S. E. Potts, M. C. M. van de Sanden, and W. M. M. Kessels. Plasma-Assisted Atomic Layer Deposition: Basics, Opportunities, and Challenges. *Journal of Vacuum Science and Technology A*, 29, 50801/1- (2011).
58. Ivo. J. M. Erkens, Marcel. A. Verheijen, H. a. r. m. C. M. Knoop, Tatiana. F. Landaluce, Fred. Roozeboom and Wilhelmus. M. M. Kessels. Plasma-Assisted Atomic Layer Deposition of  $\text{PtO}_x$  from (MeCp)  $\text{PtMe}_3$  and  $\text{O}_2$  Plasma. *Chemical Vapor Deposition*, 20, 258-268 (2014).
59. Y. Wu, P. M. Hermkens, B. W. H. van de Loo, H. C. M. Knoop, S. E. Potts, M. A. Verheijen, F. Roozeboom, and W. M. M. Kessels. Electrical transport and Al doping efficiency in nanoscale  $\text{ZnO}$  films prepared by atomic layer deposition. *Journal of Applied Physics*, 114, 24308/1- (2013).

60. N. Aslam, V. Longo, C. Rodenbuecher, F. Roozeboom, W. M. M. Kessels, K. Szot, R. Waser, and S. Hoffmann-Eifert. Impact of composition and crystallization behavior of atomic layer deposited strontium titanate films on the resistive switching of Pt/STO/TiN devices. *Journal of Applied Physics*, 116, 64503/1- (2014).
61. R. Migoni, K. H. Rieder, K. Fischer, and H. Bilz. Lattice-Dynamics and Raman-Spectra of SrTiO<sub>3</sub>. *Ferroelectrics*, 13, 377-379 (1976).
62. S. Menzel, M. Waters, A. Marchewka, U. Böttger, R. Dittmann, and R. Waser. Origin of the Ultra-nonlinear Switching Kinetics in Oxide-Based Resistive Switches. *Advanced Functional Materials*, 21, 4487-4492 (2011).
63. K. Szot, W. Speier, G. Bihlmayer, and R. Waser. Switching the electrical resistance of individual dislocations in single-crystalline SrTiO<sub>3</sub>. *Nature Materials*, 5, 312-320 (2006).
64. R. Muenstermann, T. Menke, R. Dittmann, and R. Waser. Coexistence of Filamentary and Homogeneous Resistive Switching in Fe-doped SrTiO<sub>3</sub> Thin-Film Memristive Devices. *Advanced Materials*, 22, 4819-4822 (2010).
65. K. Szot, R. Dittmann, W. Speier, and R. Waser. Nanoscale resistive switching in SrTiO<sub>3</sub> thin films. *Physica Status Solidi-Rapid Research Letters*, 1, R86-R88 (2007).
66. A. Koehl, D. Kajewski, J. Kubacki, C. Lenser, R. Dittmann, P. Meuffels, K. Szot, R. Waser, and J. Szade. Detection of Fe<sup>2+</sup> valence states in Fe doped SrTiO<sub>3</sub> epitaxial thin films grown by pulsed laser deposition. *Physical Chemistry Chemical Physics*, 15, 8311-8317 (2013).
67. K. Shibuya, S. Mi, C.L. Jia, P. Meuffels, and R. Dittmann. SrTiO<sub>4</sub> layered perovskite thin films grown by pulsed laser deposition. *Applied Physics Letters*, 92, 241918 (2008).
68. D. Rosenfeld, P. E. Schmid, S. Szeles, F. Levy, V. Demarne, and A. Grisel. Electrical transport properties of thin-film metal-oxide-metal Nb<sub>2</sub>O<sub>5</sub> oxygen sensors. *Sensors and Actuators B: Chemical*, 37, 83-89 (1996).
69. R. Puurunen. Surface chemistry of atomic layer deposition: A case study for the trimethylaluminum/water process. *Journal of Applied Physics*, 97, 121301/1-52 (2005).
70. T. Suntola. Atomic layer epitaxy. *Thin Solid Films*, 216, 84-89 (1992).



71. V. Lujala, J. Skarp, M. Tammenmaa, and T. Suntola. Atomic layer epitaxy growth of doped zinc-oxide thin-films from organometals. *Applied Surface Science*, 82-3, 34-40 (1994).
72. L. Niinisto, J. Paivasaari, J. Niinisto, M. Putkonen, and M. Nieminen. Advanced electronic and optoelectronic materials by Atomic Layer Deposition: An overview with special emphasis on recent progress in processing of high-k dielectrics and other oxide materials. *Physica Status Solidi a-Applied Research*, 201, 1443-1452 (2004).
73. G. S. Higsshi and C. G. Fleming. Sequential surface chemical-Reaction Limited Growth of high-quality  $\text{Al}_2\text{O}_3$  dielectrics. *Applied Physics Letters*, 55, 1963-1965 (1989)
74. C. Soto, R. wu, D. W. Bennett, and W. T. Tysoe. Infrared-Spectroscopy of Trimethylaluminum and dimethylaluminum chloride adsorbed on alumina. *Chemistry of Materials*, 6, 1705-1711 (1994).
75. V. Longo, N. Leick, F. Roozeboom, and W. M. M. Kessels. Plasma-Assisted Atomic Layer Deposition of  $\text{SrTiO}_3$ : Stoichiometry and Crystallinity Studied by Spectroscopic Ellipsometry. *ECS Journal of Solid State Science and Technology*, 2, N15-N22 (2013).
76. T. Blanquart, J. Niinisto, M. Heikkila, T. Sajavaara, K. Kukli, E. Puukilainen, C. Xu, W. Hunks, M. Ritala, and M. Leskela. Evaluation and Comparison of Novel Precursors for Atomic Layer Deposition of  $\text{Nb}_2\text{O}_5$  Thin Films. *Chemistry of Materials*, 24, 975-980 (2012).
77. I. Kärkkänen, A. Shkabko, K. Szot, N. Aslam, M. Heikkilä, M. Vehkamäki, J. Niinistö, M. Ritala, M. Leskelä, S. Hoffmann-Eifert, and R. Waser. Defect driven conduction and resistive switching in polycrystalline  $\text{ZrO}_2$ . (2013).
78. V. Longo, F. Roozeboom, W. M. M. Kessels, and M. A. Verheijen. ALD of  $\text{SrTiO}_3$  and Pt for  $\text{Pt/SrTiO}_3/\text{Pt}$  MIM structures: Growth and Crystallization study. *ECS Transactions*, 58, 153-162 (2013).
79. V. Longo, M. A. Verheijen, F. Roozeboom, and W. M. M. Kessels. Crystallization Study by Transmission Electron Microscopy of  $\text{SrTiO}_3$  Thin Films Prepared by Plasma-Assisted ALD. *ECS Journal of Solid State Science and Technology*, 2, N120-N124 (2013).
80. S. Witek, D. M. Smyth, and H. Pickup. Variability of the Sr/Ti Ratio in  $\text{SrTiO}_3$ . *Journal of the American Ceramic Society*, 67, 372-375 (1984).

81. G. J. McCarthy, W. B. White, and R. Roy. Phase Equilibria in the 1375°C Isotherm of the System Sr-Ti-O. *Journal of the American Ceramic Society*, 52, 463-467 (1969).
82. R. Tilley. Electron-Microscope Study of Perovskite-Related Oxides in Sr-Ti-O System. *Journal of Solid State Chemistry*, 21, 293-301 (1977).
83. K. Szot and W. Speier. Surfaces of reduced and oxidized SrTiO<sub>3</sub> from atomic force microscopy. *Physical Review B: Condensed Matter*, 60, 5909-26 (1999).
84. M. Fujimoto and M. Watanabe. Ti<sub>n</sub>O<sub>2n-1</sub> Magneli phase formation in SrTiO<sub>3</sub> dielectrics. *Journal of Materials Science*, 20, 3683-3690 (1985).
85. N. A. Benedek, A. L. Chua, C. Elsaesser, A. P. Sutton, and M. W. Finnis. Interatomic potentials for strontium titanate: An assessment of their transferability and comparison with density functional theory. *Phys. Rev. B*, 78, 064110 (2008).
86. N. A. Benedek, C. Elsaesser, and M. W. Finnis. First principles investigation of polarisation at interfaces in multilayered strontium titanate - art. no. 012005. *Journal of Physics: Conference Series*, 94, 12005-12005 (2008).
87. N. Menou, M. Popovici, S. Clima, K. Opsomer, W. Polspoel, B. Kaczer, G. Rampelberg, K. Tomida, M. A. Pawlak, C. Detavernier, D. Pierreux, J. Swerts, J. W. Maes, D. Manger, M. Badylevich, V. V. Afanas'ev, T. Conard, P. Favia, H. Bender, B. Brijs, W. Vandervorst, S. Van Elshocht, G. Pourtois, D. J. Wouters, S. Biesemans, and J. A. Kittl. Composition influence on the physical and electrical properties of Sr<sub>x</sub>Ti<sub>1-x</sub>O<sub>y</sub>-based metal-insulator-metal capacitors prepared by atomic layer deposition using TiN bottom electrodes. *Journal of Applied Physics*, 106, 94101/1-7 (2009).
88. S. Clima, G. Pourtois, N. Menou, M. Popovici, A. Rothschild, B. Kaczer, S. Van Elshocht, X. P. Wang, J. Swerts, D. Pierreux, S. DeGendt, D. J. Wouters, and J. A. Kittl. Sr excess accommodation in ALD grown SrTiO<sub>3</sub> and its impact on the dielectric response. *Microelectronic Engineering*, 86, 1936-1938 (2009).
89. M. Popovici, S. Van Elshocht, N. Menou, P. Favia, H. Bender, E. Rosseel, J. Swerts, C. Adelman, C. Vrancken, A. Moussa, H. Tielens, K. Tomida, M. Pawlak, B. Kaczer, G. Schoofs, W. Vandervorst, D. Wouters, and J. Kittl. Impact of thermal treatment upon morphology and crystallinity of strontium titanate films deposited by atomic layer deposition. *Journal of Vacuum Science and Technology B: Microelectronics and Nanometer Structures*, 29, 01A3041-01A3046 (2011).

90. K. Shibuya, R. Dittmann, S. Mi, and R. Waser. Impact of defect distribution on resistive switching characteristics of  $\text{Sr}_2\text{TiO}_4$  thin films. *Advanced Materials*, 22, 411-414 (2010).
91. D. Briggs and M. P. Seah. *Practical surface analysis: Auger and X-ray photoelectron spectroscopy*. John Wiley & Sons New York (1990).
92. B. Psiuk, J. Szade, H. Schroeder, H. Haselier, M. Mlynarczyk, R. Waser, and K. Szot. Photoemission study of  $\text{SrTiO}_3$  surface layers instability upon metal deposition. *Applied Physics a-Materials Science & Processing*, 89, 451-455 (2007).
93. M. Lukosius, Ch. Wenger, T. Blomberg, A. Abrutis, G. Lupina, P. K. Baumann, and G. Ruhl. Electrical and Morphological Properties of ALD and AVD Grown Perovskite-Type Dielectrics and Their Stacks for Metal-Insulator-Metal Applications. *Ecs Journal of Solid State Science and Technology*, 1, N1-N5 (2012).
94. M. Lukosius, T. Blomberg, D. Walczyk, G. Ruhl, and Ch. Wenger. Metal-Insulator-Metal capacitors with ALD grown  $\text{SrTiO}_3$ : Influence of Pt electrodes. *IOP Conf. Ser.: Mater. Sci. Eng.* 41, 12015/1-7 (2012).
95. Y. Wang and N. Heron. Nanometer-sized semiconductor clusters - material synthesis, quantum size effects, and photochemical properties. *Journal of Physical Chemistry*, 95, 525-532 (1991).
96. G. Hodes, A. Albuyaron, F. Decker, and P. Motisuke. 3-Dimensional quantum-size effect in chemically deposited cadmium selenide films. *Physical Review B*, 36, 4215-4221 (1987).
97. V. Kolosov and A. Thölén. Transmission electron microscopy studies of the specific structure of crystals formed by phase transition in iron oxide amorphous films. *Acta Materialia*, 48, 1829-1840 (2000).
98. T. Blomberg, J. Anttila, S. Haukka, M. Tuominen, M. Lukosius, Ch. Wenger, and T. Saukkonen. Textured strontium titanate layers on platinum by atomic layer deposition. *Thin Solid Films*, 520, 6535-6540 (2012).
99. D. Gu, S. K. Dey, and P. Majhi. Effective work function of Pt, Pd, and Re on atomic layer deposited  $\text{HfO}_2$ . *Applied Physics Letters*, 89, 82907/1-3 (2006).
100. R. K. Pandey, R. Sathiyarayanan, U. Kwon, V. Narayanan, and K. V. R. M. Murali. Role of point defects and  $\text{HfO}_2/\text{TiN}$  interface stoichiometry on effective work function modulation in ultra-scaled complementary metal-oxide-semiconductor devices. *Journal of Applied Physics*, 114, 34505/1-7 (2013).

101. W. Lee, J. H. Han, W. Jeon, Y. W. Yoo, S. W. Lee, S. K. Kim, C. H. Ko, C. Lansalot-Matras, and C. S. Hwang. Atomic Layer Deposition of  $\text{SrTiO}_3$  Films with Cyclopentadienyl-Based Precursors for Metal-Insulator-Metal Capacitors. *Chemistry of Materials*, 25, 953-961 (2013).
102. N. Aslam, V. Longo, W. Keuning, F. Roozeboom, W.M.M. Kessels, R. Waser, and S. Hoffmann-Eifert. Influence of stoichiometry on the performance of MIM capacitors from plasma-assisted ALD  $\text{Sr}_x\text{Ti}_y\text{O}_z$  films. *Physica Status Solidi (a)*, 211, 389-396 (2014).
103. D. S. Jeong, H. Schroeder, U. Breuer, and R. Waser. Characteristic electroforming behavior in  $\text{Pt/TiO}_2/\text{Pt}$  resistive switching cells depending on atmosphere. *Journal of Applied Physics*, 104, 123716/1-8 (2008).
104. M. Lanza, G. Bersuker, M. Porti, E. Miranda, M. Nafria, and X. Aymerich. Resistive switching in hafnium dioxide layers: Local phenomenon at grain boundaries. *Applied Physics Letters*, 101, 193502 (2012).
105. Y. Y. Chen, L. Goux, L. Pantisano, J. Swerts, C. Adelmann, S. Mertens, V. V. Afanas'ev, X. P. Wang, B. Govoreanu, R. Degraeve, S. Kubicek, V. Paraschiv, B. Verbrugge, N. Jossart, L. Altimime, M. Jurczak, J. Kittl, G. Groeseneken, and D. J. Wouters. Scaled X-bar  $\text{TiN}/\text{HfO}_2/\text{TiN}$  RRAM cells processed with optimized plasma enhanced atomic layer deposition (PEALD) for  $\text{TiN}$  electrode. *Microelectronic Engineering*, 112, 92-96 (2013).
106. D. Kajewski, R. Wrzalik, M. Wojtyniak, M. Pilch, J. Szade, K. Szot, Ch. Lenser, R. Dittmann, and R. Waser. Local conductivity of epitaxial Fe-doped  $\text{SrTiO}_3$  thin films. *Phase Transitions*, 84, 483-488 (2011).
107. A. Nowak, J. Persson, B. Schmelzer, J. Szade, and K. Szot. Low temperature reduction in Ta-O and Nb-O thin films. *Journal of Physics D: Applied Physics*, 47, 135301/1- (2014).
108. K. Jung, Y. Kim, Y. S. Park, W. Jung, J. Choi, B. Park, H. Kim, W. Kim, J. Hong, and H. Im. Unipolar resistive switching in insulating niobium oxide film and probing electroforming induced metallic components. *Journal of Applied Physics*, 109, 54511/1-4 (2011).
109. C. Nauenheim, C. Kuegeler, A. Ruediger, and R. Waser. Investigation of the electroforming process in resistively switching  $\text{TiO}_2$  nanocrosspoint junctions. *Applied Physics Letters*, 96, 122902 (2010).
110. X. Liu, S. M. Sadaf, M. Son, J. Park, J. Shin, W. Lee, K. Seo, D. Lee, and H. Hwang. Co-Occurrence of Threshold Switching and Memory Switching in  $\text{Pt}/\text{NbOx}/\text{Pt}$  Cells for Crosspoint Memory Applications. *IEEE Electron Device Letters*, 33, 236-238 (2012).

111. Fabien. Alibart and Dmitri. B. Strukov. Utilizing NDR effect to reduce switching threshold variations in memristive devices. *Applied Physics A: Materials Science and Processing*, 111, 199-202 (2013).
112. Prakash. Periasamy, Joseph. J. Berry, Arrelaine. A. Dameron, Jeremy. D. Bergeson, David. S. Ginley, Ryan. P. O' Hayre, and Philip. A. Parilla. Fabrication and Characterization of MIM Diodes Based on Nb/Nb<sub>2</sub>O<sub>5</sub> Via a Rapid Screening Technique. *Advanced Materials*, 23, 3080+ (2011).
113. D. C. Kim, S. Seo, S. E. Ahn, D.-S. Suh, M. J. Lee, B.-H. Park, and I. K. Yoo. Electrical observations of filamentary conductions for the resistive memory switching in NiO films. *Applied physics letters*, 88, 202102 (2006).
114. S. Kumar, M. D. Pickett, J. P. Strachan, G. Gibson, Y. Nishi, and R. S. Williams. Local Temperature Redistribution and Structural Transition During Joule-Heating-Driven Conductance Switching in VO<sub>2</sub>. *Advanced Materials*, 25, 6128-6132 (2013).
115. H. Schroeder and D.S. Jeong. Resistive switching in a Pt/TiO<sub>2</sub>/Pt thin film stack – a candidate for a non-volatile ReRAM. *Microelectronic Engineering*, 84, 1982-1985 (2007).
116. K. M. Kim, D. Kwon, J. H. Jang, M. H. Lee, S. J. Song, G. H. Kim, J. Y. Seok, B. Lee, S. Han, M. Kim, C. S. HwangS. Kar, S. VanElshocht, D. Misra, M. Houssa, D. Landheer, and K. Kita. Identity of the Conducting Nanofilaments in TiO<sub>2</sub> and the Resistance Switching Mechanism of TiO<sub>2</sub>/NiO Stacked Layers., 33, 291-298 (2010).
117. R. Muenstermann, J. J. Yang, J. P. Strachan, G. Medeiros-Ribeiro, R. Dittmann, and R. Waser. Morphological and electrical changes in TiO<sub>2</sub> memristive devices induced by electroforming and switching. *Physica Status Solidi-Rapid Research Letters*, 4, 16-18 (2010).
118. G. Dearnaley, A. M. Stoneham, and D. V. Morgan. Electrical phenomena in amorphous oxide films. *Reports on Progress in Physics*, 33, 1129-1191 (1970).
119. D. Adler, M. S. Shur, M. Silver, and S. R. Ovshinsky. Threshold switching in chalcogenide-glass thin films. *Journal of Applied Physics, USA*, 51, 3289-309 (1980).
120. K. L. Chopra. Current-controlled negative resistance in thin Niobium oxide films. *Proceedings of the IEEE*, 51, 941-& (1963).
121. D. V. Geppert. A new negative-resistance device. *Proceedings of the IEEE*, 51, 223-& (1963).

122. F. A. Chudnovskii, L.L.Odynets, A. L. Pergament, and G. B. Stefanovich. Electroforming and switching in oxides of transition metals: the role of metal-insulator transition in the switching mechanism. *Journal of Solid State Chemistry, USA*, 122, 95-9 (1996).
123. S. H. Shin, T. Halpern, and P. M. Raccach. High-speed high-current field switching of NbO<sub>2</sub>. *Journal of Applied Physics*, 48, 3150-3153 (1977).
124. M. D. Pickett, J. Borghetti, J. J. Yang, G. Medeiros-Ribeiro, and R. S. Williams. Coexistence of Memristance and Negative Differential Resistance in a Nanoscale Metal-Oxide-Metal System. *Advanced Materials*, 23, 1730+ (2011).
125. J. Kim, C. Ko, A. Frenzel, S. Ramanathan, and J. E. Hoffman. Nanoscale imaging and control of resistance switching in VO<sub>2</sub> at room temperature. *Applied Physics Letters*, 96, 213106/1- (2010).
126. K. Jung, Y. Kim, W. Jung, H. Im, B. Park, J. Hong, J. Lee, J. Park, and J. K. Lee. Electrically induced conducting nanochannels in an amorphous resistive switching niobium oxide film. *Applied Physics Letters*, 97, 233509/1-3 (2010).
127. M. D. Pickett and R. S. Williams. Sub-100 fJ and sub-nanosecond thermally driven threshold switching in niobium oxide crosspoint nanodevices. *Nanotechnology*, 23, 215202 (2012).
128. J. Bae, I. Hwang, Y. Jeong, S.-O. Kang, S. Hong, J. Son, J. Choi, J. Kim, J. Park, M.-J. Seong, Q. Jia, and B. H. Park. Coexistence of bi-stable memory and mono-stable threshold resistance switching phenomena in amorphous NbO<sub>x</sub> films. *Applied Physics Letters*, 100, 62902/1- (2012).
129. R. F. Janninck and D. H. Whitmore. Electrical conductivity and thermoelectric power of niobium dioxide. *Journal of Physics and Chemistry of Solids*, 27, 1183-& (1966).
130. C. N. Berglund. Thermal filaments in vanadium dioxide. *IEEE Transactions on Electron Devices*, ED16, 432-& (1969).
131. Y. Cassuto, S. Kvatinsky, and E. Yaakobi. Sneak-path constraints in memristor crossbar arrays. 2013 Ieee International Symposium On Information Theory (isit), 156-60 (2013).
132. S. H. Chang, S. B. Lee, D. Y. Jeon, S. J. Park, G. T. Kim, S. M. Yang, S. C. Chae, H. K. Yoo, B. S. Kang, M. Lee, and T. W. Noh. Oxide Double-Layer Nanocrossbar for Ultrahigh-Density Bipolar Resistive Memory. *Advanced Materials*, 23, 4063-4067 (2011).

133. Y. Bai, H. Wu, R. Wu, Y. Zhang, N. Deng, Z. Yu, and H. Qian. Study of Multi-level Characteristics for 3D Vertical Resistive Switching Memory.. Scientific Reports, 4, 5780-5780 (2014).
134. S. Kim, S.-J. Kim, K. M. Kim, S. R. Lee, M. Chang, E. Cho, Y.-B. Kim, C. J. Kim, U.-I. Chung, and I.-K. Yoo. Physical electro-thermal model of resistive switching in bi-layered resistance-change memory. Scientific Reports, 3, 1680/1- (2013).
135. X. B. Yan, J. Yin, Z. G. Liu, and X. Y. Xia. Studies on the reset power needed for the unipolar resistive switching in amorphous SrTiO<sub>3</sub>-delta films induced by electrical pulse. Physical Letters A, 375, 3599-3603 (2011).
136. S. Larentis, F. Nardi, S. Balatti, D. Ielmini, and D. C. Gilmer. Bipolar-switching model of RRAM by field- and temperature-activated ion migration. 2012 4th Ieee International Memory Workshop (imw), 4 pp.-4 pp. (2012).
137. F. Nardi, S. Larentis, S. Balatti, D. Gilmer, and D. Ielmini. Resistive switching by voltage-driven ion migration in bipolar RRAMPart I: Experimental study. IEEE Transactions on Electron Devices, 59, 2461-2467 (2012).
138. B. Gao, S. Yu, N. Xu, L. F. Liu, B. Sun, X. Y. Liu, R. Q. Han, J. F. Kang, B. Yu, and Y. Y. Wang. Oxide-Based RRAM Switching Mechanism: A New Ion-Transport-Recombination Model. Ieee International Electron Devices Meeting 2008, Technical Digest, 563-566 (2008).
139. N. Xu, B. Gao, L. F. Liu, B. Sun, X. Y. Liu, R. Q. Han, J. F. Kang, and B. Yu. A unified physical model of switching behavior in oxide-based RRAM. Symposium on VLSI Technology, Honolulu, HI, 2008 Symposium On VLSI Technology, Digest of Technical Papers, 100-101 (2008).
140. S. Larentis, F. Nardi, S. Balatti, D. C. Gilmer, and D. Ielmini. Resistive Switching by Voltage-Driven Ion Migration in Bipolar RRAM-Part II: Modeling. IEEE Transactions on Electron Devices, 59, 2468-2475 (2012).
141. P. Bousoulas, I. Michelakaki, and D. Tsoukalas. Influence of oxygen content of room temperature TiO<sub>2</sub>-x deposited films for enhanced resistive switching memory performance. Journal of Applied Physics, 115, 34516/1- (2014).
142. S. Z. Rahaman, S. Maikap, W. S. Chen, H. Y. Lee, F. T. Chen, T. C. Tien, and M. J. Tsai. Impact of TaOx nanolayer at the GeSex/W interface on resistive switching memory performance and investigation of Cu nanofilament. Journal of Applied Physics, 111, 63710/1- (2012).

143. Jing. Qi, Mario. Olmedo, Jian-Guo. Zheng, and Jianlin. Liu. Multimode Resistive Switching in Single ZnO Nanoisland System. *Scientific Reports*, 3, 2405/1- (2013).
144. D. Acharyya, A. Hazra, K. Dutta, R. K. Gupta, and P. Bhattacharyya. Highly repeatable multilevel resistive switching characteristics of an Au/TiO<sub>2</sub>/Ti memory device. *Semiconductor Science and Technology*, 28, 125001/1- (2013).
145. L. Zhao, H. -. Y. Chen, S. -. C. Wu, Z. Jiang, S. Yu, T. -. H. Hou, H. -. S. P. Wong, and Y. Nishi. Multi-level control of conductive nano-filament evolution in HfO<sub>2</sub> ReRAM by pulse-train operations. *Nanoscale*, 6, 5698-5702 (2014).
146. J. J. Yang, M. D. Pickett, X. Li, D. A. A. Ohlberg, D. R. Stewart, and R. S. Williams. Memristive switching mechanism for metal/oxide/metal nanodevices. *Nature Nanotechnology*, 3, 429 (2008).
147. D.-H. Kwon, K. M. Kim, J. H. Jang, J. M. Jeon, M. H. Lee, G. H. Kim, X.-S. Li, G.-S. Park, B. Lee, S. Han, M. Kim, and C. S. Hwang. Atomic structure of conducting nanofilaments in TiO<sub>2</sub> resistive switching memory. *Nature Nanotechnology*, 5, 148-153 (2010).
148. J. P. Strachan, J. J. Yang, R. Muenstermann, A. Scholl, G. Medeiros-Ribeiro, D. R. Stewart, and R. S. Williams. Structural and chemical characterization of TiO<sub>2</sub> memristive devices by spatially-resolved NEXAFS. *Nanotechnology*, 20, 485701 (2009).
149. J. P. Strachan, M. D. Pickett, J. J. Yang, S. Aloni, A. L. D. Kilcoyne, G. Medeiros-Ribeiro, and R. S. Williams. Direct Identification of the Conducting Channels in a Functioning Memristive Device. *Advanced Materials*, 22, 3573-3577 (2010).
150. J. P. Strachan, D. B. Strukov, J. Borghetti, J. J. Yang, G. Medeiros-Ribeiro, and R. S. Williams. The switching location of a bipolar memristor: chemical, thermal and structural mapping. *Nanotechnology*, 22, 254015 (2011).
151. Y. M. Lu, M. Noman, Y. N. Picard, J. A. Bain, P. A. Salvador, and M. Skowronski. Impact of Joule heating on the microstructure of nanoscale TiO<sub>2</sub> resistive switching devices. *Journal of Applied Physics*, 113, 163703/1-9 (2013).
152. Max. Avdeev, Matthew. Sale, Stefan. Adams, and R. Prasada. Rao. Screening of the alkali-metal ion containing materials from the Inorganic Crystal Structure Database (ICSD) for high ionic conductivity pathways using the bond valence method. *Solid State Ionics*, 225, 43-46 (2012).



153. M. Posternak, A. J. Freeman, and D. Ellis. Electronic band-structure, optical-properties, and generalized susceptibility of NbO<sub>2</sub>. *Physical Review B*, 19, 6555-6563 (1979).
154. A. A. Bolzan, C. Fong, B. J. Kennedy, and C. J. Howard. A powder neutron-diffraction study of semiconducting and metallic niobium dioxide. *Journal of Solid State Chemistry*, 113, 9-14 (1994).
155. A. Sawa. Resistive switching in transition metal oxides. *Materials Today*, 11, 28-36 (2008).
156. L. Chen, Q. Q. Sun, J. J. Gu, Y. Xu, S. J. Ding, and D. W. Zhang. Bipolar resistive switching characteristics of atomic layer deposited Nb<sub>2</sub>O<sub>5</sub> thin films for nonvolatile memory application. *Current Applied Physics*, 11, 849-852 (2011).
157. H. Maehne, L. Berger, D. Martin, V. Klemm, S. Slesazeck, S. Jakschik, D. Rafaja, and T. Mikolajick. Filamentary resistive switching in amorphous and polycrystalline Nb<sub>2</sub>O<sub>5</sub> thin films. *SOLID-STATE ELECTRONICS*, 72, 73-77 (2012).
158. S. Md. Sadaf, X. Liu, M. Son, S. Park, S. H. Choudhury, E. Cha, M. Siddik, J. Shin, and H. Hwang. Highly uniform and reliable resistance switching properties in bilayer WO<sub>x</sub>/NbO<sub>x</sub> RRAM devices. *Physica Status Solidi a-Applications and Materials Science*, 209, 1179-1183 (2012).
159. S. Seo, M. J. Lee, D. H. Seo, E. J. Jeoung, D. S. Suh, Y. S. Joung, I. K. Yoo, I. R. Hwang, S. H. Kim, I. S. Byun, J. S. Kim, J. S. Choi, and B. H. Park. Reproducible resistance switching in polycrystalline NiO films. *Applied Physics Letters*, 85, 5655-7 (2004).
160. S. H. Chang, J. S. Lee, S. C. Chae, S. B. Lee, C. Liu, B. Kahng, D. Kim, and T. W. Noh. Occurrence of Both Unipolar Memory and Threshold Resistance Switching in a NiO Film. *Physical review letters*, 102, 26801/1- (2009).
161. S. Kim, J. Park, J. Woo, C. Cho, W. Lee, J. Shin, G. Choi, S. Park, D. Lee, B. Lee, and H. Hwang. Threshold-switching characteristics of a nanoscale-NbO<sub>2</sub>-layer- based Pt/NbO<sub>2</sub>/Pt stack for use in cross-point-type resistive memories. *Microelectronic Engineering*, 107, 33-36 (2013).
162. V. Eyert. The metal-insulator transition of NbO<sub>2</sub>: An embedded Peierls instability. *Europhysics Letters*, 58, 851-856 (2002).
163. H. Futaki. A new type semiconductor (critical temperature resistor). *Japanese Journal of Applied Physics*, 4, 28-41 (1965).

- 164. E. Cha, J. Woo, D. Lee, S. Lee, J. Song, Y. Koo, J. Lee, C. G. Park, M. Y. Yang, K. Kamiya, K. Shiraishi, B. Magyari-Kope, Y. Nishi, and H. Hwang. Nanoscale ( ~10nm) 3D vertical ReRAM and NbO<sub>2</sub> threshold selector with TiN electrode. Electron Devices Meeting (IEDM), 2013 IEEE International, 10.5.1-10.5.4 (2013).
- 165. D. B. Strukov and R. S. Williams. Four-dimensional address topology for circuits with stacked multilayer crossbar arrays. Proceedings of the National Academy of Sciences, 106, 20155-20158 (2009).
- 166. R. Rosezin, E. Linn, L. Nielen, C. Kuegeler, R. Bruchhaus, and R. Waser. Integrated Complementary Resistive Switches for Passive High-Density Nanocrossbar Arrays. IEEE Electron Device Letters, 32, 191-193 (2011).
- 167. Mohammed. Affan. Zidan, Hossm. Aly. Hassan. Fahmy, Muhammad. Mustafa. Hussain, and Khaled. Nabil. Salama. Memristor-based memory: The sneak paths problem and solutions. Microelectronics Journal, 44, 176-183 (2013).
- 168. J.-J. Huang, Y.-M. Tseng, C.-W. Hsu, and T.-H. Hou. Bipolar Nonlinear Ni/TiO<sub>2</sub>/Ni Selector for 1S1R Crossbar Array Applications. IEEE Electron Device Letters, DOI:10.1109/LED.2011.2161601 (2011).
- 169. D. Lee, J. Park, S. Jung, G. Choi, J. Lee, S. Kim, J. Woo, M. Siddik, E. Cha, and H. Hwang. Operation Voltage Control in Complementary Resistive Switches Using Heterodevice. IEEE Electron Device Letters, 33, 600-602 (2012).
- 170. S. Kim, W. Lee, and H. Hwang. Selector Devices for Cross-point ReRAM. 13th International Workshop on Cellular Nanoscale Networks and their Applications (CNNA), Turin, ITALY, 2012 13th International Workshop On Cellular Nanoscale Networks and Their Applications (cnna) (2012).
- 171. J. J. Yang, J. Borghetti, D. Murphy, D. R. Stewart, and R. S. Williams. A family of electronically reconfigurable nanodevices. Advanced Materials, 21, 3754-3758 (2009).
- 172. J. Woo, D. Lee, G. Choi, E. Cha, S. Kim, W. Lee, S. Park, and H. Hwang. Selector-less RRAM with non-linearity of device for cross-point array applications. Microelectronic Engineering, 109, 360-363 (2013).
- 173. J. Woo, W. Lee, S. Park, S. Kim, D. Lee, G. Choi, E. Cha, J. Lee, W. Jung, C. Park, and H. Hwang. Multi-layer tunnel barrier (Ta<sub>2</sub>O<sub>5</sub>/TaO<sub>x</sub>/TiO<sub>2</sub>) engineering for bipolar RRAM selector applications. Digest of Technical Papers - Symposium on VLSI Technology, Digest of Technical Papers - Symposium on VLSI Technology, T168-T169 (2013).

174. F. Lentz, B. Roesgen, V. Rana, D. J. Wouters, and R. Waser. Current Compliance-Dependent Nonlinearity in TiO<sub>2</sub> ReRAM. *IEEE Electron Device Letters*, 34, 996-998 (2013).
175. J. J. Yang, M. Zhang, M. D. Pickett, F. Miao, J. P. Strachan, W. D. Li, W. Yi, D. A. A. Ohlberg, B. J. Choi, W. Wu, J. H. Nickel, G. Medeiros-Ribeiro, and R. S. Williams. Engineering nonlinearity into memristors for passive crossbar applications. *Applied Physics Letters*, 100, 113501/1- (2012).
176. C. Nauenheim. Integration of resistive switching devices in crossbar structures. PhD thesis, RWTH Aachen, (2009).
177. D. M. Mattox. Handbook of Physical Vapor Deposition (PVD) Processing. Elsevier, 2 ed., (2010).
178. Clariant, AZ 5214 E product data sheet. Available under:  
[http://www.microchemicals.com/micro/az\\_5214e.pdf](http://www.microchemicals.com/micro/az_5214e.pdf)
179. MicroChemicals, Softbake of Photoresist Films, 2013. Available under:  
[www.microchemicals.com/downloads/application\\_notes.htm](http://www.microchemicals.com/downloads/application_notes.htm).
180. R.P. Elliott *Trans. Am. Soc. Metals*, 52 (1960), p. 990
181. Kikuchi. M, Kusabe.K, Bannai. E, Fukuoka. K, Syono. Y, Hiraga. K. *Jpn J. Appl. Physics*. 24 (1985) 1600.
182. T. W. Hickmott, *J. Vac. Sci. Technol.* 6, 828 (1969).
183. Taylor. D, *Trans.J.Brit.Ceram. Soc.* 83(1984) 32.
184. F. Lentz. Integration of resistive Redox- Bases Resistive Switching Memory Devices. PhD thesis, RWTH Aachen, (2015).
185. X. Liu, S. M. Sadaf, M. Son, J. Park, J. Shin, W. Lee, K. Seo, D. Lee, and H. Hwang. Diode-less bilayer oxide (WO<sub>x</sub>-NbO<sub>x</sub>) device for cross-point resistive switching applications. *Nanotechnology* 22 (2011) 475702.
186. E. Herth, E. Algre. P. Tilmant, M. Francois, C.Boyaval, and B. Legrand, Performance of the Negative Tone Resist AZnLOf202 for the Nanotechnology Applications. *IEEE Transactions on Nanotechnology*, Vol. 11, No. 4, July 2012.
187. E. Reichmanis, L. F. Thompson. Polymer materials for microlithography. *Chem. Rev*, 1989, 89 (6), pp 1273–1289.
188. V. Longo, Atomic layer deposition of Strontium Titanate from material control to nanoscale devices. PhD thesis, Technische Universiteit Eindhoven, (2014).

189. S. Schneider, H. Kohlstedt, and R. Waser, Etching characteristics of noble metal electrode, in Material Research Society Symposium 655, pp. 2.5.1–2.5.6, 2001.
190. E. Kratschmer, Verification of a proximity effect correction program in electron beam lithography, *J. Vac. Sci. Technol.* 19 (4), 1264-1268 (1981)
191. S. Chou, P. Krauss, and P. Renstrom. Imprint of sub-25 nm vias and trenches in polymers. *Appl. Phys. Lett.*, vol. 67, p. 3114, 1995.
192. S. Chou, P. Krauss, and P. Renstrom. Nanoimprint lithography. *Journal of Vacuum Science and Technology B: Microelectronics and Nanometer Structures*, vol. 14, no. 6, pp. 4129–4133, 1996.
193. S. Chou, P. Krauss, and P. Renstrom. Imprint lithography with 25- nanometer resolution. *Science*, vol. 272, no. 5258, pp. 85–87, 1996.
194. J. Haisma, M. Verheijen, K. Van Den Heuvel, and J. Van Den Berg. Mold-assisted nanolithography: A process for reliable pattern replication. *Journal of Vacuum Science and Technology B: Microelectronics and Nanometer Structures*, vol. 14, no. 6, pp. 4124–4128, 1996.
195. C. Peroz, S. Dhuey, M. Cornet, M. Vogler, D. Olynick and S. Cabrini. Single digit nanofabrication by step-and-repeat nanoimprint lithography. *Nanotechnology* 23 015305, 2012.
196. T. Tuma, and A. Burmen, M. Cornet. Circuit Simulation with SPICE OPUS. *Birkhäuser*, 2009.
197. E. Linn, Complementary Resistive Switches. PhD thesis, RWTH Aachen, 2012.
198. S. Ambrogio, S. Balatti, V. Milo, R. Carboni, Z-Q. Wang, A. Calderoni, N. Ramaswamy and D. Ielmini. Neuromorphic Learning and Recognition with One-Transistor-One-Resistor Synapses and Bistable Metal Oxide RRAM. *IEEE Transactions on Electronic Devices*, Vol. 63, No. 4, April 2016
199. S. Y. Zhan, Y. Mei, L. Zheng, M. Cornet. Capability and device performance in flexible electronics for the Internet of Things. *J. Mater. Chem. C*, 2, pp. 1220-1232 (2014)
200. V. V. Zhirnov, R. Meade, R. K. Cavin, G. Sandhu. Scaling limits of resistive memories. *Nanotechnology* Vol. 22, 254027/1-21 (2011)
201. R. Waser, R. Bruchhaus, and S. Menzel. Redox-Based Resistive Random Access Memories’, Chap. 30, in R. Waser ed. *Nanoelectronics and Information Technology* (3rd edition). Wiley-VCH, 683-710 (2012).

202. C. Funck, S. Menzel, N. Aslam, H. Zhang, A. Hardtdegen, R. Waser, and S. Hoffmann-Eifert. Multidimensional Simulation of Threshold Switching in NbO<sub>2</sub> Based on an Electric Field Triggered Thermal Runaway Model. *Adv. Electron. Mater.* 2016, 1600169.
203. S. Slesazeck, H. Maehne, H. Wylezich, A. Wachowiak, J. Radhakrishnan, A. Ascoli. Physical model of threshold switching in NbO<sub>2</sub> based memristors. *RSC Adv.* 2015, 5, 102318.
204. X. Liu, S. K. Nandi, D. K. Venkatachalam, K. Belay, S. Song, R. G. Elliman. Reduced Threshold Current in NbO<sub>2</sub> Selector by Engineering Device Structure. *IEEE Electron device Lett.* 2014, 35, 1055
205. S. Li, X. Liu, S. Nandi, D. Venkatachalam, R. Elliman. in 2014 Conf. Optoelectronic Microelectronic Materials & Devices (COMMAD), IEEE, New York, 2014, 138.
206. H. L. Tuller, S. R. Bishop. Point Defects in Oxides: Tailoring Materials through Defect Engineering. *Ann. Rev. Mater. Res.*, Vol. 41, pp. 369-398 (2011).
207. D. M. Smyth. The defect chemistry of metal oxides. Oxford University Press, ISBN 0-19-511014-5 (2000).
208. S. N. Ruddlesden, P. Popper. The compound Sr<sub>3</sub>Ti<sub>2</sub>O<sub>7</sub> and its structure. *Acta Crystallographica* Vol. 11, pp. 54-55 (1958).
209. A. Magneli. Nonstoichiometry and structural disorder in some families of inorganic compounds. *Pure Appl. Chem.* Vol. 50, pp. 1261-1271 (1978).
210. R. Dittmann. Stoichiometry in epitaxial oxide thin films. Chapter 9, pp. 231-253, in G. Koster, M Huijben, G. Rijnders 'Epitaxial Growth of Complex Metal Oxides', Woodhead Publishing Series 76, Elsevier, Cambridge, UK (2015).
211. R. Waser, T. Baiatu, K. H. Hardtl. DC electrical degradation of perovskite-type titanates. I. *Ceramics. J. Am. Ceram. Soc.* Vol. 73, pp. 1645-53 (1990).
212. S. Hoffmann, R. Waser. Curie-Weiss law of (Ba<sub>1-x</sub>Sr<sub>x</sub>)TiO<sub>3</sub> thin films prepared by chemical solution deposition. *J. Phys. IV*, Vol. 8, pp. 221-224 (1998).
213. R. Woerdenweber, E. Hollmann, R. Ott, T. Hürtgen, Tai Keong Lee. Improved ferroelectricity of strained SrTiO<sub>3</sub> thin films on sapphire. *J Electroceram*, Vol. 22, pp. 363-368 (2008).
214. C. S. Hwang. (Ba, Sr) TiO<sub>3</sub> thin films for ultra large scale dynamic random access memory. A review on the process integration. *Mater. Sci. Eng. B*, Vol. 56, pp. 178-190 (1998).

215. W. Lee, W. Jeon, C. H. An, M. J. Chung, H. J. Kim, T. Eom, S. M. George, B. K. Park, J. H. Han, C. G. Kim, T. M. Chung, S. W. Lee, C. S. Hwang. Improved Initial Growth Behavior of Sr and SrTiO<sub>3</sub> Films Grown by Atomic Layer Deposition Using {Sr(demamp)(tmhd)}<sub>2</sub> as Sr-Precursor. *Chem. Mater.* 27, pp. 3881-3891 (2015).
216. V. Longo, N. Leick, F. Roozeboom, W. M. M. Kessels. Plasma-Assisted Atomic Layer Deposition of SrTiO<sub>3</sub>: Stoichiometry and Crystallinity Studied by Spectroscopic Ellipsometry. *ECS J. Solid State Sci. Technol.* 2, pp. N15-N22 (2013).
217. M. A. Pawlak, B. Kaczer, M. S. Kim, M. Popovici, K. Tomida, J. Swerts, K. Opsomer, W. Polspoel, P. Favia, C. Vrancken, C. Demeurisse, W.-C. Wang, V. V. Afanasev, W. Vandervorst, H. Bender, I. Debusschere, L. Altimime, J. A. Kittl. Impact of crystallization behavior of Sr<sub>x</sub>Ti<sub>y</sub>O<sub>z</sub> films on electrical properties of metal-insulator-metal capacitors with TiN electrodes. *Appl. Phys. Lett.*, 97, p. 162906 (2010).
218. T. Sakata, K. Sakata, G. Hofer, T. Horiuchi. Preparation of NbO<sub>2</sub> single-crystals by chemical transport reaction. *J. Cryst. Growth* 12, p. 88 (1972).
219. E. Cha, J. Woo, D. Lee, S. Lee, J. Song, Y. Koo, J. Lee, C. G. Park, M. Y. Yang, K. Kamiya, K. Shiraishi, B. Magyari-Kope, Y. Nishi, H. Hwang. Nanoscale (~10nm) 3D vertical ReRAM and NbO<sub>2</sub> threshold selector with TiN electrode. p. 268, in *2013 Electron Devices Meeting (IEDM)*, IEEE, New York (2013).
220. S. Raoux, D. Ielmini, M. Wuttig, I. Karpov. Phase change materials. *MRS Bulletin*, Vol 37, pp. 118-123 (2012).
221. G. Burr, R. Shenoy, K. Virwani, P. Narayanan, A. Padilla, B. Kurdi, H. Hwang, Access devices for 3D crosspoint memory, *J. Vac. Sci. Technol. B* 32, p. 040802 (2014).
222. Hwang, C. S. (ed.), *Atomic Layer Deposition for Semiconductors*, Springer. New York, USA (2014).
223. R. D. Leapman, L. A. Grunes, P. L. Fejes, *Phys. Rev. B* 26, 614 - 635 (1982).
224. [web.mit.edu/2.813/www/readings/Ellingham\\_diagrams.pdf](http://web.mit.edu/2.813/www/readings/Ellingham_diagrams.pdf).
225. A.L. Pergament, A.A. Velichko, G.B. Stefanovich, T. Horiuchi. Switching effect and metal-insulator transition in electric field. *Journal of Physics and Chemistry of Solids* Volume 71 2010, 874-879.
226. V. Eyert. The metal-insulator transition of NbO<sub>2</sub>. an embedded Peierls instability *Europhys Lett.* 58 2002, 851-856.

- 227. E. Cha, J. Woo, D. Lee, S. Lee, J. Song, Y. Koo, J. Lee, C. G. Park, M. Y. Yang, K. Kamiya, K. Shiraishi, B. Magyari-Kope, Y. Nishi; H. Hwang. Nanoscale ( $\sim 10\text{nm}$ ) 3D vertical ReRAM and NbO<sub>2</sub> threshold selector with TiN electrode. Electron Devices Meeting (IEDM), 2013 IEEE International, 10.5 (2013).
- 228. A. Wedig, M. Luebben, D.-Y. Cho, M. Moors; K. Skaja, V. Rana, T. Hasegawa, K. Adepli, B. Yildiz, R. Waser, I. Valov. Nanoscale cation motion in TaO<sub>x</sub>, HfO<sub>x</sub> and TiO<sub>x</sub> memristive systems. Nat. Nanotechnol. 11 (2016) 67-74
- 229. C. Baeumer, C. Schmitz; A. Marchewka, D. N. Mueller, R. Valenta; J. Hackl, N. Raab, S. P. Rogers, M. I. Khan, S. Nemsak, M. Shim, S. Menzel, C. M. Schneider, R. Waser, R. Dittmann. Quantifying redox-induced Schottky barrier variations in memristive devices via in operando spectromicroscopy with graphene electrodes. Nat. Commun. 7 (2016) 12398
- 230. R. Dittmann, R. Muenstermann, I. Krug, D. Park, T. Menke, J. Mayer, A. Besmehn, F. Kronast, C. M. Schneider, R. Waser. Scaling Potential of Local Redox Processes in Memristive SrTiO<sub>3</sub> Thin-Film Devices. Proceedings of the IEEE 100 (2012) 1979-1990
- 231. Chencheng Xu, Hongchu Du, Alexander J. H. van der Torren, Jan Aarts, Chun-Lin Jia and Regina Dittmann. Formation mechanism of Ruddlesden-Popper-type antiphase boundaries during the kinetically limited growth of Sr rich SrTiO<sub>3</sub> thin films. Sci.Rep.6, 38296; doi: 10.1038/srep38296 (2016)

Band / Volume 38

**Resistive switching phenomena of extended defects in Nb-doped SrTiO<sub>3</sub> under influence of external gradients**

C. Rodenbücher (2014), xiii, 200 pp

ISBN: 978-3-89336-980-5

Band / Volume 39

**Micro-spectroscopic investigation of valence change processes in resistive switching SrTiO<sub>3</sub> thin films**

A. Köhl (2014), viii, 166 pp

ISBN: 978-3-89336-988-1

Band / Volume 40

**Strained Silicon and Silicon-Germanium Nanowire Tunnel FETs and Inverters**

S. Richter (2014), iii, 117 pp

ISBN: 978-3-95806-002-9

Band / Volume 41

**Integration of Redox-Based Resistive Switching Memory Devices**

F. Lentz (2014), i, 166 pp

ISBN: 978-3-95806-019-7

Band / Volume 42

**Ladungstransportuntersuchungen an nanofunktionalen Bauelementen mit Diodencharakteristik basierend auf funktionalisierten Nanopartikeln**

N. Babajani (2015), iv, 138, XLVII

ISBN: 978-3-95806-026-5

Band / Volume 43

**Transport and Noise Properties of Nanostructure Transistors for Biosensor Applications**

J. Li (2015), vii, 175 pp

ISBN: 978-3-95806-034-0

Band / Volume 44

**Quantitative scanning tunneling spectroscopy of non-polar III-V compound semiconductor surfaces**

M. Schnedler (2015), 122 pp

ISBN: 978-3-95806-075-3

Band / Volume 45

**Model-based Algorithm Development with Focus on Biosignal Processing**

Y. Yao (2015), x, 169 pp

ISBN: 978-3-95806-080-7



Band / Volume 46

**Growth and characterization of crystalline rare-earth based thin oxide films for the application as gate dielectric in nanotechnology**

A. B. Schäfer (2015), xiii, 157 pp

ISBN: 978-3-95806-111-8

Band / Volume 47

**TEM/STEM Investigations of Phase Change Materials for Non-volatile Memory Applications**

M. Bornhöfft (2017), viii, 135 pp

ISBN: 978-3-95806-221-4

Band / Volume 48

**Investigation of ternary nitride semiconductor alloys by scanning tunneling microscopy**

V. Portz (2017), 140 pp

ISBN: 978-3-95806-232-0

Band / Volume 49

**Redox processes and ionic transport in resistive switching binary metal oxides**

K. Skaja (2017), VII, 203 pp

ISBN: 978-3-95806-236-8

Band / Volume 50

**Investigation of switching mechanism in Ta<sub>2</sub>O<sub>5</sub>-based ReRAM devices**

W. Kim (2017), iii, 138 pp

ISBN: 978-3-95806-261-0

Band / Volume 51

**Development of ReRAM-based Devices for Logic- and Computation-in-Memory Applications**

T. Breuer (2017), x, 179 pp

ISBN: 978-3-95806-270-2

Band / Volume 52

**Resistive switching memory devices from atomic layer deposited binary and ternary oxide thin films**

N. Aslam (2017), X, 172 pp

ISBN: 978-3-95806-274-0



**Information**  
**Band/ Volume 52**  
**ISBN 978-3-95806-274-0**

